PHYSICAL AND ELECTROCHEMICAL INTERACTIONS WITHIN HYBRID NANOCOMPOSITES OF RUTHENIUM COORDINATION COMPLEXES AND SINGLE-WALLED CARBON NANOTUBES

by

Jeffrey Resing Alston

A dissertation submitted to the faculty of
The University of North Carolina at Charlotte
in partial fulfillment of the requirements
for the degree of Doctor of Philosophy in
Nanoscale Science

Charlotte

2012

Approved by:

_____
Dr. Jordan C Poler

_____
Dr. Steve Patterson

_____
Dr. Markus Etzkorn

_____
Dr. Thomas A. Schmedake

_____
Dr Maciej Noras

ABSTRACT

JEFFREY RESING ALSTON. Physical and electrochemical interactions within hybrid nanocomposites of ruthenium coordination complexes and single-walled carbon nanotubes. (Under direction of DR. JORDAN C. POLER)

The research presented in this dissertation is a study of the interaction of ruthenium coordination complexes with single-walled carbon nanotubes (SWCNTs), a pursuit ultimately leading to the development of composite SWCNT materials. The work comprising this dissertation includes three major accomplishments: the synthesis and characterization of two new dinuclear ruthenium coordination complexes, the development of isothermal titration calorimetry (ITC) to thermodynamically quantify interactions with SWCNTs, and the fabrication and characterization of ruthenium complex—SWCNT hybrid nanocomposite electrodes.

The work leading to these major accomplishments is inspired by the goal of attaining control over assembly of nanoscale building blocks, i.e. SWCNTs. The first step towards this goal is the development of appropriate molecules that can nondestructively link two SWCNTs together without damaging the physical structure of the tube. $[Cl(trpy)Ru(tpphz)Ru(trpy)Cl](PF_6)_2$ and $[(phen)_2Ru(tpphz)Ru(trpy)Cl](PF_6)_3$ are the two ruthenium dimer molecules synthesized and discussed herein. They possess a rigid nanoscale pocket that contains conjugated π-electron density capable of interacting with the walls of SWCNTs. During the work to synthesize these complexes significant improvements were made to synthetic procedures to produce important precursors. The synthesis of the two complexes and the new synthetic procedures were novel.

The second step required the development of a new tool (ITC) to study the interaction thermodynamics of dispersions of SWCNTs. ITC is a well established tool to measure binding thermodynamics of biological proteins and enzymes. Based on the analogy that can drawn between SWCNTs in solution and proteins, I developed ITC methods and protocols for measuring interactions of solvents with SWCNTs as well as the binding of the ruthenium dimer complexes with SWCNTs. I have established that ITC can be an important nanoscale science and materials development tool which can provide detailed insight into the thermodynamic interactions of nanomaterials in solution.

I combined SWCNTs and ruthenium complexes, and developed procedures to fabricate nanocomposite films. The films produced by our method improve on previously reported techniques by avoiding surfactants and binders which retard the properties of SWCNT films. I was able to transfer these films to various substrates and they were shown to have enhanced capacitance versus pristine SWCNT films when used as an electrode in an electrochemical cell. Augmenting SWCNT electrodes in this way has not been reported and the technique is a promising vehicle for photo-induced charge transfer as well as cheaper and lighter capacitor devices.

DEDICATION

I dedicate this dissertation to my wonderful family. Particularly to my understanding and patient wife, Erin, who has put up with me over these many years of research, and to our precious daughter Ireland, who is the joy of our lives and is a reminder of what it is that I was working for. I must also thank my loving mother, father and sister, without their steadfast support I never would have had the confidence to enter graduate school. And thank you to my terrific in-laws who have given me their fullest support. Finally, I dedicate this work to my best friend, Zeus, a goofy and lovable decade long companion whose gifts of unconditional love, laughter and licks got me through every challenge I faced; he is sorely missed.

ACKNOWLEDGEMENTS

I would like to thank all of those people who helped make this dissertation possible. First, I wish to thank my advisor, Dr. Jordan C. Poler for all his guidance, encouragement, support, and patience. His sincere interests in science and education have been a great inspiration to me. Also, I would like to thank my committee members Dr. Thomas A. Schmedake, Dr. Markus Etzkorn, Dr. Steve Patterson, and Dr. Maciej Noras for their very helpful insights, comments and suggestions. Additionally, I would like to acknowledge all of those people who provided technical support and assistance with running my experiments: Dan Deadwyler and Vladimir Kubalik, for assisting me with everything to do with building electronics; Dr. John Merkert and Dr. Mike Murphy, for assistance with electrochemistry and NMR; Dr. Dan Rabinovich, for his teachings on organometallic chemistry; and Caroline Kennedy, for keeping everything running and making sure everything happened when it needed to. Many thanks also go to Dr. Bernadette Donovan-Merkert, Director of the Nanoscale Science Ph.D. program and all the great faculty and staff that support the program. Finally, I would like to thank my fellow graduate students, Dr. Mike W. Forney, Kevin Major, Natalie Herring, and Shawn Ridlen, who provided invaluable support and suggestions throughout this process.

TABLE OF CONTENTS

LIST OF FIGURES

LIST OF TABLES

CHAPTER 1: INTRODUCTION

"Coal and diamonds, sand and computer chips, cancer and healthy tissue: throughout history, variations in the arrangement of atoms have distinguished the cheap from the cherished, the diseased from the healthy."[1] ~K. Eric Drexler

Nanoscale science is a field defined by physical dimensions. The study of nanoscale science and technology refers to the pursuit of understanding and controlled manipulation of structures that have nanoscale dimensions and the resulting phenomena associated with them. While people have been utilizing nanoscale materials and phenomena for hundreds of years, they have lacked the ability to visualize the nanoscale components of these materials. With modern techniques like scanning and tunneling electron microscopes I now have the ability to see nanoscale features. And with tools like atomic force microscopy we can literally touch and move them at atomic resolution.

The inspiration of the research presented in this dissertation is the pursuit of fabricating carbon nanotube—ruthenium complex composites through controlled aggregation. The ultimate goal is to cheaply and quickly fabricate lightweight and multifunctional composites that can ultimately be transferred to different surfaces and used in many different environments. Towards this end a major focus of this dissertation is the synthesis of rigid ruthenium complexes that are uniquely structured to interact with the sidewalls of SWCNTs. CHAPTER 2: discusses the

endeavor. This synthesis project resulted in the creation of two novel ruthenium coordination compounds. The pursuit of these synthesis goals led to the development of a significantly improved procedure to synthesize dichlorotetrakis (dimethyl sulfoxide) ruthenium. This is an important precursor for an uncountable number of already published and not yet discovered ruthenium complexes. During these synthesis efforts improvements were also made to the procedure for converting phenanthroline-diamines to diones through a dioxime intermediate. This synthesis path has been a source of trouble and confusion for many groups working on similar synthesis goals. The products of this work have contributed to an important library of ruthenium coordination complexes and the improved processes developed herein will benefit the future synthesis efforts in our group as well as aid the synthesis efforts of researchers utilizing these methods.

Significant effort has also gone into the development of isothermal titration calorimetry (ITC) as a characterization tool for dispersions of nanomaterials. This work, discussed in CHAPTER 3: resulted in the first successful application of ITC to measure nonaqueous dispersions of single-walled carbon nanotubes (SWCNTs). The integration of nanoparticles into composites and devices is becoming a major component of nanoscale science development and significantly contributing to the evolution of materials science. This study provides the ground work to establish ITC as a reliable means to measure the thermodynamics and kinetics of nanomaterial interactions with other materials. This work characterizes the interaction of SWCNTs in an aprotic solvent dispersion, and contributes valuable data to the discussion about dispersion stability in mixed solvent systems. Using ITC we

measured the binding enthalpy of the above mentioned ruthenium complexes with the sidewalls of SWCNTs. The magnitude of the binding enthalpy is much higher than predicted and proves that there are strong interactions between the rigid pocket of our unique molecules and SWCNTs. These studies are firsts in the field and have significantly contributed to the discussion in the literature

Ongoing research is discussed in Chapter 4, in which the characterization of SWCNT—ruthenium complex thin film electrodes with electroanalytical methods is being conducted. This work improves on reported techniques to fabricate SWCNT films via filtering. We use aprotic solvent dispersions of SWCNTs which creates films built from pristine SWCNTs, an improvement from processes which use surfactant stabilized dispersions. It was found that we can control the micro-structure of the film by adding different quantities of ruthenium complex to the initial dispersion. This significantly changes the available surface area of the electrode and drastically reduces the specific capacitance. However, preliminary work has shown that with proper control, the inclusion of ruthenium complexes within the SWCNT thin film electrode increases conductivity and can significantly increase electrode capacitance through pseudocapacitance mechanisms. We expect that by utilizing the methods developed in this work we can integrate ruthenium complexes as well as other nanomaterials such as quantum dots into the structure of the thin film electrode. Prototype electrodes that include these materials have shown enhanced capacitance as well as fast charging upon broad spectrum illumination. The electrodes developed in this dissertation are unique in that they maintain the

pristine quality of the SWCNTs and can possibly be used for supercapacitor electrodes as well as new solar energy collection devices.

CHAPTER 2: RUTHENIUM COORDINATION COMPLEXES

2.1 Rigid Ruthenium Complexes and Nanomaterial Assembly

Understanding directed self-assembly of supramolecular systems is critical to the development of nanoscale devices. Dendrimer chemistry is capable of providing both building blocks and scaffolds for supramolecular and nanodevice engineering.[2-5] Metallodendrimers are of broad interest because of their potential use in light harvesting, sensing, signal amplification, and electron-transfer reagents in water splitting applications.[5-7] Optically and electrochemically active ruthenium metallodendrimers possess several properties which enable their versatility in supramolecular systems. By changing the morphology and the local charge density of the ruthenium complexes, we have studied how these mononuclear and decanuclear metallodendrimers (decamers)[8] interact with and coordinate to single-walled carbon nanotubes (SWCNTs).[3,4,9] Towards this end, novel dinuclear ruthenium coordination complexes (dimers) have been synthesized. The results presented below will enable further studies of the optoelectronic properties of ruthenium coordination compounds and their interactions with nanoparticles. Specifically these new compounds will help us discriminate between the supramolecular interactions due to molecular morphology and the interactions due to the electron density distributions and net molecular charge on the compounds.

I have synthesized two novel structurally similar ruthenium dimers with differing electrostatic charges. Both complexes are composed of two ruthenium mononuclear units bridged by the aromatic tetrapyrido[3,2-α:2′,3′-c:3″,2″-h:2″,3″-j]phenazine (tpphz) ligand. Coordinating various ligands to the ruthenium monomer precursors allows us to specify the charge state of the resulting dimer as either +2, +3, or +4. The new ruthenium complexes produced through this method are $[Cl(trpy)Ru(tpphz)Ru(trpy)Cl](PF_6)_2$ **(7)** and $[(phen)_2Ru(tpphz)Ru(trpy)Cl](PF_6)_3$ **(8)**. These complexes are similar in structure to the +4 complex $[(phen)_2Ru(tpphz)Ru(phen)_2](PF_6)_4$ **(9)**, previously reported by MacDonnell et al.[10] In addition to the ruthenium dimer synthesis I report a mixed solvent synthesis method for their precursor, $Ru(DMSO)_4Cl_2$ **(3)**. By using a mixed solvent, product readily precipitates from solution as it is formed, simplifying collection while maintaining high purity with yields of approximately 90%.[11,12]

By comparing the new compounds to **9**, I was able to investigate how different electrostatic charges affect the optical properties of structurally similar ruthenium complexes. The results show that the MLCT absorption is more red-shifted as the charge state is lowered. DFT level calculations of the highest occupied molecular orbital (HOMO) and the lowest unoccupied molecular orbital (LUMO) of the +2, +3, and +4 dimers suggest that electron density shifts from the ruthenium centers to the tpphz bridge during the MLCT transition. The dimensions and molecular rigidity of **7, 8**, and **9** are configured to interact effectively with nanoparticles. Catalytic metal nanoparticles, quantum dots and rods, and carbon nanotubes nanotubes are among the targets for non-covalent, site specific

functionalization and sensitization by these coordination compounds. Because I can effectively manipulate the optoelectronic properties of these ruthenium complexes and the overall charge-state while maintaining their rigid structure, I looked to use complexes like **7, 8**, and **9** as potential building blocks and integral components in the design of supramolecular nanoscale systems.

2.2 Contributions to the Field of Ru Coordination Complex Synthesis

The synthesis of polypyridine ruthenium coordination complexes is a well established field. Yet innovative new complexes are regularly created and improvements to techniques and recipes, once thought adequate, are sometimes discovered. The synthesis of the two new ruthenium dimers discussed herein is no different. Because the underlying chemistry and synthetic steps are well known, a more significant contribution to the synthetic chemistry field would be the improvement of a synthesis technique that can improve yields and aid in the synthesis efforts of many future researchers. While the synthesis of two new ruthenium complexes was the ultimate goal of my synthetic endeavors discussed below, the improvement of the penultimate synthetic processes to produce greater yields and higher purity final product was a true boon to the synthetic field. During my work two such improvements have been made.

2.2.1 Efficient Synthesis of $RuCl_2(DMSO)_4$

The first improvement is the one pot synthesis of *cis,fac*-$RuCl_2(DMSO\text{-}S)_3(DMSO\text{-}O)$. For many known and yet to be developed ruthenium complexes, $RuCl_2(DMSO)_4$ is an invaluable precursor. $RuCl_2(DMSO)_4$ is a beautiful yellow crystalline complex which is stable at room temperature and can be isolated in a *cis*

and *trans* isoform.[13,14] What makes $RuCl_2(DMSO)_4$ such an important precursor is that despite its relative stability, all five ligands are highly labile (stirring and low heat, < 90 °C) and easily exchanged with common coordinating ligands.[14-18] The improved synthetic process is described in detail in sections 2.3.2.3 and 2.4.1 and is unique from all previously reported literature techniques. The result of the technique discuss below is the exclusive production of the *cis, fac* conformation of the complex in a very clean and approximately 90% yield. There are methods known through which racemic mixtures of $RuCl_2(DMSO)_4$ can be converted to either the *cis* or *trans* conformation,[14] but those require an extra photochemical isomerization step after the initial synthetic process which reduces yield and increases cost.

Typical synthesis techniques for $RuCl_2(DMSO)_4$ use DMSO as both the reactant and solvent during synthesis. Those techniques take advantage of Le Chatelier's principle by maintaining an overabundance of DMSO driving the reaction equilibrium towards the product. While this process yields very little to no side product there are two major disadvantages with this track. The first disadvantage is that the solubility of the product in DMSO is very high. The best way to effectively retrieve the produced $RuCl_2(DMSO)_4$ from solution is to flood the reaction mixture with more than 20 times the initial volume with dry acetone and crash product out of solution. While acetone is not the most expensive solvent this practice can become costly and is both environmentally unfriendly and physically unwieldy when attempted on large scales. The second disadvantage is that the as produced $RuCl_2(DMSO)_4$ is nearly racemic and can contain detectable amounts of unreacted $RuCl_3$.

The process developed during my studies takes advantage of Le Chatelier's principle in a more efficient manner. By studying the solubility of the reactants and products in many common solvents I was able to determine that the solubility of $RuCl_3$ and DMSO in isopropanol was high, while the solubility of both *cis*- and *trans*- $RuCl_2(DMSO)_4$ was low. It was also observed that *cis,fac*-$RuCl_2(DMSO)_4$ is significantly more soluble than the *trans* form. This allowed us to take advantage of the difference in physical properties of the product and the reactants to design a reaction in which DMSO was used strictly as a reactant and added in appropriate stoichiometric amounts with $RuCl_3$ into the reaction vessel containing isopropanol as the supporting solvent. The insolubility of $RuCl_2(DMSO)_4$ in isopropanol caused the product to precipitate from solution as soon as it is produced driving the reaction equilibrium toward the product.

2.2.2 Synthesis and Purification of 1,10-phenanthroline 5,6-dioxime

The second major contribution that resulted from the synthesis work in this section involves the deconvolution and correction of literature procedures to produce 1,10-phenanthroline 5,6-dioxime (phendioxime). The synthesis of phendioxime is not an essential precursor but rather an alternative more efficient reaction pathway to an essential ligand. Oxime functional groups can be used for the synthesis of amine containing ligands, such as 1,10-phenanthroline-5,6-diamine. The synthetic pathway to 1,10-phenanthroline-5,6-diamine through phendioxime is a great improvement over the the most commonly used pathways toward producing phananthroline-diamine products, such as the one cited in section 2.3.1. The common process involves the conversion of a 1,10-phenanthroline-5,6-dione to a 5-nitro-6-amino-

phenanthroline. This first step of the process has average yields near 30%. The following conversion to a diamine has a relatively high yield, however by this point the damage is done and the overall yield of the final product is extremely low.

Even though the dioxime pathway has been known for some time, it has been avoided by many groups, including our own due to unreliable results even when following seemingly identical procedures. Until now the synthesis of phendioxime has been a troublesome and highly irreproducible product. The reaction scheme for phendioxime shown in FIGURE 2.1 is a refined reaction sequence from those suggested in literature.[19-21] For the detailed discussion of the oxime synthesis mechanism see appendix A. A major source of confusion when we initially tried to produce phendioxime was the disagreement of various literature sources with each other over the proper reactants and methods. Our important adjustment to the reported literature process was the selection of hydroxylamine hydrochloride as the limiting reagent and the addition of a stoichiometric excess of barium carbonate to the reaction. As hydroxylamine is consumed during the reaction, protons and HCl are released. Without proper accounting for the release of acidic species during synthesis the dioxime product will continue to react with acidic species and form 1,2,5-oxadiazolo[3,4-f]-1,10-phenanthroline shown in FIGURE 2.2. The addition of $BaCO_3$ serves as a weak base that does not greatly affect the pH of the final solution, but does react with free protons and HCl in solution to form $BaCl_{2(s)}$, $CO_{2(g)}$ and water. CO_2 readily escapes the system and $BaCl_2$ is insoluble in ethanol so it precipitates from solution. Because the hydroxylamine hydrochloride is the limiting reagent and $BaCO_3$ is in slight excess when the reaction has run to completion the

solution is approximately neutral. Care must still be taken to extract the dioxime product because it is slightly soluble in ethanol. The reaction mixture is taken to dryness under vacuum and $BaCl_2$ is removed with water. A water ethanol mixture is then used to remove any unreacted $BaCO_3$ (slightly soluble in water, soluble in ethanol) and the remaining 1,10-phenanthroline-5,6-dioxime is collected with vacuum filtration and dried with ether.

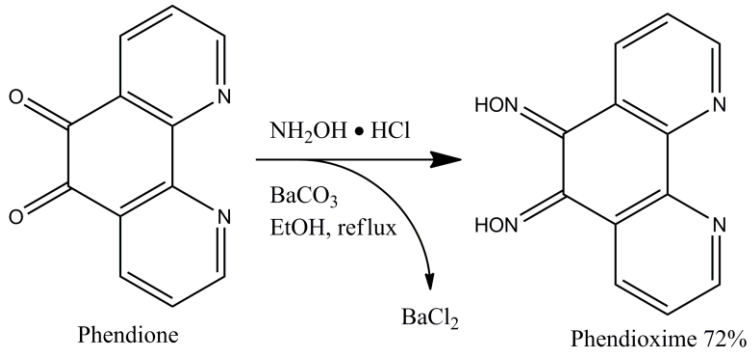

FIGURE 2.1. Reaction scheme to synthesize 1,10-phenanthroline-5,6-diamine via 1,10-phenanthroline-5,6-dioxime.

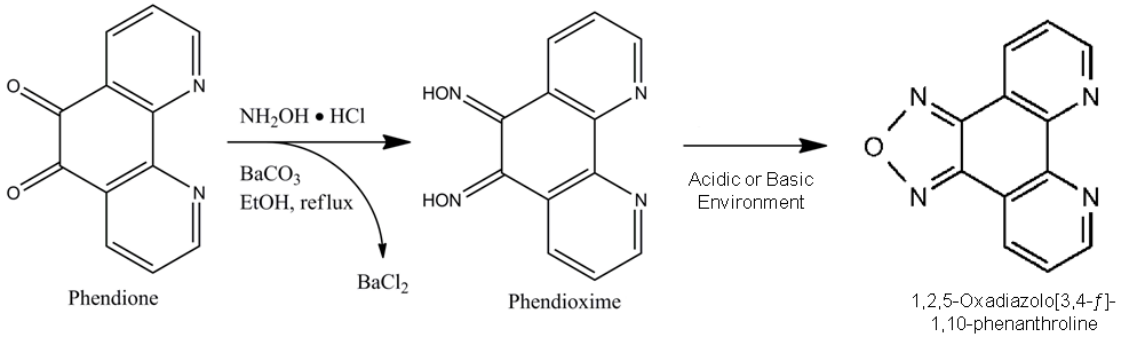

FIGURE 2.2. 1,2,5-oxadiazolo[3,4-f]-1,10-phenanthroline is the product of either basic or acidic conditions during phendioxime synthesis.

2.3 Experimental

2.3.1 Materials and Methods

1,10-phenanthroline (phen), $RuCl_3 \cdot 3H_2O$, dimethyl sulfoxide (DMSO), 2,2';6',2''-terpyridine (trpy), hydrazine hydrate, and Palladium/Carbon catalyst were purchased from Sigma-Aldrich or Alfa and were used without further processing or purification unless otherwise noted. 1,10-phenanthroline-5,6-dione (phendione),[22,23] 1,10-phenanthroline-5,6-diamine (phendiamine), and tpphz **(6)**[24] were prepared via literature procedures with any variations noted herein. $RuCl_2(phen)_2$[25] was prepared via literature procedures substituting phen for bipyridine (bipy). $RuCl_2(DMSO)_4$ **(3)**[11,12,14,26] was prepared through an improvement to literature procedures, detailed in section 2.3.2.3. $RuCl_2$(trpy)DMSO **(5)**[18] was prepared with slight variations to literature procedures with changes noted below. $[(phen)_2Ru(tpphz)Ru(phen)_2](PF_6)_4$ **(9)** was prepared following literature methods.[10,24] All solvents were analytical grade and dried on molecular sieves when applicable.

C, H and N elemental analysis was performed by Atlantic Microlab, Inc. ^1H and ^{13}C NMR spectra of **7**, **8**, and **9** in DMSO-d_6 were obtained at room temperature on a JEOL 500 MHz Fourier Transform (FT) spectrometer unless otherwise noted. Chemical shifts are reported in parts per million (ppm) using TMS as an internal reference for ^1H and ^{13}C. Assignment of ^1H NMR peaks for **7**, and **8** were accomplished by high resolution phase sensitive COSY 2D ^1H NMR. ESI mass spectrometry was performed in positive ion mode on a Mariner Biospectrometry Workstation in acetonitrile. All m/z are reported for the most abundant isotope and $[Ru_2 - XPF_6^-]$ represents the dinuclear species without X of its associated PF_6^-

counterions. Electronic absorption spectra were recorded on a Varian Cary 5000 spectrometer in dimethylformamide (DMF). Infrared (IR) spectra were obtained on a Perkin Elmer Spectrum One FT-IR with a universal diamond attenuated total reflectance top plate. Melting/degradation points (MP_{deg}) of **7** and **8** were measured on a Mettler-Toledo Thermogravimetric Analysis TGA/SDTA 851e under $N_{2(g)}$ atmosphere. Photodegradation studies were done in air saturated DMF under a 5 mW illumination of a 450 (±5) nm source for 12 h. Limiting Molar Conductivity (Λ°_{m}, S cm^2 mol^{-1}) in DMF was measured with an Accumet AR20 calibrated with a $KCl_{(aq)}$ standard.

2.3.2 Synthesis of Ruthenium Precursors and Complexes

2.3.2.1 $RuCl_2(phen)_2$ (1)

LiCl and $RuCl_3 \cdot 3H_2O$ were dried under vacuum at 125 °C for 15 hr. A mixture of LiCl (8.89 g, 210 mmol), $RuCl_3$ (5.33 g, 25.0 mmol), phen (7.11 g, 40.0 mmol) and DMF (40 mL) was stirred and refluxed for 15 h. The purple/black solution was cooled to room temperature (RT) and then rinsed from the reaction flask and diluted with acetone. This solution was then kept at 0 °C for 12-15 h. The resulting purple/black solid precipitate was collected by filtration. The product was washed with acetone (50 mL, 2x) and then several times with ice cold water (30 mL, 3x), yielding a dark purple solid. This compound is used best without further purification due to degradation during recrystallization. Yield: 6.85 g, 65%; UV-Vis λ_{MLCT} (DMF) nm $\varepsilon_{\lambda 552}$: 3400 M^{-1} cm^{-1}.

2.3.2.2 $[Ru(phen)_2phendione](PF_6)_2$ (2)

A mixture of absolute ethanol (50 mL) degassed with $Ar_{(g)}$, complex **1** (0.408 g, 0.80 mmol), and phendione (0.210 g, 1.0 mmol) was stirred and refluxed under an inert atmosphere of $Ar_{(g)}$ for 24 h. After the mixture was cooled to RT, a saturated $KPF_{6(aq)}$ solution was added dropwise to precipitate the brown product. The solution was kept at 4 °C for 12-15 h and the brown solid was collected by filtration. The solid was washed several times with cold ethanol (95%, 20 mL, 3x), then with cold absolute ethanol (20 mL, 2x), and finally with diethyl ether (20 mL, 2x). The yellow brown solid was air dried. Yield: 0.490g, 66%; UV-vis (DMF) λ_{MLCT} $\varepsilon_{\lambda 430}$: 14,000 M^{-1} cm^{-1}.

2.3.2.3 cis,fac-$RuCl_2(DMSO\text{-}S)_3(DMSO\text{-}O)$ (3)

DMSO (10 mL) was degassed with $Ar_{(g)}$ for 20 min. $RuCl_3 \cdot 3H_2O$ (3.247 g, 12.0 mmol) was added to DMSO and stirred under $Ar_{(g)}$ until dissolved. Isopropanol (35 mL) was then added, and the light orange solution was heated at 85 °C under an inert atmosphere of $Ar_{(g)}$ for 30 h. During heating, the product readily precipitated from solution. After the reaction cooled to RT, the bright yellow precipitate was broken up with a glass rod and collected by vacuum filtration, washed liberally with dry acetone, rinsed with toluene (2x), and finally dried on the filter. Yield: 5.240 g, 87%; UV-vis (DMF) λ_{max} $\varepsilon_{\lambda 356}$: 380 M^{-1} cm^{-1}. Selected FT-IR absorptions, cm^{-1}: ν(DMSO-S) 1083.1 (s), ν(DMSO-O) 923.4 (s).

2.3.2.4 $[Ru(phen)_2tpphz](PF_6)_2$ (4)

A mixture of **2** (0.200 g, 0.20 mmol) in acetonitrile (10 mL) was stirred and brought to a boil. A separate volume of methanol (35 mL) was heated to a boil then phendiamine (0.051 g, 0.20 mmol) was dissolved into the hot methanol. The hot

phendiamine solution was added to the boiling acetonitrile solution containing **2** and brought to reflux while stirring under $Ar_{(g)}$ for 5 h. The reaction was cooled to RT, and then saturated $KPF_{6(aq)}$ was added dropwise until the brown precipitate stopped forming. The precipitate was collected by vacuum filtration and the solid washed with ice cold water (20 mL, 2x), cold ethanol (95%, 20 mL, 2x), and finally with diethyl ether (20 mL, 2x). The brown solid was dried on the filter. Yield: 0.168 g, 71%; UV-vis (DMF) $\lambda_{tpphz\ \pi\text{-}\pi^*}$ $\varepsilon_{\lambda 385}$: 28,000 M^{-1} cm^{-1}, λ_{MLCT} $\varepsilon_{\lambda 455}$: 19,700 M^{-1} cm^{-1}. ^{1}HNMR: 300 MHz (CD_3CN) δ (ppm): 9.80 (d, J = 8.25 Hz, 2H), 9.71 (d, J = 7.32 Hz, 2H), 9.01 (d, 2H), 8.65 (d, J = 2.76 Hz, 2H), 8.62 (d, J = 2.76 Hz, 2H), 8.40 (d, J = 4.77 Hz, 2H), 8.23 (s, 4H), 8.19 (d, J = 5.52 Hz, 2H), 8.06 (d, J = 5.13 Hz, 2H), 7.92 (dd, J = 8.43, 2H), 7.81 (dd, J = 8.04, 2H), 7.68 (m, 4H).

2.3.2.5 $RuCl_2$(trpy)DMSO (5)

A mixture of ethanol (95%, 20 mL) and methanol (6 mL) was slowly stirred as **3** (1.263 g, 2.20 mmol) was added. The mixture was stirred and refluxed under an inert $Ar_{(g)}$ atmosphere for 15 min. A separate mixture of ethanol (95%, 10 mL) and trpy (0.604 g, 2.6 mmol) was prepared and slowly transferred under Ar(g) to the refluxing solution of **3**. The resulting brown mixture was refluxed and stirred under $Ar_{(g)}$ for another 8.5 h. The brown precipitate was collected by vacuum filtration. The solid was washed with cold water (20 mL, 3x), and then cold ethanol (95%) until the filtrate was clear and colorless. The brown product was vacuum dried at 90 °C. Yield: 0.916 g, 88%; UV-vis (DMF) λ_{MLCT} $\varepsilon_{\lambda 513}$: 3000 M^{-1} cm^{-1}.

2.3.2.6 [Cl(trpy)Ru(tpphz)Ru(trpy)Cl]$(PF_6)_2 \cdot 5H_2O$ (7)

A mixture 0.166 g (0.40 mmol) of **6** and 0.415 g (0.90 mmol) of complex **5** were added to a mixed solvent solution of ethanol (95%, 15 mL) and water (15 mL). The resulting solution was stirred and refluxed for 24 h. After the reaction cooled to RT, the dark purple mixture was brought to dryness under vacuum, and then residue was dissolved in a minimal amount of water (~30 mL). The dark purple solution was added dropwise to a saturated $KPF_{6(aq)}$ solution to yield a precipitate. The purple solid was collected by vacuum filtration, and then washed with water until the filtrate was clear and colorless. The solid was dried under vacuum at 90 °C. Yield: 0.468 g, 77 %; UV-vis (DMF) $\lambda_{tpphz\ \pi\text{-}\pi^*}$ $\varepsilon_{\lambda 375}$: 33,000 M^{-1} cm^{-1}, λ_{MLCT} $\varepsilon_{\lambda 518}$: 28,000 M^{-1} cm^{-1}. Melting Point of degradation (MP_{deg}): 360 °C. Anal. Calcd for $C_{54}H_{34}N_{12}$-$Ru_2P_2F_{12}\cdot 5H_2O$: C, 43.12; H, 2.95; N, 11.18. Found: C, 43.13; H, 2.60; N, 10.87. Lim. Mol. Conductivity, Λ°_m: 230 S cm^2 mol^{-1}. ESI-MS: $[Ru_2\ -2PF_6^-]^{2+}$ m/z = 562.1, $[Ru_2\ -1PF_6^-]^{+}$ m/z = 1269.3. ^{1}HNMR (DMSO-d_6) δ (ppm): 10.57 (d, J = 5.15 Hz, tpphz), 10.53 (d, J = 4.60 Hz, tpphz), 10.38 (d, J = 8.30 Hz, tpphz), 10.21 (d, J = 5.70 Hz, tpphz), 10.18 (d, J = 9.15 Hz, tpphz), 9.82 (d, J = 8.05 Hz, tpphz), 9.62 (d, 8.00 Hz, tpphz), 8.89 (d, J = 8.05 Hz, trpy 2H), 8.84 (d, J = 8 Hz, tpphz), 8.37 – 8.24 (m, tpphz & trpy 4H), 8.37 – 8.24 (m, tpphz & trpy 4H), 8.04 – 7.90 (m, tpphz & trpy 4H), 7.73 (d, J = 6.30 Hz, trpy 4H), 7.77 – 7.62 (m, tpphz), 7.44 (apparent dd, J = 6.30 Hz, tpphz), 7.32-7.27 (m, tpphz & trpy 4H); ^{13}C NMR (DMSO) δ 158.24, 157.51, 152.48, 151.60, 149.54, 137.11, 127.21, 123.65, 122.73.

2.3.2.7 $[(phen)_2Ru(tpphz)Ru(trpy)Cl](PF_6)_3\cdot 2H_2O$ (8)

A mixture of **4** (0.105 g, 0.10 mmol), **5** (0.046 g, 0.10 mmol) and DMF (15 mL) were stirred and refluxed under $Ar_{(g)}$ for 23 h. The reaction was cooled to RT,

and then saturated $KPF_{6(aq)}$ was added dropwise, producing a reddish precipitate. The mixture was then held at 4 °C for 12 h. The dark orange-red solid was collected by vacuum filtration, washed with cold water (20 mL, 2x), and then cold ethanol (95%, 20 mL, 2x), and finally with diethyl ether (20 mL, 2x) and dried under vacuum at 90 °C for 12 h. Yield: 0.087 g, 52 %; UV-vis (DMF) $\lambda_{tpphz\ \pi\text{-}\pi^*}$ $\varepsilon_{\lambda 375}$: 35,000 M^{-1} cm^{-1}, λ_{MLCT} $\varepsilon_{\lambda 453}$: 26,000 M^{-1} cm^{-1}. MP_{deg}: 371-373 °C. Anal. Calcd for $C_{63}H_{39}N_{13}$-$Ru_2P_3F_{18}$·$2H_2O$: C, 44.86; H, 2.57; N, 10.80. Found: C, 44.47; H, 2.46; N, 10.87. Lim. Mol. Conductivity, Λ°_m: 310 S cm^2 mol^{-1}. ESI-MS: $[Ru_2\ -3PF_6^-]^{3+}$ m/z = 405.4, $[Ru_2\ -2PF_6^-]^{2+}$ m/z = 680.5, $[Ru_2\ -1PF_6^-]^{+}$ m/z = 1506.1. ^{1}H NMR (DMSO-d_6) δ (ppm): 10.54 (d, J = 5.20 Hz, 1H), 10.26 (d, J = 8.05 Hz, 1H), 10.18 (d, J = 7.45 Hz, 1H), 9.97 (d, J = 8.00, 1H), 9.70 (d, J = 8.00 Hz, 1H), 8.91 (d, J = 8.05 Hz, 1H), 8.81 (app. t, J = 8.00 Hz, 4H), 8.76 (d, J = 8.00 Hz, 2H), 8.72 (dd, 8 Hz, 1H), 8.43 (d, J = 6.90 Hz, 4H), 8.34-8.26 (m, 4H), 8.12-8.06 (m, 5H), 8.01-7.95 (m, 3H), 7.85-7.77 (m, 5H), 7.71 (app. d, 2H), 7.30 (dd, 12.6 Hz, 3H); ^{13}C NMR (DMSO-d_6) δ 158.26, 157.51, 154.42, 153.17, 152.50, 152.49, 151.71, 150.33, 149.64, 147.05, 139.69, 137.16, 136.92, 130.40, 129.40, 128.63, 127.99, 127.21, 126.31, 123.68, 122.77.

2.4 Results and Discussion

2.4.1 Synthesis of *cis,fac*-$RuCl_2$(DMSO-S)$_3$(DMSO-O) **(3)**.

Addition of $RuCl_3$·$3H_2O$ in DMSO to give **3** can yield either *cis* or *trans* isomers.[26] X-ray crystallography has previously shown the *cis* product coordinates one of the DMSO ligands through the oxygen and the other three through the sulfur while the *trans* product coordinates DMSO exclusively through sulfur.[14] The

kinetically stable isomer, *trans*-$RuCl_2(DMSO\text{-}S)_4$, should be the most likely product at low temperatures (<100 °C),[27] whereas the thermodynamically stable isomer, *cis,fac*-$RuCl_2(DMSO\text{-}S)_3(DMSO\text{-}O)$, should be the primary product of $RuCl_3$ in hot (120-150 °C) DMSO.[12,14] The synthesis procedure described above was performed at low temperature (85 °C) in mixed solvent, predicting *trans*-$RuCl_2(DMSO\text{-}S)_4$ as the primary product. Contrary to the predicted kinetically favorable trans product, we report the synthesis of pure *cis,fac*-$RuCl_2(DMSO\text{-}S)_3(DMSO\text{-}O)$, the unlikely thermodynamically favorable product. Using FT-IR spectroscopy, the as-produced product was analyzed to determine the orientation of the coordinated DMSO from our mixed solvent procedure. The S=O stretching frequency of free DMSO is approximately 1055 cm^{-1}.[28] This transition is not found in our IR therefore we do not observe any free DMSO in this sample. The stretching frequency of Ru—S-bonded DMSO is reported to resonate at 1080 cm^{-1}. While the Ru—O-bonded DMSO stretching frequency is reported to appear between 890 – 950 cm^{-1}.[28,29] We experimentally detected stretching frequencies at 923.4 cm^{-1} and 1083.1 cm^{-1} from our as-produced sample suggesting the *cis* product. To confirm the sole production of the thermodynamically favorable *cis* product, procedures reported by Alessio et al.[26] were carried out to convert samples of $RuCl_2(DMSO)_4$ to pure *cis* and *trans* isoforms. IR spectra of the pure samples were overlain with that of the as-produced sample in (FIGURE 2.3) The spectra of the pure *cis,fac*-$RuCl_2(DMSO\text{-}S)_3(DMSO\text{-}O)$ is identical to that of our as-produced product. The spectra of the pure *trans*-$RuCl_2(DMSO\text{-}S)_4$ not only lacks the stretching frequency of Ru—O-bonded DMSO, the frequency of Ru—S-bonded DMSO is at a lower energy, ν1076.7 cm^{-1}, versus

ν1083.1 cm^{-1} in the *cis* spectra. This energy decrease is likely caused by the decrease of ruthenium electron donation due to the additional S-bonded DMSO competition.[28]

Exclusive production of the thermodynamically favored *cis* isoform even at low reaction temperatures can be explained by the solubility of the different isomers in the mixed solvent environment. To produce $RuCl_2(DMSO)_4$ it is common to use DMSO both as a reactant and the primary solvent. In these cases the *cis* product is very soluble in DMSO while the *trans* product can precipitate as the reaction mixture cools.[14,26,28,29] Temperature tends to be the isoform determining factor during these procedures. During our synthesis procedure we chose to use DMSO as a reactant in slight excess and use isopropanol (IPA) as the primary solvent. Isopropanol was selected as a solvent due to

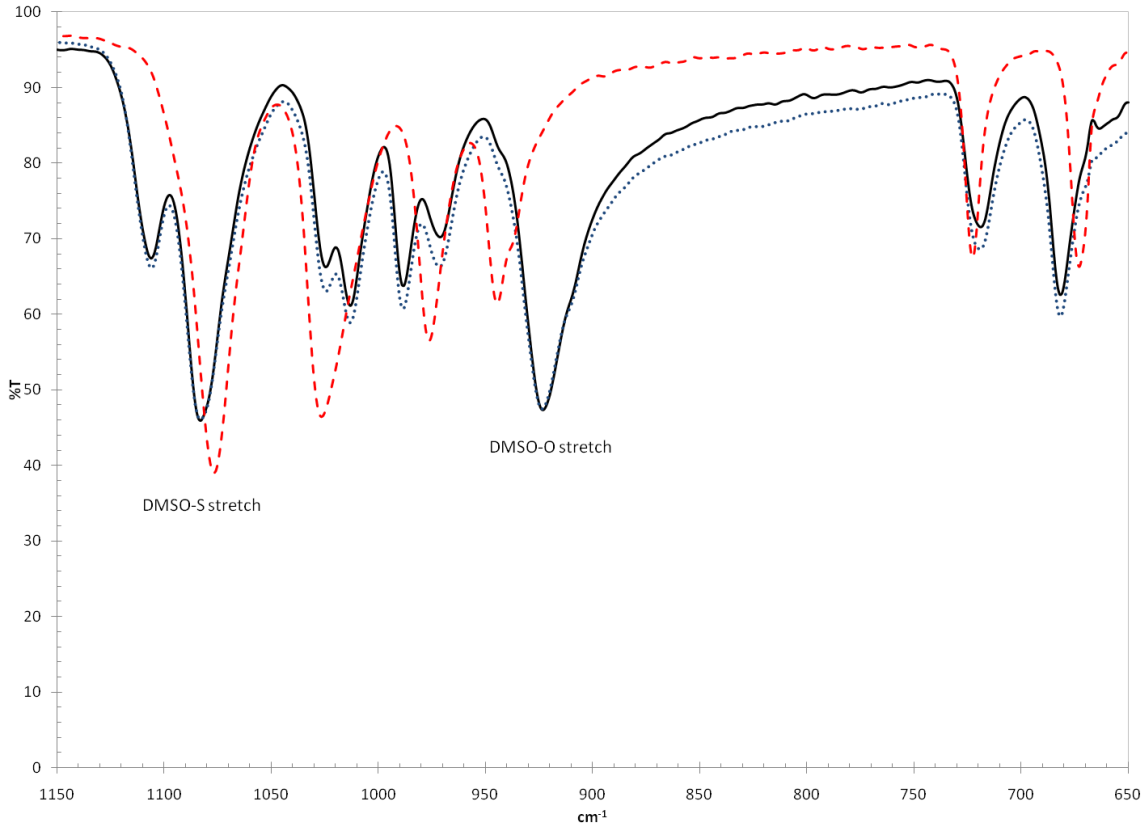

FIGURE 2.3. IR spectra of cis- and trans- tetrakis-dimethylsulphoxide dichlororuthenium. (blue dots) cis,fac-$RuCl_2(DMSO\text{-}S)_3(DMSO\text{-}O)$, (red dashes) trans-$RuCl_2(DMSO\text{-}S)_4$, (solid line) as-produced-$RuCl_2(DMSO\text{-}S)_4$.

the limited solubility of $RuCl_2(DMSO)_4$ which had the intended consequence of precipitating product as it was formed, simplifying the collection of product. The unforeseen result was the precipitation of a pure *cis*,*fac*-$RuCl_2(DMSO\text{-}S)_3(DMSO\text{-}O)$ product. A follow up solubility experiment showed that the solubility of *cis* in IPA is 0.6 mg/mL while the solubility of *trans* is 5.0 mg/mL. The solubility of the isomers in IPA explains how the precipitation of the relatively less soluble *cis* isoform versus the more soluble *trans* would drive production toward the *cis*, despite the reaction temperature favoring the *trans* isomer.

2.4.2 Synthesis and Stability of 7 and 8.

The reaction scheme in (FIGURE 2.4) illustrates the two synthetic routes through which we manipulated the final charge state and optical properties of **7** and **8**. The phen derivatives, 1,10-phenanthroline-5,6-dione, [22,23] 1,10-phenanthroline-5,6-diamine [24] and tpphz [24] were produced via previously reported synthetic procedures. Complex **7** was synthesized from a ligand exchange reaction of two molar equivalents of **5** and one molar equivalent of **6**. Complex **8** was synthesized from a ligand exchange reaction between **5** and the PF_6 salt of **4**. Following synthesis, compounds **7** and **8** were characterized by EA, UV-Vis, SDTA, ESI-MS, ^{1}H NMR, and ^{13}C NMR. ^{13}C NMR of **7** and **8** are shown in (FIGURE 2.5) and (FIGURE 2.6) respectively. ESI-MS was essential to identifying and characterizing the compounds. There are seven ruthenium isotopes with large enough natural abundances to be measured in ESI-MS.

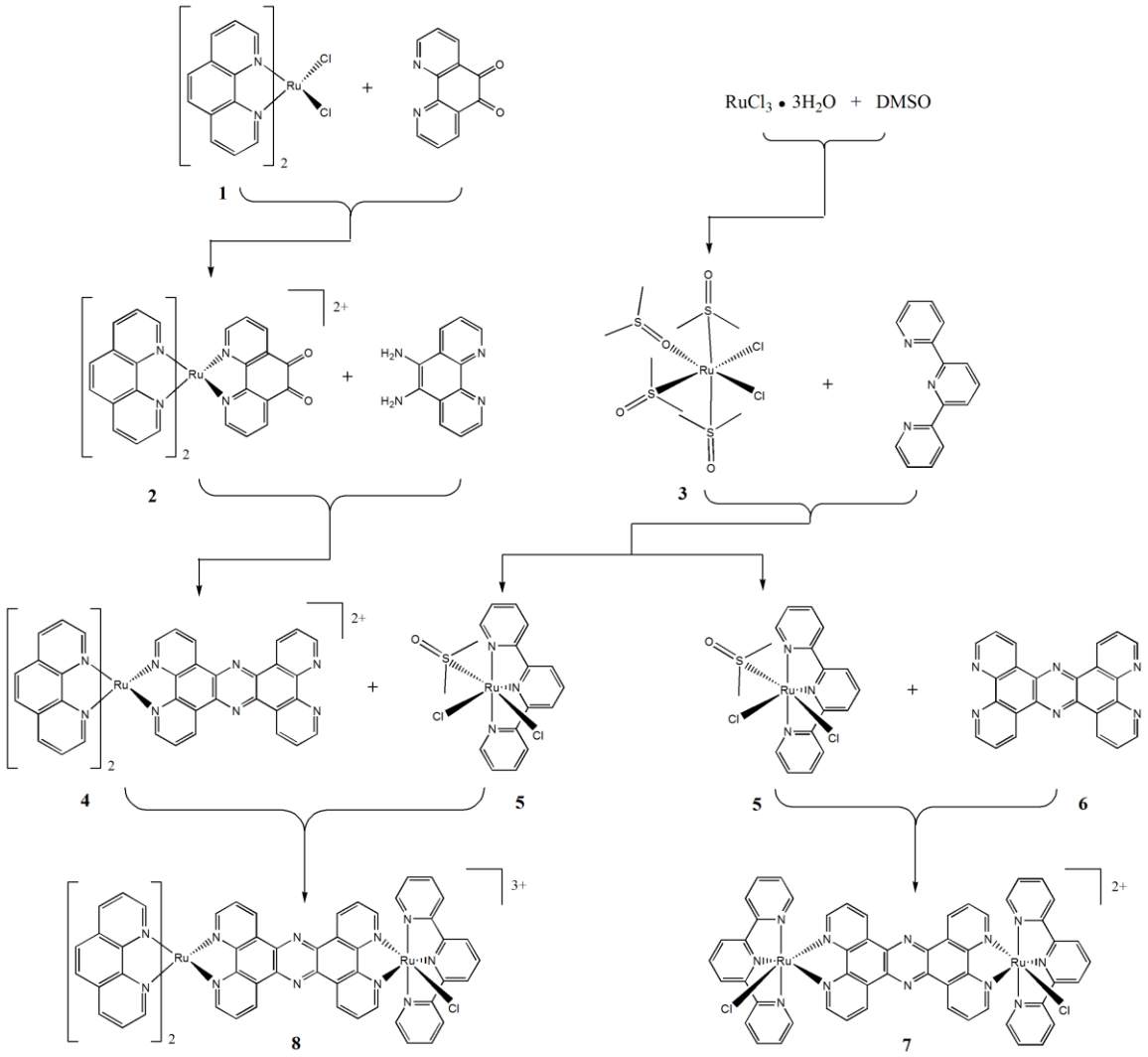

FIGURE 2.4. Reaction sequence for the synthesis of +2 Ru dimer and +3 Ru dimer.

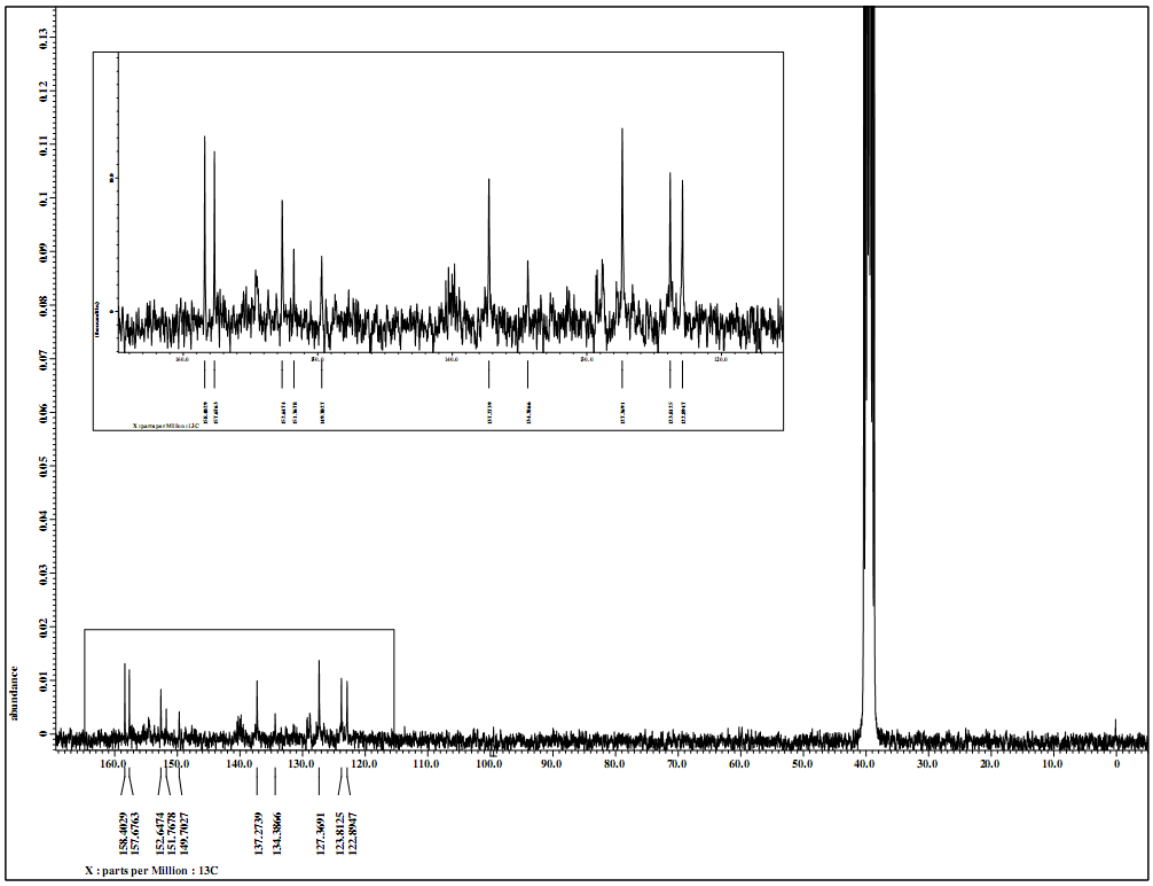

FIGURE 2.5. 13CNMR in DMSO of the +2 Ru dimer.

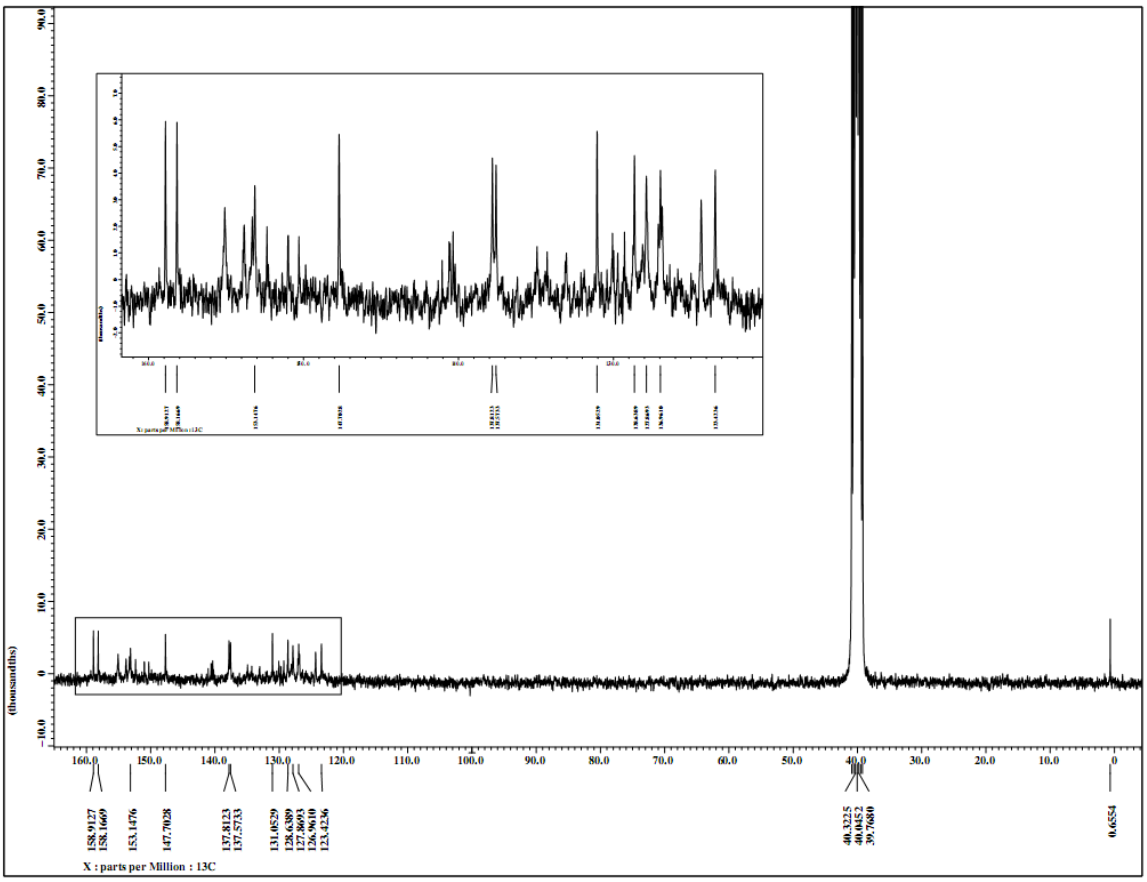

FIGURE 2.6. 13CNMR in DMSO of the +3 Ru dimer.

The signature of a mononuclear complex is easily distinguished (7 isotope peaks) from the isotope patter of a dinuclear species (13 easily identified peaks for one complex). There was no observable monomer in the ESI-MS of any of the dimers reported here. The dimers show excellent stability in solution. Each dimer has a unique mass to charge (m/z) pattern. The calculated isotope patterns of **4**, **7**, and **8** accurately match the measured mass spectrum presented in (FIGURE 2.7), (FIGURE 2.8), and (FIGURE 2.9). The difference in m/z within the isotope pattern allows us to determine the absolute charge on the species. When the resulting isotope peaks are separated by 1.0 m/z unit the overall electrostatic charge on the complex is +1. Correspondingly, the separation is 0.50 m/z units for +2 and 0.33 m/z units for +3, and 0.25 m/z units for a +4 charge.

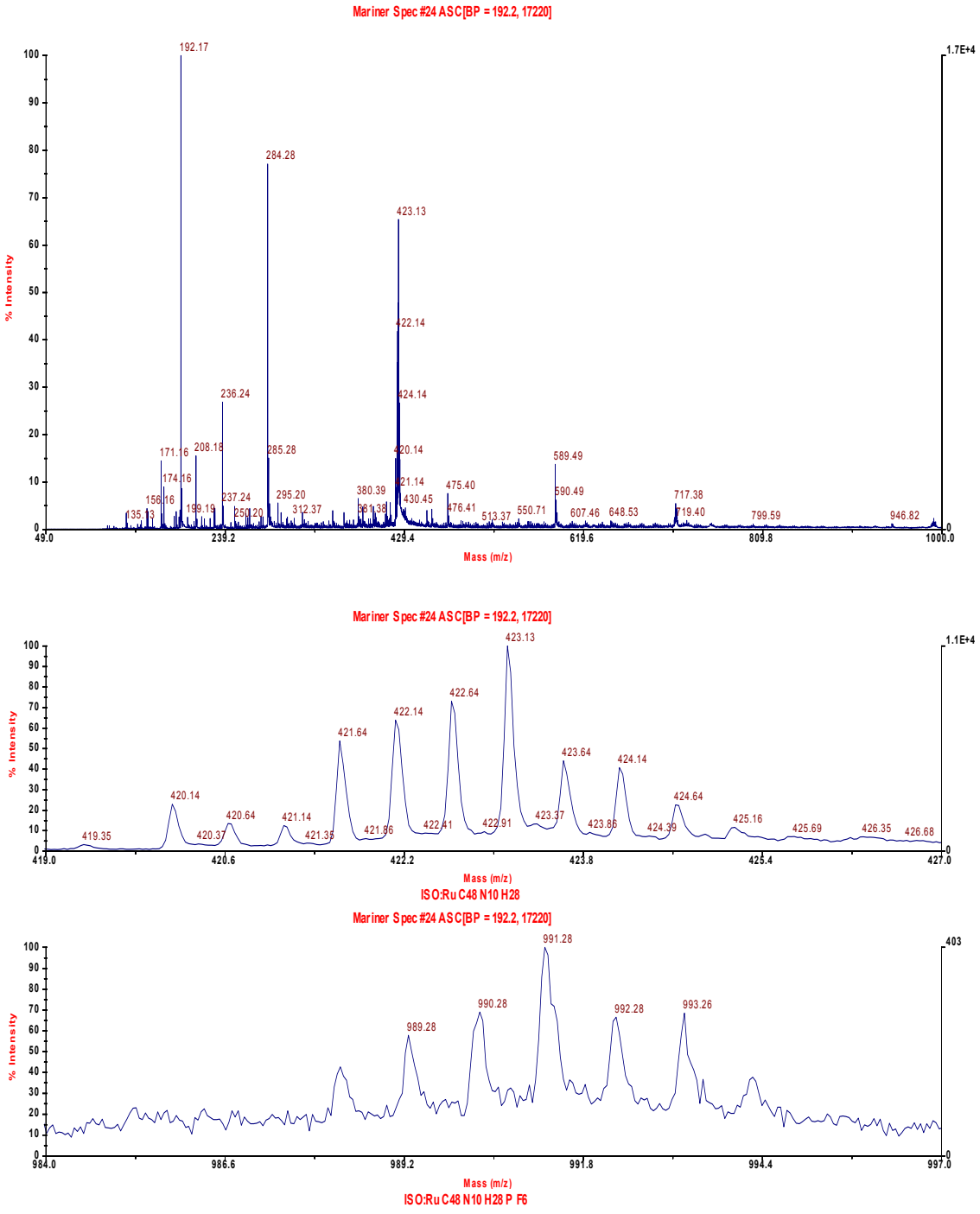

FIGURE 2.7. Electrospray mass spectrograph of Ru(phen)2tpphz.

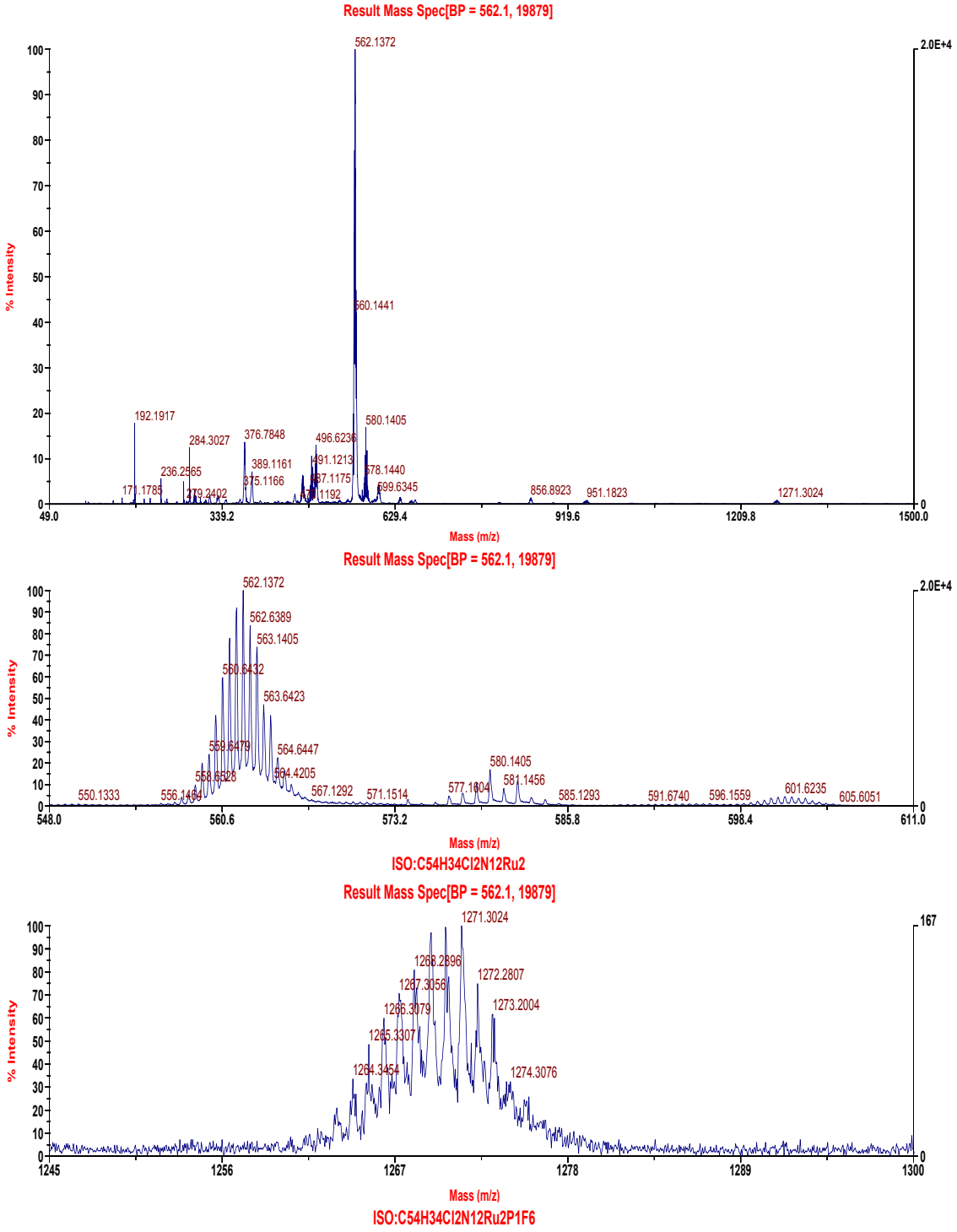

FIGURE 2.8. Electrospray mass spectrograph of the +2 Ru dimer.

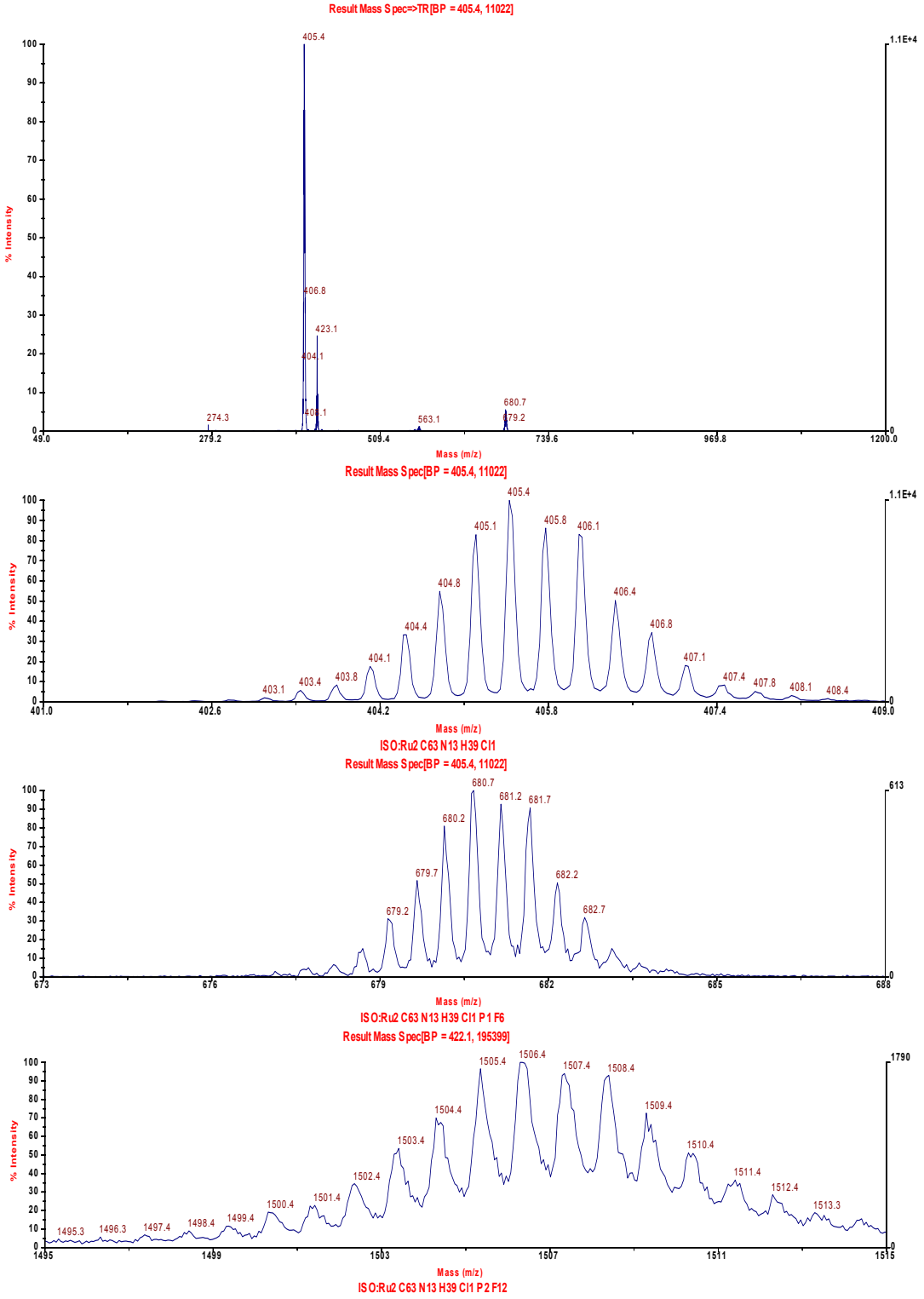

FIGURE 2.9. Electrospray mass spectrograph of the +3 Ru dimer.

Thermal stability of the ruthenium coordination complexes **7, 8,** and **9** were measured using scanning differential thermal analysis, SDTA. Differential gravimetric thermograms of **7**, **8**, and **9** are shown in (FIGURE 2.10a-c) respectively. The dimers were thermally stable under $N_{2(g)}$ up to 356 °C. **7** began decomposing at 356 °C, noted as the melting point onset temperature of degradation ($MP_{deg.}$) for the PF_6 salt. **8** and **9** followed suit, beginning decomposition at 370 ºC and 380 ºC respectively. Photodegradation of **7**, **8**, and **9** evaluated with UV-Vis showed no measurable decomposition after 12 h of 5 mW/cm^2 of 450 (±5) nm illumination. A series of ^{1}H NMR spectra as a function of time showed that the ruthenium coordination complexes are air stable. Free phendiamine was prone to degradation. We use the phendiamine immediately after it was prepared to synthesize **6**. The other free polypyridine ligands such as phen-5,6-dione, 5-nitro-phen and trpy are air and light stable.

2.4.3 ^{1}H NMR of 7, 8 and 9

On the basis of previous reports [8,16,24,30] and the spectra of **9**, used in conjunction with high resolution phase sensitive COSY 2D spectroscopy, the proton signals of **7** and **8** were assigned. The magnetic patterns of **7** and **8** shown (FIGURE 2.11) and (FIGURE 2.12) respectively, do not have a simple pattern as with **9** displayed in (FIGURE 2.13). The large distance between the ancillary ligands and the tpphz bridge make it so the ^{1}H NMR spectra of all eight magnetically unequivalent protons belonging to the same ancillary phens overlap identically.[16]

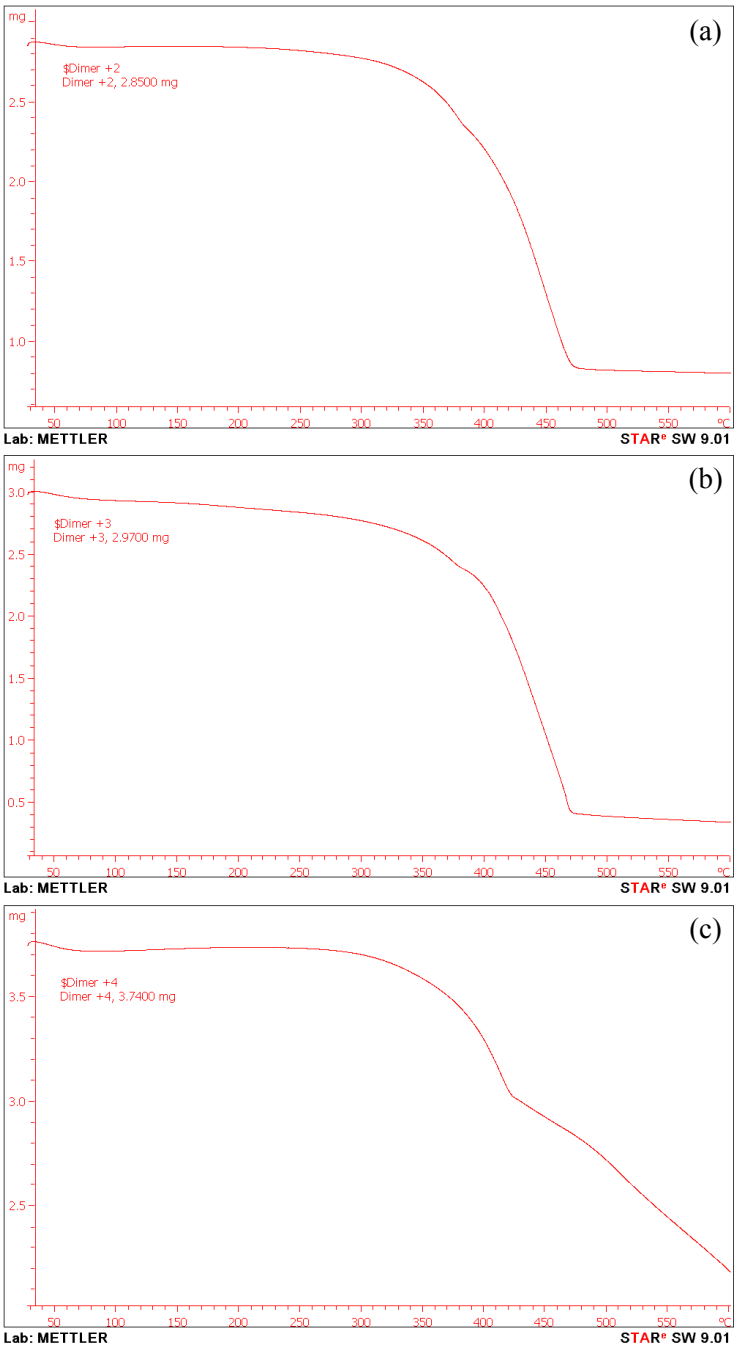

FIGURE 2.10. Thermal gravimetric analysis to determine the melting point (decomp.) of the dinuclear ruthenium species. (a) +2 Ru Dimer, (b) +3 Ru Dimer, (c) +4 Ru Dimer.

The proton signals of the trpy ligands are also easily distinguished. This is due to their position; away from and out of plain of the tpphz system, regardless of rotation

of the pyridyl units around the 2,2′ and 6′,2″ single bonds. However, the presence of syn and anti forms of **7** and the novel heteroleptic arrangement of **8** is certainly responsible for anisotropic magnetic effects on the pyridine cycle of tpphz. This varying magnetic unequivalence of the tpphz protons causes 12 distinct proton signals, spread throughout the spectra. For **7** in particular the presence of syn and anti forms presents significant challenges integrating for the number of tpphz proton signals. For this reason the peak integrations presented in section 2.3.2.6 are integrated only for the trpy protons. This observation is in total agreement with the data reported for the mononuclear $[Ru(L)_2tpphz]^{2+}$ complexes [L = phen or bipy]. For bipy coordinated monomer, signals for protons near the metal and signals at the unclomplexed end were found at 7.89 and 7.83 ppm. Whereas opposite behaviors were observed for the phen analogue, where coordinated and uncoordinated resonated at respectively 7.87 and 7.96 ppm.[16,30] This anisotropic effect is split further by the heteroleptic coordination of trpy and chlorine, making assignment of the tpphz protons difficult at best. For assignment of the tpphz proton signals COSY was utilized to establish neighboring proton sets, shown in (FIGURE 2.14) and (FIGURE 2.15). To distinguish between the sets the deshielding effects of the ancillary ligands were considered. Those sets opposite ancillary phen ligands would be furthest downfield, followed by those opposite trpy and then chlorine.[31]

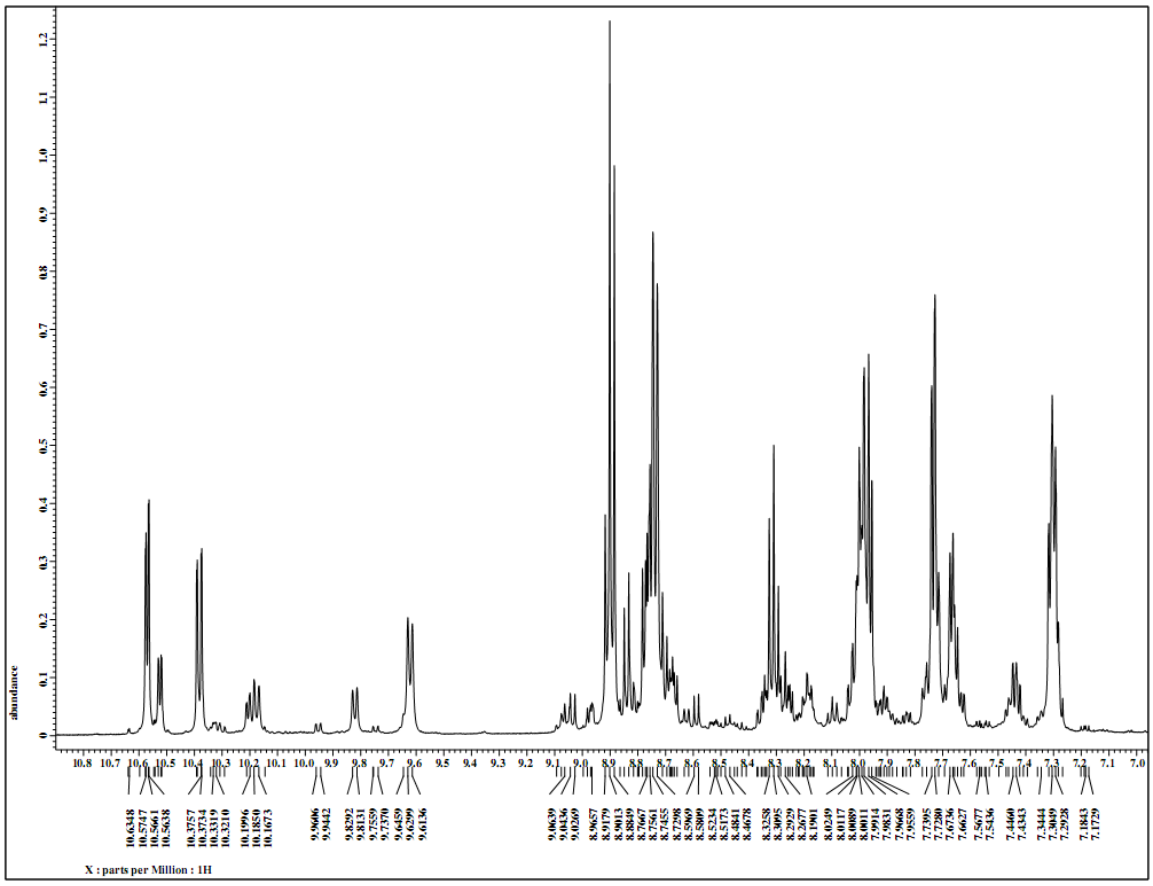

FIGURE 2.11. HNMR in DMSO of the +2 Ru dimer.

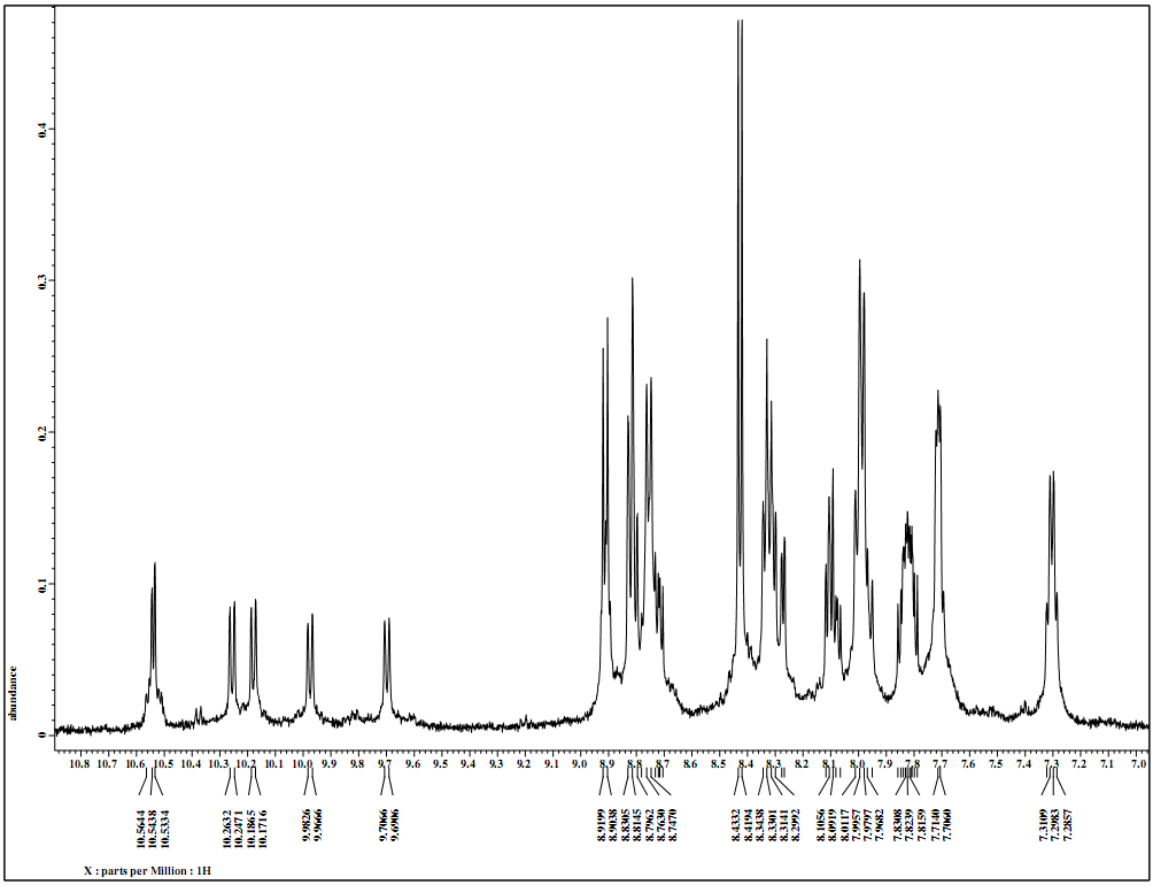

FIGURE 2.12. HNMR in DMSO of the +3 Ru dimer.

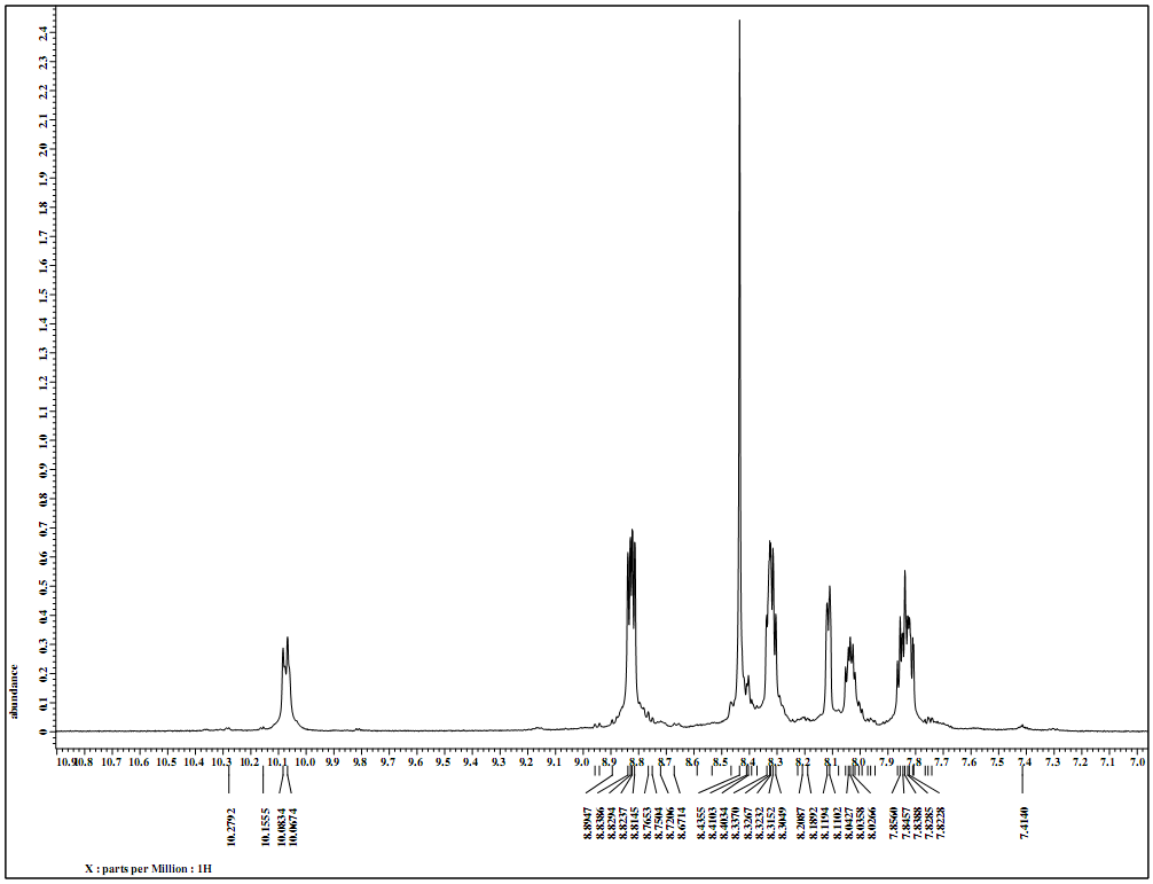

FIGURE 2.13. HNMR in DMSO of the +4 Ru dimer.

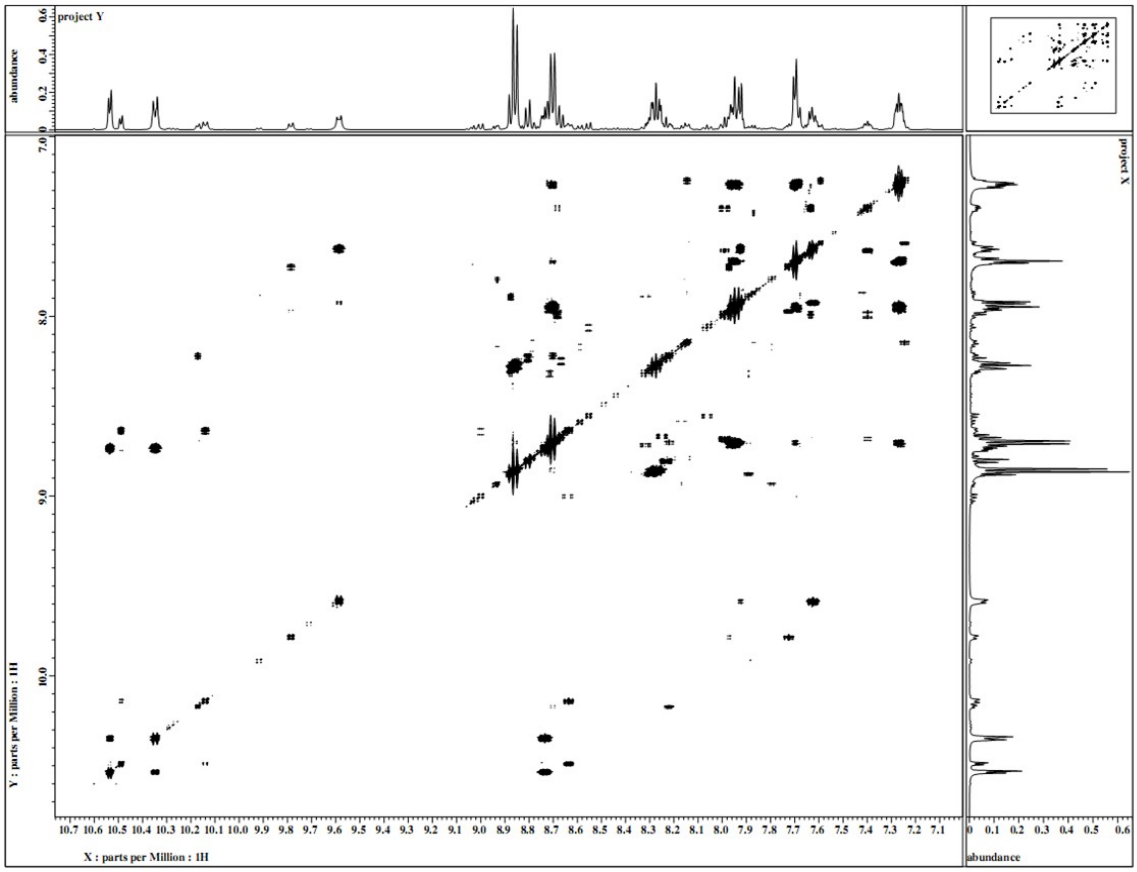

FIGURE 2.14. 2DCOSY NMR in DMSO of the +2 dimer.

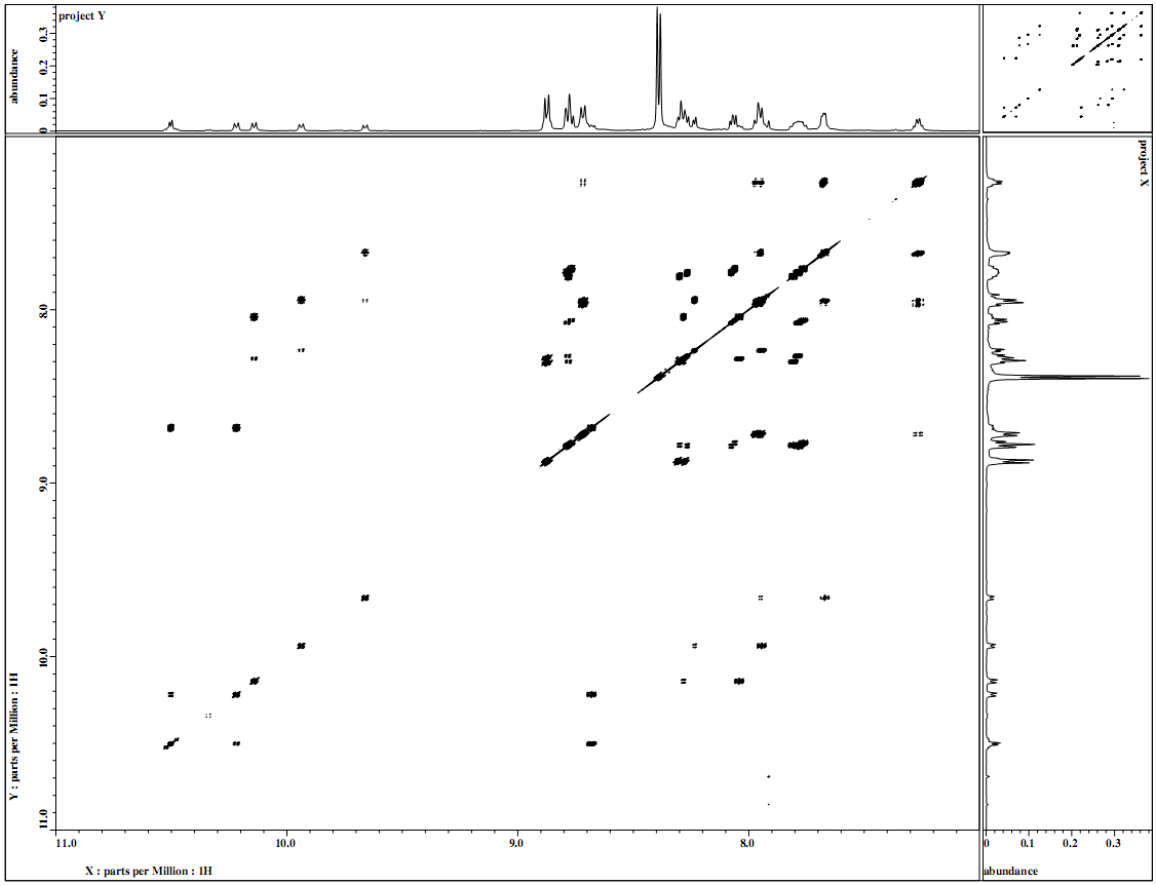

FIGURE 2.15. 2DCOSY NMR in DMSO of the +3 Ru dimer.

2.4.4 Electronic Spectral Studies

The absorption spectra of **7**, **8**, and **9** in DMF are shown in (FIGURE 2.16). As observed for free polypyridine ligands and mononuclear ruthenium complexes the ruthenium dimer complexes retain many of the features of their components. The absorption spectra for compounds **7, 8**, and **9** show an absorption at approximately 375 nm with a higher energy shoulder for **9** which evolves into another peak for **7** and **8**. These two bands are characteristic of free tpphz and correspond to the (tpphz)n– π^* and (tpphz)π – π^* transitions.[24] This π – π^* transition is red-shifted compared to the corresponding λ_{max} of 365 nm for free tpphz shown in (FIGURE 2.17) due to the back-donation from the ruthenium.

Each ruthenium dimer displays a strong and characteristic MLCT band at 400 – 600 nm. For **7** the MLCT bands are attributed to the overlap of Ru → tpphz(π^*) and Ru → trpy(π^*). The MLCT bands of **8** appear more broad which is attributed to the overlap of Ru → phen(π^*) and Ru → tpphz(π^*) from one half of the dimer combining with the overlap of Ru → tpphz(π^*) and Ru → trpy(π^*) from the other half. For comparison the absorption spectra of **9** in (FIGURE 2.16) the spectra of polypyridine coordinate runthenium monomers are provided in (FIGURE 2.18). The MLCT bands of **9** have been reported and assigned to the corresponding transitions, Ru → phen(π^*) and Ru → tpphz(π^*), which correlate well with our observations.[8,16,24,32] A red-shift from **9** of the MLCT bands for **7** and **8** is observed, with decreasing energy relative to their formal charge. The electron density over ruthenium centers is increased due to the coordination of chloride

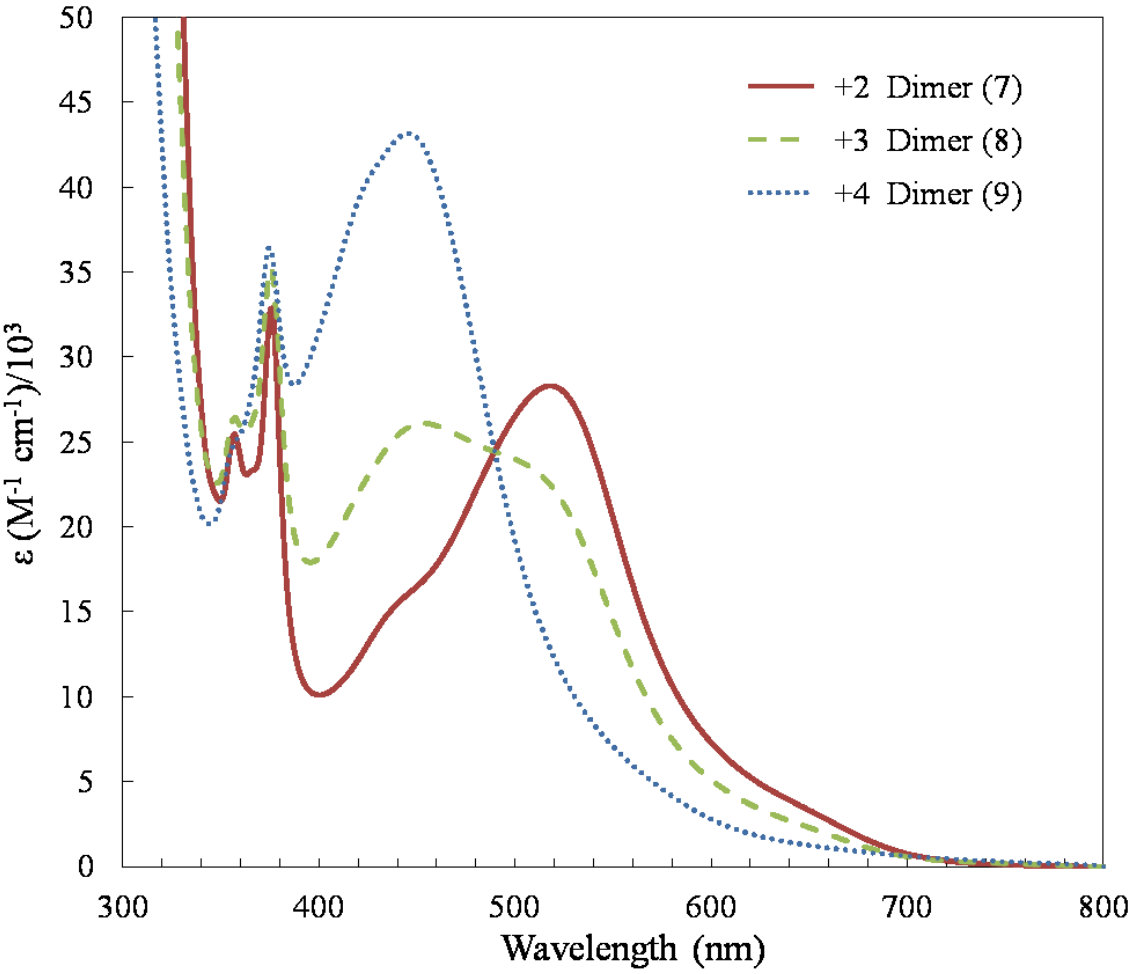

FIGURE 2.16. UV-vis absorption spectra of +2, +3, and +4 Ru Dimers. +2 λMLCT 518 nm (ε = 28,000 M-1 cm-1), +3 λMLCT 453 nm (ε = 26,000 M-1 cm-1), and +4 λMLCT 444 nm (ε = 41,000 M-1 cm-1).

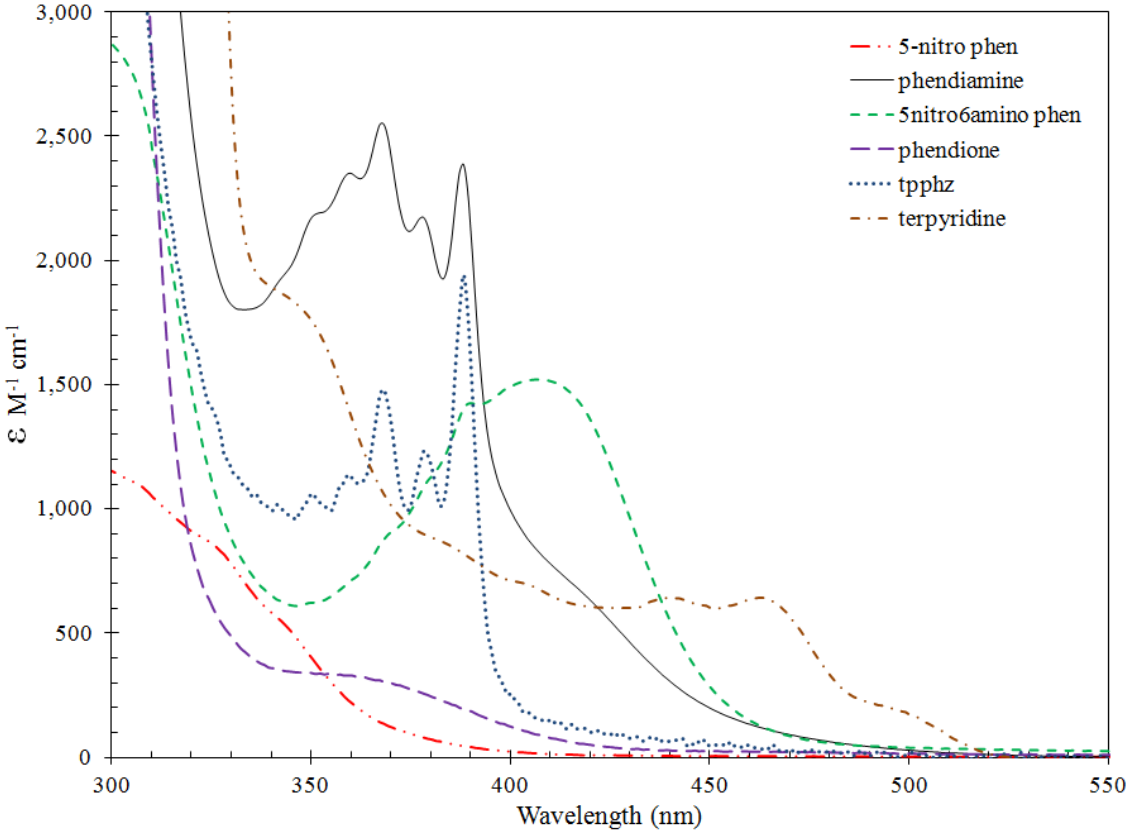

FIGURE 2.17. UV-vis spectra of the ligands used for Ru complex coordination chemistry.

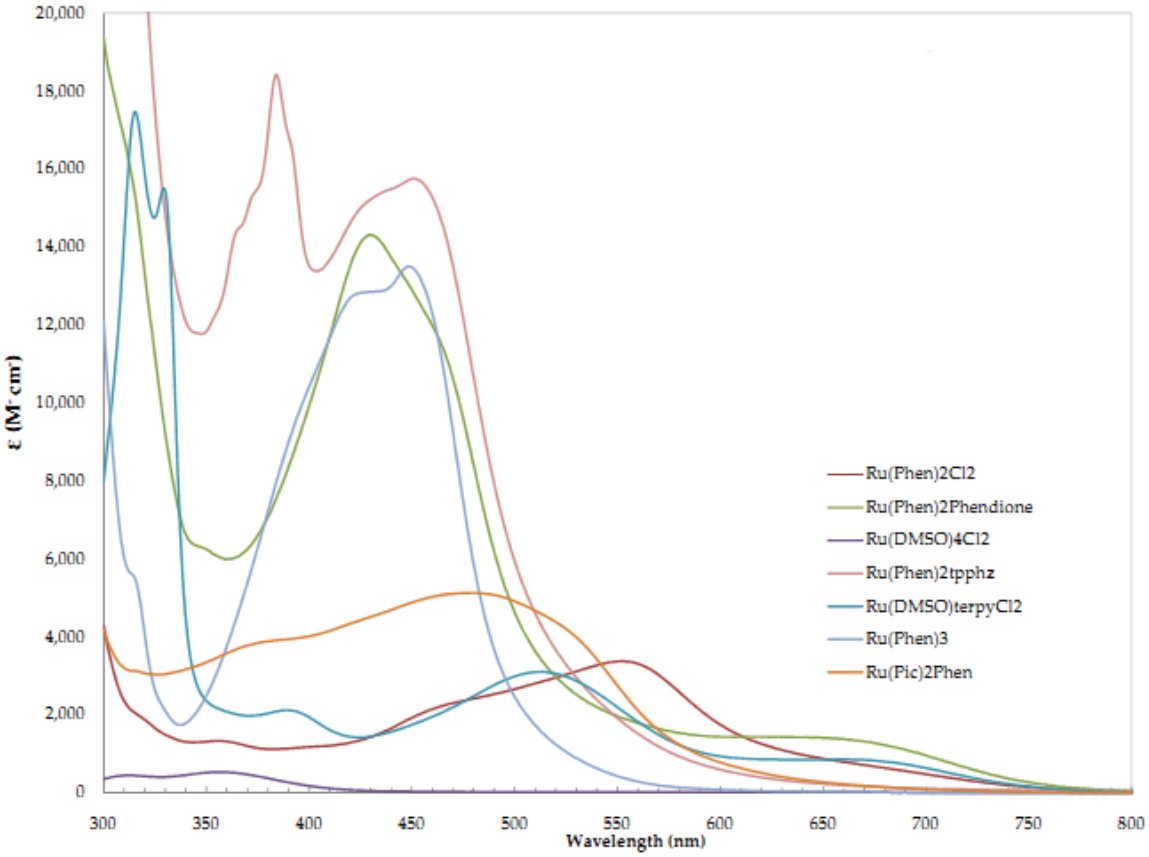

FIGURE 2.18. UV-vis spectra of Ru monomer and precursors in MeCN. Plotted as extinction coefficient against wavelength (nm).

ligands and also by the smaller back-donation from ruthenium to trpy versus ruthenium to two phens. The increased e^--density narrows the energy gap between the HOMO and LUMO, red shifting the MLCT.[24]

2.4.5 Molecular Modeling

DFT calculations were completed with Materials Studio 4.4 (Accelrys) using a gradient corrected Becke, Lee, Yang, and Parr functional. All core electrons were treated fully and with relativistic effects. A self consistent field tolerance of 10^{-6} Ha and geometry optimization tolerance of 10^{-5} Ha were imposed with a maximum atom displacement of 0.005 Å (or a maximum force gradient of 0.002 Ha/Å). All optimizations were treated with a conductor-like screening model with a dielectric constant of 36.7 to simulate DMF, the solvent used for our electronic spectral studies. Frontier molecular orbitals for the three dinuclear species are shown in (FIGURE 2.19). Although **7** and **8** have electron donating chlorides on at least one of their ruthenium centers, the shape and distribution of the LUMO across the tpphz bridge is almost identical between compounds **7, 8**, and **9**. Interestingly, the most prominent difference between each compound was observed in the HOMO. Orbitals on the ruthenium centers of **9**, the +4 complex, had very strong d_{z^2} character. The HOMO through HOMO-5 orbitals of **9** were similar on the two metal centers and nearly degenerate ($<7x10^{-4}$ Ha). The HOMO through HOMO-5 orbitals of **7** were also similar and nearly degenerate ($<7x10^{-4}$ Ha). These molecular orbitals overlap both the metal center and the chloride ligand. In contrast, the HOMO through HOMO-5 orbitals on **8** all resided on the metal center with the chloride ligand. We have also completed excited state calculations using configuration interaction singles

with the semi-empirical Zerner's Independent Neglect of Differential Overlap (ZINDO) Hamiltonian. The transition energies, determined using this model, are consistent with our observation that the MLCT transition is red-shifted as the charge state is lowered. These computational models are consistent with our spectrometric observations.

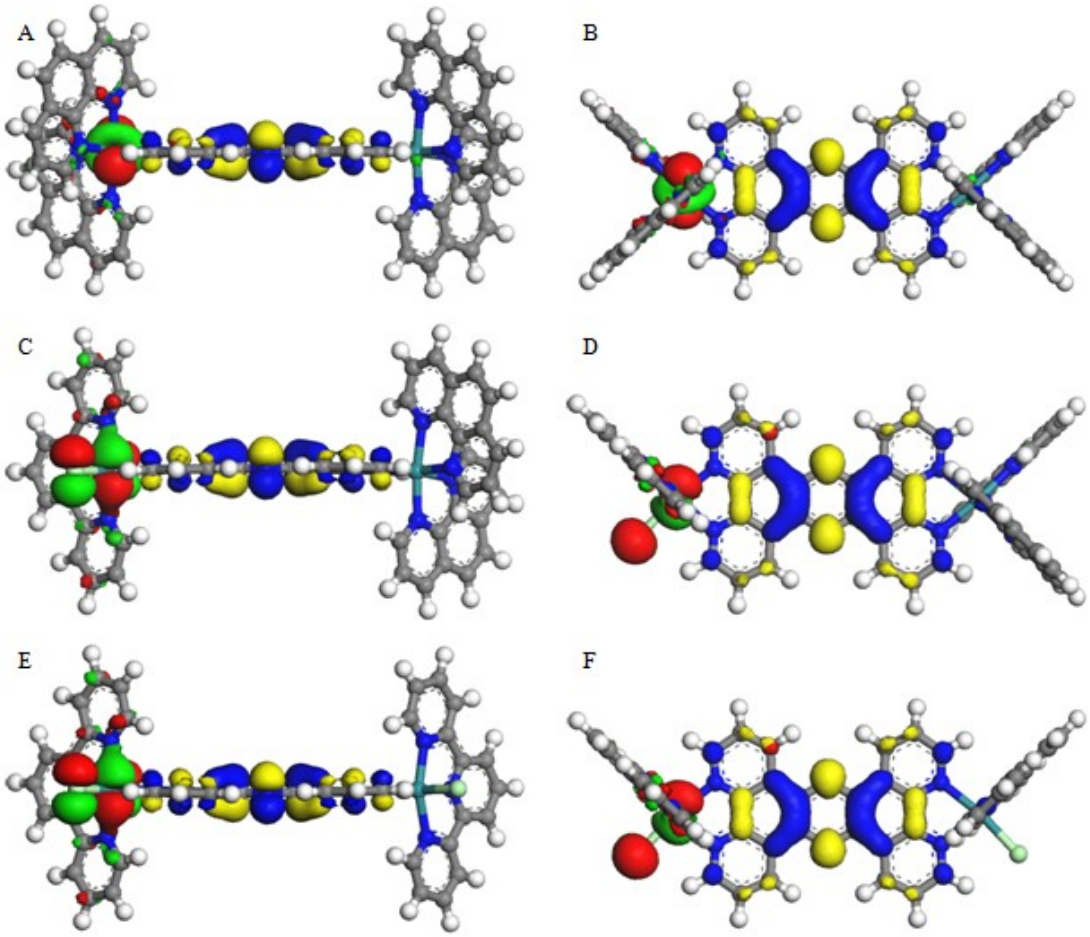

FIGURE 2.19. Frontier molecular orbitals for binuclear Ru complexes. (A, C, E) illustrate the +4, +3, and +2 dimers, respectively looking along the tpphz edge, and (B, D, F) illustrate +4, +3, and +2 dimers, respectively looking perpendicular to the tpphz ligand. The HOMO is depicted on the Ru center and colored green-red; the LUMO is located across the tpphz bridge and colored blue-yellow. Notice the LUMO is similar across species whereas the HOMO at the Ru centers varies depending on the presence of chloride ligand. The only significant difference between the enhanced dz2 character on the Ru center of the +4 dimer (A, B) as compared to the orbital on the chloride on the +2 dimer (E, F).

2.5 Conclusions

In summary, in this work we have presented the synthesis of two new heteroleptic binuclear ruthenium(II) coordination complexes, $[Cl(trpy)Ru(tpphz)Ru(trpy)Cl](PF_6)_2$ **(7)** and $[(phen)_2Ru(tpphz)Ru(trpy)Cl](PF_6)_3$ **(8)**. It has been demonstrated that the two compounds are stable and have been produced in good yield. The optical absorption of these complexes, specifically the MLCT transitions have been shown to be influenced by the electron withdrawing nature of ligands opposite the tpphz bridging ligand. Both complexes exhibit characteristic electronic absorption spectra that correlate well with the morphologically similar +4 dimer **(9)** and with the calculated HOMO and LUMO of both complexes. It is important to note that regardless of the varying terminal ligands or the resulting charge state of the dimer, the calculated molecular orbitals show that the LUMO maintains a similar shape on all three complexes while predominantly residing on the bridging ligand between the two ruthenium centers. Our ZINDO calculated transition energies lack accuracy, but are consistent with our observed trends in the shifting MLCT bands of **7, 8**, and **9**. More time dependent DFT studies are required to further analyze the differences in these spectra. Presently, our data supports previous work suggesting that ruthenium complexes bridged by tpphz could interact with nanoscale materials through the extension of that complex's electron density.[2-4] This phenomena can be stimulated by optical excitation of a MLCT band[4] which we have shown resides solely on the bridging ligand and in the nanoscale pocket formed by the rigid structure.

The complexes synthesized herein are new members of a nascent family of rigid ruthenium complexes that have optical properties that could be useful for controlling nanoparticle interactions as well as being utilized in charge transfer applications. Using the synthetic strategies described above we are able to shift the MLCT band to longer wavelengths enabling a more efficient overlap with the solar spectrum, which implies more utility for involvement in photovoltaic and photocatalytic applications. Preliminary results show strong interactions with nanoparticles such as carbon nanotubes and metal nanoparticles and show great potential for becoming building blocks and scaffold for technologically viable supramolecular structures with specified shape and charge.[2,4,9] The key to this goal is a better understanding of how morphology and charge state of supramolecular systems affects their optoelectronic properties. Further study and synthesis of photoactive ruthenium coordination complexes as well as study of nanostructures that integrate rigid coordination complexes will hopefully contribute to this goal.

2.6 Acknowledgements for Synthesis Work

Acknowledgement is made to the Donors of the American Chemical Society Petroleum Research Fund for partial support of this research. Financial support was also provifed through the Nanoscale Science Ph.D. program and the Center for Optoelectronics and Optical Communications at UNC Charlotte is appreciated. I would also like to thank Dr. Schmedake, Dr. Cliff Carlin, Dr. Jon Merkert, Dr. Michael Murphy and Dr. John Pickett for instrumental assistance and discussion.

CHAPTER 3: THERMODYNAMIC MEASUREMENTS OF RU COMPLEXES AND SWCNTS

3.1 Isothermal Titration Calorimetry: Background

In the last 10 years a large amount of high resolution structural data has been accumulated on different nanoscale materials. However, examination of structural data is only one piece of the bigger picture. In the context of building macroscale devices from nanoscale materials it will be necessary to characterize the energetic forces that drive complex formation and composite combination of different nanomaterials. Structural details alone do not give us the full picture. In order to gain a fuller understanding of nanomaterial interactions with other matter it will be necessary to combine established structural characterization techniques such as SEM, TEM, and AFM with an understanding of the thermodynamics and kinetics of nanomaterial interaction processes. To this end, this chapter describes in detail the development of isothermal titration calorimetry as a tool to measure the underlying thermodynamics of nanomaterial interactions with supporting solvent as well as ruthenium coordination complexes. Because the focus of our group is on the directed assembly of nanomaterials, specifically SWCNTs, the subject of the following ITC studies involves dispersions of SWCNTs as the nanomaterial of interest and dinuclear ruthenium coordination complexes as the interacting molecule.

To preface this work it is helpful to draw an analogue between interactions of SWCNTs and molecular complexes and enzyme—receptor protein binding interactions, a system well characterized by ITC. FIGURE 3.1 shows a comparison of two binding interactions. FIGURE 3.1b is the binding interaction between a rigid dinuclear ruthenium complex and a SWCNT which will be discussed in is section 3.4. FIGURE 3.1a is the analogous biological interaction of a receptor protein and enzyme I would like the reader to imagine as the concept of ITC is discussed further.

ITC has been established as a powerful tool for examining biological interactions.[33-35] In a well designed experiment the binding enthalpy (ΔH_B), the equilibrium binding constant (K_b) and the reaction stoichiometry (n) of a given interaction can be determined. Also by performing the experiments over a range of temperatures the change in heat capacity (ΔC_P) can be determined. The calorimeter used for the work in this dissertation is the NanoITC – Low Volume purchased from TA Instruments (FIGURE 3.2).

In a typical ITC instrument such as the NanoITC, binding enthalpy is measured within one of two small cells, the reaction cell and the reference cell. The two cells are located within an adiabatic jacket which is kept between 5 – 10 °C. The sample cell is arranged so that a combination syringe/stirring device, containing one reactant can be inserted into it. Aliquots of the reactants in question are combined

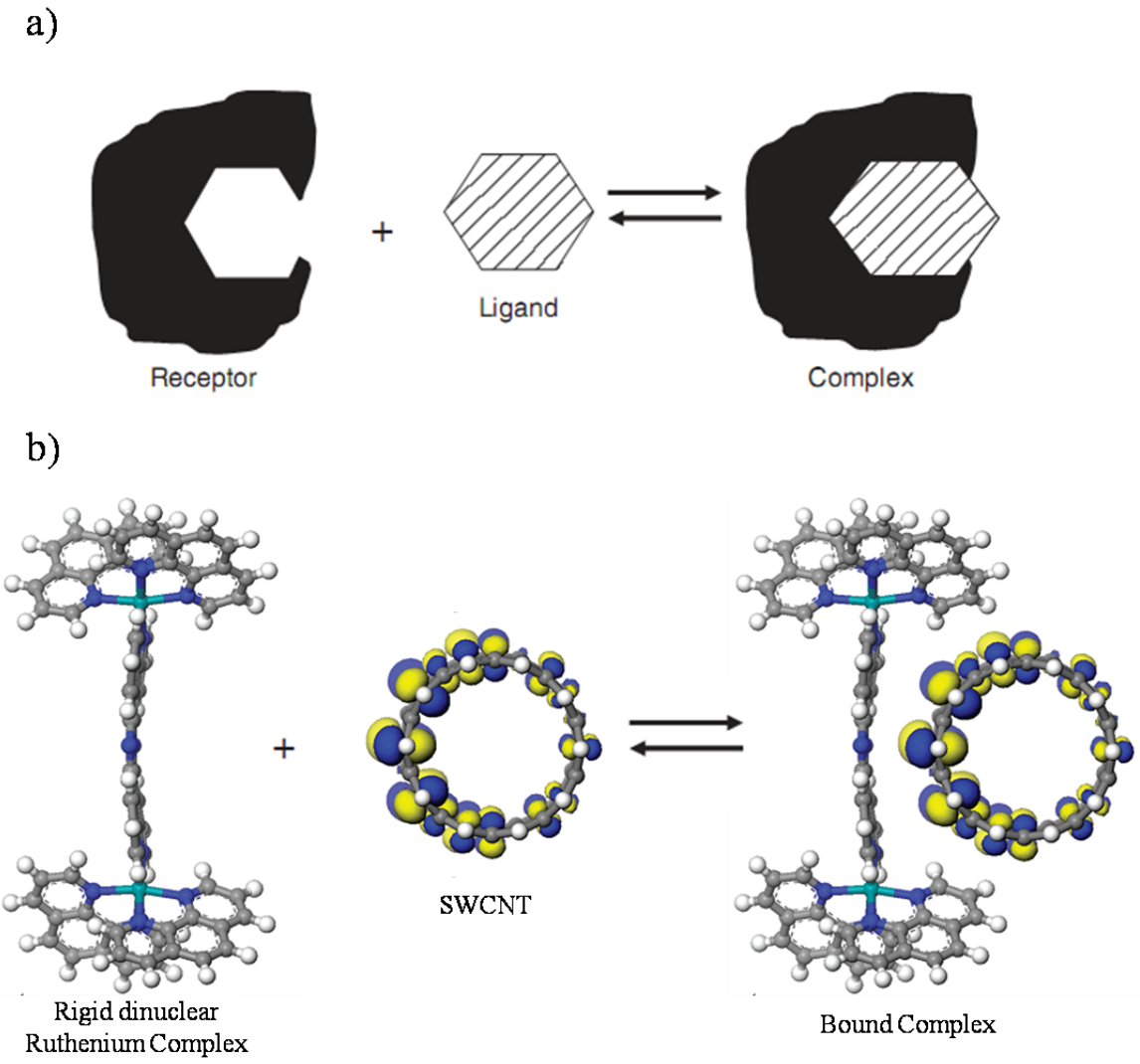

FIGURE 3.1. Binding of a receptor protein and enzyme compared to the binding of a rigid molecular complex and a SWCNT. a) Cartoon of receptor protein and enzyme binding to form a complex. b) Molecular model depicting a dinuclear ruthenium complex binding to the side wall of a SWCNT.

in known quantities by injecting one into the other with the syringe. The reference cell contains the same supporting solution that is in the sample cell and syringe, with the purpose of maintaining the same heat capacity as the analyte solution. The reference cell is usually sealed and contains a dummy syringe to more closely mimic the thermal profile of the sample cell. Each cell is heated and a set amount of power is delivered to each to maintain thermal equilibrium. FIGURE 3.3 is a detailed schematic that highlights the main components of a typical ITC. During titration, ITC measures the sum of the heat associated with all processes occurring upon addition of aliquots of the titrant. As the reaction progresses, a thermocouple detects the difference in temperature between the sample and reference cells and the power delivered to the sample cell is adjusted accordingly which is the raw data recorded in the experiment; an example is illustrated in FIGURE 3.4. The injection enthalpy is determined directly from the raw data by integration of the power delivered to the cell with respect to time followed by concentration normalization. The determination of thermodynamic parameters is accomplished from fitting the ITC binding isotherm to an appropriate model (independent binding sites, sequential binding sites, etc.).[35,36]

Because pristine SWCNTs can be thought of as rolled graphene sheets, one can assume that they have homogeneous and uniform surfaces on which to bind, regardless of diameter and length. For the experiments described herein and to simplify the development of this tool for use with nanomaterials we will assume the simple independent binding sites model and that there is no competing equilibria.

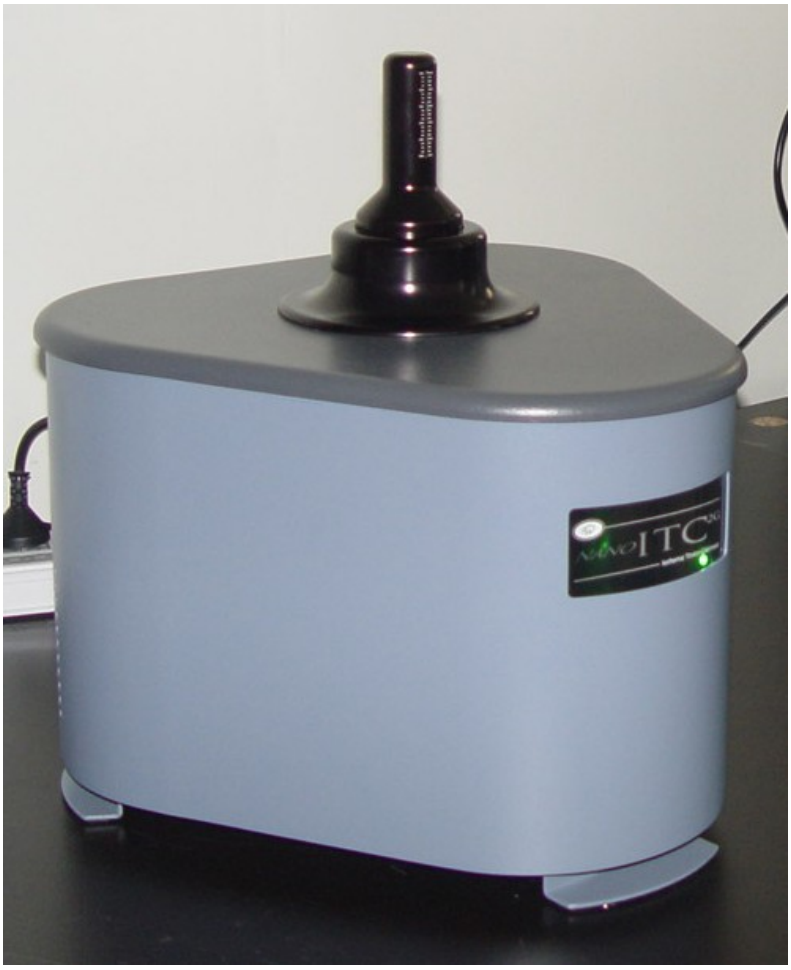

FIGURE 3.2. NanoITC - Low Volume, purchased from TA Instruments.

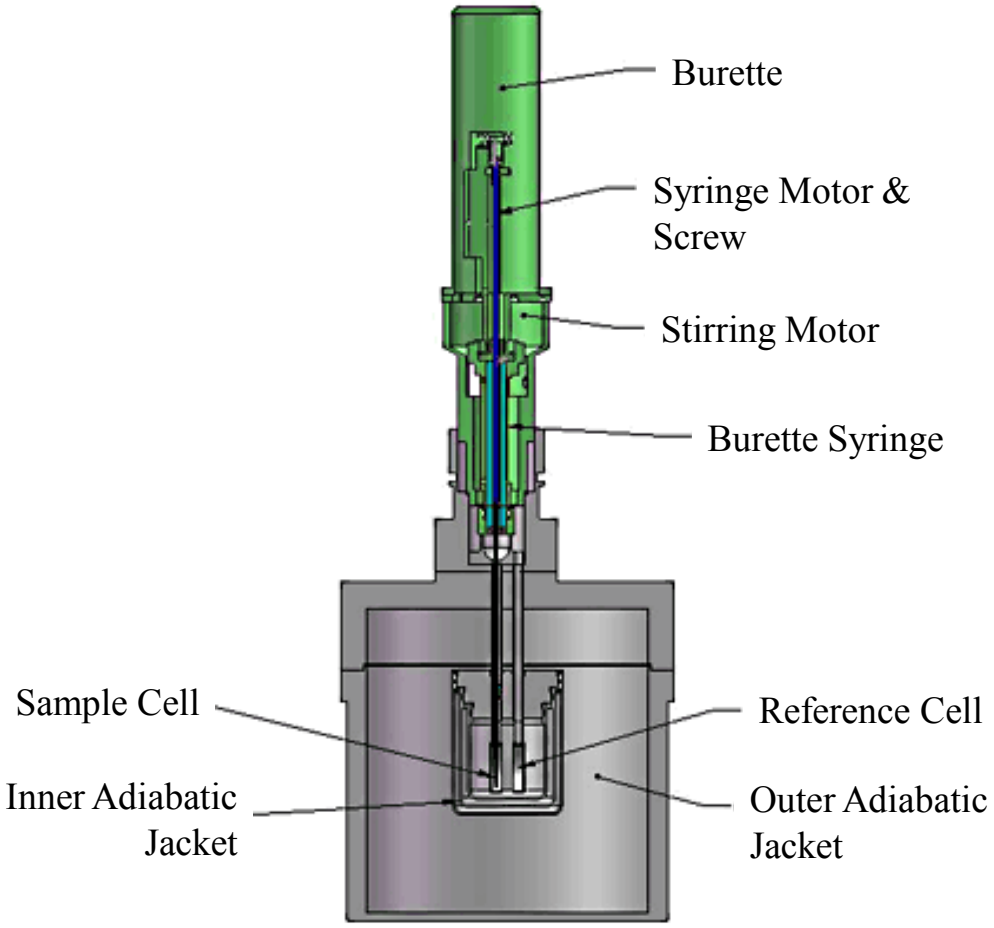

FIGURE 3.3. Diagram of ITC cells and syringe. The syringe rotates in place during the ITC experiment. The end of the syringe provides continuous mixing in the ITC sample cell. The plunger is computer-controlled and injects precise volumes of titrant. Adapted from microcal.com/technology/itc.

This model quantifies the amount of bound complex that is formed over the course of a titration by measuring its heat of formation, and the desired thermodynamic parameters (K, ΔH, n) are obtained directly from the best fit of the data. As mentioned above the determination of thermodynamic parameters from heat data relies upon the nonlinear least squares fit of the data with an appropriate binding model. The parameters n, K, ΔH, are the independent variables of thermodynamic interest and the entropy ΔS and free energy ΔG of binding are dependent obtained from calculation discussed below. FIGURE 3.4 is a representative illustration of raw ITC data from an experiment of 20 equal injections of a ligand into a macromolecule solution. The thermodynamic values determined from the fit are provided in the legend. These data represent an ideal isotherm by which the quality of our data presented in this dissertation can be judged. In a system with independent homogeneous binding sites and a reaction stoichiometry of 1:1 a sigmoidal shape like the one in FIGURE 3.4 should be observed.

The ITC work discussed in this chapter uses the single site binding model established to characterize biological analytes, and applies it to the thermodynamic characterization of SWCNT dispersions. It will be shown that ITC can be an important analytical tool to gain a fuller understanding of nanomaterial interactions. The work presented in this dissertation establishes an important step toward using thermodynamic techniques like ITC to characterize nanomaterial interactions. Eventually, building on this work will allow ITC measurements to contribute important insight into the thermodynamics and kinetics of structures formed

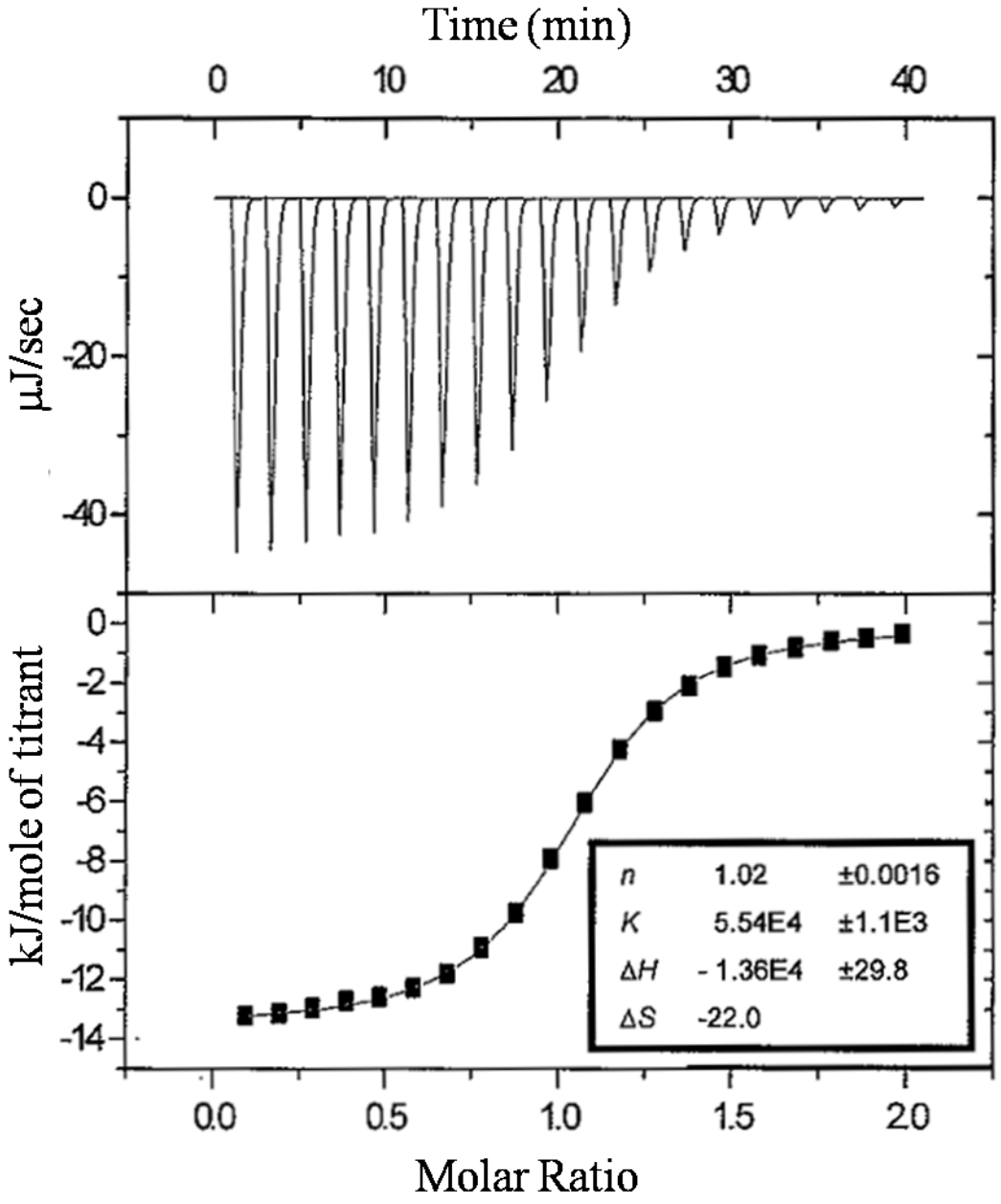

FIGURE 3.4. Typical data derived from an ITC experiment. a) the raw data output. The peaks are plotted as power against time. b) the integrated raw data output plotted as molar change in enthalpy against mole ratio. Illustrates the nonlinear least squares fit of the data by the independent binding model.

from nanomaterial and imaged by SEM, TEM, and AFM.

3.2 SWCNT Integration, Functionalization and Interactions

Our capacity to manipulate nanomaterials and integrate them into devices and composites depends on our ability to predict and understand the surface interactions of nanoparticles with solvents and other species, i.e., ligands, proteins, polymers and other nanomaterials. Many as-produced nanomaterials can be effectively handled in a liquid matrix which lends them to uses in medicine and industry.[37] Fullerenes,[38] gold nanoparticles,[39,40] quantum dots,[41] ultrananocrystalline diamond,[42] and carbon nanotubes[43-45] are among the many nanomaterials currently being developed within liquid media for medical and industrial applications. Single-walled carbon nanotubes (SWCNTs) are an example of a nanomaterial that is primarily handled in a liquid dispersion, as they can be dispersed in a wide range of aqueous[46] and organic solvents.[47] Due to their unique mechanical, thermal and electrical properties[43-45,48,49] SWCNTs have been used for sensing and electronics,[45,50] reinforcement in polymers, substrate coatings,[51,52] and advanced fibers and filtration.[53] Solution based processing is an efficient and effective method of bringing different materials, including SWCNTs together to form those composite devices.[54-56] However, pristine SWCNTs are insoluble in all known solvents.[47] Insolubility leads to imprecise integration of SWCNTs into materials due to the high probability that SWCNTs will bundle and aggregate while in solution.

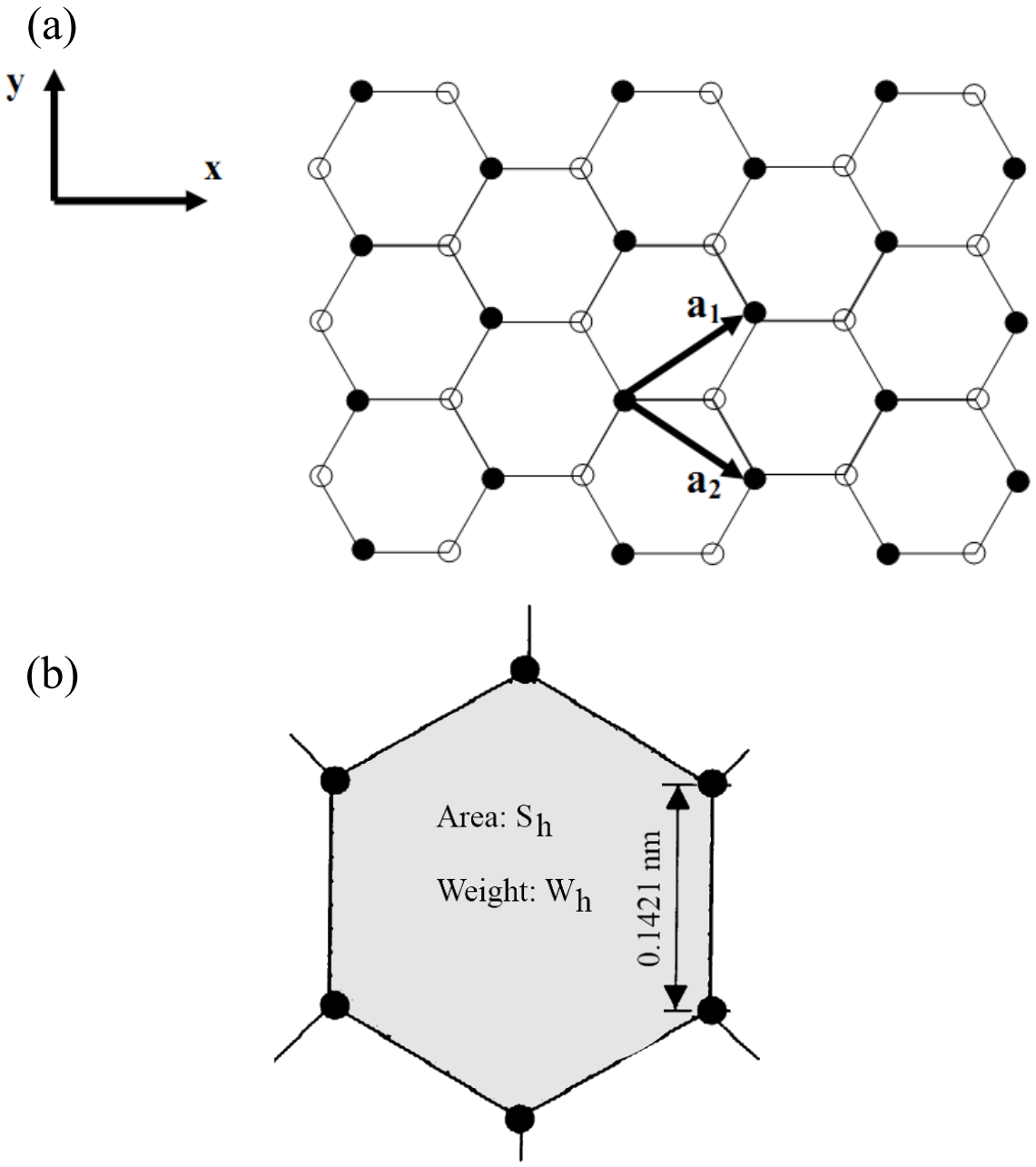

FIGURE 3.5. Arrangement of carbon atoms in graphene. (a) Lattice of graphene. A pair of carbon atoms denoted by solid and open dot respectively, forms a unit cell. (b) Schematic arrangement of carbon atoms within the graphene layer.

3.2.1 SWCNTs Solubility and Functionalization

The solubility of carbon nanotubes is often augmented by a dispersant phase such as a surfactant or polymer,[46] or through chemical functionalization. Both methods tend to inhibit or adversely affect the desired properties of pristine nanotubes.[59] The tendency of SWCNTs to bundle has been the primary challenge for industrial applications that utilize carbon nanotubes in polymer matrices and composites. Coleman et al. reported a positive correlation of available carbon nanotube surface area in dispersions with improved mechanical properties of a polymer composite containing dispersed carbon nanotubes (CNTs).[51] Notably, the inverse correlation was also shown; the increase of nanotube diameter and presence of CNT bundles reduces the effectiveness of CNTs as reinforcing agents in nanocomposites.[51] There is a need for solutions of individually dispersed carbon nanotubes. If solutions of pristine unbundled nanotubes could be made it would allow carbon nanotubes to be used in many established liquid processing techniques.[47] To this end, it has been shown both thermodynamically and kinetically that the selection and treatment of appropriate solvents and solvent mixtures can have dramatic effects on the quality and stability of dispersions of nanomaterials such as SWCNTs and could lead to true thermodynamic dissolution of single-walled carbon nanotubes.[47,60-62]

3.3 Isothermal Titration Calorimetry of Amide Solvents and SWCNTs

By directly measuring the interaction enthalpy of two different polar aprotic solvents with a dispersion of highly purified single-walled carbon nanotubes, this section presents significant contributions to the development of ITC as a tool to

probe the thermodynamics of solvent interactions with dispersed nanomaterials. Physical, chemical, and biological interactions are accompanied by heat exchange. The ability of calorimetry to directly measure this heat makes it one of the most important and effective tools for measuring thermodynamic processes at constant temperature and pressure. Other analytical techniques require enthalpy values to be calculated from other physical measurements. These van't Hoff analyses are processes in which concentrations of reactants in a thermodynamic equilibrium are monitored or measured *via* appropriate analytical techniques and used to establish an equilibrium constant as a function of temperature. Interaction enthalpies calculated using the van't Hoff equation are limited to small temperature ranges and by larger propagated errors.[33,63] Isothermal titration calorimetry allows the direct thermodynamic measurement of nanomaterials without the demands and complications of indirect measurements from spectroscopy or physical tagging types of analysis.

ITC was developed for, and has been routinely used to measure the binding interactions between biological substituents.[35] However, ITC is not limited to biological measurements[64] and its use is becoming wide spread. The use of ITC to study the interactions of solvent supported nanoscale materials is still a nascent pursuit but has shown promise. In the last 10 years there have only been about 30 publications that use ITC measurements on nanoscale or nanopatterned materials, some of which are cited here.[65-73] All but a few of these studies are primarily focused on measuring the interactions of biologically relevant molecules with nanomaterials and only a few were conducted in non-aqueous media. To our

knowledge, this is the first reported use of ITC to measure SWCNTs dispersed in non-aqueous media. Earlier publications[69,70] have set a conceptual precedent to measure the interaction of molecules with SWCNTs with ITC. However, previous SWCNT-ITC work has been conducted in aqueous media and has resulted in nondescript binding curves with approximated binding enthalpies. Those studies were unable to determine the association constants or entropy contributions of the analyzed interactions. Water is not a solvent that favors dispersing individual or even small bundles of pristine SWCNTs. An important differentiation between our work and previous studies is that we use two well known polar aprotic SWCNT solvents, facilitating the ability to probe the surface of highly dispersed SWCNTs.[47,62]

This section discusses the use of ITC to measure the enthalpic and entropic contributions of the interactions of polar aprotic solvents with SWCNT dispersions in pure *N*,*N*-dimethyl-formamide (DMF) or pure *N*-methyl-2-pyrilidone (NMP). We find that injection of a NMP:DMF mixture into a DMF dispersion has an exothermic interaction enthalpy with SWCNTs of approximately -20 J mol^{-1}. The injection of the NMP:DMF into an NMP dispersion produces a significantly smaller exothermic interaction enthalpy of approximately -7 J mol^{-1}. An additional outcome of this study is the direct measurement of the dilution enthalpy of NMP:DMF as it is titrated into pure DMF or pure NMP. From the dilution curves, the enthalpic interaction coefficients for both processes were calculated. Our results suggest that spontaneous exfoliation of SWCNT bundles occurs due partly to dilution[74] and also to the increasingly favorable solvent parameters as the mole ratio of NMP:DMF

approaches 0.5. These results are consistent with previous observations that NMP is a better carbon nanotube dispersant and that spontaneous exfoliation occurs when NMP is added to a SWCNT dispersion,[62] possibly approaching thermodynamic stability of a carbon nanotube solution.[74]

3.3.1 Thermodynamic Measurements using ITC

3.3.1.1 Calculations of Dilution Enthalpy and Enthalpic Interaction Coefficients

The determination of dilution enthalpy and the enthalpic interaction coefficients from an ITC experiment are calculated by the relationships established by Fini et al and McMillan et al.[75,76] The following explanations can be found in Fini's work[75] and in the supplemental information of Zhang et al.[77] Dilution enthalpy per injection are expressed by the combination of equation (3.1) and equation (3.2).[75] Where N is the injection number and n_{inj} is the moles of solute in volume of injected titrant (V_{inj_N}). m_{inj} is the concentration of the solute in the titration syringe (mol kg^{-1}) and ρ_{inj} is the density of syringe solution.

$$\Delta H_{\left(m_{N-1} \rightarrow m_N\right)} = \frac{\Delta H_{(m_{N-1}, m_N)}}{n_{inj}} \quad 3.1$$

$$n_{inj} = V_{inj_N} * \rho_{\text{inj}} * m_{inj} \quad 3.2$$

When a solute is dissolved in a solvent a solution is formed. During dissolution of a solute in any solvent, heat is either absorbed or evolved and the amount is unique to the specific solute and solvent combination. Heat changes produced by dissolution under constant pressure conditions are known as the enthalpy of solution. Enthalpy of solution is defined by the enthalpy change that occurs when one mole of a solute is dissolved in a specified quantity of a solvent at a given temperature. To deconvolute the value from the specific amount of solvent,

heat of solution is usually defined for an infinitely dilute solution. Thus, the heat of solution at infinite dilution (enthalpy of "infinite" dilution, ΔH_{dln}) is the heat change when one mole of a substance is dissolved in such a large quantity of solvent so that further dilution does not give any further heat change.

The coefficients h_{xx} and h_{xxx} are obtained from measurements of enthalpy of dilution, solution or mixing using the thermodynamic treatments established by McMillan and Mayer.[76]

Since the titrant solution studied was a significantly different density (0.991 kg L^{-1} NMP:DMF solution) to the sample cell solvents (1.028 kg L^{-1} NMP, 0.944 kg L^{-1} DMF) the densities of the mixture following each injection was adjusted and the resulting concentration (mol kg^{-1}) was calculated from the new density given by equation (3.4). Denisty tables for each experiment type NMP:DMF into DMF and NMP:DMF into NMP were constructed on the principle of mass conservation and the assumption that the new active volume of sample cell (V_{cell_N}) is the volume of injected titrant (V_{inj_N}) and the active volume of the sample cell ($V_{cell_{N-1}}$), equation (3.3). The new density (ρ_{cell_N}) within the active volume of the sample cell is the mass of injected titrant (m_{inj_N}) and the mass within the sample cell ($m_{cell_{N-1}}$) before injection N, divided by the new active volume (V_{cell_N}) given by equation (3.3). Density calculations are presented in TABLE 3.1 and TABLE 3.2.

$$V_{cell_N} = V_{inj_N} + V_{cell_{N-1}} \tag{3.3}$$

$$\rho_{cell_N} = \frac{\left[\left(\rho_{inj_N} * V_{inj_N}\right) + \left(\rho_{cell_{N-1}} * V_{cell_{N-1}}\right)\right]}{V_{cell_N}} \tag{3.4}$$

The concentration of titrant solvent in the active volume of the sample cell after injection N was then calculated by equation (3.5). The concentration (mol kg^{-1}) of NMP, DMF and SWCNTs in all the experiments is presented in TABLE 3.3 and TABLE 3.4.

$$m_{cell_N} = \frac{\left[\left(m_{inj}{*}\rho_{inj}{*}V_{inj_N}\right)+\left(m_{cell_{N-1}}{*}\rho_{cell_{N-1}}{*}V_{cell_0}\right)\right]}{\rho_{cell_N}{*}V_{cell_0}} \tag{3.5}$$

According to McMillan and Mayer, excess enthalpy in a binary solution with m_S moles of solute per kg of solvent can be expressed as equation (3.6). Higher order terms of m_S within the virial expansion for excess enthalpy, $H^E(m_S)$, of the mixture are typically neglected unless interested in high concentration of solute in the active volume of the sample cell. Coefficients of the first and second order terms are typically sufficient to describe the interaction of solute molecules in most cases.[75]

TABLE 3.1. Density values ρcell (g/L) for the active volume Vcell (L) after each injection N. Vinj (L) is the volume of the injection, ρinj (g/L) is the density of the injection solution. Vdmf (L) and ρdmf (g/L) are the remaining volume of DMF originally in the cell and the density of pure DMF, respectively. .

Density Table (NMP:DMF into DMF)						
N	V_{inj} (L)	ρ_{inj} (g/L)	V_{cell} (L)	ρ_{cell} (g/L)	V_{dmf} (L)	ρ_{dmf} (g/L)
1	9.80E-07	991	1.65E-04	944.3	1.64E-04	944
2	2.00E-06	991	1.67E-04	944.8	1.63E-04	944
3	2.00E-06	991	1.69E-04	945.4	1.61E-04	944
4	2.00E-06	991	1.71E-04	945.9	1.59E-04	944
5	2.00E-06	991	1.73E-04	946.4	1.57E-04	944
6	2.00E-06	991	1.75E-04	946.9	1.55E-04	944
7	2.00E-06	991	1.77E-04	947.4	1.53E-04	944
8	2.00E-06	991	1.79E-04	947.9	1.51E-04	944
9	2.00E-06	991	1.81E-04	948.4	1.49E-04	944
10	2.00E-06	991	1.83E-04	948.9	1.47E-04	944
11	2.00E-06	991	1.85E-04	949.3	1.45E-04	944
12	2.00E-06	991	1.87E-04	949.8	1.43E-04	944
13	2.00E-06	991	1.89E-04	950.2	1.41E-04	944
14	2.00E-06	991	1.91E-04	950.6	1.39E-04	944
15	2.00E-06	991	1.93E-04	951.1	1.37E-04	944
16	2.00E-06	991	1.95E-04	951.5	1.35E-04	944
17	2.00E-06	991	1.97E-04	951.9	1.33E-04	944
18	2.00E-06	991	1.99E-04	952.3	1.31E-04	944
19	2.00E-06	991	2.01E-04	952.6	1.29E-04	944
20	2.00E-06	991	2.03E-04	953.0	1.27E-04	944
21	2.00E-06	991	2.05E-04	953.4	1.25E-04	944
22	2.00E-06	991	2.07E-04	953.8	1.23E-04	944
23	2.00E-06	991	2.09E-04	954.1	1.21E-04	944
24	2.00E-06	991	2.11E-04	954.5	1.19E-04	944
25	2.00E-06	991	2.13E-04	954.8	1.17E-04	944

TABLE 3.2. Density values ρcell (g/L) for the active volume Vcell (L) after each injection N. Vinj (L) is the volume of the injection, ρinj (g/L) is the density of the injection solution. Vnmp (L) and ρnmp (g/L) are the remaining volume of NMP originally in the cell and the density of pure NMP, respectively. .

Density Table (NMP:DMF into NMP)						
N	V_{inj} (L)	ρ_{inj} (g/L)	V_{cell} (L)	ρ_{cell} (g/L)	V_{nmp} (L)	ρ_{nmp} (g/L)
1	9.80E-07	991	1.65E-04	1027.8	1.64E-04	1028
2	2.00E-06	991	1.67E-04	1027.3	1.63E-04	1028
3	2.00E-06	991	1.69E-04	1026.9	1.61E-04	1028
4	2.00E-06	991	1.71E-04	1026.5	1.59E-04	1028
5	2.00E-06	991	1.73E-04	1026.1	1.57E-04	1028
6	2.00E-06	991	1.75E-04	1025.7	1.55E-04	1028
7	2.00E-06	991	1.77E-04	1025.3	1.53E-04	1028
8	2.00E-06	991	1.79E-04	1024.9	1.51E-04	1028
9	2.00E-06	991	1.81E-04	1024.5	1.49E-04	1028
10	2.00E-06	991	1.83E-04	1024.2	1.47E-04	1028
11	2.00E-06	991	1.85E-04	1023.8	1.45E-04	1028
12	2.00E-06	991	1.87E-04	1023.5	1.43E-04	1028
13	2.00E-06	991	1.89E-04	1023.1	1.41E-04	1028
14	2.00E-06	991	1.91E-04	1022.8	1.39E-04	1028
15	2.00E-06	991	1.93E-04	1022.4	1.37E-04	1028
16	2.00E-06	991	1.95E-04	1022.1	1.35E-04	1028
17	2.00E-06	991	1.97E-04	1021.8	1.33E-04	1028
18	2.00E-06	991	1.99E-04	1021.5	1.31E-04	1028
19	2.00E-06	991	2.01E-04	1021.2	1.29E-04	1028
20	2.00E-06	991	2.03E-04	1020.9	1.27E-04	1028
21	2.00E-06	991	2.05E-04	1020.6	1.25E-04	1028
22	2.00E-06	991	2.07E-04	1020.3	1.23E-04	1028
23	2.00E-06	991	2.09E-04	1020.0	1.21E-04	1028
24	2.00E-06	991	2.11E-04	1019.8	1.19E-04	1028
25	2.00E-06	991	2.13E-04	1019.5	1.17E-04	1028

TABLE 3.3. Concentration Values of NMP, DMF and SWCNTs after each injection, N, during a titration of NMP:DMF mixture into a dispersion of SWCNTs in DMF.

Concentration Table (NMP:DMF into DMF)							
N	mol NMP	NMP mol/kg	mol DMF	DMF mol/kg	SWCNT g/kg	mol SWCNT	SWCNT mol/kg
1	5.69E-06	0.04	2.12E-03	13.68	4.12E-03	2.65E-08	1.71E-04
2	1.72E-05	0.11	2.10E-03	13.58	4.09E-03	2.64E-08	1.70E-04
3	2.86E-05	0.18	2.09E-03	13.48	4.04E-03	2.61E-08	1.68E-04
4	3.99E-05	0.26	2.08E-03	13.38	3.99E-03	2.57E-08	1.66E-04
5	5.10E-05	0.33	2.06E-03	13.28	3.93E-03	2.54E-08	1.64E-04
6	6.20E-05	0.40	2.05E-03	13.18	3.88E-03	2.51E-08	1.62E-04
7	7.29E-05	0.47	2.03E-03	13.09	3.84E-03	2.48E-08	1.60E-04
8	8.36E-05	0.54	2.02E-03	13.00	3.79E-03	2.45E-08	1.58E-04
9	9.42E-05	0.61	2.01E-03	12.91	3.74E-03	2.42E-08	1.56E-04
10	1.05E-04	0.67	1.99E-03	12.81	3.69E-03	2.39E-08	1.54E-04
11	1.15E-04	0.74	1.98E-03	12.73	3.64E-03	2.36E-08	1.52E-04
12	1.25E-04	0.80	1.97E-03	12.64	3.60E-03	2.33E-08	1.50E-04
13	1.35E-04	0.87	1.96E-03	12.55	3.55E-03	2.30E-08	1.48E-04
14	1.45E-04	0.93	1.94E-03	12.46	3.51E-03	2.28E-08	1.46E-04
15	1.55E-04	0.99	1.93E-03	12.38	3.46E-03	2.25E-08	1.44E-04
16	1.65E-04	1.06	1.92E-03	12.30	3.42E-03	2.22E-08	1.42E-04
17	1.74E-04	1.12	1.91E-03	12.21	3.38E-03	2.19E-08	1.41E-04
18	1.84E-04	1.18	1.89E-03	12.13	3.33E-03	2.17E-08	1.39E-04
19	1.93E-04	1.24	1.88E-03	12.05	3.29E-03	2.14E-08	1.37E-04
20	2.02E-04	1.30	1.87E-03	11.97	3.25E-03	2.12E-08	1.35E-04
21	2.12E-04	1.35	1.86E-03	11.90	3.21E-03	2.09E-08	1.34E-04
22	2.21E-04	1.41	1.85E-03	11.82	3.17E-03	2.06E-08	1.32E-04
23	2.30E-04	1.47	1.84E-03	11.74	3.13E-03	2.04E-08	1.30E-04
24	2.38E-04	1.52	1.83E-03	11.67	3.09E-03	2.01E-08	1.29E-04
25	2.47E-04	1.58	1.82E-03	11.60	3.05E-03	1.99E-08	1.27E-04

TABLE 3.4. Concentration Values of NMP, DMF and SWCNTs after each injection, N, during a titration of NMP:DMF mixture into a dispersion of SWCNTs in NMP.

Concentration Table (NMP:DMF into NMP)							
N	mol NMP	NMP mol/kg	mol DMF	DMF mol/kg	SWCNT g/kg	mol SWCNT	SWCNT mol/kg
1	1.70E-03	10.09	5.57E-06	0.03	3.78E-03	2.65E-08	1.57E-04
2	1.69E-03	10.04	1.69E-05	0.10	3.76E-03	2.64E-08	1.57E-04
3	1.68E-03	9.99	2.80E-05	0.17	3.72E-03	2.61E-08	1.55E-04
4	1.67E-03	9.94	3.91E-05	0.23	3.67E-03	2.57E-08	1.53E-04
5	1.66E-03	9.89	5.00E-05	0.30	3.63E-03	2.54E-08	1.51E-04
6	1.66E-03	9.85	6.07E-05	0.36	3.59E-03	2.51E-08	1.49E-04
7	1.65E-03	9.80	7.14E-05	0.42	3.54E-03	2.48E-08	1.48E-04
8	1.64E-03	9.75	8.19E-05	0.49	3.50E-03	2.45E-08	1.46E-04
9	1.63E-03	9.71	9.22E-05	0.55	3.46E-03	2.42E-08	1.44E-04
10	1.62E-03	9.66	1.02E-04	0.61	3.42E-03	2.39E-08	1.42E-04
11	1.61E-03	9.61	1.13E-04	0.67	3.38E-03	2.36E-08	1.41E-04
12	1.61E-03	9.57	1.23E-04	0.73	3.34E-03	2.33E-08	1.39E-04
13	1.60E-03	9.53	1.32E-04	0.79	3.30E-03	2.30E-08	1.37E-04
14	1.59E-03	9.48	1.42E-04	0.85	3.26E-03	2.28E-08	1.36E-04
15	1.58E-03	9.44	1.52E-04	0.91	3.22E-03	2.25E-08	1.34E-04
16	1.57E-03	9.39	1.61E-04	0.96	3.18E-03	2.22E-08	1.33E-04
17	1.57E-03	9.35	1.71E-04	1.02	3.15E-03	2.19E-08	1.31E-04
18	1.56E-03	9.31	1.80E-04	1.07	3.11E-03	2.17E-08	1.29E-04
19	1.55E-03	9.27	1.89E-04	1.13	3.07E-03	2.14E-08	1.28E-04
20	1.55E-03	9.23	1.98E-04	1.18	3.03E-03	2.12E-08	1.26E-04
21	1.54E-03	9.19	2.07E-04	1.24	3.00E-03	2.09E-08	1.25E-04
22	1.53E-03	9.15	2.16E-04	1.29	2.96E-03	2.06E-08	1.23E-04
23	1.52E-03	9.11	2.25E-04	1.34	2.93E-03	2.04E-08	1.22E-04
24	1.52E-03	9.07	2.33E-04	1.40	2.89E-03	2.01E-08	1.20E-04
25	1.51E-03	9.03	2.42E-04	1.45	2.86E-03	1.99E-08	1.19E-04

$$H^E(m_X) = h_{XX}m_X + h_{XXX}m_X^2 + \cdots \quad (3.6)$$

h_{XX} and h_{XXX} are coefficients which measure enthalpic contributions due to the interaction of pairs and triplets of solute molecules. h_{XXX} describes the complicated interaction contributions of a triplet of solute molecules and h_{xx} is the enthalpic pairwise coefficient related to the change in enthalpy of a solution due to two solvated molecules moving from infinity to a finite interaction distance. Linear regression of the resulting $\Delta H_{(m_{N-1} \rightarrow m_N)}$ versus N data allows the calculation of h_{xx} and h_{xxx} by the equations (3.18) from the following treatment.

The thermodynamic formula commonly used to determine the excess enthalpy of a binary solution containing solute X and solvent Y (Y = DMF or NMP) can be expressed as equation (3.6). To evaluate the coefficients, the dilution enthalpies of a binary solution of solute and solvent are needed.

Dilution begins with the sample cell filled with n_Y^0 moles of solvent Y. When the first amount of titrant containing n_X moles of solute and n_Y moles of solvent Y the resulting solution in the sample cell contains the sum of the three quantities and enthalpy of the initial state has two parts:

$$\text{Initial State} \quad \text{Syringe:} \quad n_X H^{\phi}(m_{inj}) + n_Y H_Y^0$$

$$\text{Cell:} \quad n_Y^0 H_Y^0 \quad (3.7)$$

where H_Y^{ϕ} is the molar enthalpy of Y and $H^{\phi}(m_{inj})$ is the apparent molar enthalpy of the solution at concentration m_{inj} in the syringe, making the final enthalpy state:

$$\text{Final State} \quad \text{Cell:} \quad n_X H^{\phi}(m_1) + n_Y^0 H_Y^0 + n_Y H_Y^0 \quad (3.8)$$

where $H^{\phi}(m_1)$ is the apparent enthalpy of solution at m_1 in the cell after injection *N* = 1 and the change in enthalpy from the initial state becomes

$$\Delta H(m_0, m_1) = n_X\left[H^{\phi}(m_1) - H^{\phi}(m_{inj})\right] \tag{3.9}$$

It then follows that before the second injection the enthalpy state is

$$\begin{aligned} \text{Syringe:} \quad & n_X H^{\phi}\left(m_{inj}\right) + n_Y H_Y^0 \\ \text{Cell:} \quad & n_X H^{\phi}(m_1) + n_Y^0 H_Y^0 + n_Y H_Y^0 \end{aligned} \tag{3.10}$$

So that the total enthalpy of the final state is

$$\text{Cell:} \quad 2n_X H^{\phi}(m_2) + n_Y^0 H_Y^0 + 2n_Y H_Y^0 \tag{3.11}$$

where $H^{\phi}(m_2)$ is the total apparent enthalpy within the sample cell at concentration m_2. The change in enthalpy from m_1 to m_2 then becomes

$$\Delta H(m_1, m_2) = n_X\left[2H^{\phi}(m_2) - H^{\phi}(m_1) - H^{\phi}(m_{inj})\right] \tag{3.12}$$

The same progression applies to the *N*th injection into the sample cell where the change in enthalpy from m_{N-1} to m_N can be expressed as

$$\Delta H(m_{N-1}, m_N) = n_X\left[NH^{\phi}(m_N) - (N-1)H^{\phi}(m_{N-1}) - H^{\phi}(m_{inj})\right] \tag{3.13}$$

Equation (3.13) can then be rearranged as

$$\begin{aligned} \Delta H_{\left(m_{N-1} \rightarrow m_N\right)} &= \Delta H_{(m_{N-1},\, m_N)}/n_X \\ &= (N-1)[H^{\phi}(m_N) - H^{\phi}(m_{N-1})] + [H^{\phi}(m_N) - H^{\phi}(m_{inj})] \end{aligned} \tag{3.14}$$

so that the terms $[H^{\phi}(m_N) - H^{\phi}(m_{N-1})]$ are the enthalpic change do to dilution from m_{N-1} to m_N and the terms $[H^{\phi}(m_N) - H^{\phi}(m_{inj})]$ are the change from m_0 to m_N. From the definitions of the apparent and excess thermodynamic quantities the following relationships can be expressed:

$$[H^{\phi}(m_N) - H^{\phi}(m_{N-1})] = [H^{E}(m_N) - H^{E}(m_{N-1})]$$
$$[H^{\phi}(m_N) - H^{\phi}(m_{inj})] = [H^{E}(m_N) - H^{E}(m_{inj})] \quad (3.15)$$

Substitution of equation (3.6) into the relationships (3.15) and from that, (3.15) into (3.14) gives

$$\Delta H_{\left(m_{N-1} \rightarrow m_N\right)} = (N-1)\,[h_{XX}(m_N - m_{N-1}) + h_{XXX}(m_N^2 - m_{N-1}^2) + h_{XXX}[(m_N - m_{inj}) + (m_N^2 - m_{inj}^2)] \quad (3.16)$$

When the volume of the injected solution is much less that the solution in the cell and m_1 is much less than 1 we can consider $\Delta H_{\left(m_{N-1} \rightarrow m_N\right)}$ linearly dependent on N such that

$$\Delta H_{\left(m_{N-1} \rightarrow m_N\right)} = 2h_{XX}m_1N - [h_{XX}(m_1 + m_{inj}) + h_{XXX}m_{inj}^2] \quad (3.17)$$

And the values of the intercept and slope of the linear regression of $\Delta H_{\left(m_{N-1} \rightarrow m_N\right)}$ versus N provide the determination of h_{XX} and h_{XXX}:

$$h_{XX} = slope/2m_1$$
$$h_{XXX} = \frac{[intercept - slope(h_{XX})]}{m_{inj}^2} \quad (3.18)$$

3.3.2 Heat of Interaction - Calculation of Constants and Enthalpies.

For a given interaction as with a dispersed nanomaterial and a coordinating solvent, where *N* is a binding site on the nanomaterial and *S* in an equivalently sized unit of solvent,

$$S + N \overset{K_A}{\leftrightarrow} SN \tag{3.19}$$

K_A is the interaction or binding constant which describes the equilibrium concentrations of free solvent, free nanomaterial and bound solvent-nanomaterial:

$$K_A = \frac{[SN]_{eq}}{[S]_{eq}[N]_{eq}} \tag{3.20}$$

K_A effectively measures the affinity of the solvent for the nanomaterial. By definition, equation (3.20), after an injection the equilibrium concentrations of *S* and *N* are equal to the total concentrations of *S* and *N* minus what is bound. Substitution of this relationship into equation (3.20) gives an equation relating K_A to the concentration of bound solvent-nanomaterial to the total concentration of both reactants.

$$K_A = \frac{[SN]}{([S_t]-[SN])([N_t]-[SN])} \tag{3.21}$$

The calculation of interaction enthalpy is based on a similar treatment to that needed to calculate enthalpy at infinite dilution, where Q_i is the heat produced or absorbed during an injection. With respect to isothermal titration calorimetry, the heat generated by an injection, Q_i is related to the equilibrium concentration $[SN]_{eq}$. When the quantity of heat generated per injection is divided by the amount of coordinating solvent contained in that injection and plotted against the ratio of *S* and

N in the active volume of the sample cell you get the sigmoidal curve and ΔH_{int} can be calculated from Q_i by,

$$Q_i = n_{SN_i} \Delta H_{int} \tag{3.22}$$

and,

$$n_{SN_i} = V_{cell} \rho_{\mathrm{cell}_i} K_A [(m_{S_t} - m_{SN_i})(m_{N_t} - m_{SN_i})] \tag{3.23}$$

where ΔH_{int} is the interaction enthalpy of the solvent-nanomaterial, n_{SN_i} is the moles of bound solvent-nanomaterial after injection, and V_{cell} is the active volume of the sample cell with a solution density, ρ_{cell_i}. FIGURE 3.6 shows the thermograms of the average Q_i versus injection number for all the ITC trials at 298.15 K and 308.15 K. The error bars are the standard deviation of the experimental values from the average of the sigmoidal fit. TABLE 3.5 and TABLE 3.6 are the data presented in FIGURE 3.6 and are the average of three to four trials with the standard deviation from the average of the nonlinear regression of each trial.

ITC can determine the change in free energy, ΔG, enthalpy, ΔH, entropy, ΔS, and the interaction equilibrium constant, K_A, in a single experimental run by the standard relationship

$$\Delta G = -RT \ln(K_A) = \Delta H - T\Delta S \tag{3.24}$$

where R is the gas constant and T is the absolute temperature. The association constant,

TABLE 3.5. Heats of interaction per injection, N, during the titration of NMP:DMF mixture in to SWCNTs dispersed in DMF. The value of the fit (mJ) is determined from corresponding y-coordinate of injection Ni for the non-linear regression of the Q values.

Heat of Interaction and Fits NMP:DMF into $SWCNTs_{DMF}$						
298.15 K Average				308.15 K Average		
Q (μJ)	Fit (μJ)	stdev (μJ)		Q (μJ)	Fit (μJ)	stdev (μJ)
-40.087	-153.848	-		-90.790	-209.633	-
-153.574	-153.178	8.308		-223.555	-208.959	8.698
-131.650	-152.587	15.313		-213.978	-208.458	3.913
-160.414	-151.878	15.043		-208.798	-207.897	2.391
-160.490	-151.016	7.137		-207.115	-207.263	3.011
-182.131	-149.955	23.424		-210.526	-206.541	2.851
-153.429	-148.627	10.978		-196.997	-205.709	5.234
-131.452	-146.943	12.448		-201.372	-204.740	4.092
-139.173	-144.778	7.690		-202.787	-203.596	1.582
-137.620	-141.969	3.280		-201.247	-202.222	0.861
-135.263	-138.314	5.988		-197.921	-200.541	2.002
-129.796	-133.605	3.432		-195.998	-198.438	1.470
-124.551	-127.692	4.604		-196.870	-195.739	2.400
-114.392	-120.567	4.368		-192.051	-192.177	1.650
-104.773	-112.356	7.633		-185.380	-187.339	2.564
-115.363	-103.154	9.915		-179.149	-180.620	1.415
-91.344	-92.858	6.631		-167.768	-171.242	3.128
-81.935	-81.233	1.338		-158.335	-158.524	1.137
-71.268	-68.285	2.965		-143.914	-142.445	4.571
-55.335	-54.662	0.490		-126.099	-123.761	4.213
-43.912	-41.596	5.391		-105.501	-102.932	3.540
-33.180	-30.275	2.944		-87.706	-80.520	7.221
-18.678	-21.249	10.533		-50.873	-60.164	5.886
-12.822	-14.424	1.392		-32.071	-45.396	10.562
13.925	-9.389	22.048		-34.965	-35.522	20.471

TABLE 3.6. Heats of interaction per injection, N, during the titration of NMP:DMF mixture in to SWCNTs dispersed in NMP. The value of the fit (mJ) is determined from corresponding y-coordinate of injection Ni for the non-linear regression of the Q values.

Heat of Interaction and Fits NMP:DMF into $SWCNTs_{NMP}$						
298.15 K Average				308.15 K Average		
Q (μJ)	Fit (μJ)	stdev (μJ)		Q (μJ)	Fit (μJ)	stdev (μJ)
68.918	-76.994	-		148.985	1.024	-
-79.872	-76.788	5.388		-4.388	0.301	2.970
-78.765	-76.622	1.876		-16.119	-0.423	9.062
-78.635	-76.430	7.529		-1.553	-1.146	6.135
-78.732	-76.209	2.161		10.958	-1.870	7.657
-82.166	-75.949	4.267		-0.735	-2.594	2.434
-90.058	-75.643	8.627		-4.052	-3.317	4.592
-75.675	-75.276	2.758		3.776	-4.041	5.099
-69.505	-74.833	3.086		-11.258	-4.765	4.096
-69.401	-74.291	3.126		-7.667	-5.488	1.475
-65.444	-73.619	6.255		-7.670	-6.212	3.510
-72.412	-72.774	2.629		-8.944	-6.935	2.900
-68.508	-71.698	2.472		4.741	-7.659	9.009
-66.886	-70.309	2.503		-3.494	-8.383	4.115
-65.494	-68.495	2.445		-10.960	-9.106	4.003
-55.852	-66.111	4.810		1.012	-9.830	13.518
-61.344	-62.977	2.716		-21.297	-10.554	6.296
-58.076	-58.903	1.050		-6.854	-11.277	3.189
-56.599	-53.736	3.060		-8.478	-12.001	3.433
-50.762	-47.445	3.220		-12.716	-12.724	3.116
-48.108	-40.230	5.671		-11.714	-13.448	4.524
-32.082	-32.617	0.930		-14.710	-14.172	1.622
-26.137	-25.399	1.484		-23.443	-14.895	4.945
-14.274	-19.280	3.450		-19.665	-15.619	3.674
-5.000	-14.534	5.709		-112.413	-16.342	2.285

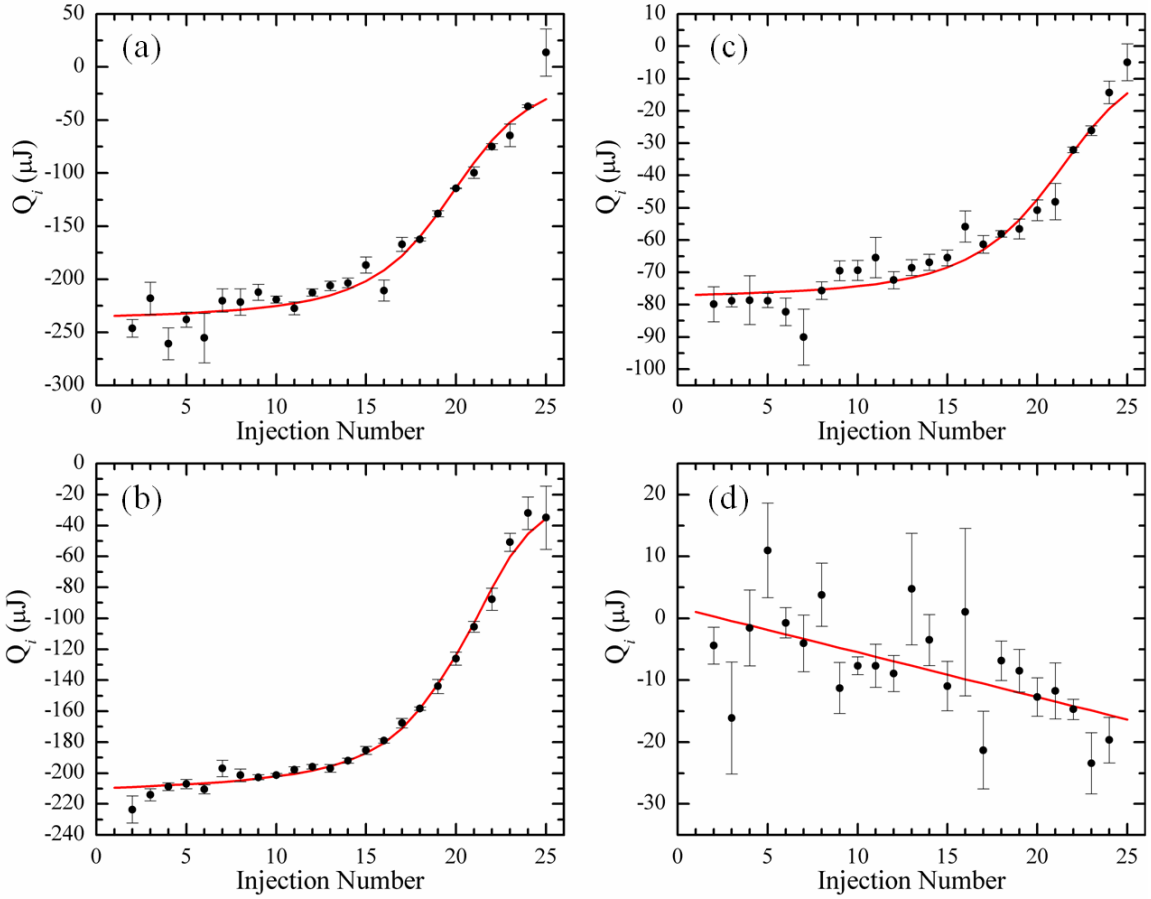

FIGURE 3.6. Thermograms of the average Qi (μJ) versus injection number; the error bars are the standard deviation (μJ). Heat of interaction of NMP:DMF with SWCNTs dispersed in DMF at 298.15 K (a) and 308.15 K (b). Heat of interaction of NMP:DMF with SWCNTs dispersed in NMP at 298.15 K (c) and 308.15 K (d). K (b). Heat of interaction of NMP:DMF with SWCNTs dispersed in NMP at 298.15 K (c) and 308.15 K (d).

K_A, of a given interaction is the equilibrium constant of the reaction which describes the concentration of the bound reactants and concentration of unbound free reactants in solution at equilibrium, given by equation 3.21. Rearrangement of equation 3.21 and substitution of [*SN*] for S_B and N_B gives a quadratic equation where, $0 < [SN] \leq [N_t]$. From the experimental determination of K_A the [*SN*] after each injection can be determined. The enthalpy for each injection, ΔH_{int_i}, of the solvent and nanoparticle interaction can be calculated by the following relationship;

$$\Delta H_{int_i} = \frac{Q_i}{\Delta[SN]_i V_0} \tag{3.25}$$

ΔH_{int} for a particular interaction is the extrapolated y-intercept of the fit data.

3.3.3 Measurement of Solvent Interactions

N,*N*-dimethyl-formamide was purchased from Fisher, and *N*-methyl-2-pyrrolidone, purchased from (OmniSolv) and were used as received and stored under nitrogen once opened. A stock solution of mixed NMP:DMF with a mole fraction $\chi_{NMP:DMF} = 0.51$ was prepared by weight with a precision of 0.1 mg (~3 ppm). The resulting concentration of the stock solution was 5.857 mol kg^{-1} NMP and 5.737 mol kg^{-1} DMF. SWeNT SG65 single-walled carbon nanotubes (CoMoCAT) were purchased from SouthWest NanoTechnologies and used as supplied (lot no. MKBD4116V). Sample dispersions of pristine SG65 nanotubes (3.98 mg L^{-1}) were diluted from stock dispersions in either pure NMP or pure DMF. Initial stock dispersions of SG65 SWCNTs were produced by ultrasonicating nanotube powder in the selected solvent (~15 mg L^{-1}) at 10 W RMS for 20 min using an ultrasonic tip dismembrator (Fisher Scientific Sonic Dismembrator, 1/8" tip). The initial

dispersions were subsequently ultracentrifuged (Beckman Optima XL-100K) at 14500 rpm (~ 20000 g) for 20 min to remove any large aggregates. After centrifugation the supernatant was carefully collected and resonicated for another 10 min. Sample dispersions (3.98 mg L^{-1}) of the nanotubes were created by dilution from the stock dispersion and ultrasonicated a final time at 10 W RMS for 5 min. The concentration of the dispersions was determined using UV-vis-NIR absorption measurements made with a Varian Cary 5000 UV-vis-NIR spectrometer (see Appendix B). To prepare solutions for use in the calorimeter, samples were degassed for 15 min at 81.6 kPa prior to use. Before each consecutive experimental trial sample solutions of SG65 SWCNTs were resonicated and degassed again prior to each titration.

Measurement of dilution enthalpies and the thermodynamic values of interaction were accomplished by use of an isothermal titration calorimeter (NanoITC – Low Volume, TA Instruments) at 298.15 K and 308.15 K. The accuracy of the instrument was verified by measuring heat of neutralization by titration of 0.1 M $NaOH_{(aq)}$ into 5 M $HNO_{3(aq)}$ at 298.15 K. Each experimental trial consisted of the sample cell being loaded with 300 μL of pure, degassed NMP or DMF. The active volume of the sample cell was 164 μL. A 50 μL injection syringe was filled with the DMF:NMP stock solution. With a continuous stir speed of 350 rpm, each titration run consisted of 25 consecutive injections of 2 μL aliquots, except for the first injection which was 0.98 μL. The injections were spaced at 300 s intervals with a lead time of 300 s before and after the run to establish a baseline. The differential power during the titrations is plotted as positive μJ s^{-1} (μW) for heat released during exothermic

processes and negative μW for heat absorbed during endothermic processes, against time. FIGURE 3.7 is a representative plot of collected data during a dilution titration of NMP:DMF into DMF at 298.15 K. The dilution enthalpy per injection was determined by equation (3.1) through the integration of each individual peak. These data are presented in TABLE 3.7 and TABLE 3.8 for trials at 298.15 K and 308.15 K respectively. Thermal contributions related to the frictional heat, temperature gradients, other systematically generated heat were measured by a blank titration of the DMF:NMP solution into the same DMF:NMP solution. These exotherms were typically -1.4 μJ per injection and were subtracted from all experimental trials. The 1:1 mixture of NMP and DMF used as the titrant was needed because of the large enthalpy of dilution. Adding pure solute into pure solvent is too exothermic and adds experimental error. Our technique is reproducible with a standard error of 1.8 J mol^{-1} in ΔH_{dln}.

Solvent-nanotube interactions were measured by subtracting the appropriate dilution titrations from the solvent-nanotube titrations. In order to accurately subtract the heat of dilution from the interaction enthalpy, it is necessary that the protocols of the dilution and sample titrations be identical. For solvent-nanotube interaction measurements, SG65 SWCNT dispersions (3.98 mg L^{-1}, 300 μL) in either pure NMP or DMF were placed in the sample cell. Three to four trials of each titration were collected.

TABLE 3.7. Experimental Dilution Enthalpies of NMP:DMF mixture into pure DMF and pure NMP at 298.15 K.

	NMP into DMF			DMF into NMP		
N	m_{N-1} (mol kg^{-1})	m_N (mol kg^{-1})	$\Delta H_{(m_{N-1} \rightarrow m_N)}$ (J mol^{-1})	m_{N-1} (mol kg^{-1})	m_N (mol kg^{-1})	$\Delta H_{(m_{N-1} \rightarrow m_N)}$ (J mol^{-1})
1	0	0.0368	-95.777	0	0.0339	-114.9
2	0.037	0.111	-105.7	0.034	0.102	-129.6
3	0.111	0.183	-104.8	0.102	0.168	-125.7
4	0.183	0.253	-101.9	0.168	0.233	-123.1
5	0.253	0.321	-100.6	0.233	0.296	-119.4
6	0.321	0.388	-95.8	0.296	0.358	-115.9
7	0.388	0.453	-94.9	0.358	0.419	-112.7
8	0.453	0.516	-92.5	0.419	0.478	-110.3
9	0.516	0.579	-89.7	0.478	0.536	-106.7
10	0.579	0.639	-87.7	0.536	0.593	-104.0
11	0.639	0.698	-85.2	0.593	0.648	-100.9
12	0.698	0.756	-83.4	0.648	0.703	-98.5
13	0.756	0.813	-81.3	0.703	0.756	-95.7
14	0.813	0.868	-79.3	0.756	0.808	-93.1
15	0.868	0.922	-78.1	0.808	0.859	-90.7
16	0.922	0.975	-76.4	0.859	0.909	-88.3
17	0.975	1.03	-74.7	0.909	0.958	-86.2
18	1.03	1.08	-72.6	0.958	1.01	-83.6
19	1.08	1.13	-71.7	1.01	1.05	-81.9
20	1.13	1.18	-70.1	1.05	1.10	-80.2
21	1.18	1.22	-68.6	1.10	1.14	-78.5
22	1.22	1.27	-67.0	1.14	1.19	-77.0
23	1.27	1.32	-65.2	1.19	1.23	-75.5
24	1.32	1.36	-63.3	1.23	1.28	-48.9
25	1.36	1.40	-62.2	1.28	1.32	-47.8

TABLE 3.8. Experimental Dilution Enthalpies of NMP:DMF mixture into pure DMF and pure NMP at 308.15 K.

	NMP into DMF				DMF into NMP		
N	m_{N-1} (mol kg^{-1})	m_N (mol kg^{-1})	$\Delta H_{(m_{N-1} \rightarrow m_N)}$ (J mol^{-1})		m_{N-1} (mol kg^{-1})	m_N (mol kg^{-1})	$\Delta H_{(m_{N-1} \rightarrow m_N)}$ (J mol^{-1})
1	0	0.0368	-73.113		0	0.0339	-107.329
2	0.0368	0.1106	-78.706		0.0339	0.1018	-120.542
3	0.1106	0.1825	-77.244		0.1018	0.1682	-117.812
4	0.1825	0.2526	-75.796		0.1682	0.2330	-115.125
5	0.2526	0.3210	-73.412		0.2330	0.2964	-112.438
6	0.3210	0.3877	-71.841		0.2964	0.3583	-108.769
7	0.3877	0.4529	-70.453		0.3583	0.4189	-105.144
8	0.4529	0.5164	-69.051		0.4189	0.4781	-102.584
9	0.5164	0.5785	-67.640		0.4781	0.5361	-99.513
10	0.5785	0.6391	-66.220		0.5361	0.5928	-97.125
11	0.6391	0.6984	-64.772		0.5928	0.6482	-94.523
12	0.6984	0.7563	-63.415		0.6482	0.7026	-91.836
13	0.7563	0.8129	-61.933		0.7026	0.7558	-89.404
14	0.8129	0.8682	-60.914		0.7558	0.8079	-86.717
15	0.8682	0.9224	-59.646		0.8079	0.8589	-84.934
16	0.9224	0.9753	-58.399		0.8589	0.9089	-82.396
17	0.9753	1.0272	-57.287		0.9089	0.9579	-79.713
18	1.0272	1.0779	-56.132		0.9579	1.0059	-78.049
19	1.0779	1.1275	-54.940		1.0059	1.0530	-75.776
20	1.1275	1.1762	-54.013		1.0530	1.0992	-73.754
21	1.1762	1.2238	-53.000		1.0992	1.1445	-71.933
22	1.2238	1.2704	-51.816		1.1445	1.1889	-70.205
23	1.2704	1.3161	-50.349		1.1889	1.2325	-68.188
24	1.3161	1.3609	-48.792		1.2325	1.2752	-66.648
25	1.3609	1.4049	-48.203		1.2752	1.3172	-64.703

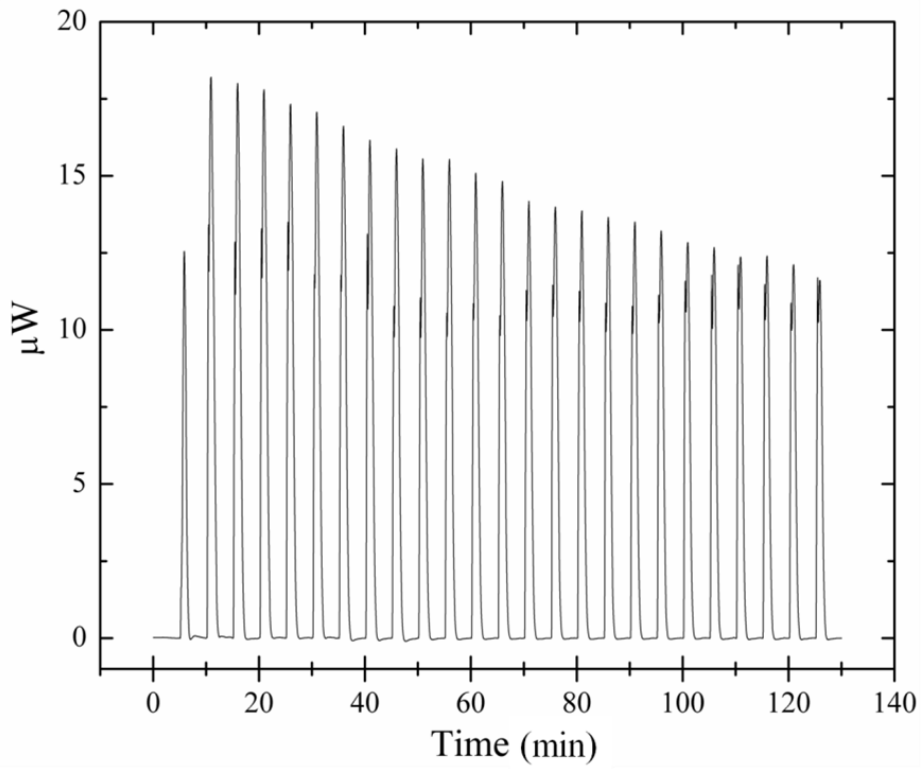

FIGURE 3.7. Representative dilution titration curve of NMP:DMF mixture into DMF at 298.15 K.

3.3.4 Measurement of Dilution Enthalpies, ΔH_{dln}

The stepwise enthalpies of dilution, $\Delta H_{(m_{N-1},\, m_N)}$, at 298.15 K for NMP into DMF and DMF into NMP are listed in TABLE 3.7. The enthalpies at infinite dilution, ΔH_{dln}, and enthalpic interaction coefficients calculated from linear regression of the data in TABLE 3.7 are given in TABLE 3.9. The enthalpy at infinite dilution, ΔH_{dln} is extrapolated from the linear regression of $\Delta H_{(m_{N-1},\, m_N)}$ as a function of titrant concentration, m_x. FIGURE 3.8 is a representative plot of $\Delta H_{(m_{N-1},\, m_N)}$ values for NMP titration into pure DMF at 298.15 K. The dilution enthalpies (ΔH_{dln}) measured within this study are similar to the dilution enthalpies of other amide solvents titrated into DMF, measured at 298.15 K.[78] The range of solution enthalpies reported by Marcus et al.,[78] varied from 20.2 to -3.88 kJ mol^{-1}, where smaller solution enthalpies correlated with the similarity in molecular structure of the solute and solvent molecules. DMF and NMP are very similar polar aprotic solvents with large dipole moments and high dielectric constants (DMF μ = 3.8 D, ε = 37.7 at 298.15 K; NMP μ = 4.09 D at 293.15 K, ε = 32.2 at 298.15 K). They are miscible with water and with each other. The dilution enthalpies measured in this study for NMP titrated into DMF (ΔH_{dln} = -0.109 kJ mol^{-1}, 298.15 K; -0.0807 kJ mol^{-1}, 308.15 K) and for DMF titrated into NMP (ΔH_{dln} = -0.135 kJ mol^{-1}, 298.15 K; -0.127 kJ mol^{-1}, 308.15 K) are well within the measured range of values for molecularly similar amide solvents (e.g., the solution enthalpy of N,N-dimethylacetamide into DMF is -0.08 kJ mol^{-1}).[78]

TABLE 3.9. Dilution Enthalpies and Enthalpic Interaction Coefficients of NMP:DMF into DMF and NMP.

	ΔH_{dln} (J mol^{-1})	h_{xx} (J kg mol^{-2})	h_{xxx} (J kg^2 mol^{-3})
NMP:DMF into DMF			
298.15 K	-109	26.327	4.579
308.15 K	-80.7	17.987	3.129
NMP:DMF into NMP			
298.15 K	-135	39.162	6.944
308.15 K	-127	38.117	6.758

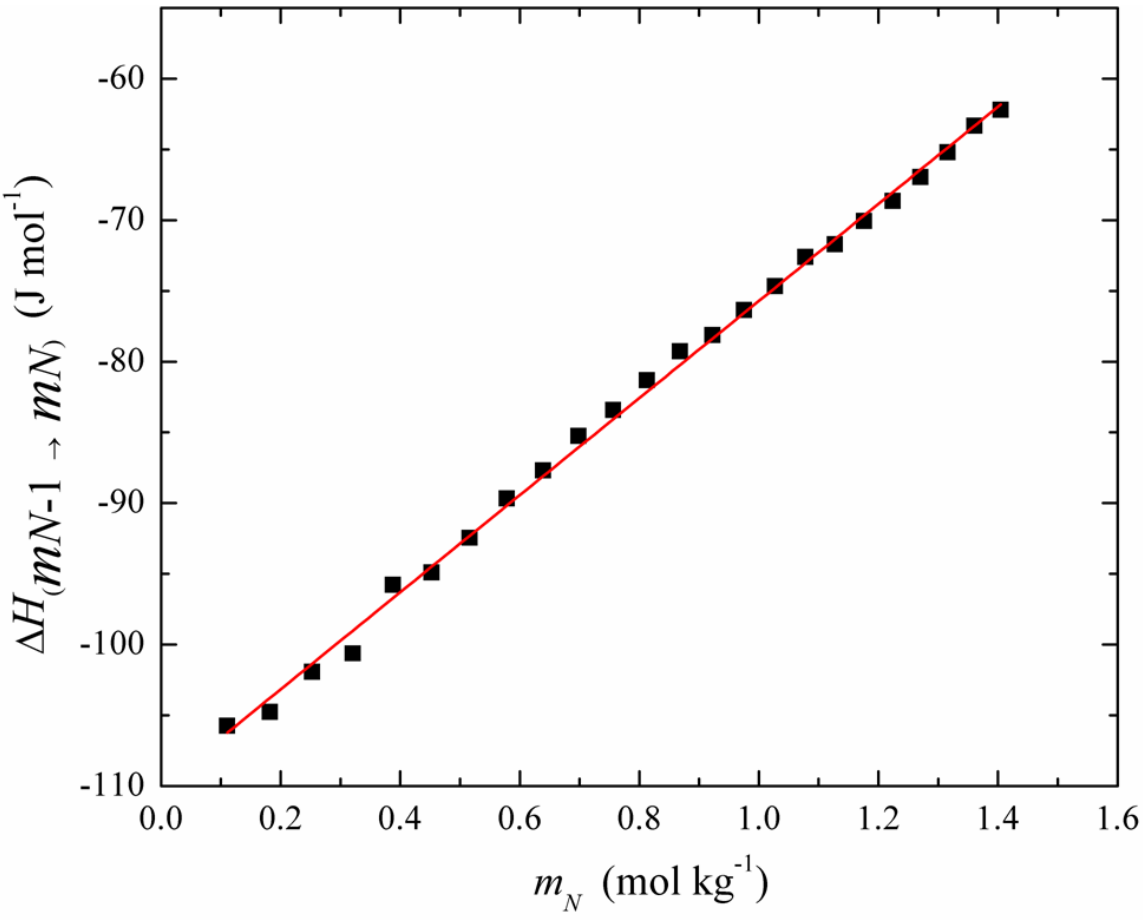

FIGURE 3.8. Integrated heat values of ΔH(mN-1 → mN) for NMP:DMF mixture into DMF titration peaks as a function of mN, moles of NMP per kg of DMF, at 298.15 K. Average of 4 trials. ΔH(dln) = 110.0 ± 0.3 J mol-1, slope = 34.3 ± 0.4 J kg mol-2.

Electrostatics, partial desolvation and solvent reorganization all contribute to the enthalpic interaction and entropic interactions of the system. It has been shown that ITC is remarkably well suited for measuring interaction enthalpies do to its high sensitivity and its ability to measure the heat produced by sequential titrations.[75] ITC provides a direct method to measure interaction coefficients that contribute to the characterization of solvent mixtures and can potentially help tailor solvent mixtures to maximize the stability of nanoparticles in solution.

3.3.5 Measuring Interactions of NMP and DMF with SWCNTs

Using ITC to measure the energetics of these reversible interactions is an accurate and precise method because calorimetry directly measures the heat of a given process. Measuring the thermodynamic interactions of SWCNT dispersions however, brings with it inherent challenges. As-produced SWCNTs mainly exist in bundles containing hexagonally packed tubes.[57] π-π interactions and other van der Waals forces between the walls of SWCNTs strongly bind them to each other and thermodynamically stabilize the bundles. Significant energy, often applied ultrasonically, is needed to exfoliate those bundles and disperse individual tubes into solution since the enthalpy of mixing (ΔH_{Mix}) is positive.[74] According to Coleman et al., the spontaneous exfoliation of bundles can be promoted by certain solvent properties which favor solvent interactions with SWCNTs in solution and results in a smaller mixing enthalpy.[47] These solvent properties largely describe the favorable energetics between the surfaces of SWCNTs and the solvent molecules. These solvent-SWCNT interactions are what our study quantifies.

It is widely accepted that NMP is one of the best solvents used to disperse SWCNTs and it has been suggested that dispersions of SWCNTs in NMP can in fact be thermodynamically stable, making them true solutions.[62,74] At best, thermodynamically stable solutions of carbon nanotubes are difficult to achieve. It is more probable that higher stability dispersions will be the result of more favorable solvent-nanotube interactions. Minimizing ΔH_{Mix} of SWCNTs is the dominant determining factor for the minimization of the free energy of mixing (ΔG_{Mix}) do to small changes in the mixing entropy (ΔS_{Mix}) when SWCNTs exfoliate from bundles.[74] Favorable solvent-nanotube interaction enthalpy lowers tube-tube enthalpic interactions[61] and thereby minimizes ΔH_{Mix}. According to solvent theory, a true thermodynamically stable dispersion (solution) would be the result of a favorable solvent-nanotube interaction in which the free-energy of mixing is negative.[47] This goal has not yet been directly measured for solutions of SWCNTs in pure solvents.

This study directly measures the interaction enthalpy (ΔH_{int}) of amide solvents with dispersed SWCNTs. As NMP is titrated into DMF SWCNT dispersions, equilibrium is established between the bound and unbound solvent molecules. During each injection heat is released (exothermic) or absorbed (endothermic) until all potential interaction pathways are saturated and an observed association constant (K_A) can be calculated.[79] The concentrations of solvent and SWCNTs are known, so it is also possible to determine stoichiometric information about the interaction.[35] The results of the thermodynamic analysis of a 1:1 NMP:DMF mixture titrated into SWCNTs dispersed in DMF or NMP are presented in TABLE 3.10. A

representative ITC thermogram of these data is presented in FIGURE 3.9. FIGURE 3.9(a,d) shows the differential power of the ITC as a function of time (min). The peaks correspond to the differential power required to maintain a small temperature difference between the sample cell and reference cell during the evolution or absorption of the interaction heat as aliquots of the NMP:DMF titrant are added to the SWCNT dispersion. Comparing FIGURE 3.9(a,d) to the thermogram in FIGURE 3.7 we show that the exothermic dilution enthalpy (ΔH_{dln}) of one solvent into the other produces a large portion of the resulting heat. FIGURE 3.9(b,e) for the DMF and NMP titrations, respectively, are the result of the control dilution titrations being subtracted from the sample titration. The area under each injection peak is shown in FIGURE 3.9(c,f) and are plotted as ΔH_{int_i} (J mol^{-1}) against injection number on the lower x-axis and mole percent of titrant solute in the reaction cell on the upper x-axis.

FIGURE 3.9(f) shows a sigmoidal curve characteristic of the saturation of single-site homogeneous binding often seen in well behaved ITC standards.[36] The sigmoidal shape is produced in all of our titrations of NMP:DMF into SWCNT-DMF dispersions (at both 298.15 K and 308.15 K). However, the analogous NMP:DMF titrations into SWCNT-NMP dispersions at 298.15 K exhibit only the onset of a sigmoidal curve at 298.15 K and do not show any sigmoidal character for titrations at 308.15 K. Nonlinear least-square fitting of the experimental data, illustrated by the solid line in FIGURE 3.9(c,f), using the single-site homogeneous

TABLE 3.10. Thermodynamic values of solvent interactions with SWCNT dispersions.

T (K)	ΔG_{int} (J mol^{-1})	ΔH_{int} (J mol^{-1})	ΔS_{int} (J mol^{-1} K^{-1})
	NMP into SG65 SWCNTs in DMF		
298.15	-10500 ± 1200	-18.2 ± 0.6	35 ± 4
308.15	-9500 ± 750	-20.8 ± 0.3	31 ± 3
	DMF into SG65 SWCNTs in NMP		
298.15	-9000 ± 1400	-4.3 ± 0.2	31 ± 5
308.15	-	0	-

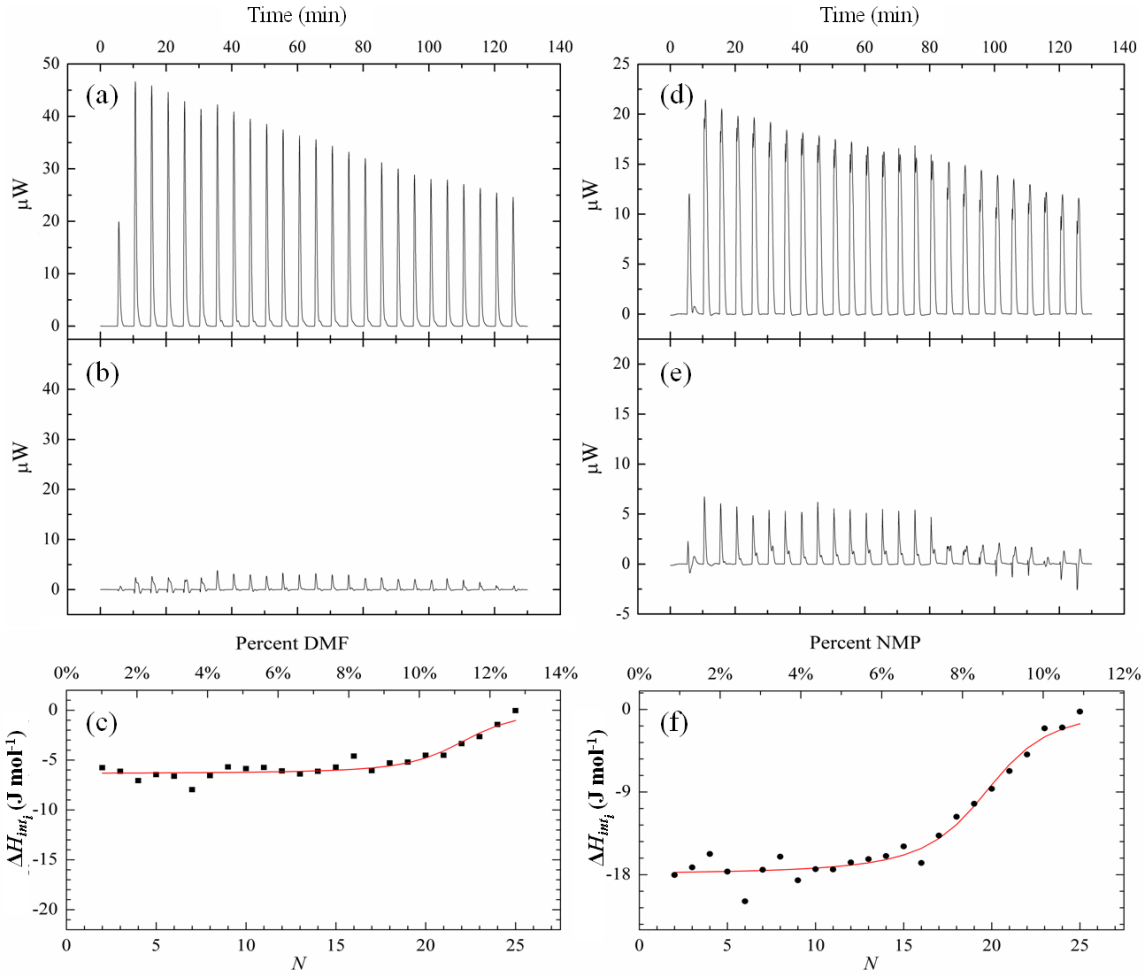

FIGURE 3.9. The raw ITC response (µW) for the titration of DMF into SWCNTs dispersed in NMP (a), and the titration of NMP into SWCNTs dispersed in DMF (d). Resulting heat of interaction (µW) of DMF into SWCNTs dispersed in NMP (b), and the titration of NMP into SWCNTs dispersed in DMF (e) after blank subtraction. The integrated enthalpy of interaction (J mol-1) per injection for DMF into SWCNTs dispersed in NMP (c), and of NMP into SWCNTs dispersed in DMF (f). Representative data of single trials at 298.15 K.

binding model allows for thermodynamic parameters K_A and ΔH_{int} to be determined.[34] K_A is determined from the slope of the sigmoidal curve at its inflection point.[79] Substitution of K_A into equation (3.24) allows the calculation of ΔG_{int} and ΔS_{int} which are presented in TABLE 3.10. The titrations into DMF dispersions at 308.15 K did not form a sigmoidal shape and were fit with a straight line to extrapolate ΔH_{int}. The average ΔH_{int} for these trials was approximately zero.

The results presented above are consistent with the recent work of Coleman et al.,[80] that determined the dispersion limits of SWCNTs in various solvents, and supports previous work from our group that determined a dispersion stability enhancement in mixed solvents.[61] The Hildebrand/Hansen solvent parameters for many pure solvents[80] and mixtures of DMF and NMP were calculated.[61] Individually, NMP and DMF possess good solvent properties that favor interaction with SWCNTs. As the solvents are mixed in increasing ratio approaching mole fraction $\chi = 0.5$ the solvent properties become more favorable and SWCNT dispersion stability is significantly enhanced.[61]

Our results show the interaction enthalpy of NMP with SWCNTs (ΔH_{int} = -18.2 J mol^{-1} at 298.15 K, -20.8 J mol^{-1} at 308.15 K) and the interaction enthalpy of DMF with SWCNTs (ΔH_{int} = -7.3 J mol^{-1} at 298.15 K, ~ 0 at 308.15 K). The negative ΔH_{int} we measure is the combination of competing endothermic and exothermic processes. The displacement of DMF from the surface of the SWCNTs is an endothermic process as is the exfoliation of SWCNT bundles as solvent parameters improve.[61,74] The binding of NMP with the SWCNT surface as DMF is displaced is an exothermic interaction as is the adsorption of either solvent with newly exposed

SWCNT surface area during spontaneous exfoliation. Our observations are consistent with similar studies in which SWCNT coordinating molecules were titrated into heavily bundled aqueous dispersions and resulted in spontaneous exfoliation.[70] Exfoliation in aqueous solvent would result in unfavorable interactions with newly exposed surface and water molecules. While in dispersions with NMP or DMF, intercalation of coordinating solvent molecules into the SWCNT bundle would expose additional surface area to favorable solvent conditions resulting in an exothermic release.

The differences in sigmoidal character and ΔH_{int} during titrations (FIGURE 3.9c,f) are characterized by the competing processes discussed above. Since the experimental protocols of the different trials are identical, the only factor that can contribute to differences in the exotherms is the interaction of SWCNT surface with the titrant solvent. The magnitude of ΔH_{int} is proportional to the favorability of the solvent-SWCNT interaction. If two reactants, such as NMP and SWCNTs, in the bulk solvent (DMF), display binding behavior, (FIGURE 3.9), they must have a greater affinity for each other than they do for the supporting solvent. The improvement of solvent properties by mixing NMP and DMF and the dilution of nanotube concentration will promote the exfoliation of SWCNT bundles.[74] During a DMF titration into a NMP dispersion the large excess of NMP would result in favorable NMP-SWCNT interactions as exfoliated surfaces were exposed.

Bundles of SWCNTs have been shown to exfoliate in optimized solvents such as those used here. Spontaneous exfoliation of bundles during titration is driven by dilution and by the change in the negative interaction free energy of the mixed

solvent-SWCNT interactions. In all trials in which values could be calculated, we observed small positive changes in the interaction entropy during each titration. Due to the size and rigidity of SWCNTs their entropy of mixing is small.[80] Therefore our results suggest the measured positive entropy is the combination of spontaneous exfoliation of the bundles and the subsequent solvent reorganization around the newly exposed surfaces of the unbundled SWCNTs.

3.3.6 Summary of SWCNT Solvent Interactions

An important result presented in this section was the thermodynamic observation of SWCNT bundle exfoliation. Our data directly supports the observations that NMP is a better (enthalpically more favorable) solvent for SWCNTs than is DMF and the observation of positive interaction entropy in both titrations, due to exfoliation and the exposure of SWCNT surface, supports the favorability of mixed solvent dispersions.

In this study ITC has been used to determine the dilution enthalpy of DMF into pure NMP and NMP into pure DMF, two widely used solvents to disperse nanomaterials. From the dilution enthalpies, enthalpic coefficients h_{xx} and h_{xxx} were determined. Mixing NMP or DMF into dispersions of SG65 SWCNTs was the focus of this study. We determined the thermodynamic values of the resulting interactions without the use of labeling molecules or any functionalization that disrupts the pristine SWCNT surface. Because of this we were able to directly observe the thermodynamic effect of SWCNT exfoliation. The advantages of using ITC over structural or spectroscopic methods have been reported,[33,63] and the simplicity of newer ITC instrumentation provides the added benefit of requiring low volumes and

low concentrations of analyte.

This quick and efficient characterization of solvent-SWCNT interactions can eventually lead to the identification of the most favorable solvents and the mixtures thereof. Tuning mixtures to have better solvent properties can lead to more precise control of nanomaterials and their interactions and of processing into nanocomposite assemblies. Future studies of nanomaterials with ITC will seek to directly measure the mixing enthalpy of SWCNTs into different pure solvents for direct characterization of solubility and thermodynamic stability. We believe that this method can quantify exposed surface area of dispersed nanomaterials. Moreover, more accurate solute-nanoparticle association constants and binding kinetics will enable rational design for the directed assembly of hybrid nanoparticle systems.

3.4 SWCNT—Dinuclear Ruthenium Complex Interactions

Integration of nanomaterials into functional composite systems is the next evolutionary step in the development of nanoscale science.[81-85] To date nanomaterial composites are formed primarily by embedding nanomaterials in matrices, through chemical bonding or with various wrapping agents.[81,83,85] The intrinsic properties of the individual components are often damped or altered by the mechanical wrapping or chemical functionalization.[86,87] Directed self assembly of nanomaterials is a means to avoid those affects and to advance nanocomposite construction beyond cement/matrix and aggregate construct. By directing assembly of nanomaterials with other dynamic chemical and/or nanoscale components complex hybrid structures can be constructed. Aggregation of carbon nanotubes with rigid metallodendrimers is an example of directed assembly that involves non-covalent binding interactions.[2-4]

Mechanical binding of metallodendrimers to SWCNTs do not alter the intrinsic properties of the nanotubes, but rather contribute structural and other functional properties to the resulting composite. Polypyridine coordinated ruthenium metallodendrimers[88,89] for example, exhibit characteristic photochemical and electrochemical properties which can enhance charge transfer, catalysis and solar energy collection.[90-93] To begin exploring the electronic interactions within ruthenium complex – SWCNT hybrid nanocomposites made in this fashion it is important to understand how they are binding; i.e. the strength of the binding event and the relative stoichiometric binding capacity. Isothermal titration calorimetry (ITC)[65,69,70,73,94-96] and adsorption isotherms[97-103] derived from UV-vis spectroscopy data are established techniques used to measure binding events.

In the following sections the adsorption interactions of ruthenium dimer complexes onto SWCNTs is discussed. The three ruthenium dimers (synthesis and characterization discussed in chapter 2) possess a rigid structure formed by a tetradentate tetrapyridophenazine ligand bridging two ruthenium centers. The rigid structure of these complexes form a nanoscale pocket lined with the conjugated π electron systems of the tpphz and terminal phenanthroline and terpyridine ligands. The proposed adsorption/binding configuration of the +4 dimer and a (6,5) SWCNT is illustrated in FIGURE 3.10. FIGURE 3.10(top) is a typical ball and stick model, showing the LUMO of the SWCNT extending towards the π-pocket of the dimer. FIGURE 3.10(bottom) shows the overlapping electron density of the bound complex.

SWCNTs have an average diameter around 1 nm. In an ideal dispersion their

maximum available surface area is 1315 m^2/g (discussed in section 0). Their dimensions and ample surface area makes SWCNTs complimentary binding partners for our unique family of dinuclear ruthenium species. Rigid molecular structures such as these can serve as building blocks for hybrid nanocomposite systems. Aside from possibly directing the assembly of dispersions of SWCNTs, the combination of ruthenium complexes and SWCNTs is intriguing due to the rich photo and electrochemical properties of ruthenium complexes. It is our hypothesis that these dimers will adsorb to the surface of SWCNTs in solution and mechanically dock with them due to their complimentary dimensions and availability of conjugated π-orbitals for π-π stacking. If the binding strength of this system is significant charge transfer could occur through this interaction. Charge transfer via this mechanism would be important due to the fact that neither the ruthenium complex nor the SWCNTs are physically or chemically altered, meaning their pristine properties and structure remain intact.

3.4.1 UV-visible-NIR Spectroscopy to Measure Binding Isotherms

As discussed in chapter 2 our ruthenium dimers present strong light absorption character in the UV and visible spectrum (FIGURE 2.16). UV-visible spectroscopy can be used to establish the theoretical monolayer surface coverage of ruthenium dimer on SWCNTs. Adsorption isotherms are used to represent the amount of adsorbate bound to a particular adsorbent as a function of its concentration in solution at constant temperature. Isotherms are typically normalized to the mass of the absorbent and are used to calculate relative values for binding affinity (K), and the heterogeneity of adsorbent (n). Theoretical monolayer surface coverage for the

adsorbate (q_m) can also be extrapolated from isotherms. The following summarizes the adsorption experiments and data collected for the interaction proposed above.

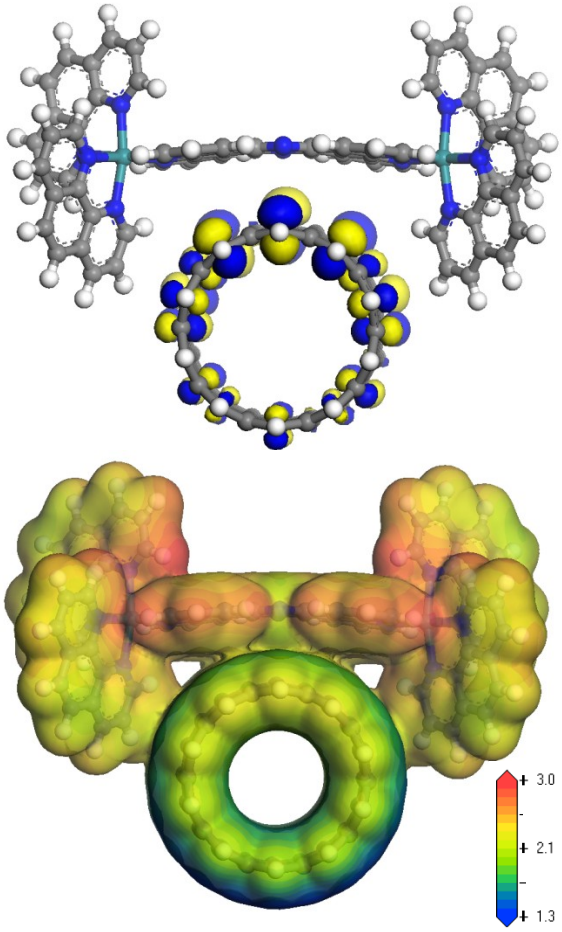

FIGURE 3.10. Ruthenium dimers, such as the +4 dimer shown here, adsorb to the surface of SWCNTs in solution and mechanically dock with them due to their complimentary dimensions and the high likelihood of π-π stacking.

3.4.2 Ru Dimers—SWCNT Adsorption Isotherms: Experimental

SWCNTs were purchased from Carbon Nanotechnologies, Inc. Stock dispersions were prepared by addition of SWCNT powder (0.5 mg) into *N,N*-dimethylformamide (DMF, 40 mL). The resulting solution was ultrasonicated for a period of 30 min at 10 W at ambient temperature. Immediately after sonication the SWCNT dispersions were centrifuged (Beckman Optima XL-100 ultracentrifuge) at 20,000 G at 20 ^{o}C for a period of 20 min.[60] The upper 90% of the supernatant was carefully removed and the concentration was confirmed by UV-vis spectroscopy to be approximately 10 mg/L. For detailed instruction on how to measure the concentration of carbon nanotube dispersions refer to appendix B. Sample dispersions were prepared from the stock solution and diluted with DMF to the desired concentration of 5 mg/L.

Ruthenium dimer complexes, $[Cl(terpy)Ru(tpphz)Ru(terpy)Cl](PF_6)_2$ **(1)**, $[(phen)_2Ru(tpphz)Ru(terpy)Cl](PF_6)_3$ **(2)** and $[(phen)_2Ru(tpphz)Ru(phen)_2](PF_6)_4$ **(3)** were prepared and characterized via procedures discussed in chapter 2.[10,15] The solid ruthenium dimers were dissolved in DMF to produce 20 μM stock solutions.

Throughout this study solution of the three previously synthesized ruthenium dimers, $[Cl(terpy)Ru(tpphz)Ru(terpy)Cl](PF_6)_2$ **(1)**, $[(phen)_2Ru(tpphz)Ru(terpy)Cl](PF_6)_3$ **(2)** and $[(phen)_2Ru(tpphz)Ru(phen)_2](PF_6)_4$ **(3)** are dissolved to form solutions in DMF and concentrations were determined by absorption spectroscopy in the visible range of the spectrum. A Varian Cary model 5000 double beam spectrophotometer, with a 1 cm path length was used. UV quartz cuvettes (100 μL volume) were used to contain the samples, DMF was used as the

reference. The maximum absorbtions wavelengths (nm) for the dimers **1**, **2** and **3** are 518, 453 and 448 nm respectively.

Adsorption isotherms for this work were carried out at 25 ^{o}C. A 0.5 mL amount of stock solution of SWCNTs plus the appropriate amount of DMF was used to dilute samples to maintain a constant mass of SWCNTs for each of seven samples. The 20 μM stock of each ruthenium dimer was diluted accordingly to obtain seven concentrations within the range of 0.1 - 20 μM. Control samples were prepared by diluting the ruthenium dimer to identical concentrations with DMF. Disposable polypropylene centrifuge tubes (1.5 mL volume) were used to contain each of the runthenium dimer control samples and for all sample solutions of dimer and SWCNTs during equilibration. Samples are prepared with 0.5 mL alloquots of the stable dispersion. A paired control is made with 0.5 mL DMF samples. Then into each pair of centrifuge tubes another 0.5 mL of ruthenium complex/DMF solution is added at a precise concentration (mol/L). The pairs of samples are left sealed and undisturbed for several days to allow adsorption equilibrium to be reached. Each solution was agitated vigorously upon dilution and then left for a period of 3 days to equilibrate. Upon equilibration the centrifuge tubes were centrifuged at 10000 Gs for 20 min to remove aggregated SWCNTs and bound ruthenium dimer. 100 μL aliquots were removed from the supernatant of each sample and analyzed to determine the residual equilibrium liquid phase concentration of ruthenium dimer. Once the SWCNTs are removed from the samples and UV-vis spectroscopy is used to measure the concentration of ruthenium complex remaining in both the SWCNT

and control samples. The difference in concentration can then be assumed to be bound to the SWCNTs removed from solution.

3.4.3 Ru Dimers—SWCNT Adsorption Isotherms: Discussion

The Langmuir and Fruendlich isotherms can be used to model the binding and subsequent removal of dissolved cationic dinuclear ruthenium complexes from solution by a kinetically stable dispersion of SWCNTs (~5 mg/L). The data were fit with two different empirical isotherm models, the Langmuir isotherm (FIGURE 3.11) and Freundlich isotherm (FIGURE 3.12). Both isotherms are derived from the original thermodynamic interpretations described by Gibbs and Thomson,[101,103] and differ only by the assumptions made about the system. Both equations contain two adjustable parameters and assume that adsorption occurs at constant solution pH. The Fruendlich isotherm (equation 3.26) is widely used for describing the adsorption behavior of organic molecules on activated carbon.[99] In this equation, q and C are the concentration of adsorbate bound to adsorbant (mmol/kg) and the equilibrium adsorbate concentration in solution (mmol/L) respectively. K_f and n are the Freundlich constants. This equation assumes adsorbate interacts and the affinity term decreases exponentially as adsorption increases also assuming unlimited binding sites, which tends to fit a heterogeneous system[97,104] more closely than the Langmuir equation. The Langmuir isotherm (equation 3.27), where q_m is the theoretical monolayer capacity and K_L is the Langmuir constant,

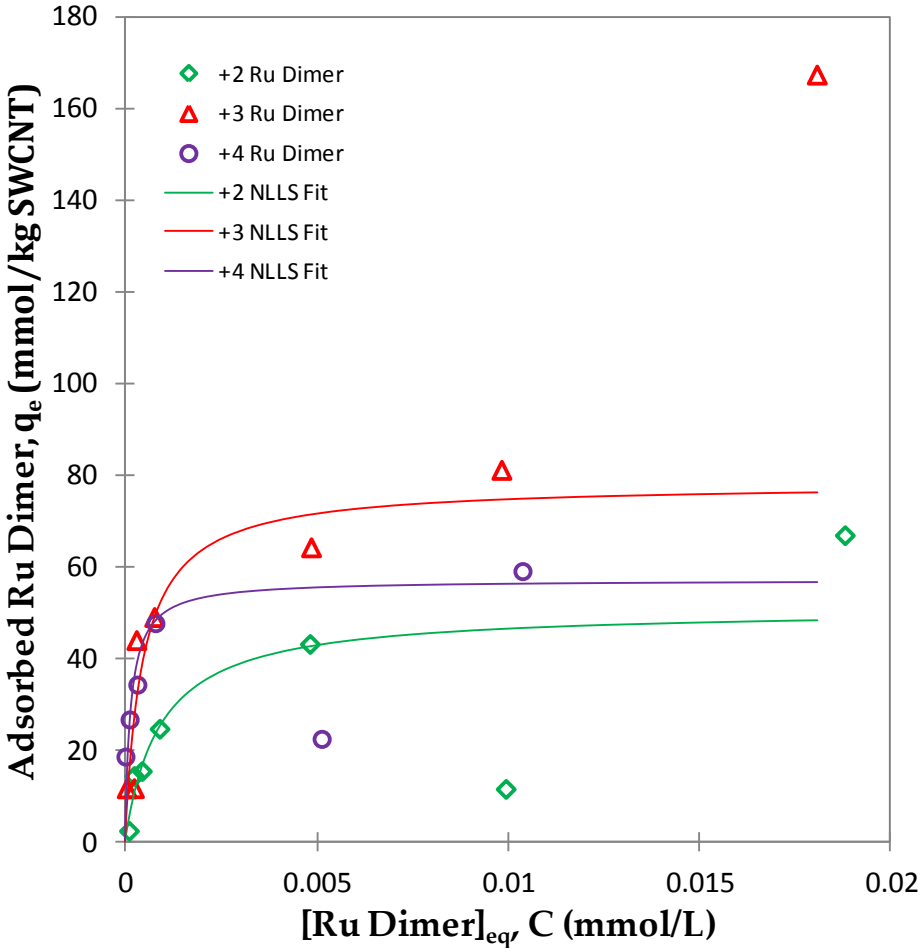

FIGURE 3.11. Binding isotherm for cationic polypyridine ruthenium dimers (adsorbate) and SWCNTs (adsorbent). Data fit by NLLS with the Langmuir isotherm equation.

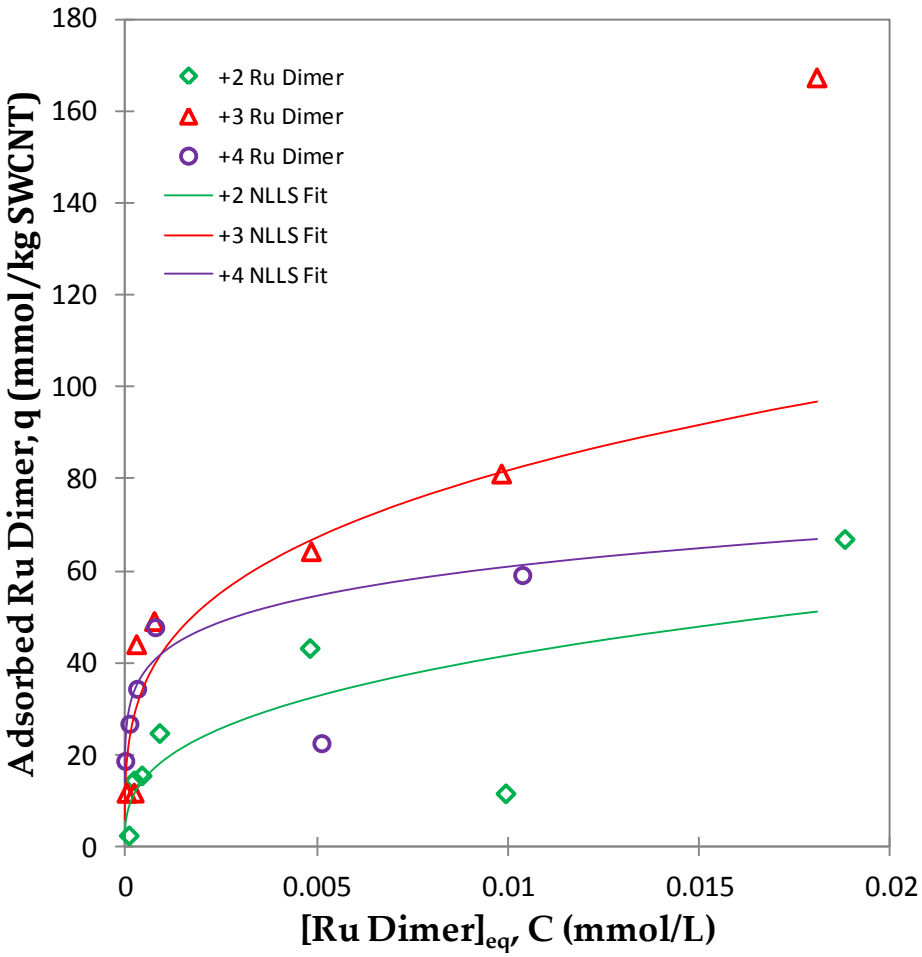

FIGURE 3.12. Binding isotherm for cationic polypyridine ruthenium dimers (adsorbate) and SWCNTs (adsorbent). Data fit by NLLS with the Fruendlich isotherm equation.

assumes that binding saturates at monolayer coverage and that no significant interaction occurs between adsorbate. A benefit of the Langmuir isotherm is that, q_m, can be calculated.

$$q = K_f C^{(1/n)} \quad 3.26$$

$$q = \frac{q_m K_L C}{1+K_L C} \quad 3.27$$

Typically both Freundlich and Langmuir isotherms are evaluated through linearization due to the ease of processing. However, it is well known that linear regression tends to be heavily biased towards some range within a data set.[101] It has been shown that for the Langmuir and Fruendlich isotherms and indeed for isotherms with more than two parameters, nonlinear regression is preferable and necessary. This usually involves the minimization of residual sums of squares and fitting the data with nonlinear least squares (NLLS) regression.[101] Data in FIGURE 3.11 and FIGURE 3.12 is fit to Langmuir and Fruendlich isotherms using NLLS and the resulting parameters are displayed in TABLE 3.11. The error of the fit was determined using the "jackknife" procedure.[105,106]

The isotherms presented here are overly simplistic and when applied to complicated systems the significant shortcomings and assumptions of the models reduce the quality of fit. A full discussion of binding isotherm analysis is not merited within the scope of this dissertation and is adequately discussed in literature sources.[101-103] It is for those reasons it was important to develop ITC protocols to measure these interactions. What is clear from the results is that to lower error more experimental data points are needed. It is also evident that simple two parameter

isotherms are not the best fit for these data. Regardless of bad goodness of fit the q_m for the ruthenium dimers is in the ballpark of similar literature values (10^2 mmol/ kg SWNTs).[98] In all cases the model fits relatively well for low concentrations but varies at higher concentrations. This observation is consistent with the major assumption of the Langmuir model that adsorption never reaches and/or stops at monolayer coverage. One important observation from this experment is the general trend of K_L, which is commonly associated with binding affinity. K_L increases with the charge state of the ruthenium dimer. Within the experimental error it can also be said that the monolayer coverage, q_m, saturates around the same value for all three dimers. This observation is consistent with the dimers having the same molecular footprint.[15] In regard to the molecular footprint of the ruthenium complexes it is also important to note that the Langmuir isotherm can be converted using the relationship established in section 0 to estimate the stoichiometry of the adsorption/binding interaction. By converting both the concentration of adsorbed ruthenium complex and concentration of SWCNTs to units of available surface area (m^2) a unitless ratio for the saturation of m^2 Ru complex to m^2 SWCNTs can be evaluated. FIGURE 3.13 shows the concentration converted to surface area data fit with a Langmuir isotherm, where a coverage of y = 1 would be 100%.

TABLE 3.11. Binding data for cationic polypyridine ruthenium dimers (adsorbate) and SWCNTs (adsorbent). Fruendlich and Langmuir isotherm parameters derived from NLLS regression.

+4 Ru Dimer		error(±)	%error	+3 Ru Dimer		error(±)	%error	+2 Ru Dimer		error(±)	%error
$\mathbf{K_f}$	127	54	43%	$\mathbf{K_f}$	303	1166	385%	$\mathbf{K_f}$	207	177	86%
$\mathbf{K_L}$	6851	94330	1377%	$\mathbf{K_L}$	2185	1845	84%	$\mathbf{K_L}$	1089	2044	188%
n	6.27	11	171%	**n**	3.53	1.4	41%	**n**	2.87	2.7	94%
$\mathbf{q_m}$	57	25	44%	$\mathbf{q_m}$	78	2063	2636%	$\mathbf{q_m}$	51	26	52%

†Fruendlich Values: $\mathbf{K_f}$ ($mmol^{1-n}$ L^n Kg^{-1}), **n** (unitless); Langmuir Values: $\mathbf{K_L}$ (L Kg^{-1}), $\mathbf{q_m}$ (mmol Kg^{-1} SWNTs).

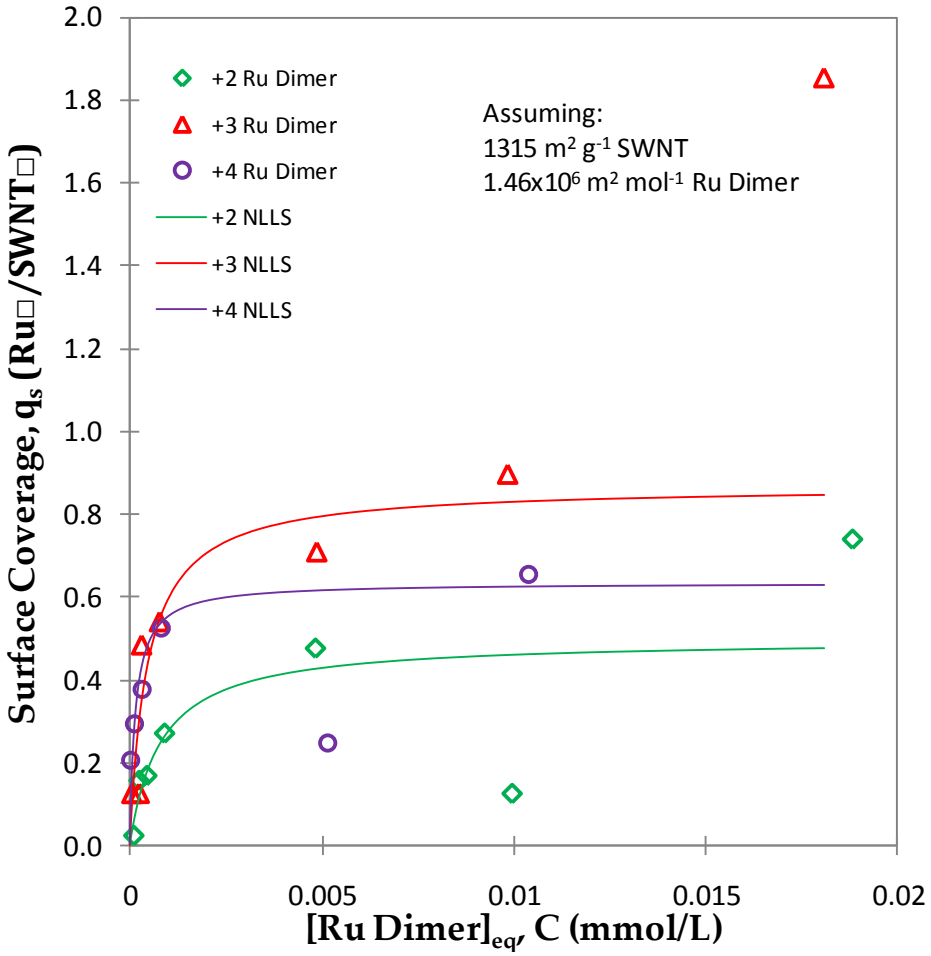

FIGURE 3.13. Binding isotherm for cationic polypyridine ruthenium dimers (adsorbate) and SWCNTs (adsorbent). Data fit by NLLS with the Langmuir isotherm equation. The concentrations have been converted to m^2 to show the amount of SWCNT surface area that is covered by ruthenium complex at saturation.

3.4.4 ITC Measurement of Ru Dimer—SWCNT Binding: Experimental

The binding of ruthenium dimer $[(phen)_2Ru(tpphz)Ru(phen)_2](PF_6)_4$ **(3)** with SWCNTs was achieved by mixing 50 μL of the 20 μM dimer stock solution with 164 μL of a SWCNT solution (4 mg/L). This is the first report of an ITC procedure run in pure nonaqueous solvent, namely dimethylformamide (DMF). We have chosen to use aprotic solvent due to its ability to disperse SWCNTs in solution without the aid of surfactants or stabilizing agents.[9,60] Calorimetric titrations were performed at 25 ^oC with a TA Instruments NanoITC isothermal titration calorimeter. The instrument was chemically calibrated[94] and the stabilization was checked by solvent-solvent titrations. A rotating stirrer-syringe (350 rpm) containing 50 μL of 20 μM dimer **(3)** solution injects in equal steps of 1 μL at 300 s intervals into a cell containing 164 μL of SWCNT solution until saturation is reached.

At constant temperature and pressure, ITC directly measures the enthalpy (ΔH) of a binding reaction. As one binding partner is titrated into another, equilibrium of bound and unbound partners is established after each injection. At each injection heat is released (exothermic) or adsorbed (endothermic) until all the binding sites are occupied and an observed association constant can be calculated (K_a).[79] Because the concentration of both binding partners is known it is also possible to approximate stoichiometric (n) information about the binding interaction.[35]

3.4.5 ITC of +4 Ru Dimer and SWCNTs: Discussion

A representative display of the integrated ITC data of a titration of 20 μM ruthenium dimer **(3)** into DMF is shown in FIGURE 3.14. The integrated ITC data of the titration of 20 μM ruthenium dimer **(3)** into 4 mg/L SWCNTs is presented in FIGURE 3.15. Within each titration there are two components; an endothermic component (negative values) and exothermic components (positive values). The endothermic component is largely due to the dilution of ruthenium dimer as it is injected into DMF as seen by the large endothermic values in FIGURE 3.16. The decrease of the endothermic phase in FIGURE 3.16 is indicative of self-dilution phenomenon.[70] FIGURE 3.17 depicts the titration of **(3)** into SWCNTs. The endothermic phase is reduced in this case due to the exothermic contribution produced by the large binding interaction of the ruthenium dimer to the surface of SWCNTs.

FIGURE 3.18 is the result of subtraction of the control data from the binding titration. When FIGURE 3.18 is fit with the independent binding model, the typical ITC isotherm is produced. FIGURE 3.18 shows the integration of heat released during the binding of ruthenium dimer to SWCNTs in solution. The heat released during the first few injections is assumed to be related to all available ruthenium dimer finding available SWCNT surface area and binding. From this assumption ΔH can be calculated. The heat produce per injection begins to gradually reduce as binding sites are filled on the surface of the tubes. By using the surface area to mass relationship discussed in section 0 we can evaluate the binding isotherm in terms of the ratio of ruthenium footprint (m^2) to maximum available surface area of SWCNTs (m^2). From this relationship a stoichiometry of ~1.3 was extrapolated which is very

close to one and suggests that the adsorption isotherm discussed previously were correct in the assumption that around a monolayer of ruthenium dimer is adsorbing the surface of dispersed SWCNTs.

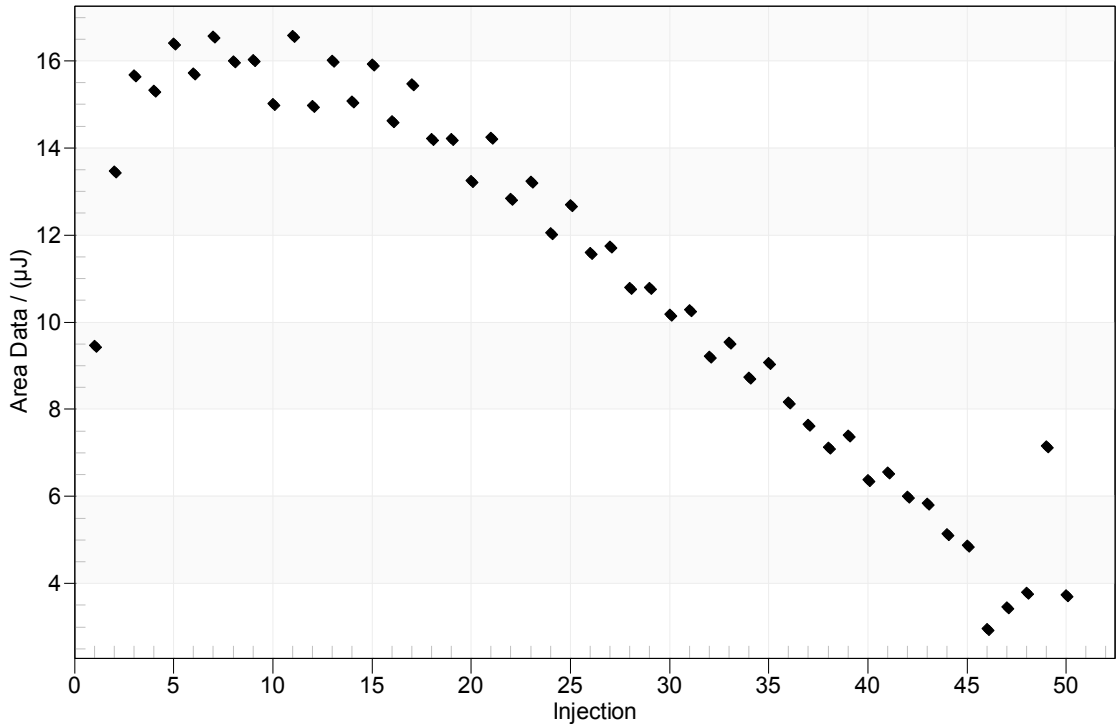

FIGURE 3.14. Blank titration of 20 µM +4 ruthenium dimer (3) into DMF. The plot is the integrated peaks of the raw ITC signal. .

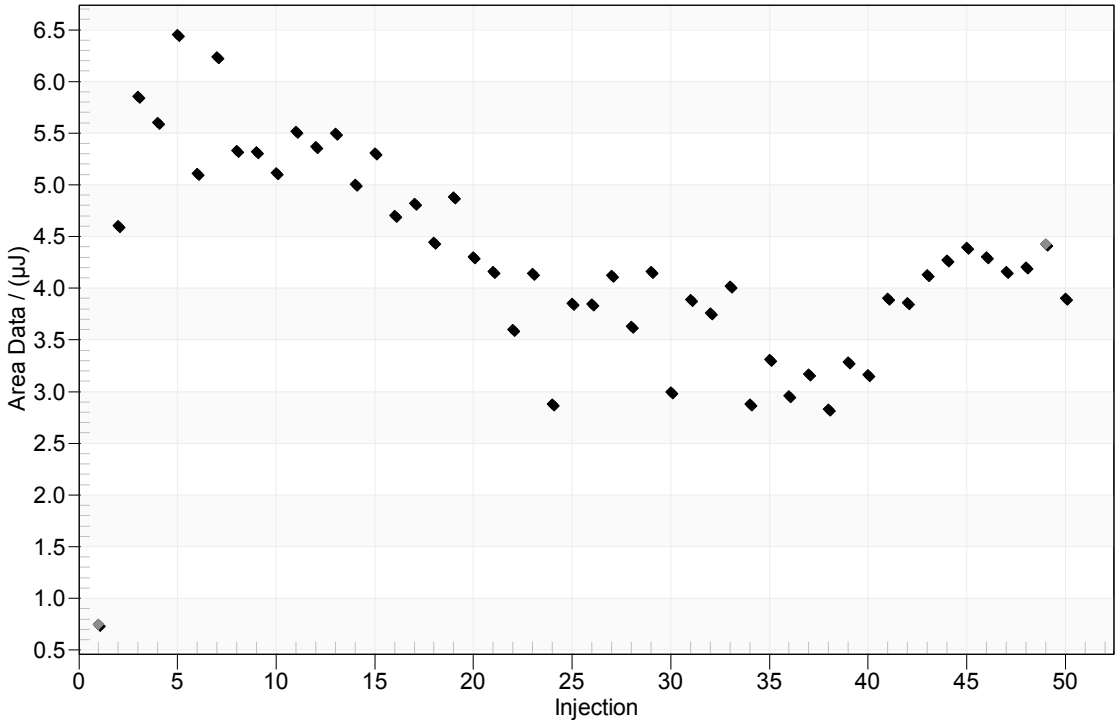

FIGURE 3.15. Binding titration of 20 µM +4 ruthenium dimer (3) into 4mg/L SWCNTs in DMF. The plot is the integrated peaks of the raw ITC signal. .

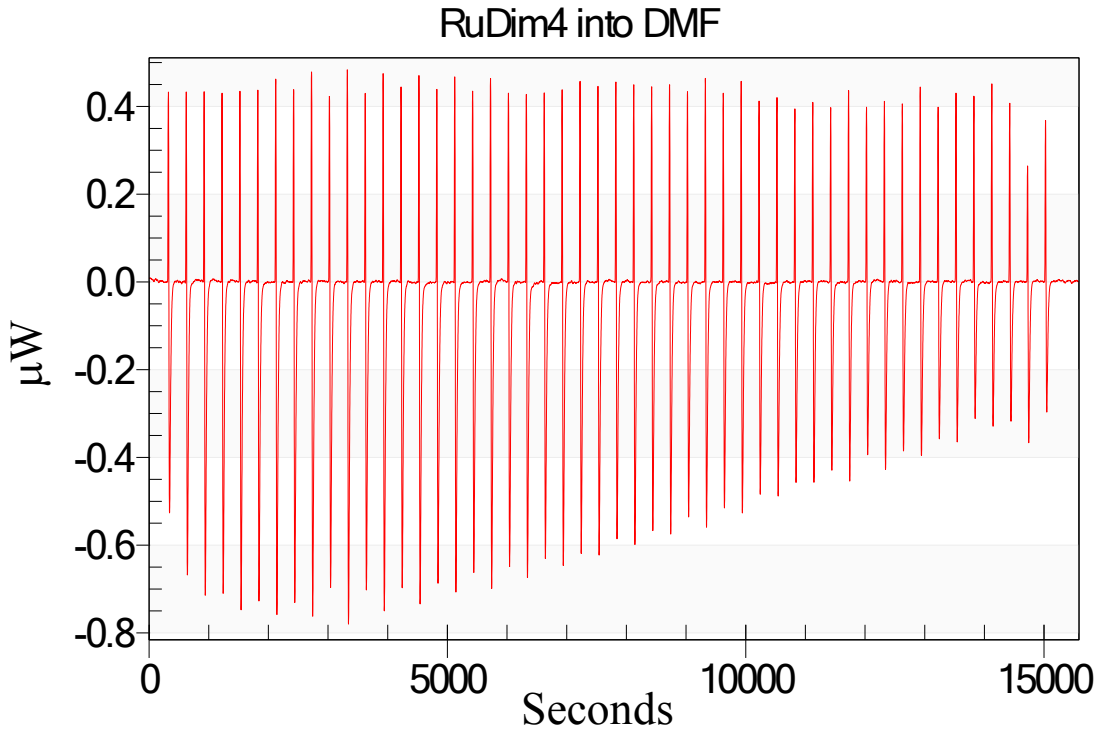

FIGURE 3.16. Blank titration of 20 µM +4 ruthenium dimer (3) into DMF. The raw ITC signal. .

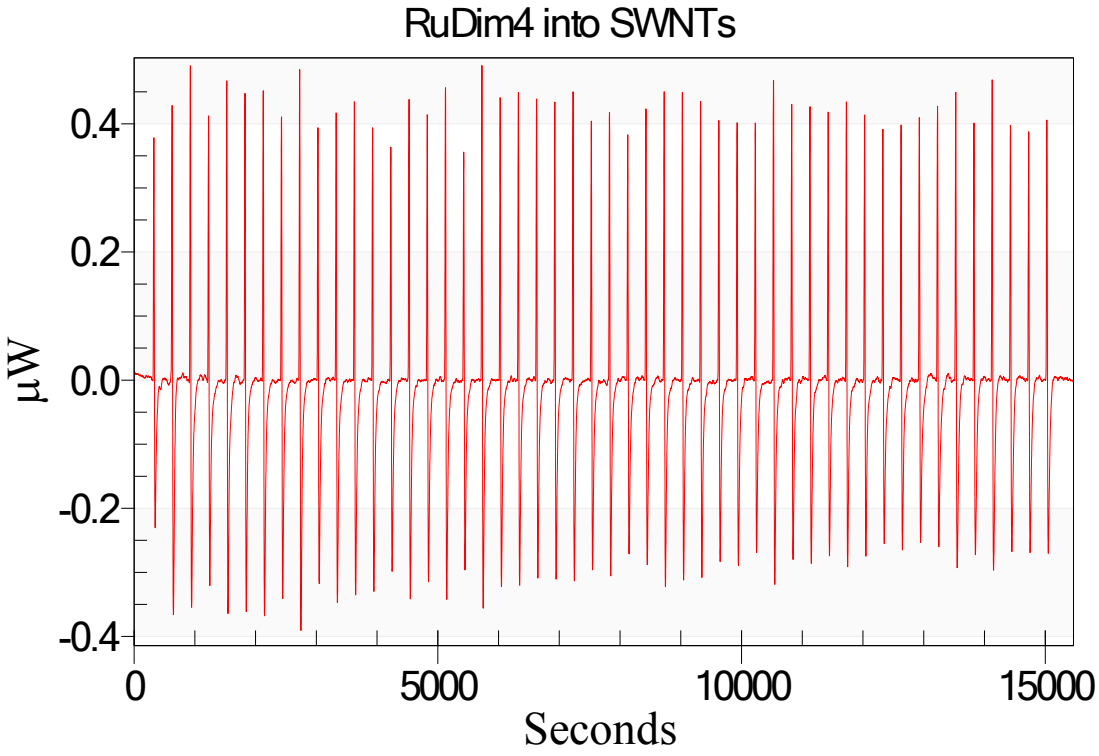

FIGURE 3.17. Binding titration of 20 µM +4 ruthenium dimer (3) into 4mg/L SWCNTs in DMF. The plot is the raw ITC signal. .

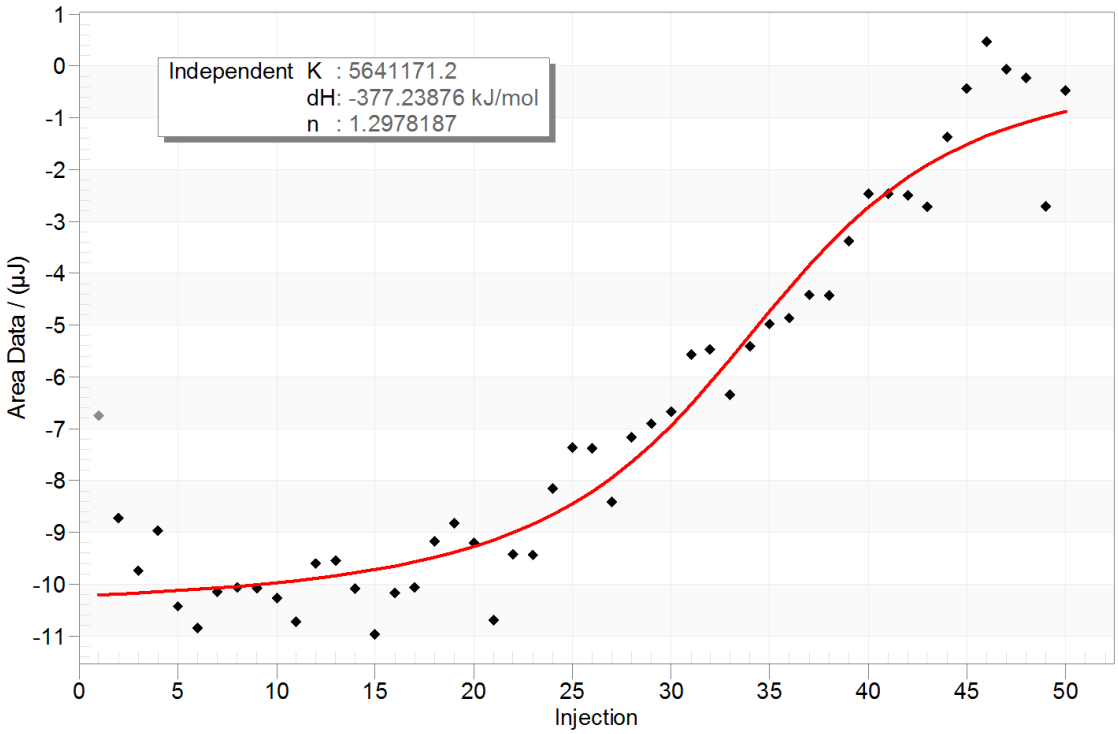

FIGURE 3.18. Results of the subtraction of the dilution blank from the raw binding signal. The red line represents the non-linear fit of the data by the independant binding model. K is the binding constant, ΔH is the binding enthalpy and n is the stoichiometry of the interaction.

3.4.6 Summary of Ru SWCNT Interaction Measurements

This study expands on the previous solvent work and directly measures the binding of $[(phen)_2Ru(tpphz)Ru(phen)_2]^{4+}$ with DMF dispersed SWCNTs. It has been shown that adsorption isotherms can be used to model the dynamics of the surface interaction of nanoparticle in solution, as well as give a good estimate of binding stoichiometry. The binding affinity of the ruthenium dimers is dependent on the charge of the molecule where as the monolayer saturation concentration is not. It is encouraging and interesting that the measured binding enthalpy of the +4 ruthenium dimer is so high, -377 kJ mol^{-1}, suggesting that charge transfer across this interface is indeed possible.

3.5 Acknowledgements for ITC Work

Acknowledgement is made to the Donors of the American Chemical Society Petroleum Research Fund for partial support of this research. Financial support to J.R. Alston through North Caroline Space Grant and the Nanoscale Science Ph.D. program and the Energy Production and Infrastructure Center at UNC Charlotte is appreciated.

CHAPTER 4: SWCNT NANOCOMPOSITE THIN FILMS AND ELECTRODES

4.1 Single-Walled Carbon Nanotubes

Carbon nanotubes are grown in many processes where carbon based species are broken down at high temperatures. It has even been shown (FIGURE 4.1) that carbon nanotubes were "man-made" in the forges of blacksmiths over 400 years ago.[107] However, the official discovery and credit of their synthesis is awarded to Sumio Iijima for his work with arc-discharge fullerene growth and imaging using an electron microscope.[108] Since the discovery of CNTs, they have become one of the most widely researched and highly publicized nanomaterials.

Carbon has been used for electrodes in electrochemical systems for many years because of its high conductivity, chemical robustness and the adjustable surface area to volume ratio of different forms of carbon. Using carbon nanotubes (CNTs) for electrochemical sensing was first published in 2003,[109-111] for the application of detecting uric acid[110] and nitrates.[111] The electronic properties and high surface area to mass ratio of CNTs make them perfect candidates for electrode and sensing materials. SWCNTs are composed solely of surface terminated atoms which makes the conductivity of individual carbon nanotubes, and composites made from them, extremely sensitive to interactions with their sidewalls.[112] Another benefit of

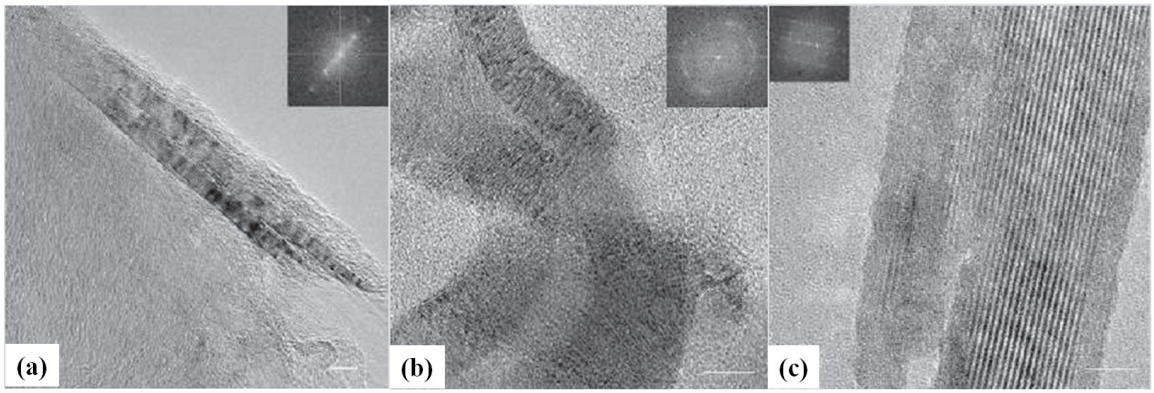

FIGURE 4.1. High-resolution transmission electron microscopy images of carbon nanotubes in a genuine Damascus sabre after dissolution in hydrochloric acid. a, b, Multiwalled tubes with the characteristic layer distance d ≈ 0.34 nm (ref. 12), as indicated by the Fourier transforms (see insets). Scale bars: 5 nm (a) and 10 nm (b). In b, the tubes are bent like a rope. c, Remnants of cementite nanowires encapsulated by carbon nanotubes, which prevent the wires from dissolving in acid. Scale bar, 5 nm. The fringe spacing of the wire is 0.635 nm, taken from the Fourier transform (inset), and is attributed to the (010) lattice planes of cementite. Copied from Reibold, M. Nature 2006, 444, 286.

using CNTs for an electrode is their high chemical stability and extraordinary mechanical strength.[84] Meckoci et al.[84] have compiled an extensive review that describes the current state of CNT electrochemical sensing.

CNTs can serve as electrodes, chemical sensing materials or be used to modify an existing electrode surface. Single-walled carbon nanotubes (SWCNTs) are unique in that their electronic properties are tunable based on their chirality. Essentially, SWCNTs can be thought of as rolled sheets of graphene, as illustrated in FIGURE 4.2. For a more detailed discussion of SWCNT structure and properties refer to appendix B. The photoconductive properties of SWCNTs were first reported by Chen et al in 2001.[113] Like other semiconducting materials it is possible to excite an electron from the valence band to the conduction band of the material if a photon with energy equal or greater than the band gap is absorbed. The unique transport properties of SWCNTs are related to their band structure and because of their morphology have very low carrier scattering rates.[114] The electron-hole pairs generated by photon excitation cause the electrons to become ballistic charge carriers free to move along the length of a nanotube. This excited charge can also be carried across π-π interactions onto other SWCNTs within a film. When a bias voltage is applied to a film being excited by light those ballistic electrons can be directed towards an electrode and into a circuit.[114] The use of SWCNT thin films in photoelectronic devices is still in its infancy. However if SWCNTs can be aggregated into structures such as films or mats SWCNTs could become the basic building blocks for future electronic and photonic devices.

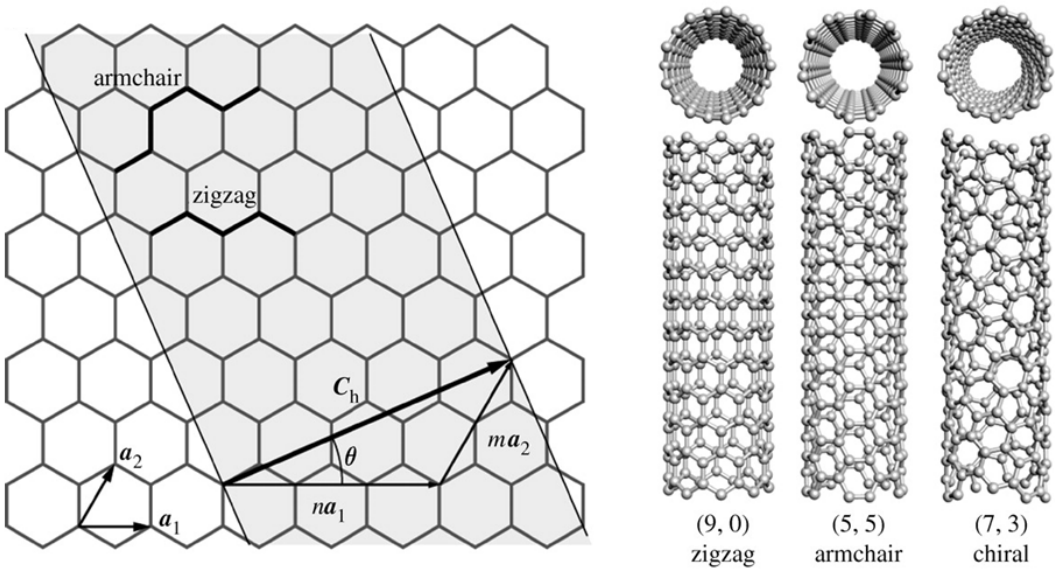

FIGURE 4.2. Schematic of nanotube formation by theoretically rolling-up a graphene sheet with models of zigzag, armchair and chiral nanotubes. Copied from Kis, A, , Zettl, A. Phil. Trans. R. Soc. A. 2008; 366:1591-1611.

Section 4.2 describes in detail the ways in which SWCNTs can be manipulated into films and mats followed by attachment to substrates to produce pristine SWCNT electrodes. This work is based on previous studies in which CNTs have been used as aggregates in composites.[115] These earlier works suggest that they could be used as conducting scaffold, for sensing agents, photosensitizers or electroactive components.

When single walled carbon nanotubes (SWCNTs) were discovered in 1991[116] they became the subject of many studies and encouraged the application of these unique carbon allotropes in many fields. Multi-walled and single-walled CNTs are attractive to researchers because their physical and electrical properties differ incredibly from any other form of carbon. The nanoscale dimensions of their physical constraints combined with the graphitic hybridization of carbon bonds augment the typical physical and electrical properties of carbon The properties that make CNTs so unique could enhance common devices and or produce new ones that would exceed previously assumed limitations. Devices based on classical physics, such as textile, building or polymer materials would gain enhanced tensile strength and durability, or for electrical components gain the benefit of both the physical properties and tunable electrical properties of CNTs. New devices based on quantum physics and confinement phenomena are also possible when SWCNTs are the building blocks. Even so, citing the benefits of devices incorporating SWCNTs begs the question: How does one build a device with carbon nanotubes?

There are two methods of nanofabrication when constructing nanoscale building blocks. The two methods are commonly referred to as the bottom-up approach and

top-down approach; where an example of bottom-up nanoscale fabrication in the growth of CNTs by chemical vapor deposition (FIGURE 4.3),[117] and an example of top-down nanofabrication is the etching of nanopillars from a bulk semiconductor material (FIGURE 4.4).[118] The top-down and bottom-up methods are typically referring to the fabrication of nanoscale components. When building a device composed of nanoscale building blocks such as CNTs, similarly, there are two broad approaches one can take depending on the desired outcome. Similar to the bottom up approach a device can be fabricated tube by tube with the final devices containing one to several CNTs. These bottom-up nanoscale devices exploit the properties and phenomena of individual CNTs and can then be combined to form arrays and/or be integrated into larger devices as components in circuits. An example of such a device is the CNT-FET.[119,120] The second method of utilizing CNTs in devices is not necessarily a top-down approach but rather a bulk approach. Through controlled mass assembly of CNT dispersions devices can be fabricated with large amounts of CNTs. These devices would incorporate larger amounts of CNTs formed together as a quasi-bulk material which could be manipulated at the macroscale and be incorporated into larger more complicated devices. Examples of this method involve many established compositing techniques.[81] A nanocomposite made in this way could utilize established macroscale fabrication techniques while still taking advantage of the unique phenomena presented by the individual carbon nanotubes interspersed throughout

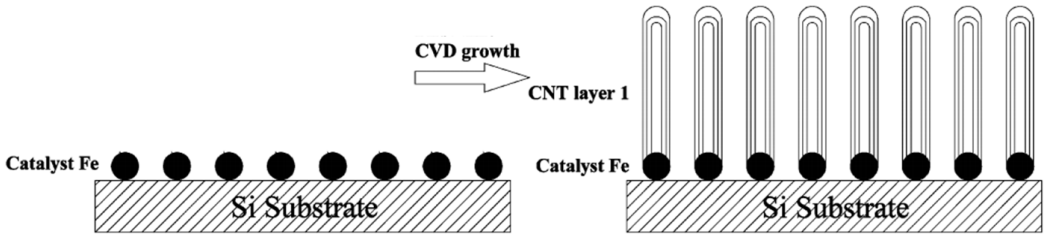

FIGURE 4.3. Schematic process of the growth of vertically aligned CNTs on a Si substrate with Iron catalyst. Adapted from Zhu et al. Nano Lett., 5, 12, 2005. .

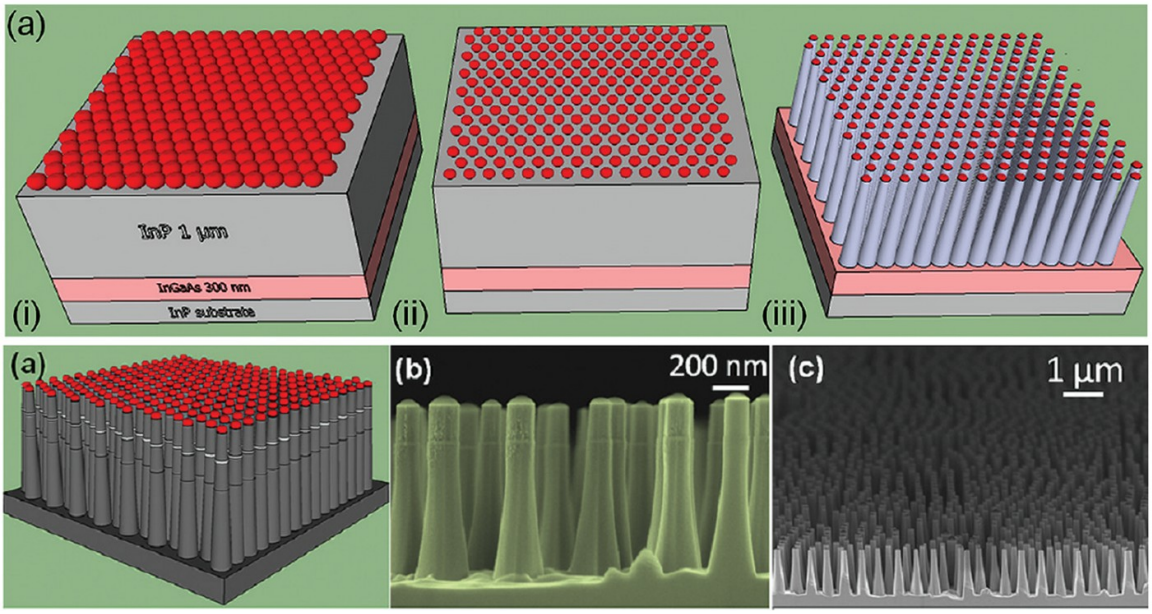

FIGURE 4.4. Fabrication of nanopillars in epitaxial layers on InP substrate: (a) A schematic illustration of the typical fabrication steps, (i) dispersed SiO_2 colloidal particles on InP surface forming a hcp array, (ii) SiO_2 particle array after size reduction process, and (iii) etched nanopillar array; (b) Cross sectional SEM image of the nanopillars. (c) Tilted SEM view showing a larger area of the nanopillar array. Adapted from Naureen, S. et al. Nano Lett. 2011, 11, 4805.

the device. These macroscale devices will utilize bulk-like agglomerations of CNTs such as, CNT bundles of ropes or fibers, as-grown SWCNT forests,[121] or deposited as sheets of CNTs referred to as films,[121-137] mats[125,138,139] or buckypaper.[140,141]

The work discussed in this section explores a subset of the aforementioned bulk-like fabrication method. To construct our SWCNT films and electrodes we use utilize van der Waals and other attractive forces to fabricate randomly aligned films from pristine SWCNTs. The methods established below avoid the use of binders, surfactants or other components that could otherwise inhibit the properties of pristine SWCNTs. In the place of surfactant or stabilizing binder we incorporate our previously discussed ruthenium coordination complexes. The unique structure and interaction of our ruthenium complexes with SWCNTs (discussed in CHAPTER 2: & CHAPTER 3:) direct the eventual microscale features of the resulting composite while also contributing favorable optical and electrical properties. The topics covered include SWCNT film fabrication techniques, functionalization of SWCNT films with ruthenium complex and electrochemical characterization of the SWCNT films.

4.2 Fabrication of SWCNT Films

Regardless of naming conventions almost all CNT film fabrication processes consist of two major steps, organization of the CNTs into a film and attachment of said film to a substrate. An important distinction needs to be made between CNT film fabrication and mats formed during CNT growth. Some of the most common CNT synthesis methods like arc discharge and pulsed laser vaporization produce complex structures of CNT ropes that are intertwined and entangled into mats.[125]

These mats are highly disordered and there is very little control of their final morphology and properties. CNT film fabrication techniques on the other hand can employ many different methods that affect changes to every conceivable property of a CNT film. Currently, the fabrication of CNT films involves a variation of one of the following five fabrication methods, (A) Vacuum Filtration, (B) Spray-Coating, (C) Dip-Coating, (D) Electrophoretic Deposition, and (E) Post-Growth Extrusion which are depicted in FIGURE 4.5.

4.2.1 Vacuum Filtration

Vacuum filtration of CNTs to form a film is the most widely used method of film formation[123,135,141,142] due to the ease of setup and the many adjustable parameters. It is by far the most accessible method to researchers and labs that need to quickly and cheaply make CNT films. With the vacuum filtration technique one can produce films ranging from transparent 100nm thickness flexible films to buckypaper so thick and rigid they are referred to as buckydiscs. The diameter of films fabricated by this method is limited only by the size of the filter.[141] FIGURE 4.6[135,141] clearly illustrates the two extremes of film thickness that can be achieved with this method.

There are two steps to the vacuum filtration production of CNT films. The first step required a dispersion of CNTs to be filtered through a porous membrane or filter. The beauty of this method is that by the nature of filtration the uniformity of

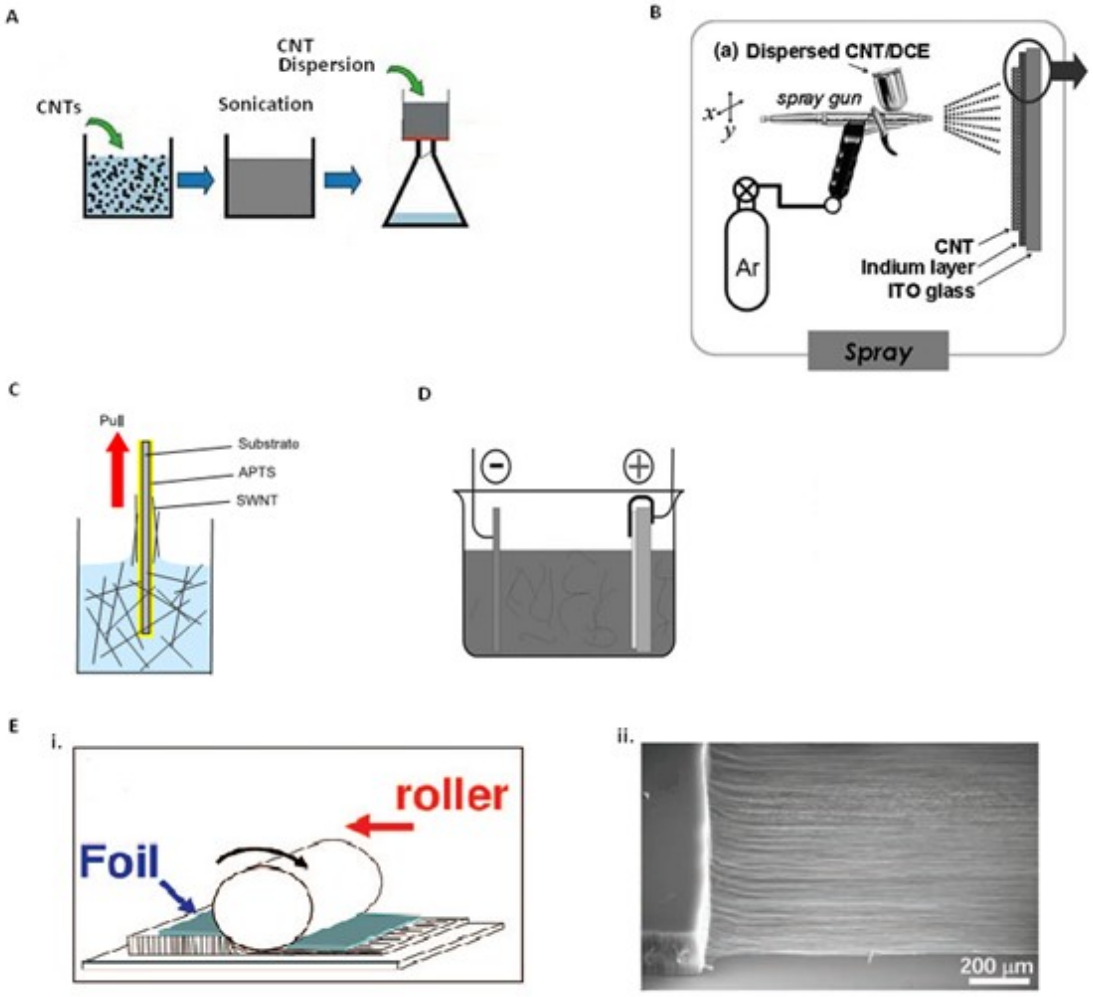

FIGURE 4.5. CNT Film Fabrication Methods. (A) Vacuum Filtration, (B) Spray-Coating, (C) Dip-Coating, (D) Electrophoretic Deposition, (E) Post-Growth Extrusion.

the deposited film is self regulated as the CNTs deposit on the filter. The second step involves transferring the deposited CNT film from the membrane or filter paper or removing the filter paper. In the case of a buckypaper thick enough to be self supporting, transfer to a substrate may not be necessary as evidenced by the image in FIGURE 4.6B.[141] The electrode work discussed below involves SWCNT films made by this method. The procedure for the vacuum filtration fabrication of SWCNT thin films used in these studies is continued in section 4.3.

4.2.2 Spray-Coating

Spray-coating is a common fabrication method employed by many fields, including CNT film fabrication, to produce different types of thin-films. Using spray-coating to deposit CNT films is unique in that it is the most precise method of deposition. FIGURE 4.5B illustrates the spray-coating method using an air brushing technique, not unlike that which is used by numerous painting applications. Another variation of this film fabrication method is inkjet printing. Inkjet printing has been used by many research groups to print patterned layers of nanoparticles on substrates in the same way a printer lays down ink when printing on paper. These two variations can print highly resolved images using either masks or computer controlled printing mechanisms which pattern CNT films onto a substrate.

The initial preparation of the CNT dispersions for spray coating is similar to that of vacuum filtration, however high CNT concentrations can cause clogging problems. A dispersion of CNTs is made following techniques discussed in section 3.4.2. N-methyl-2-pyrolidone (NMP) has been established as being a good solvent for this purpose.[143] The CNT dispersion in NMP is then loaded into an air gun or

printing mechanism and the CNT dispersion is sprayed as an aerosol onto the substrate.[123,130,143,144] Intricate electrodes, shown in FIGURE 4.7, can be constructed with CNTs by this method.[143] However, continuity and uniformity problems can arise while using this method. Depending on the temperature, conditions of the substrate, droplet size, and solvent type, the final morphology of the resulting CNT film will change. Commonly, the capillary forces induced by the drying droplets will ball up the CNTs which will bundle and/or separate CNTs within a droplet creating an incongruent layer which will manifest as a higher film resistivity. Uniformity is controlled by applying equal applications of CNT dispersion sprayed onto the surface of the substrate. Uniformity is well controlled via the printer mechanism but can be difficult if not impossible to control when sprayed by hand.

4.2.3 Dip-Coating

Dip coating has the distinction of being the most simple of the CNT film deposition techniques. Using previously described methods CNT dispersions are created with very high CNT concentrations on the order of milligrams per milliliter.[131,132] Then much like one would dip a candle the substrate is immersed into the dispersion in a vertical orientation. The dipping process is repeated until a coating of CNTs of the desired thickness has formed. Thickness can often be estimated by a calibrated absorption curve correlated with AFM measurements. As

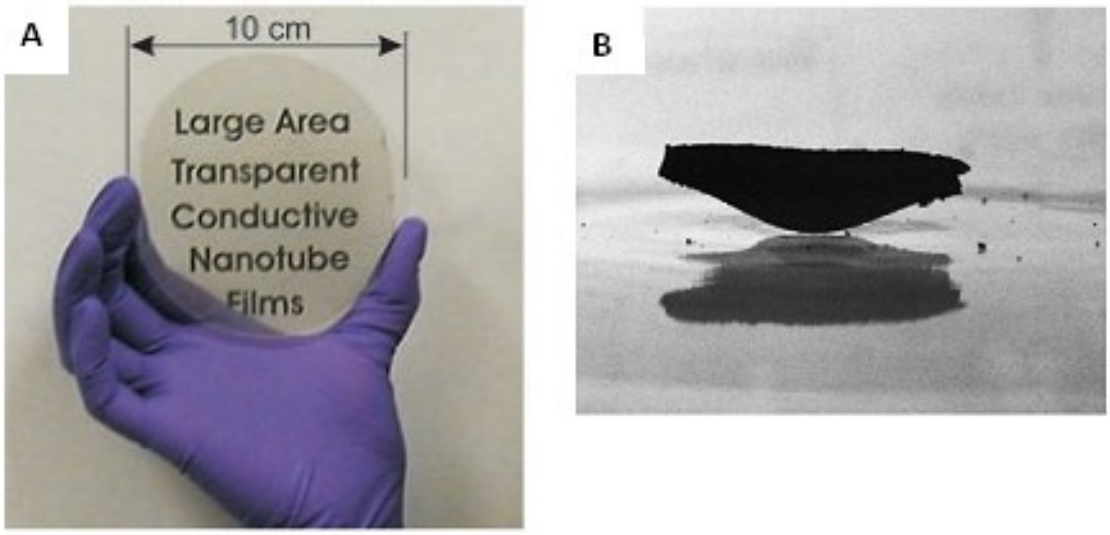

FIGURE 4.6. CNTs can be formed into transparent thin films (A) and self supporting mm thick mats (B).

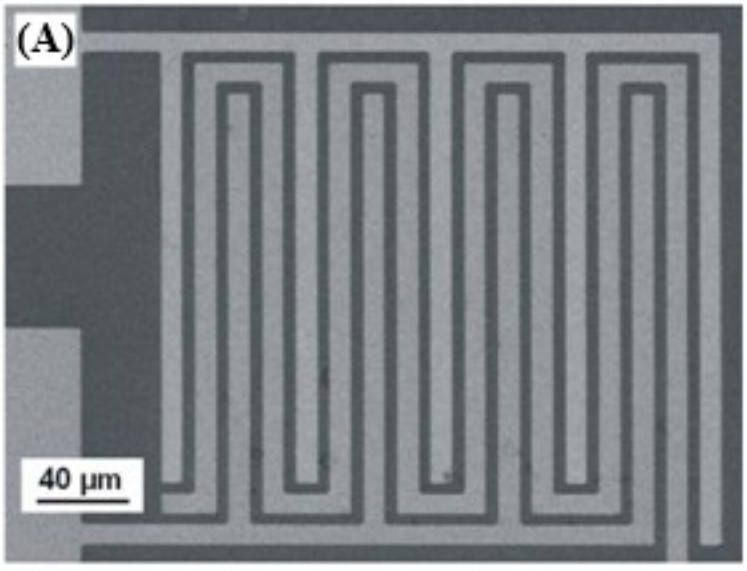

FIGURE 4.7. Using an air gun or printing mechanism, CNT dispersions can be sprayed as an aerosol onto a substrate to form intricate patterns. Intricate electrode pattern in which the gaps are printed with CNTs (A).[143]

one would imagine this process is highly dependent on the attraction and adhesion of CNTs to the substrate surface, so clean substrate is always required and in many cases a coating of polyethylene terephthalate (PET) is used as the substrate coated on glass.[132] In other cases when a conductive substrate is required a binding agent can be utilized.[131] FIGURE 4.5C illustrates the dip-coating method with a glass substrate utilizing 1,2-aminopropyltriethoxysilane (APTS) as an adhesion promoter.

This method is not often found in the literature likely due to the imprecise quality of the resultant film. Among the major drawbacks of this process are the length of time needed to allow each dipping to dry before the next, the uncertainty of thickness and highly bundled state of the CNTs in the initial dispersion.

4.2.4 Electrophoretic Deposition

Electrophoretic deposition (EPD) of CNTs utilizes the surface charge of CNTs dispersed in a suspension driven by electric field which deposits them on an electrode.[128,145-151] EPD and the reverse electrophoretic dissolution is of particular interest and concern to those that would want to incorporate CNTs and electrodes, a topic which will be discussed below. Typically for the deposition of CNT films using EPD a conductive material acts as both an electrode and a substrate attracting CNTs towards an oppositely charged electrode and build up a densely and uniformly packed/bonded layer. Until recently this method produced CNT films attached to opaque conductive substrates. Recently is has been shown that a substrate coated with a very thin layer of metal, which is opaque will serve as an electrode for the deposition of CNTs. If the proper metal is selected, when the thin layer oxidizes it will form an optically transparent metal-oxide such as Al_2O_3 or TiO_2.[128]

4.2.5 Post-Growth Extrusion

Post-growth extrusion (PGE) is a noteworthy recent development to form films from CNTs. PGE refers to extruding a film from an as-grown CNT material, typically a CNT forest. Two different methods have been utilized for this technique.[121,152] The first uses an adhesive to adhere to the exterior edge of a MWCNT forest which is followed by the application of a constant pulling force which extends a continuous transparent sheet from the unraveling MWCNT forest.[152] The second technique uses a foil laid over the top of a CNT forest and a roller pressing the foil to lean the CNTs over each other pressing them into a highly aligned dense film.[121] FIGURE 4.5E illustrates these concepts. Either chemical or physical means can be used to attach these films to new substrates. While these films do not provide the researcher an opportunity to fully functionalize the CNTs before they are made into a film, many innovative and even fun devices have been produce from this process such as high efficiency nanoparticle filters[153] and CNT film speakers.[154]

4.3 Functionalization and Transfer of SWCNT Films

The SWCNT electrodes and films constructed for this work utilize the filtration method discussed above. In an ideal situation, while carbon nanotubes are dispersed in solution (refer to section 3.4.2 for techniques to disperse CNTs in solution) they are completely unbundled; meaning their surfaces are free to be modified either chemically or physically. The filtration fabrication method was chosen because the use of SWCNT dispersions allows us the ability to functionalize the SWCNT films

in several ways. This important concept sets this simple method apart from many of the more complicated techniques discussed previously.

It was shown in chapter 3 that our ruthenium complexes bind strongly to the walls of SWCNTs. This adsorption phenomena gives us the capability to functionalize individual SWCNTs in solution before they are integrated into bulk materials. Because both the SWCNTs and the ruthenium complex can be weighed and dissolved(dispersed) in NMP or DMF this technique also gives us precise control of the amount of ruthenium complex or any other component we would like to add to the film. Changing the amount of SWCNTs dispersed in solution is also the most effective way to adjust physical properties, such as thickness, opacity, rigidity and also conductivity, of the resulting film. The filtration step is simple. A large fritted glass two piece Buchner funnel in used, shown in FIGURE 4.8.

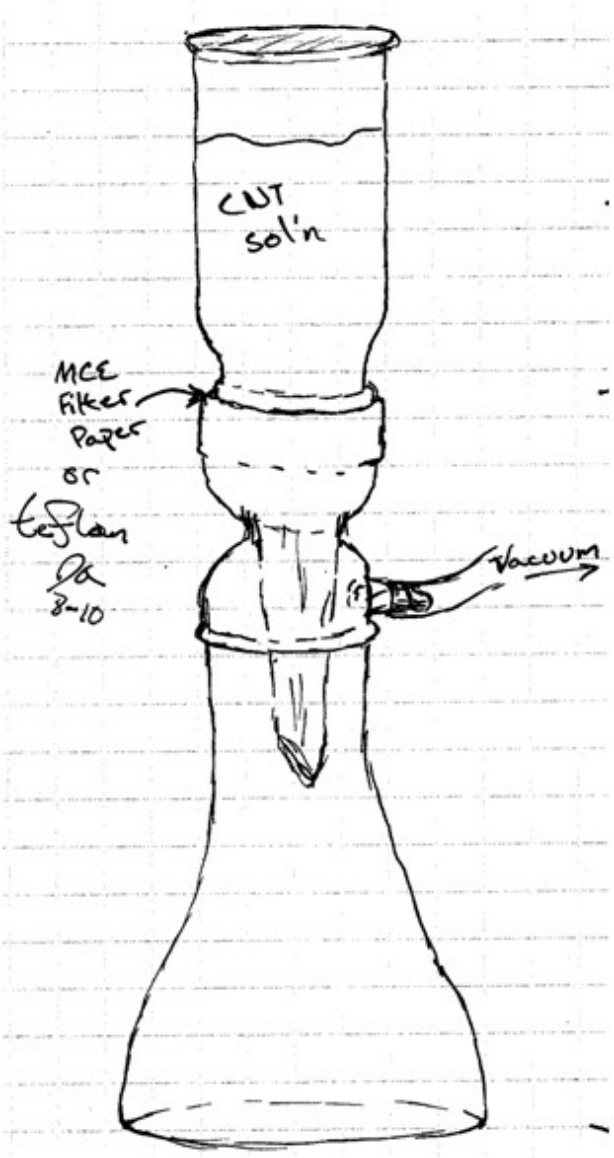

FIGURE 4.8. Typical filtering apparatus used to form SWCNT thin films. 0.2 μm MCE or PTFE membranes can be used.

4.3.1 Aqueous Dispersions vs Aprotic Solvent Dispersions

Our ability to functionalize SWCNTs is affected by the selection of solvent and whether or not a surfactant is used to stabilize the SWCNTs in solution. Ideally for surfactant stabilized dispersion, the stabilizing surfactant is present only in the solution phase of the process and is removed from the CNTs during filtration. However it has been shown that vigorous washing of a deposited film is required to completely remove a surfactant. This is due to the intercalating process which traps surfactant molecules between the intermingled and woven SWCNTs within the film. The most apparent symptom of inadequate removal of surfactant is the greatly reduced integrity of the film. Intercalated surfactant will inhibit the van der Waals interactions between the SWCNTs and also retards the intrinsic electrical properties of the film due to the interferance of π-π interactions resulting in an increased film resistance.[123] To reduce the risk of having excess surfactant, the minimum amount of surfactant required to maintain a stable dispersion should be used.

Many publications report a surfactant concentration of 0.1-1% by weight[123,135,141,142] which seems to be appropriate for maintaining stable dispersions with concentrations on the order of mg in mL. However, it is has been difficult to remove surfactant from a film made from filtrate containing 1% by weight surfactant. We have found that an efficient way to reduce the amount of surfactant in the filtrate is to create two separate dispersions; a stock dispersion with a high concentration of SWCNTs and 0.1-1% surfactant and a second dispersion; a serial dilution of the first, to be filtered, made from an aliquot of the first and approximately 1 liter of solvent. This allows the surfactant molecules that are bound

with the SWCNTs to remain associated and maintain dispersion stability while the excess surfactant is dispersed in a large amount solvent. This reduces the required washings of a surfactant stabilized SWCNT film to a minimum which helps maintain film uniformity and integrity.

While the use of surfactant allows us to work with SWCNTs in aqueous media, the mechanism of surfactant wrapping competes with and effectively impedes the noncovalent functionalization discussed in chapter 3. To avoid the use of surfactant and enable our ability to functionalize our films with ruthenium complex it was necessary to establish a filtration procedure that utilized well known nonaqueous nanotube solvents.

For nonaqueous filtration fabrication we use aprotic solvents such as DMF or NMP. These are well known SWCNT solvents and can create kinetically stable dispersions of SWCNTs at concentrations approaching 20 mg L^{-1}.[61] By dispersing SWCNTs in a supporting solvent SWCNT the suface area of the tube walls are adequately exposed and are only associated with solvent molecules. In this type of dispersion we were able to functionalized the nanotube film with our ruthenium complexes, proven by the work presented in chapter 3.

4.3.2 Hybrid Nanocomposite Functionalization

Another major benefit of the filtration fabrication method is that the film can be deposited in multiple steps. This unique concept allows us to design novel electrodes which place a layer of nanoparticles between two layers of SWCNTs. FIGURE 4.19 is a representative image of a CdSe quantum dot (QD) electrode made by this process. The substrate is a conductive ITO coated glass.

The fabrication is a simple variation of the procedure described above. A dispersion of SWCNTs in NMP is prepared and then divided into three aliquots. The first aliquot is filtered through the membrane, leaving a small amount on top to keep the setup wet. The second aliquot is combined with a quantity of QDs dispersed in the same solvent and filtered through the membrane SWCNT film. The third aliquot is then pulled through the filter-SWCNT-QD ensemble effectively trapping the QDs in the center of the film. This process is a simple and effective way to trap nanomaterials or any other analyte inside a SWCNT electrode.

4.3.3 SWCNT Film Transfer

Once a SWCNT film is deposited the delicate act of removing the film from the filter and attachment to a substrate needs to be addressed. We have found through extensive testing and analysis that the best time to trim and shape the SWCNT electrode is while the nanotube film is still attached to the PTFE membrane. During this process the film should be kept wet with a clean solvent such as methanol. It is important to not allow the SWCNTs to dry while sitting on the filter or membrane. The capillary action of the drying solvent will permanently attach the film to the filter. The transfer of the film to a substrate is a fairly straightforward process but successful transfer depends heavily on having an extremely clean substrate surface. (Refer to appendix D for detailed substrate cleaning methods.) To transfer the film, the film/filter should be placed nanotube side against a clean, solvent wetted substrate. A porous lint-free cloth is placed on the back side of the filter membrane and the entire ensemble is pressed with clamps to maintain firm contact between the substrate and SWCNT film. It is important to include the porous cloth backing to

provide a path for solvent wicking and evaporation while maintaining even pressure across the film surface. The capillary action of the drying solvent is the mechanism through which the SWCNTs are pulled into van der Waals contact with substrate. FIGURE 4.9 is an image of two SWCNT films formed by the filtration method being transferred onto glass substrates.

Once the film is intimately attached to a new substrate the filter membrane can be removed either by peeling the filter from the back of the film or dissolving the filter depending of the material of the filter. The latter tends to be the least destructive method for thinner SWCNT films. The success of this process is extremely dependent on the cleanliness and dryness of the pressed ensemble. A common problem that occurs during this process is that adhesion of the film to the new substrate does not occur. The idea behind this technique is that a wetted CNT film can be pressed to substrate and as the wetting agent (water or methanol) dries, capillary forces will pull the CNT film into intimate contact with the substrate where van der Waals forces hold them together firmly. For inorganic substrates it is best to have an extremely clean surface, by means of piranha etchant and oxygen

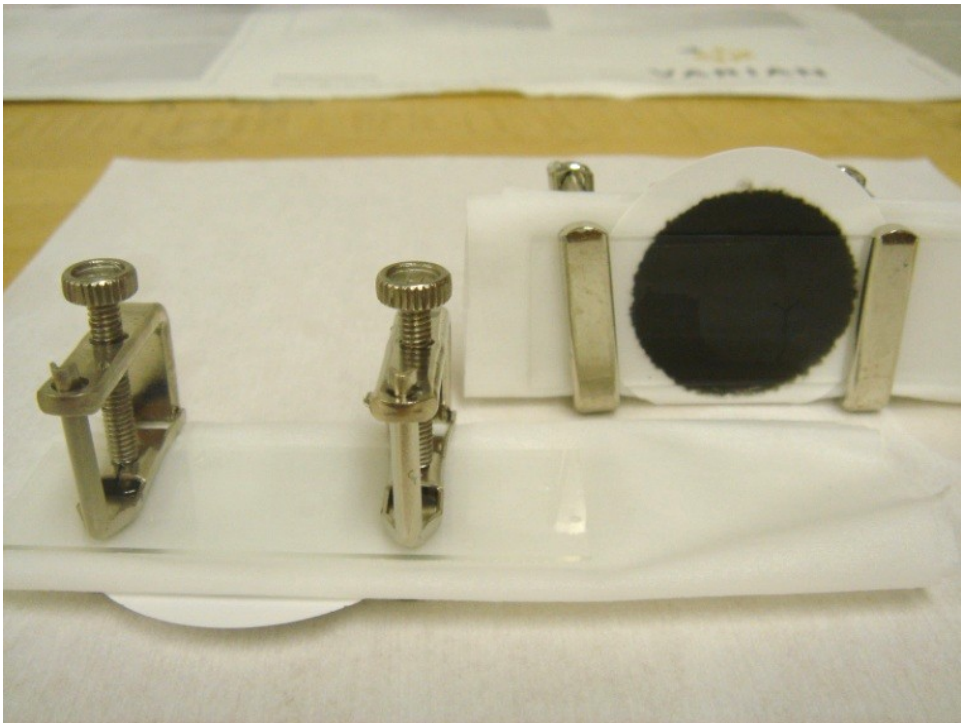

FIGURE 4.9. SWCNT films formed by the filtration method being transferred to a glass substrate. SWCNTs are filtered onto a 0.2 μm PTFE membrane. The film is wetted with methanol and pressed against a clean glass substrate. It is backed with a porous lint-free cloth to allow solvent wicking and evaporation.

plasma scrubbing to removed any surface contaminants and polymer substrates cleaned by similar methods also exhibit sufficient attachment.

4.4 Hybrid Nanocomposite SWCNT Thin Film Electrodes

Innovative electrochemical systems such as solar energy collectors and electrochemical double-layer capacitors (EDLC) have garnered much interest over the past decade due to the world's steadily increasing energy storage demands[155]. The promise of supercapacitor research is that EDLCs could one day bridge the gap between the energy density of batteries and power density of classical capacitors. Carbon and ruthenium oxide are materials which have received large amounts of focus in this pursuit. SP2 hybridized carbon serves as an almost ideal electrochemical electrode due its superb chemical resistance and high electron transport capabilities. Nanoscale forms of SP2 carbon such as graphene and fullerenes (C60, SWCNTs, MWCNTs) have the additional benefit of theoretically high specific surface area greater than 1315 m^2 g^{-1}.[57] Supercapacitors differ from classical EDLCs in that they gain additional capacitance through a mechanism of charge storage called pseudocapacitance discussed in section 4.5. Pseudocapacitance can increase specific capacitance (C_{sp}) to more than 900 F g^{-1} [155] through faradaic charge transfer processes.[156] Transition metal oxides such as ruthenium oxide (RuO_2) show significant pseudocapacitance, and EDLCs that incorporate this material can increase charge storage greatly.[155] Pseudocapacitance in RuO_2 and CNT composites is derived from redox chemistry of functional groups (defects) on CNT walls and through the redox couples of RuO_2. CNT-metal oxide composites have good charge-discharge stability and are good candidates in EDLCs. However,

minor drawbacks of decorating CNT electrodes with RuO_2 are decreased porosity and decreased surface area of the active mass of the electrode.[157,158] These drawbacks are often outweighed by huge increases in specific capacitance. The major drawback of using ruthenium oxides as well as many other rare metal-oxides is that they can be expensive, and material costs can become prohibitive for wide spread use. To counter the cost, efforts have been made to reduce the mass of metal-oxides[159] such as RuO_2 while improving the specific capacitance of CNT electrodes with alternative pseudocapacitive materials. Conductive polymers are promising materials for this purpose.[160] However, CNT-polymer electrodes have poor long-term stability due to the degradation of conducting polymers.[160] New materials are needed that compete with the low weight and low cost of conducting polymers while maintaining the good charge-discharge stability of metal-oxides.

4.5 Electrochemical Capacitor Testing

The performance of an electrochemical capacitor can be characterized by galvanostatic and cyclic voltammetry methods. When using the galvanostatic charge and discharge method (constant current charge/discharge, CD), the electrochemical capacitor electrode is charged and discharged at a constant current within a potential range of 0 V to a higher limit potential, V_{max} (V_{max} is the decomposition voltage of the electrolyte). The potential (V) is recorded as a function of time (s). FIGURE 4.10 shows a representative plot of typical CD charge/discharge cycle. The sharp drop of electrode potential at the beginning of discharge is often due to solution resistance.

When using the cyclic voltammetry (CV), the potential (V) is swept between two voltages (V_1 and V_2) at a constant scan rate (v). The resulting current (I) is recorded as a function of time (s). The current is plotted as a function of voltage. For an ideal double layer capacitor, the current is independent of potential and shows a rectangular plot. However, if redox reactions occur, the rectangular shape is distorted, showing reduction and oxidation peaks. FIGURE 4.11 is an overlay of a cyclic voltamagram of an ideal capacitor vs a carbon electrode system that contains redox active components.

In an ideal double layer capacitor, energy is stored in a double layer and no charge transfer occurs across the interface between the electrode and the electrolyte. In this case capacitance is directly proportional to surface area. However, due to imperfections (functional groups) along the surface of the SWCNTs it is possible that some redox reactions will occur. If the redox reactions are relatively reversible the charge transferred to and from these electroactive species behave like capacitance. The charge storage arising from these faradaic reactions is called "pseudocapcitance". Pseudocapcitance is the source of the large specific capacitance values of capacitor containing transition metal oxides like MnO_2 and RuO_2.[157,159,161-164] Therefore the total capacitance on an electrode is defined by equation 4.1. It is not only from electrostatic charge but also arises from quick faradaic charge transfer reactions:

$$C_T = C_{dl} + C_F \qquad 4.1$$

where C_T is total capacitance, C_{dl} is electrical double layer capacitance, C_F is faradaic pseudocapacitance. There are three common pseudocapacitance

mechanisms that contribute faradaic charge storage to an EDLC. TABLE 4.1from Conway & Pell[165] lists the mechanisms and gives example systems that contribute to this phenomena. By introducing functional groups onto the SWCNTs by depositing ruthenium coordination complexes or by inserting electroactive particles of transition metals or semiconductor quantum dots charge transfer can be observed through increases in pseudocapacitance.

TABLE 4.1. Pseudocapacitance systems giving rise to pseudocapacitance with application to electrochemical capacitors. Adapted from Conway, B. E.; Pell, W. G. J. Solid State Electrochem. 2003, 7, 637.

System type
(a) Redox system: $Ox + ze^- \rightleftharpoons Red$ and $O^{2-} + H^+ \rightleftharpoons$ in lattice
(b) Intercalation system: Li^+ into "MA_2"
(c) Underpotential deposition of metal adatoms, $M^{z+} + S + ze^- \rightleftharpoons SM$ (S = surface lattice sites) or $H^+e^- + S \rightleftharpoons SH$.

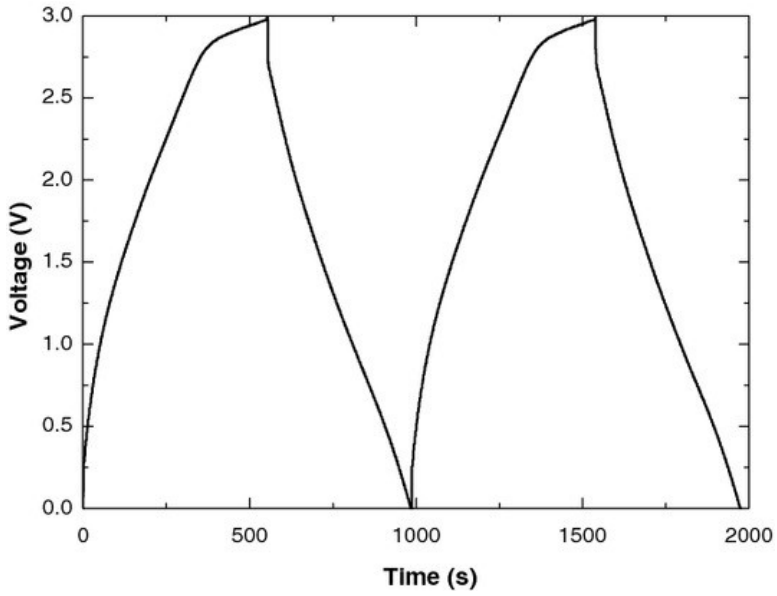

FIGURE 4.10. Representative galvanostatic charge and discharge cycles. CD in organic electrolytes and ionic liquids can allow Vmax to reach 3 V.

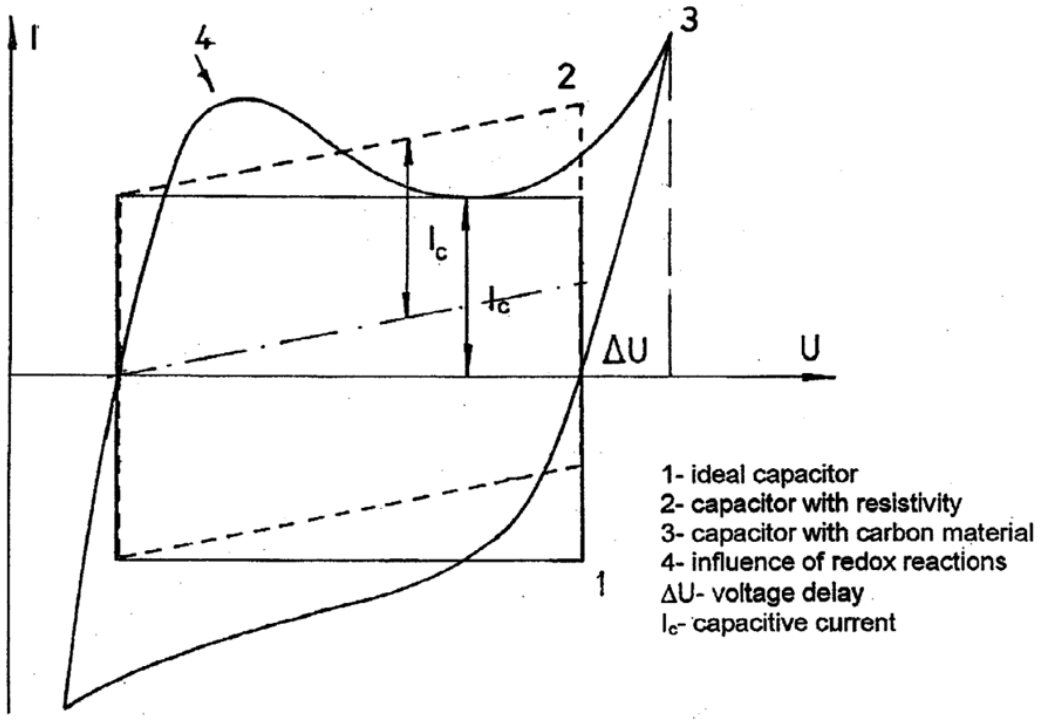

FIGURE 4.11. Typical charge / discharge voltammetry characteristics of an electrochemical capacitor. Copied from Frackowiak, E.; Béguin, F. Carbon 2001, 39, 937.

4.6 Ru Complex—SWCNT Nanocomposite Electrodes

In this section we present a novel method to create nanocomposite electrodes composed of SWCNTs noncovalently functionalized with ruthenium coordination complexes. Our complexes interact with the walls of SWCNTs through overlapping π molecular orbitals and have well known electrochemical processes.[166] During integration into a SWCNT composite, our ruthenium complexes can affect the pourosity of the electrode and also contribute a yet to be identified pseudocapacitance mechanism that appreciably increases C_{sp}. With this electrode design, we address material costs by reducing the content of expensive transition metals and address long-term stability by utilizing a unique ruthenium complex that tightly binds with SWCNTs, has reversible redox chemistry, and significantly enhances faradaic pseudocapacitance with minimal loading capacities of only 0.3 % wt. ruthenium.

The molecule used in this study is the +4 dinuclear ruthenium coordination complex, *[(phen)$_2$Ru(tpphz)Ru(phen)$_2$](PF6)$_4$*, discussed previously in chapter 2, and will from now on be referred to as Ru_{Dim}^{4+}. The synthesis of Ru_{Dim}^{4+} is discussed elsewhere.[10] The composite electrode is formed via a solution phase process described in section 4.3. SWCNTs are dispersed into a solution of N,N-dimethyl formamide (DMF) using ultrasonication and purified via ultracentrifugation [60]. The resulting supernatant is a well dispersed solution of SWCNTs which is then diluted to 10 mg L^{-1}. 20 mL of the SWCNT dispersion (0.2 mg SWCNTs) and a stock solution of Ru_{Dim}^{4+} (20 μM) are combined into a larger volume of DMF at ratio of 0.3

% wt. ruthenium to active electrode mass. The functionalization mixture is stirred and left to equilibrate for 24 hours to allow adsorption of Ru_{Dim}^{4+} to the nanotubes to reach equilibrium before the entire mixture is filtered through a PTFE membrane. Vacuum filtration of the functionalization solution deposits the SWCNT- Ru_{Dim}^{4+} homogeneously on the PTFE membrane which can then be transferred to an ITO-coated glass current collector for electrochemical testing.

The dimensions of SWCNTs and the rigid structure of Ru_{Dim}^{4+} that forms a pocket rich in π-electron density, enables the interaction of the π-surface of SWCNTs with the π-pocket of the molecule through π-π stacking as they come into contact while dispersed in solution. A DFT geometry optimization of Ru_{Dim}^{4+} bound and wrapped around a (10,0) SWCNT is shown in FIGURE 4.12, illustrating the proposed SWCNT-Ru_{Dim}^{4+} functionalization mechanism. When Ru_{Dim}^{4+} is placed 5 nm from the SWCNT (unbound), the optimized tpphz bridging ligand is planar. In contrast, the tpphz ligand of the bound Ru_{Dim}^{4+} wraps around the SWCNT with a radius of curvature of 2.7 nm. The unoccupied molecular orbital shown resides on the tpphz ligand and is consistent with the LUMO of unbound Ru_{Dim}^{4+} and free tpphz. [166] The calculated energy of this orbital on the bound complex is 41.6 meV lower than the energy of the same orbital on the unbound complex predicting an anodic shift of the first reduction of tpphz when bound to a SWCNT.

Adsorption isotherm measurements of Ru_{Dim}^{4+} on the surface of dispersed the SWCNTs were used to determine the amount of Ru_{Dim}^{4+} that was binding to the SWCNTs. The results of Ru_{Dim}^{4+} adsorption to SWCNTs (5.44 mg L^{-1} in DMF) are

shown in FIGURE 4.13. Adsorption is determined by measuring the decrease in concentration of Ru_{Dim}^{4+} as SWCNTs are removed from solution. From the molecular weight of Ru_{Dim}^{4+} the mass of Ru can be determined. The adsorbed Ru is plotted as a % wt. of the mass of SWCNTs in the functionalization solution versus the ratio of unbound Ru_{Dim}^{4+} to mass of SWCNTs (mg mg^{-1}). The data is fit by a Langmuir adsorption isotherm [156], showing the binding of Ru_{Dim}^{4+} to SWCNTs. The electrodes measured in this study contain 0.3 % wt. Ru in the active mass as confirmed by EDX (Oxford INCA). Consequently the ruthenium does not contribute significantly to the material cost of the electrode.

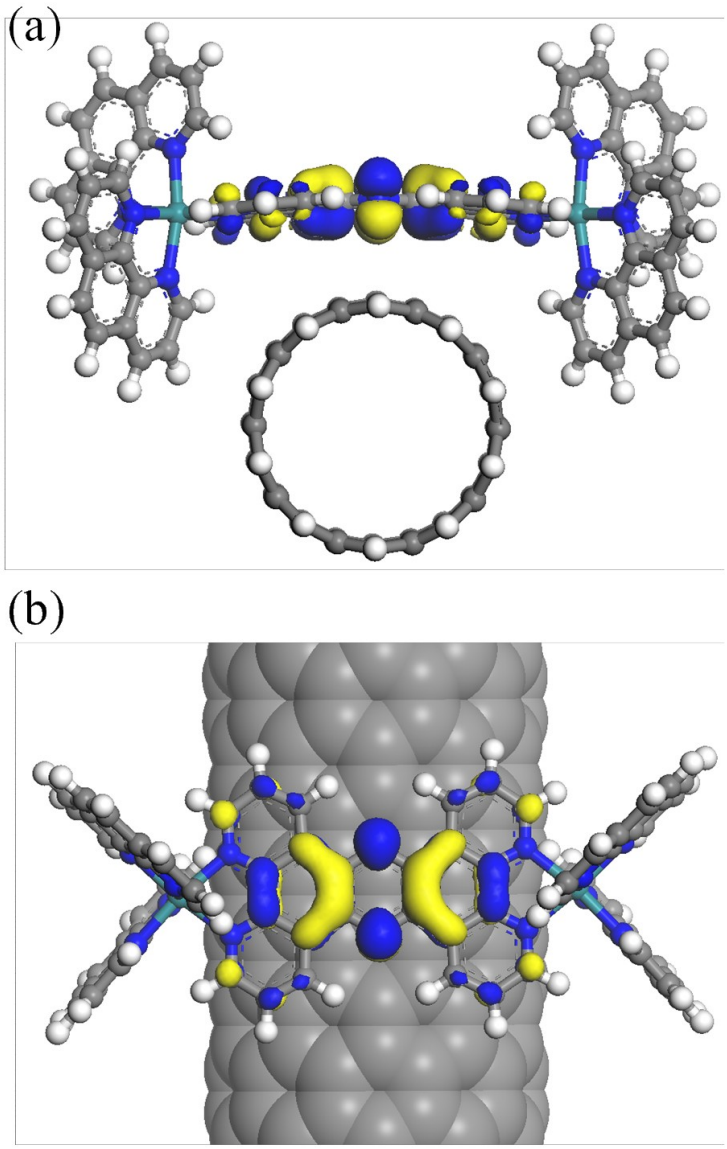

FIGURE 4.12. DFT geometry optimization of +4 ruthenium complex bound to a (10, 0) SWCNT. (a) edge view. (b) plan view. When RuDim4 is bound to a (10, 0) SWCNT the tpphz bridging ligand (planar when unbound) wraps around the SWCNT with a radius of curvature of 2.7 nm. The unoccupied molecular orbital shown resides on the tpphz ligand and the energy is lower by 41.6 meV in the bound state.

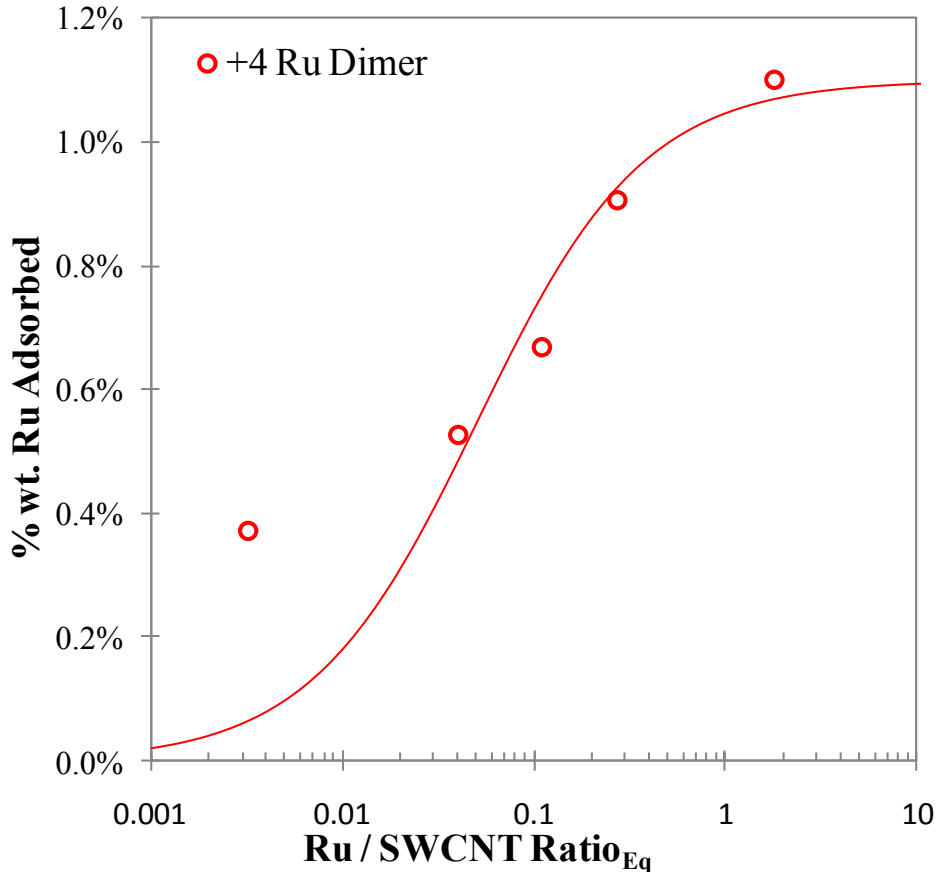

FIGURE 4.13. Langmuir adsorption isotherm. % wt. Ru is the mass of ruthenium adsorbed per mass of the SWCNT-Ru composite. Ru/SWCNT ratio is the concentration of ruthenium complex in solution at equilibrium per concentration of SWCNTs in solution, (5.44 mg L^{-1}).

Solution based processing allows us to control the porosity of the final structure. Porosity is controlled by keeping the Ru_{Dim}^{4+} concentration of the functionalization solution low. Higher concentrations of ions in solution can aggregate SWCNTs [9] while low concentrations avoid aggregation and allow us to functionalize the surface of the tubes while they remain mostly unbundled. The functionalized, unbundled tubes can then be deposited as an active mass without reduced pore structure or significantly decreased surface area as determined by SEM. FIGURE 4.14 and FIGURE 4.15 show the small bundles of SWCNTs and consistent pore structure of the pristine and 0.3% Ru functionalized SWCNTs respectively. FIGURE 4.16 shows a film with larger bundles and collapsed porosity. Aggregation of the SWCNTs is caused by the higher Ru_{Dim}^{4+} concentration in the functionalization solution. Any benefits that may be gained from ruthenium complex intercalation have been lost due to the heavily reduced surface area.

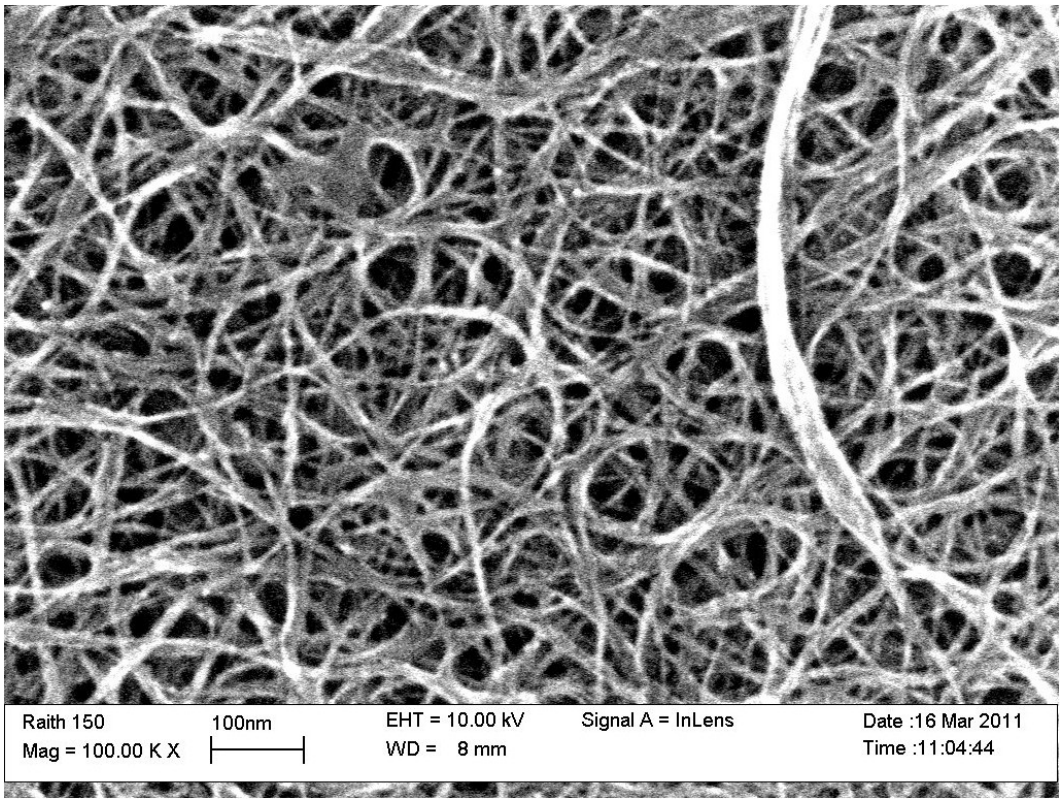

FIGURE 4.14. SEM of a pristine SWCNT working electrode. Film is formed from a low concentration of SWCNT dispersed in aprotic solvent, providing maximal specific surface area with minimal bundling during dispersion.

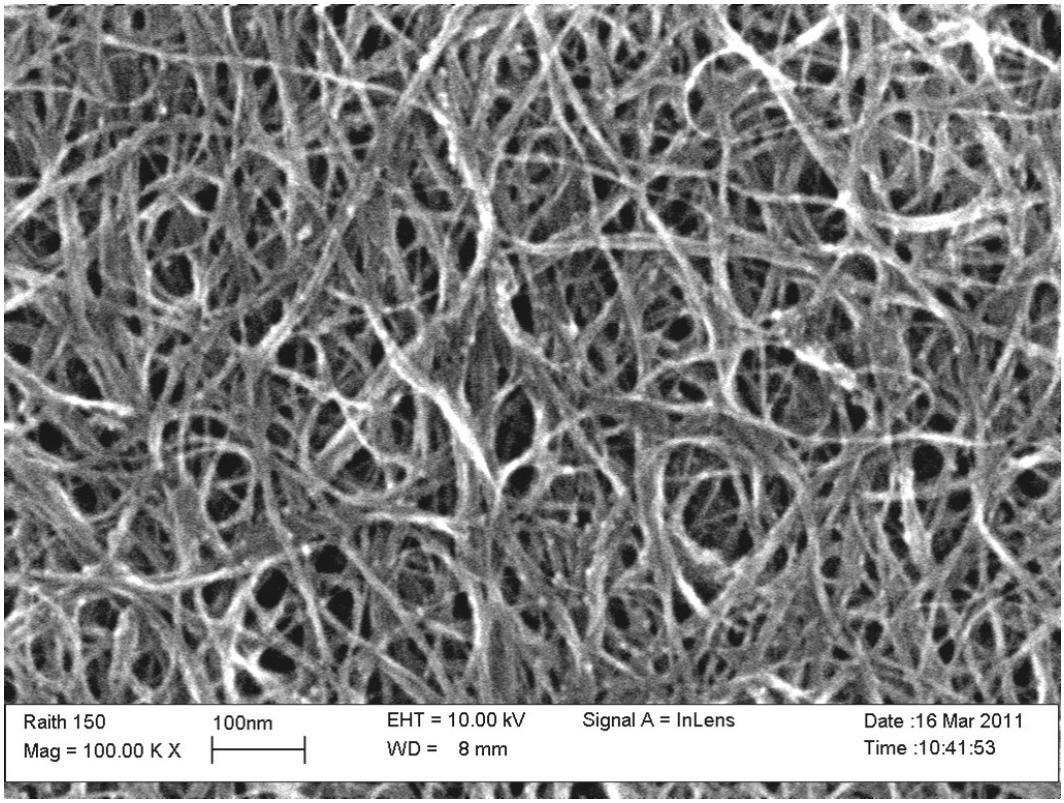

FIGURE 4.15. SEM of a SWCNT working electrode with 0.3% Ru functionalization. 0.3% functionalization creates no noticeable increase in bundling of SWCNTs in solution which maintains relatively the same specific surface area as the pristine electrode.

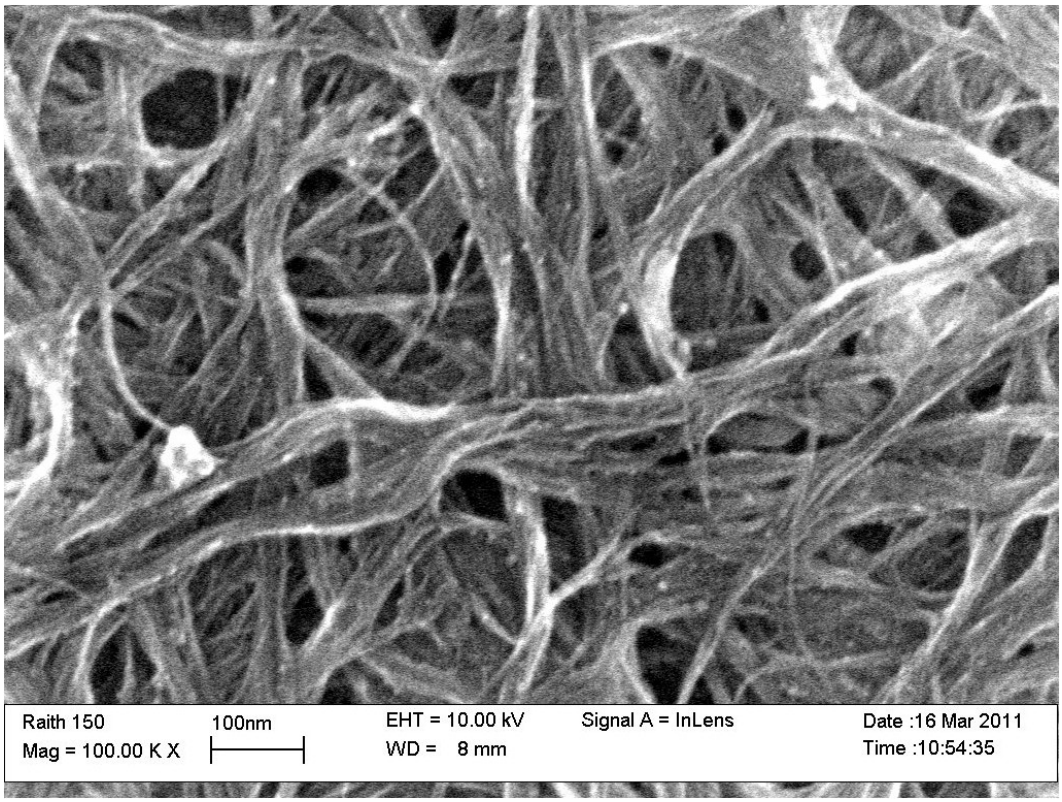

FIGURE 4.16. SEM of a SWCNT working electrode with 0.9% Ru functionalization. Bundle size has increased to ~80 nm which translates roughly to a 90% reduction of specific surface area.

4.6.1 Measuring SWCNT Thin Film Electrode Capacitance

Electrochemical capacitive properties of the SWCNT-Ru_{Dim}^{4+} nanocomposite and pristine SWCNT films were tested on a PAR 273A (Princeton Applied Research) electrochemical work station with a standard 3-electrode cell. The films, with submerged areas of 1 cm^2, were used as working electrodes. A platinum wire served as the counter electrode and silver/silver chloride (Ag/Ag^+) was the reference electrode. Capacitance was measured in 1 M $H_2SO_{4(aq)}$, using galvanostatic charge-discharge (CD) and cyclic voltammetry (CV). CD cycling ranged between 0.1 and 10 A g^{-1} and CV scans between 1 mV s^{-1} and 1000 mV s^{-1}. Representative CV data presented in FIGURE 4.17, show an increase in current density when SWCNTs are functionalized with Ru_{Dim}^{4+} which corresponds with increased capacitance. The appearance of reversible redox peaks in both the CV of the pristine and composite film is consistent with faradic charge transfer introduced by redox active defects on the surface of the SWCNTs.[155,167,168] The dispersion used to fabricate these electrode were treated to the exact same protocol and are from the same source, so it is reasonable to assume that the defects exist in the same quantities in both electrodes. So it can also be assumed that contributions by these defects to the overall capacitance will be the same for both electrodes. FIGURE 4.18 shows the CD response of the electrodes at a constant current density of 10 A g^{-1} is a 1.6 V window which corresponds to a C_{sp} of 350 F g^{-1} for SWCNT-Ru_{Dim}^{4+} vs 40 F g^{-1} for pristine SWCNTs. The capacitance was calculated from

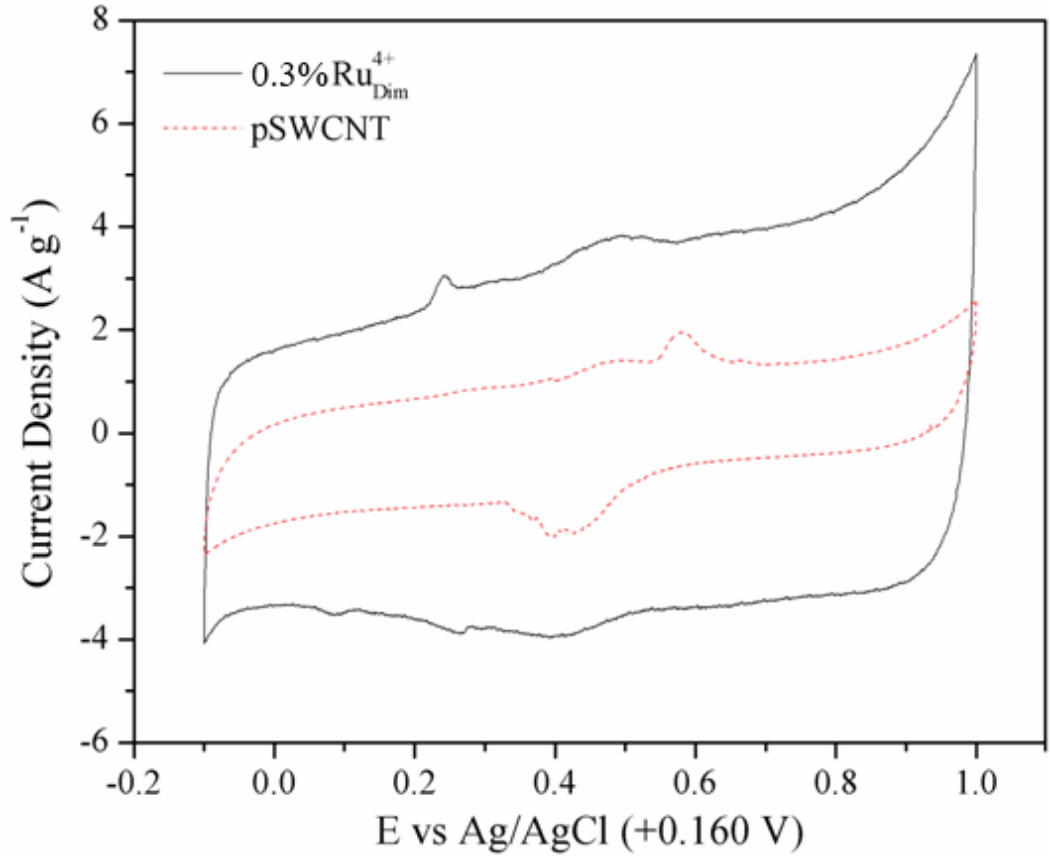

FIGURE 4.17. Cyclic voltamagrams of a pristine SWCNT film and 0.3% Ru functionalized film. The increase of current density vs. potential for the functionalized film translates as an increase in capacitance.

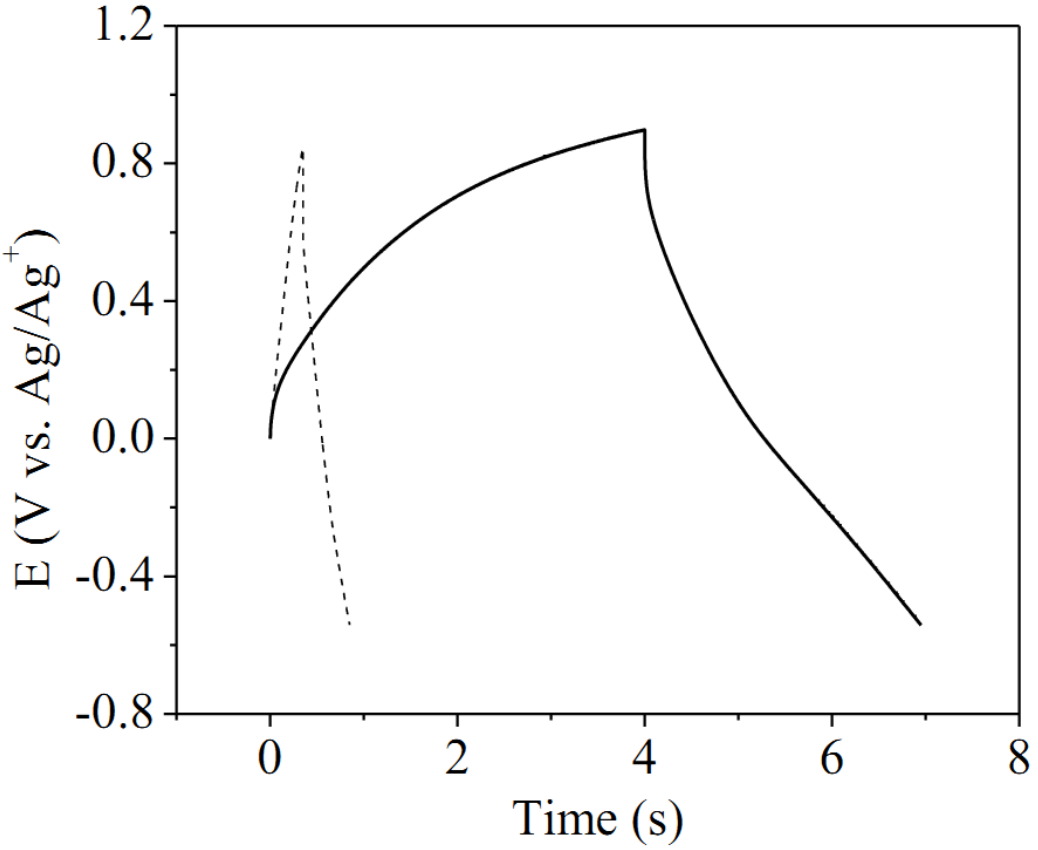

FIGURE 4.18. Galvanostatic charge-discharge of a pristine SWCNT film and 0.3% Ru functionalized film. Charge–discharge response at current density of 10 A g^{-1}. (Dashed line) SWCNT film and (Solid line) 0.3% Ru-SWCNT film. The longer charge and discharge cycles for the functionalized film translates as an increase in capacitance.

equation 4.2, where m (13 μg cm^{-2}) is the active mass of the electrode, i is the current. $(dU/dt)^{-1}$ is the potential change with time:

$$C = i(dU/dt)^{-1}m^{-1} \quad 4.2$$

The increased capacitance caused by the addition of Ru_{Dim}^{4+} is a combination of double-layer capacitance and adsorption pseudocapacitance[156] with the introduction of faradaic pseudocapacitance. Double-layer capacitance is a function of the surface area of active mass available to ions in the electrolyte and scales with the simple parallel plate capacitor relationship 4.3, where A is the surface area (m^2), ε is the permativity of the medium (F m^{-1}) and d is the distance between charges.

$$C = \varepsilon A/d \quad 4.3$$

By controlling aggregation, the surface area of our functionalized and unfunctionalized electrodes is essentially the same. However, by binding Ru_{Dim}^{4+} to the walls of SWCNTs as they are processed in solution we embed +4 ions into normally inaccessible pores which can effectively increase the double-layer capacitance surface area within the electrode as the nanotubes are deposited.

4.7 SWCNT Quantum Dot Hybrid Nanocomposites

It was mentioned earlier in this chapter that it should be possible to fabricate hybrid nanocomposites (HNC) using the filtration method. One such HNC, shown in FIGURE 4.19, is a CdSe quantum dot—SWCNT composite electrode. This prototype electrode fabricated by the method described in section 4.3.2 was subjected to the standard electroanalytical tests described above and it exhibited some interesting phenomena. FIGURE 4.19b shows the orange hue that the QD electrode became at a potential of 2 V. In addition, during CD it was observed that

the QD containing electrode exhibited enhanced capacitance and charging during white light illumination. FIGURE 4.20 is the CD curves of the QD electrode discharging with a current of 1 μA after charging with the same current. The dark discharge shows a typical discharge curve. The black line is the same electrode during a second charge-discharge cycle in which white light was intermittently shined upon the surface.

4.8 Summary of Electrochemical Nanocomposite Study

This is a novel method to produce supercapacitor electrodes from SWCNT thin films and ruthenium coordination complexes. C_{sp} of 350 F g^{-1} is achieved by controlling the available surface area of the electrode during fabrication and by intercalating Ru_{Dim}^{4+} into the SWCNT film. This results in faradaic charge transfer with minimal amounts of expensive transition-metal material in the active mass. An important distinction of this design is that it incorporates no binders or harsh chemical functionalization of the SWCNTs that have been shown to inhibit the electrical and mechanical performance of SWCNTs. The SWCNTs and composites are processed from a stable dispersion in DMF and formed into uniform thin films. Due to our solution based methods, surface area to mass ratio can be controlled while the pristine SWCNT electrical and mechanical properties are preserved.

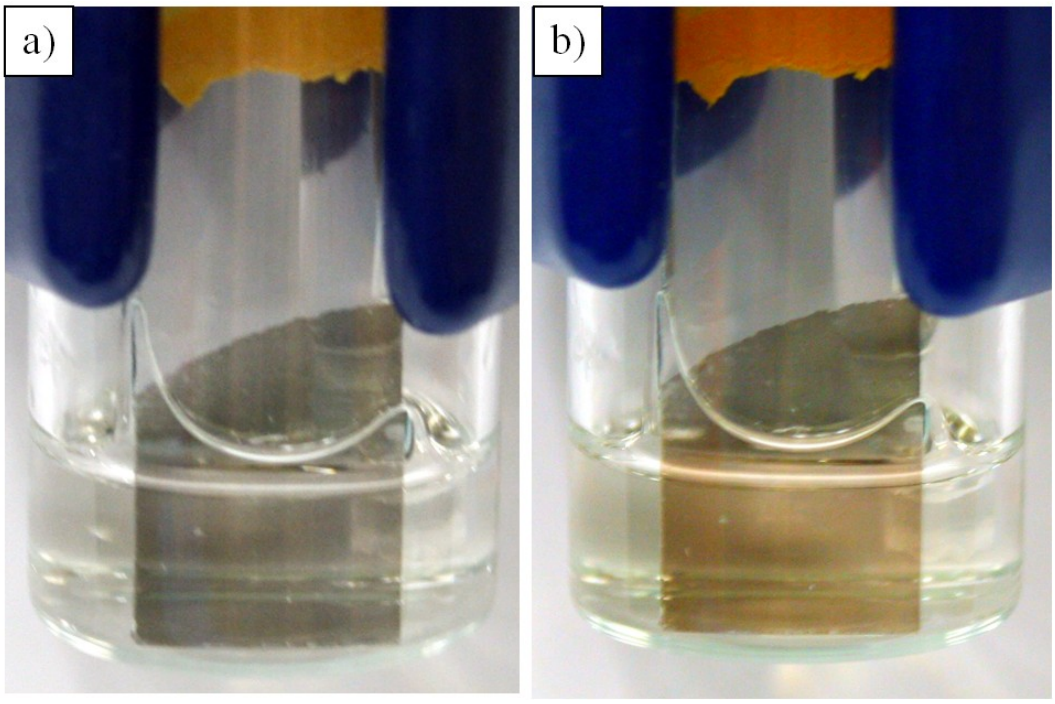

FIGURE 4.19. CdSe QD-SWCNT Thin Film Electrode. a) Electrode held at 0 V vs SHE. b) Electrode held at 2 V vs SHE.

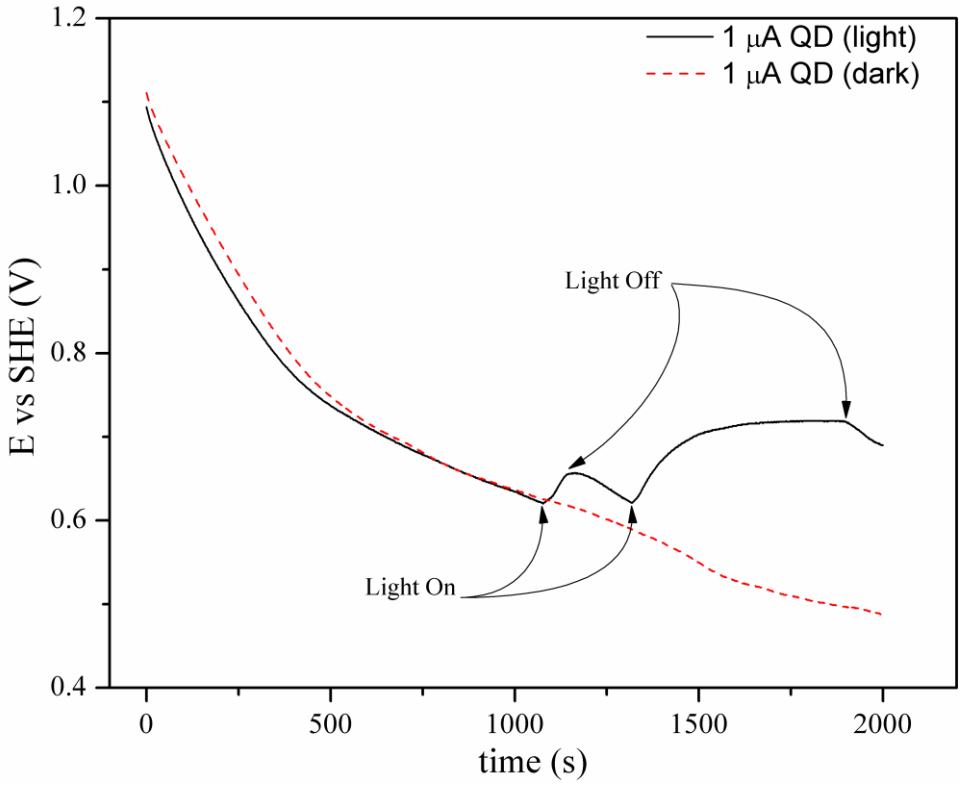

FIGURE 4.20. Galvanostatic discharce of a thin film CdSe quantum dot-SWCNT hybrid nanocomposite electrode. Discharge current was 1 μA. The dashed red line is the electrode discarging in the dark. The black line is the electrode discharging under periods of white light illumination, as noted by the arrows. .

CHAPTER 5: CONCLUSION

The use of carbon nanotubes (CNTs), both multi-wall carbon nanotubes (MWCNTs) and single-wall nanotubes (SWCNTs), is of major importance for the design and development of advanced technologies and the future of nanocomposites. In particular, great efforts are devoted to the production and the study of electrically conductive CNT nanocomposites that incorporate interesting molecules and nanomaterials. In conjunction, the development of new ruthenium complexes compliments the use of CNT electronics and they are hugely important components in the pursuit of solar and energy production technologies. The work described in this Ph.D. dissertation is clearly a contribution to these fields of research. It not only describes the novel synthesis of two new ruthenium coordination complexes, but also developed new and improved synthesis procedures for several precursor molecules that will aid future synthetic efforts.

The two novel ruthenium complexes synthesized during this work are $[Cl(trpy)Ru(tpphz)Ru(trpy)Cl](PF_6)_2$ and $[(phen)_2Ru(tpphz)Ru(trpy)Cl](PF_6)_3$. In the pursuit of these two complexes a new more efficient procedure was developed for the synthesis of dichlorotetrakis(dimethyl sulfoxide)Ruthenium. This complex has been an important precursor for a large percentage of ruthenium coordination complexes for many years. Confusion created by multiple reports for the synthesis of phendioxime was also cleared up during this synthesis work. A new and reliable

procedure has been established for the synthesis of phendiamine through the phendioxime intermediate.

In this dissertation isothermal titration calorimetry (ITC) has been established as a powerful analytical tool to measure the interaction thermodynamics of nanomaterials. This is of major importance since this tool is the first and only instrument that has directly measured the interaction thermodynamics of solvent and large molecules with SWCNTs. Furthermore, this technique appeared to be a valuable tool to gain insight into the exfoliation process of SWCNTs in aprotic dispersions in general. In particular, this technique improves on UV-Vis (van't Hoff) analysis with respect to understand the binding and interaction of our ruthenium coordination complexes with the walls of SWCNTs.

Based on the study of SWCNT-ruthenium complex interactions; generic knowledge was developed about the influence of these complexes on the aggregation and deposition of SWCNTs as they were formed into thin films. It is now understood that the addition of our dinuclear ruthenium complexes to a dispersion of SWCNTs initiates an equilibrium of adsorption (binding) and desorption to the walls of SWCNTs. These binding interactions can direct the assembly of SWCNTs as they are filtered out of solution to form thin films with drastically enhanced and inhibited electronic properties. It was demonstrated that our SWCNT thin film can be transferred to several different substrates and the resulting device can be used as a working electrode in an electrochemical system.

The work described in this dissertation was aimed at characterizing and studying the electrical properties and capacitance of the nanocomposites fabricated herein.

SWCNTs are an almost ideal electrode material. Experimental measurements of our nanocomposites show that the high binding enthalpy we measured between the ruthenium complexes and SWCNTs was an accurate predictor of some type of charge transfer ability between the two components. And not only was charge transferred between the molecular complex and SWCNTs, significant charge was stored within the electrode when compared to a pristine SWCNT film. This is an important discovery when one considers the high cost of ruthenium and ruthenium loading utilized in this work. And despite the low loading percent of ruthenium, the specific capacitance which was produced approached values that are typically achieved with much higher quantities of ruthenium in ruthenium oxide.

The techniques established in this dissertation provide the foundation to propel forward multiple lines of inquiry. Appendix E consists of two drawings which outline possible synthetic routes to unique ruthenium complexes. In the spirit of the work presented here, a neutrally charged dinuclear ruthenium complex is proposed. The use of which will allow a comparison of our groups studies with charged complexes to a ruthenium complex that has a similar structure but lacks ionic influences on binding and aggregation.

Work must continue with the ITC. There are a significant number of complexes, nanomaterials and solvent systems which can be thermodynamically characterized with this instrument. Systems that may be particularly interesting are ligand exchange reactions with ligand stabilized quantum dots as well as measuring the mixing enthalpy of SWCNTs in mixed solvent systems. The former would be an

important contribution to discussion about and the pursuit of an ideal CNT solvent system.

Finally, the preliminary work accomplished with SWCNT thin film electrodes and SWCNT-quantum dot hybrid nanocomposites is promising. As the different components of this dissertation are developed in the future, with more study, it will be possible to more fully understand the interaction of building blocks within nanocomposites. The work presented here shines a positive light on the use of SWCNT films as supercapacitor electodes as well as showing an application as a scaffold for other electrochemically interesting materials. Electrodes built by this design could have real world applications in electrochromic coatings and solar energy generation.

BIBLIOGRAPHY

1 Drexler, K. E. *Engines of Creation 2.0*. 20th Anniversary Edition edn, (WOWIO LLC. , 2006).

2 Chaturvedi, H. *et al.* "Mechanically Docked" Metallodendrimers About Single-Walled Carbon Nanotubes. *Journal of Physical Chemistry C* **113**, 11254-11261, doi:10.1021/jp902229v (2009).

3 Chaturvedi, H. & Poler, J. C. Binding of Rigid Dendritic Ruthenium Complexes to Carbon Nanotubes. *Journal of Physical Chemistry B* **110**, 22387-22393, doi:10.1021/jp061952f (2006).

4 Chaturvedi, H. & Poler, J. C. Photon Enhanced Aggregation of Single Walled Carbon Nanotube Dispersions. *Applied Physics Letters* **90**, 3, doi:10.1063/1.2744489 (2007).

5 Balzani, V., Bergamini, G. & Ceroni, P. From the Photochemistry of Coordination Compounds to Light-Powered Nanoscale Devices and Machines. *Coordination Chemistry Reviews* **252**, 2456-2469, doi:10.1016/j.ccr.2007.11.009 (2008).

6 Arachchige, S. M. *et al.* Design Considerations for a System for Photocatalytic Hydrogen Production from Water Employing Mixed-Metal Photochemical Molecular Devices for Photoinitiated Electron Collection. *Inorganic Chemistry* **48**, 1989-2000, doi:10.1021/ic8017387 (2009).

7 Balzani, V. *et al.* Designing Dendrimers Based on Transition Metal Complexes. Light-Harvesting Properties and Predetermined Redox Patterns. *Accounts of Chemical Research* **31**, 26-34 (1998).

8 MacDonnell, F. M., Kim, M. J. & Bodige, S. Substitutionally Inert Complexes as Chiral Synthons for Stereospecific Supramolecular Syntheses. *Coordination Chemistry Reviews* **185-6**, 535-549 (1999).

9 Giordano, A. N., Chaturvedi, H. & Poler, J. C. Critical Coagulation Concentrations for Carbon Nanotubes in Nonaqueous Solvent. *Journal of Physical Chemistry C* **111**, 11583-11589, doi:10.1021/jp0729866 (2007).

10 MacDonnell, F. M. & Bodige, S. Efficient Stereospecific Syntheses of Chiral Ruthenium Dimers. *Inorganic Chemistry* **35**, 5758-5759 (1996).

11 James, B. R., Ochiai, E. & Rempel, G. I. Ruthenium (Ii) Halide Dimethylsulphoxide Complexes from Hydrogenation Reactions. *Inorganic & Nuclear Chemistry Letters* **7**, 781 (1971).

12 Evans, I. P., Spencer, A. & Wilkinso.G. Dichlorotetrakis(Dimethyl Sulphoxide)Ruthenium(Ii) and Its Use as a Source Material for Some New Ruthenium(Ii) Complexes. *Journal of the Chemical Society-Dalton Transactions*, 204-209 (1973).

13 Alessio, E. *et al.* Synthesis, Molecular-Structure, and Chemical Behavior of Hydrogen Trans-Bis(Dimethyl Sulfoxide)Tetrachlororuthenate(Iii) and Mer-Trichlorotris(Dimethyl Sulfoxide)Ruthenium(Iii) - the 1st Fully Characterized Chloride Dimethyl-Sulfoxide Ruthenium(Iii) Complexes. *Inorganic Chemistry* **30**, 609-618 (1991).

14 Alessio, E. *et al.* Cis-Dihalotetrakis(Dimethyl Sulfoxide)Ruthenium(Ii) and Trans-Dihalotetrakis(Dimethyl Sulfoxide)Ruthenium(Ii) Complexes (Rux2(Dmso)4, X = Cl, Br) - Synthesis, Structure, and Antitumor-Activity. *Inorganic Chemistry* **27**, 4099-4106 (1988).

15 Alston, J. R., Kobayashi, S., Younts, T. J. & Poler, J. C. Synthesis and Characterization of Rigid +2 and +3 Heteroleptic Dinuclear Ruthenium(Ii) Complexes. *Polyhedron* **29**, 2696-2702, doi:DOI: 10.1016/j.poly.2010.06.012 (2010).

16 Ishow, E. *et al.* Tetranuclear Tetrapyrido[3,2-A : 2 ',3 '-C : 3 ",2 "-H : 2 '",3 '"-J]Phenazineruthenium Complex: Synthesis, Wide-Angle X-Ray Scattering, and Photophysical Studies. *Inorganic Chemistry* **37**, 3603-3609 (1998).

17 Lutterman, D. A., Rachford, A. A., Rack, J. J. & Turro, C. Theoretical Insight on the S -> O Photoisomerization of Dmso Complexes of Ru(Ii). *Journal of Physical Chemistry A* **113**, 11002-11006, doi:10.1021/jp903048n (2009).

18 Ziessel, R., Grosshenny, V., Hissler, M. & Stroh, C. Cis-[Ru(2,2 ': 6 ',2 "-Terpyridine)(Dmso)Cl-2]: Useful Precursor for the Synthesis of Heteroleptic Terpyridine Complexes under Mild Conditions. *Inorganic Chemistry* **43**, 4262-4271, doi:10.1021/ic049822d (2004).

19 Abeywickrama, C. & Baker, A. D. Efficient Synthesis of 1,4,5,12-Tetraazatriphenylene and Derivatives. *The Journal of Organic Chemistry* **69**, 7741-7744, doi:10.1021/jo0495283 (2004).

20 Bodige, S. & MacDonnell, F. M. Synthesis of Free and Ruthenium Coordinated 5,6-Diamino-1,10-Phenanthroline. *Tetrahedron Letters* **38**, 8159-8160 (1997).

21 Kleineweischede, A. & Mattay, J. Synthesis of Amino- and Bis(Bromomethyl)-Substitued Bi- and Tetradentate N-Heteroaromatic Ligands: Building Blocks for Pyrazino-Functionalized Fullerene Dyads.

European Journal of Organic Chemistry, 947-957, doi:10.1002/ejoc.200500548 (2006).

22 Dickeson, J. E. & Summers, L. A. Derivatives of 1,10-Phenanthroline-5,6-Quinone. *Australian Journal of Chemistry* **23**, 1023 (1970).

23 Hiort, C., Lincoln, P. & Norden, B. DNA-Binding of Delta-[Ru(Phen)2dppz]2+ and Lambda-[Ru(Phen)2dppz]2+. *Journal of the American Chemical Society* **115**, 3448-3454 (1993).

24 Bolger, J., Gourdon, A., Ishow, E. & Launay, J. P. Mononuclear and Binuclear Tetrapyrido[3,2-Alpha:2',3'-C:3",2'"-H:2'",3'"-J]Phenazine (Tpphz) Ruthenium and Osmium Complexes. *Inorganic Chemistry* **35**, 2937-2944 (1996).

25 Sullivan, B. P., Salmon, D. J. & Meyer, T. J. Mixed Phosphine 2,2'-Bipyridine Complexes of Ruthenium. *Inorganic Chemistry* **17**, 3334-3341 (1978).

26 Alessio, E. Synthesis and Reactivity of Ru-, Os-, Rh-, and Ir-Halide-Sulfoxide Complexes. *Chemical Reviews (Washington, DC, United States)* **104**, 4203-4242, doi:10.1021/cr0307291 (2004).

27 Jaswal, J. S., Rettig, S. J. & James, B. R. Ruthenium(Iii) Complexes Containing Dimethylsulfoxide or Dimethylsulfide Ligands, and a New Route to Trans-Dichlorotetrakis(Dimethylsulfoxide)Ruthenium(Ii). *Canadian Journal of Chemistry-Revue Canadienne De Chimie* **68**, 1808-1817 (1990).

28 Calligaris, M. Structure and Bonding in Metal Sulfoxide Complexes: An Update. *Coordination Chemistry Reviews* **248**, 351-375, doi:10.1016/j.ccr.2004.02.005 (2004).

29 Davies, J. A. in *Advances in Inorganic Chemistry* Vol. Volume 24 (eds H. J. Emeléus & A. G. Sharpe) 115-187 (Academic Press, 1981).

30 Bodige, S. *et al.* First-Generation Chiral Metallodendrimers: Stereoselective Synthesis of Rigid D-3-Symmetric Tetranuclear Ruthenium Complexes. *Journal of the American Chemical Society* **119**, 10364-10369 (1997).

31 Norrby, T. *et al.* Synthesis, Structure, and Photophysical Properties of Novel Ruthenium(Ii) Carboxypyridine Type Complexes. *Inorganic Chemistry* **36**, 5850-5858 (1997).

32 Ishow, E., Gourdon, A., Launay, J. P., Chiorboli, C. & Scandola, F. Synthesis, Mass Spectrometry, and Spectroscopic Properties of a Dinuclear

Ruthenium Complex Comprising a 20 Angstrom Long Fully Aromatic Bridging Ligand. *Inorganic Chemistry* **38**, 1504-1510 (1999).

33 Liu, Y. & Sturtevant, J. M. Significant Discrepancies between Van't Hoff and Calorimetric Enthalpies. Ii. *Protein Science* **4**, 2559-2561, doi:10.1002/pro.5560041212 (1995).

34 Jelesarov, I. & Bosshard, H. R. Isothermal Titration Calorimetry and Differential Scanning Calorimetry as Complementary Tools to Investigate the Energies of Biomolecular Recognition. *Journal of Molecular Recognition* **12**, 3-18 (1999).

35 Velazquez-Campoy, A., Ohtaka, H., Nezami, A., Muzammil, S. & Freire, E. in *Current Protocols in Cell Biology* 17.18.11 - 17.18.24 (John Wiley & Sons, Inc., 2004).

36 Velázquez Campoy, A. & Freire, E. Itc in the Post-Genomic Era...? Priceless. *Biophysical Chemistry* **115**, 115-124 (2005).

37 Paul, E. L., Atiemo-Obeng, V. A. & Kresta, S. M. *Handbook of Industrial Mixing Science and Practice*, <http://www.knovel.com/knovel2/Toc.jsp?BookID=1455> (2004).

38 Yang, J., Wang, K., Driver, J., Yang, J. & Barron, A. R. The Use of Fullerene Substituted Phenylalanine Amino Acid as a Passport for Peptides through Cell Membranes. *Organic & Biomolecular Chemistry* **5**, 260-266 (2007).

39 Kim, B. & Sigmund, W. M. Functionalized Multiwall Carbon Nanotube/Gold Nanoparticle Composites. *Langmuir* **20**, 8239-8242, doi:10.1021/la049424n (2004).

40 Bei, F. L., Hou, X. L., Chang, S. L. Y., Simon, G. P. & Li, D. Interfacing Colloidal Graphene Oxide Sheets with Gold Nanoparticles. *Chemistry-a European Journal* **17**, 5958-5964, doi:10.1002/chem.201003602 (2011).

41 Georgakilas, V. *et al.* Decorating Carbon Nanotubes with Metal or Semiconductor Nanoparticles. *Journal of Materials Chemistry* **17**, 2679-2694 (2007).

42 Auciello, O. & Sumant, A. V. Status Review of the Science and Technology of Ultrananocrystalline Diamond (Uncd (Tm)) Films and Application to Multifunctional Devices. *Diamond and Related Materials* **19**, 699-718, doi:10.1016/j.diamond.2010.03.015 (2010).

43 Colbert, D. T. & Smalley, R. E. Fullerene Nanobutes for Molecular Electronics. *Trends in Biotechnology* **17**, 46-50, doi:10.1016/s0167-7799(98)01256-6 (1999).

44 Martinez-Hernandez, A. L., Velasco-Santos, C. & Castano, V. M. Carbon Nanotubes Composites: Processing, Grafting and Mechanical and Thermal Properties. *Current Nanoscience* **6**, 12-39 (2010).

45 Xu, B. *et al.* Single-Walled Carbon Nanotubes as Electrode Materials for Supercapacitors. *Chinese Journal of Chemistry* **24**, 1505-1508 (2006).

46 Moore, V. C. *et al.* Individually Suspended Single-Walled Carbon Nanotubes in Various Surfactants. *Nano Letters* **3**, 1379-1382, doi:10.1021/nl034524j (2003).

47 Bergin, S. D. *et al.* Towards Solutions of Single-Walled Carbon Nanotubes in Common Solvents. *Advanced Materials (Weinheim, Germany)* **20**, 1876-1881, doi:10.1002/adma.200702451 (2008).

48 Wong, E. W., Sheehan, P. E. & Lieber, C. M. Nanobeam Mechanics: Elasticity, Strength, and Toughness of Nanorods and Nanotubes. *Science* **277**, 1971-1975, doi:10.1126/science.277.5334.1971 (1997).

49 Yu, M.-F. *et al.* Strength and Breaking Mechanism of Multiwalled Carbon Nanotubes under Tensile Load. *Science* **287**, 637-640, doi:10.1126/science.287.5453.637 (2000).

50 Heller, D. A. *et al.* Multimodal Optical Sensing and Analyte Specificity Using Single-Walled Carbon Nanotubes. *Nature Nanotechnology* **4**, 114-120, doi:10.1038/nnano.2008.369 (2009).

51 Cadek, M. *et al.* Reinforcement of Polymers with Carbon Nanotubes: The Role of Nanotube Surface Area. *Nano Letters* **4**, 353-356, doi:10.1021/nl035009o (2004).

52 Kaempgen, M., Duesberg, G. S. & Roth, S. Transparent Carbon Nanotube Coatings. *Applied Surface Science* **252**, 425-429, doi:10.1016/j.apsusc.2005.01.020 (2005).

53 Lee, C. H., Johnson, N., Drelich, J. & Yap, Y. K. The Performance of Superhydrophobic and Superoleophilic Carbon Nanotube Meshes in Water-Oil Filtration. *Carbon* **49**, 669-676 (2011).

54 Rana, S., Alagirusamy, R. & Joshi, M. A Review on Carbon Epoxy Nanocomposites. *Journal of Reinforced Plastics and Composites* **28**, 461-487, doi:10.1177/0731684407085417 (2009).

55 Tan, Y. & Resasco, D. E. Dispersion of Single-Walled Carbon Nanotubes of Narrow Diameter Distribution. *Journal of Physical Chemistry B* **109**, 14454-14460, doi:10.1021/jp052217r (2005).

56 Baughman, R. H., Zakhidov, A. A. & de Heer, W. A. Carbon Nanotubes—the Route toward Applications. *Science* **297**, 787 (2002).

57 Peigney, A., Laurent, C., Flahaut, E., Bacsa, R. R. & Rousset, A. Specific Surface Area of Carbon Nanotubes and Bundles of Carbon Nanotubes. *Carbon* **39**, 507-514 (2001).

58 Ando, T. The Electronic Properties of Graphene and Carbon Nanotubes. *NPG Asia Materials*, 17-21 (2009).

59 Capek, I. Dispersions, Novel Nanomaterial Sensors and Nanoconjugates Based on Carbon Nanotubes. *Advances in Colloid and Interface Science* **150**, 63-89, doi:DOI: 10.1016/j.cis.2009.05.006 (2009).

60 Forney, M. W. & Poler, J. C. Sonochemical Formation of Methyl Hydroperoxide in Polar Aprotic Solvents and Its Effect on Single-Walled Carbon Nanotube Dispersion Stability. *Journal of the American Chemical Society* **132**, 791-797, doi:10.1021/ja9085462 (2010).

61 Forney, M. W. & Poler, J. C. Significantly Enhanced Single-Walled Carbon Nanotube Dispersion Stability in Mixed Solvent Systems. *Journal of Physical Chemistry C* **115**, 10531-10536, doi:10.1021/jp202559m (2011).

62 Giordani, S. *et al.* Debundling of Single-Walled Nanotubes by Dilution: Observation of Large Populations of Individual Nanotubes in Amide Solvent Dispersions. *Journal of Physical Chemistry B* **110**, 15708-15718, doi:10.1021/jp0626216 (2006).

63 Mizoue, L. S. & Tellinghuisen, J. Calorimetric Vs. Van't Hoff Binding Enthalpies from Isothermal Titration Calorimetry: Ba2+-Crown Ether Complexation. *Biophysical Chemistry* **110**, 15-24 (2004).

64 Arnaud, A. & Bouteiller, L. Isothermal Titration Calorimetry of Supramolecular Polymers. *Langmuir* **20**, 6858-6863, doi:10.1021/la049365d (2004).

65 Weber, A., Dettling, M., Brunner, H. & Tovar, G. E. M. Isothermal Titration Calorimetry of Molecularly Imprinted Polymer Nanospheres. *Macromolecular Rapid Communications* **23**, 824-828 (2002).

66 Lindman, S. *et al.* Systematic Investigation of the Thermodynamics of Hsa Adsorption to N-Iso-Propylacrylamide/N-Tert-Butylacrylamide Copolymer

Nanoparticles. Effects of Particle Size and Hydrophobicity. *Nano Letters* **7**, 914-920, doi:10.1021/nl062743+ (2007).

67 Cedervall, T. *et al.* Understanding the Nanoparticle–Protein Corona Using Methods to Quantify Exchange Rates and Affinities of Proteins for Nanoparticles. *Proceedings of the National Academy of Sciences of the United States of America* **104**, 2050-2055, doi:10.1073/pnas.0608582104 (2007).

68 Meister, A. *et al.* Helical Nanofibers of Self-Assembled Bipolar Phospholipids as Template for Gold Nanoparticles. *Journal of Physical Chemistry B* **112**, 4506-4511, doi:10.1021/jp710119j (2008).

69 Das, A. *et al.* Binding of Nucleobases with Single-Walled Carbon Nanotubes: Theory and Experiment. *Chemical Physics Letters* **453**, 266-273, doi:10.1016/j.cplett.2008.01.057 (2008).

70 Marquis, R., Greco, C., Schultz, P., Meunier, S. & Mioskowski, C. Isothermal Microcalorimetry, a Tool for Probing Swnt Bundles. *Journal of Nanoscience and Nanotechnology* **9**, 6777-6782, doi:10.1166/jnn.2009.1319 (2009).

71 Chiad, K. *et al.* Isothermal Titration Calorimetry: A Powerful Technique to Quantify Interactions in Polymer Hybrid Systems. *Macromolecules* **42**, 7545-7552, doi:10.1021/ma9008912 (2009).

72 Varghese, N. *et al.* Binding of DNA Nucleobases and Nucleosides with Graphene. *ChemPhysChem* **10**, 206-210, doi:10.1002/cphc.200800459 (2009).

73 Varghese, N., Ghosh, A., Voggu, R., Ghosh, S. & Rao, C. N. R. Selectivity in the Interaction of Electron Donor and Acceptor Molecules with Graphene and Single-Walled Carbon Nanotubes. *Journal of Physical Chemistry C* **113**, 16855-16859, doi:10.1021/jp9075355 (2009).

74 Coleman, J. N. Liquid-Phase Exfoliation of Nanotubes and Graphene. *Advanced Functional Materials* **19**, 3680-3695, doi:10.1002/adfm.200901640 (2009).

75 Fini, P. & Castagnolo, M. Determination of Enthalpic Interaction Coefficients by Itc Measurements. 2-Hydroxypropyl-B-Cyclodextrin in Aqueous Solution of Nacl. *Journal of Thermal Analysis and Calorimetry* **66**, 91-102, doi:10.1023/a:1012435631222 (2001).

76 McMillan, W. G. & Mayer, J. E. The Statistical Thermodynamics of Multicomponent Systems. *Journal of Chemical Physics* **13**, 276-305, doi:10.1063/1.1724036 (1945).

77 Zhang, H., Hu, X. & Shao, S. Enthalpies of Dilution of L-Alanine in Dimethylsulfoxide + Water and Dimethylformamide + Water Mixtures at 298.15 K. *Journal of Chemical and Engineering Data* **55**, 941-946, doi:10.1021/je9005322 (2009).

78 Bloemendal, M., Marcus, Y., Booij, M., Hofstee, R. & Somsen, G. Enthalpies of Solution and Solvation of Amides in N,N-Dimethylformamide: Application of the Random Contact Point Approach. *Journal of Solution Chemistry* **17**, 15-33, doi:10.1007/bf00651850 (1988).

79 Wiseman, T., Williston, S., Brandts, J. F. & Lin, L.-N. Rapid Measurement of Binding Constants and Heats of Binding Using a New Titration Calorimeter. *Analytical Biochemistry* **179**, 131-137, doi:Doi: 10.1016/0003-2697(89)90213-3 (1989).

80 Bergin, S. D. *et al.* Multicomponent Solubility Parameters for Single-Walled Carbon Nanotube−Solvent Mixtures. *ACS Nano* **3**, 2340-2350, doi:10.1021/nn900493u (2009).

81 Ajayan, P. M., Schadler, L. S. & Braun, P. V. *Nanocomposite Science and Technology*. (Wiley-VCH Verlag GmbH & Co. KGaA, 2003).

82 Balzani, V. Molecular Devices and Machines. *ChemPhysChem* **10**, 21-21 (2009).

83 Merhari, L. *Hybrid Nanocomposites for Nanotechnology: Electronic, Optical, Magnetic and Biomedical Applications*. 1st edn, (Springer, 2009).

84 Merkoci, A. *et al.* New Materials for Electrochemical Sensing Vi: Carbon Nanotubes. *Trac-Trends in Analytical Chemistry* **24**, 826-838, doi:10.1016/j.trac.2005.03.019 (2005).

85 Paul, D. R. & Robeson, L. M. Polymer Nanotechnology: Nanocomposites. *Polymer* **49**, 3187-3204, doi:10.1016/j.polymer.2008.04.017 (2008).

86 Bottari, G., de la Torre, G., Guldi, D. M. & Torres, T. s. Covalent and Noncovalent Phthalocyanine−Carbon Nanostructure Systems: Synthesis, Photoinduced Electron Transfer, and Application to Molecular Photovoltaics. *Chemical Reviews (Washington, DC, United States)*, doi:10.1021/cr900254z (2010).

87 Guldi, D. M., Rahman, G. M. A., Jux, N., Tagmatarchis, N. & Prato, M. Integrating Single-Wall Carbon Nanotubes into Donor-Acceptor Nanohybrids. *Angewandte Chemie-International Edition* **43**, 5526-5530, doi:10.1002/anie.200461217 (2004).

88 Alston, J. R., Kobayashi, S., Younts, T. J. & Poler, J. C. Synthesis and Characterization of Rigid +2 and +3 Heteroleptic Dinuclear Ruthenium(Ii) Complexes. *Polyhedron* **In Press, Accepted Manuscript**, doi:DOI: 10.1016/j.poly.2010.06.012.

89 MacDonnell, F. M., Kim, M.-J., Wouters, K. L. & Konduri, R. Hierarchical Structure in Assemblies of Enantiopure Ruthenium Trisdiimine Complexes: A Biomimetic Approach Utilizing Primary, Secondary, Tertiary and Quaternary Structural Elements. *Coordination Chemistry Reviews* **242**, 47-58 (2003).

90 Gratzel, M. Photoelectrochemical Cells. *Nature* **414**, 338-344 (2001).

91 Guldi, D. M. *et al.* Donor-Acceptor Nanoensembles of Soluble Carbon Nanotubes. *Chemical Communications (Cambridge, United Kingdom)*, 2034-2035, doi:10.1039/b406933a (2004).

92 Welter, S., Brunner, K., Hofstraat, J. W. & De Cola, L. Electroluminescent Device with Reversible Switching between Red and Green Emission. *Nature* **421**, 54-57 (2003).

93 Yu, J. X., Mathew, S., Flavel, B. S., Johnston, M. R. & Shapter, J. G. Ruthenium Porphyrin Functionalized Single-Walled Carbon Nanotube Arrays - a Step toward Light Harvesting Antenna and Multibit Information Storage. *Journal of the American Chemical Society* **130**, 8788-8796, doi:10.1021/ja801142k (2008).

94 Baranauskienė, L., Petrikaitė, V., Matulienė, J. & Matulis, D. Titration Calorimetry Standards and the Precision of Isothermal Titration Calorimetry Data. *International Journal of Molecular Sciences* **10**, 2752-2762 (2009).

95 Brown, A. Analysis of Cooperativity by Isothermal Titration Calorimetry. *International Journal of Molecular Sciences* **10**, 3457-3477 (2009).

96 Saboury, A. Binding Isotherm Determination by Isothermal Titration Calorimetry. *Journal of Thermal Analysis and Calorimetry* **77**, 997-1004 (2004).

97 Allen, S. J., Gan, Q., Matthews, R. & Johnson, P. A. Comparison of Optimised Isotherm Models for Basic Dye Adsorption by Kudzu. *Bioresource Technology* **88**, 143-152 (2003).

98 Chen, W., Duan, L. & Zhu, D. Adsorption of Polar and Nonpolar Organic Chemicals to Carbon Nanotubes. *Environmental Science and Technology* **41**, 8295-8300, doi:10.1021/es071230h (2007).

99 Furuya, E. G., Chang, H. T., Miura, Y. & Noll, K. E. A Fundamental Analysis of the Isotherm for the Adsorption of Phenolic Compounds on Activated Carbon. *Separation and Purification Technology* **11**, 69-78 (1997).

100 Jiang, J. W. & Sandler, S. I. Nitrogen Adsorption on Carbon Nanotube Bundles: Role of the External Surface. *Physical Review B* **68**, doi:10.1103/PhysRevB.68.245412 (2003).

101 Kinniburgh, D. G. General Purpose Adsorption Isotherms. *Environmental Science and Technology* **20**, 895-904, doi:10.1021/es00151a008 (1986).

102 Skopp, J. Derivation of the Freundlich Adsorption Isotherm from Kinetics. *Journal of Chemical Education* **86**, 1341-null, doi:10.1021/ed086p1341 (2009).

103 Tóth, J. in *Encyclopedia of Surface and Colloid Science: Second Edition* 279 - 294 (Taylor & Francis, 2006).

104 Jensen, C. R. C. & Seaton, N. A. An Isotherm Equation for Adsorption to High Pressures in Microporous Adsorbents. *Langmuir* **12**, 2866-2867, doi:10.1021/la9509460 (1996).

105 Caceci, M. S. Estimating Error Limits in Parametric Curve Fitting. *Analytical Chemistry* **61**, 2324-2327, doi:10.1021/ac00195a023 (1989).

106 Efron, B. & Gong, G. A Leisurely Look at the Bootstrap, the Jackknife, and Cross-Validation. *The American Statistician* **37**, 36-48, doi:citeulike-article-id:371867 (1983).

107 Reibold, M. *et al.* Materials: Carbon Nanotubes in an Ancient Damascus Sabre. *Nature* **444**, 286-286, doi:10.1038/444286a (2006).

108 Iijima, S. Helical Microtubules of Graphitic Carbon. *Nature* **354**, 56-58 (1991).

109 Cai, H., Cao, X. N., Jiang, Y., He, P. G. & Fang, Y. Z. Carbon Nanotube-Enhanced Electrochemical DNA Biosensor for DNA Hybridization Detection. *Analytical and Bioanalytical Chemistry* **375**, 287-293, doi:10.1007/s00216-002-1652-9 (2003).

110 Ye, J. S. *et al.* Selective Voltammetric Detection of Uric Acid in the Presence of Ascorbic Acid at Well-Aligned Carbon Nanotube Electrode. *Electroanalysis* **15**, 1693-1698, doi:10.1002/elan.200302752 (2003).

111 Zhao, Y. D., Zhang, W. D., Luo, Q. M. & Li, S. F. Y. The Oxidation and Reduction Behavior of Nitrite at Carbon Nanotube Powder Microelectrodes. *Microchemical Journal* **75**, 189-198 (2003).

112 Rocha, C. G., Wall, A. & Ferreira, M. S. Electronic Properties of Nanotube-Based Sensors: An Inverse Modeling Approach. *EPL* **82**, 5, doi:10.1209/0295-5075/82/27004 (2008).

113 Chen, R. J. *et al.* Molecular Photodesorption from Single-Walled Carbon Nanotubes. *Applied Physics Letters* **79**, 2258-2260 (2001).

114 Newson, R. W., Menard, J. M., Sames, C., Betz, M. & van Driel, H. M. Coherently Controlled Ballistic Charge Currents Injected in Single-Walled Carbon Nanotubes and Graphite. *Nano Letters* **8**, 1586-1589, doi:10.1021/nl0733051 (2008).

115 Pumera, M., Merkoci, A. & Alegret, S. Carbon Nanotube-Epoxy Composites for Electrochemical Sensing. *Sensors and Actuators B-Chemical* **113**, 617-622, doi:10.1016/j.snb.2005.07.010 (2006).

116 Iijima, S. & Ichihashi, T. Single-Shell Carbon Nanotubes of 1-Nm Diameter. *Nature* **363**, 603-605 (1993).

117 Zhu, L. B., Xiu, Y. H., Hess, D. W. & Wong, C. P. Aligned Carbon Nanotube Stacks by Water-Assisted Selective Etching. *Nano Letters* **5**, 2641-2645, doi:10.1021/nl051906b (2005).

118 Naureen, S., Sanatinia, R., Shahid, N. & Anand, S. High Optical Quality Inp-Based Nanopillars Fabricated by a Top-Down Approach. *Nano Letters* **11**, 4805-4811, doi:10.1021/nl202628m (2011).

119 Chaste, J. *et al.* Single Carbon Nanotube Transistor at Ghz Frequency. *Nano Letters* **8**, 525-528, doi:10.1021/nl0727361 (2008).

120 Wang, S. D. & Grifoni, M. Schottky-Barrier Double-Walled Carbon-Nanotube Field-Effect Transistors. *Physical Review B* **76**, 4, doi:033413

Artn 033413 (2007).

121 Pint, C. L., Xu, Y.-Q., Pasquali, M. & Hauge, R. H. Formation of Highly Dense Aligned Ribbons and Transparent Films of Single-Walled Carbon Nanotubes Directly from Carpets. *ACS Nano* **2**, 1871-1878 (2008).

122 Behnam, A., Guo, J. & Ural, A. Effects of Nanotube Alignment and Measurement Direction on Percolation Resistivity in Single-Walled Carbon Nanotube Films. *Journal of Applied Physics* **102**, 7, doi:10.1063/1.2769953 (2007).

123 de Andrade, M. J., Lima, M. D., Skakalova, V., Bergmann, C. P. & Roth, S. Electrical Properties of Transparent Carbon Nanotube Networks Prepared through Different Techniques. *Physica Status Solidi-Rapid Research Letters* **1**, 178-180, doi:10.1002/pssr.200701115 (2007).

124 Gonnet, P. *et al.* Thermal Conductivity of Magnetically Aligned Carbon Nanotube Buckypapers and Nanocomposites. *Current Applied Physics* **6**, 119-122, doi:10.1016/j.cap.2005.01.053 (2006).

125 Gupta, S., Hughes, M., Windle, A. H. & Robertson, J. In Situ Raman Spectro-Electrochemistry Study of Single-Wall Carbon Nanotube Mat. *Diamond and Related Materials* **13**, 1314-1321, doi:10.1016/j.diamond.2003.10.015 (2004).

126 Kavan, L. *et al.* In Situ Raman Spectroelectrochemistry of Single-Walled Carbon Nanotubes: Investigation of Materials Enriched with (6,5) Tubes. *Journal of Physical Chemistry C* **112**, 14179-14187, doi:10.1021/jp800481b (2008).

127 Kazaoui, S., Minami, N., Nalini, B., Kim, Y. & Hara, K. Near-Infrared Photoconductive and Photovoltaic Devices Using Single-Wall Carbon Nanotubes in Conductive Polymer Films. *Journal of Applied Physics* **98**, 6, doi:10.1063/1.2113419 (2005).

128 Lima, M. D., de Andrade, M. J., Bergmann, C. P. & Roth, S. Thin, Conductive, Carbon Nanotube Networks over Transparent Substrates by Electrophoretic Deposition. *Journal of Materials Chemistry* **18**, 776-779, doi:10.1039/b713054f (2008).

129 Liu, C. Y., Bard, A. J., Wudl, F., Weitz, I. & Heath, J. R. Electrochemical Characterization of Films of Single-Walled Carbon Nanotubes and Their Possible Application in Supercapacitors. *Electrochemical and Solid State Letters* **2**, 577-578 (1999).

130 Merchant, C. A. & Markovic, N. Effects of Diffusion on Photocurrent Generation in Single-Walled Carbon Nanotube Films. *Applied Physics Letters* **92**, 3, doi:10.1063/1.2949742 (2008).

131 Ng, M. H. A., Hartadi, L. T., Tan, H. & Poa, C. H. P. Efficient Coating of Transparent and Conductive Carbon Nanotube Thin Films on Plastic

Substrates. *Nanotechnology* **19**, 5, doi:10.1088/0957-4484/19/20/205703 (2008).

132 Song, Y. I., Yang, C. M., Kim, D. Y., Kanoh, H. & Kaneko, K. Flexible Transparent Conducting Single-Wall Carbon Nanotube Film with Network Bridging Method. *Journal of Colloid and Interface Science* **318**, 365-371, doi:10.1016/j.jcis.2007.10.051 (2008).

133 Takenobu, T. *et al.* High-Performance Transparent Flexible Transistors Using Carbon Nanotube Films. *Applied Physics Letters* **88**, 3, doi:10.1063/1.2166693 (2006).

134 Wang, D., Song, P. C., Liu, C. H., Wu, W. & Fan, S. S. Highly Oriented Carbon Nanotube Papers Made of Aligned Carbon Nanotubes. *Nanotechnology* **19**, 6, doi:10.1088/0957-4484/19/7/075609 (2008).

135 Wu, Z. C. *et al.* Transparent, Conductive Carbon Nanotube Films. *Science* **305**, 1273-1276 (2004).

136 Zhang, X. F., Sreekumar, T. V., Liu, T. & Kumar, S. Properties and Structure of Nitric Acid Oxidized Single Wall Carbon Nanotube Films. *Journal of Physical Chemistry B* **108**, 16435-16440, doi:10.1021/jp0475988 (2004).

137 Zhu, H. W. & Wei, B. Q. Assembly and Applications of Carbon Nanotube Thin Films. *Journal of Materials Science & Technology* **24**, 447-456 (2008).

138 Deck, C. P., Flowers, J., McKee, G. S. B. & Vecchio, K. Mechanical Behavior of Ultralong Multiwalled Carbon Nanotube Mats. *Journal of Applied Physics* **101**, 9, doi:10.1063/1.2426940 (2007).

139 Sun, J. L., Xu, J., Zhu, J. L. & Li, B. L. Disordered Multiwalled Carbon Nanotube Mat for Light Spot Position Detecting. *Applied Physics a-Materials Science & Processing* **91**, 229-233, doi:10.1007/s00339-008-4398-1 (2008).

140 Rinzler, A. G. *et al.* Large-Scale Purification of Single-Wall Carbon Nanotubes: Process, Product, and Characterization. *Applied Physics a-Materials Science & Processing* **67**, 29-37 (1998).

141 Whitby, R. L. D., Fukuda, T., Maekawa, T., James, S. L. & Mikhalovsky, S. V. Geometric Control and Tuneable Pore Size Distribution of Buckypaper and Buckydiscs. *Carbon* **46**, 949-956, doi:10.1016/j.carbon.2008.02.028 (2008).

142 Lu, S. X. & Panchapakesan, B. Photoconductivity in Single Wall Carbon Nanotube Sheets. *Nanotechnology* **17**, 1843-1850, doi:10.1088/0957-4484/17/8/006 (2006).

143 Beecher, P. *et al.* Ink-Jet Printing of Carbon Nanotube Thin Film Transistors. *Journal of Applied Physics* **102**, 7, doi:10.1063/1.2770835 (2007).

144 Artukovic, E., Kaempgen, M., Hecht, D. S., Roth, S. & GrUner, G. Transparent and Flexible Carbon Nanotube Transistors. *Nano Letters* **5**, 757-760, doi:10.1021/nl0505254o (2005).

145 Boccaccini, A. R. *et al.* Electrophoretic Deposition of Carbon Nanotubes. *Carbon* **44**, 3149-3160, doi:10.1016/j.carbon.2006.06.021 (2006).

146 Du, C. S., Heldbrant, D. & Pan, N. Preparation and Preliminary Property Study of Carbon Nanotubes Films by Electrophoretic Deposition. *Materials Letters* **57**, 434-438 (2002).

147 Guo, Z. H., Wood, J. A., Huszarik, K. L., Yan, X. H. & Docoslis, A. Ac Electric Field-Induced Alignment and Long-Range Assembly of Multi-Wall Carbon Nanotubes inside Aqueous Media. *Journal of Nanoscience and Nanotechnology* **7**, 4322-4332, doi:10.1166/jnn.2007.871 (2007).

148 Poulin, P., Vigolo, B. & Launois, P. Films and Fibers of Oriented Single Wall Nanotubes. *Carbon* **40**, 1741-1749 (2002).

149 Thomas, B. J. C. *et al.* in *Electrophoretic Deposition: Fundamentals and Applications Ii* Vol. 314 *Key Engineering Materials* (ed A. R. VanderBiest O. Clasen R. Boccaccini) 141-146 (Trans Tech Publications Ltd, 2006).

150 Wang, L. L., Chen, Y. W., Chen, T., Que, W. X. & Sun, Z. Optimization of Field Emission Properties of Carbon Nanotubes Cathodes by Electrophoretic Deposition. *Materials Letters* **61**, 1265-1269, doi:10.1016/j.matlet.2006.07.011 (2007).

151 Zhao, H. F., Song, H., Li, Z. M., Yuan, G. & Jin, Y. X. Electrophoretic Deposition and Field Emission Properties of Patterned Carbon Nanotubes. *Applied Surface Science* **251**, 242-244, doi:10.1016/j.apsusc.2005.03.202 (2005).

152 Zhang, M. *et al.* Strong, Transparent, Multifunctional, Carbon Nanotube Sheets. *Science* **309**, 1215-1219, doi:10.1126/science.1115311 (2005).

153 Nasibulin, A. G. *et al.* Multifunctional Free-Standing Single-Walled Carbon Nanotube Films. *ACS Nano* **5**, 3214-3221, doi:10.1021/nn200338r (2011).

154 Xiao, L. *et al.* Flexible, Stretchable, Transparent Carbon Nanotube Thin Film Loudspeakers. *Nano Letters* **8**, 4539-4545, doi:10.1021/nl802750z (2008).

155 Frackowiak, E. & Béguin, F. Carbon Materials for the Electrochemical Storage of Energy in Capacitors. *Carbon* **39**, 937-950, doi:Doi: 10.1016/s0008-6223(00)00183-4 (2001).

156 Conway, B. E., Birss, V. & Wojtowicz, J. The Role and Utilization of Pseudocapacitance for Energy Storage by Supercapacitors. *Journal of Power Sources* **66**, 1-14, doi:Doi: 10.1016/s0378-7753(96)02474-3 (1997).

157 Kim, H. & Popov, B. N. Characterization of Hydrous Ruthenium Oxide/Carbon Nanocomposite Supercapacitors Prepared by a Colloidal Method. *Journal of Power Sources* **104**, 52-61, doi:Doi: 10.1016/s0378-7753(01)00903-x (2002).

158 Zheng, J. P. Ruthenium Oxide-Carbon Composite Electrodes for Electrochemical Capacitors. *Electrochemical and Solid-State Letters* **2**, 359-361, doi:10.1149/1.1390837 (1999).

159 Deng, G. H. *et al.* A New Method to Prepare Ruo2 · xh2o/Carbon Nanotube Composite for Electrochemical Capacitors. *Carbon* **43**, 1566-1569, doi:DOI: 10.1016/j.carbon.2004.12.031 (2005).

160 Frackowiak, E., Khomenko, V., Jurewicz, K., Lota, K. & Béguin, F. Supercapacitors Based on Conducting Polymers/Nanotubes Composites. *Journal of Power Sources* **153**, 413-418 (2006).

161 Cheng, Q. *et al.* Graphene and Nanostructured Mno2 Composite Electrodes for Supercapacitors. *Carbon* **In Press, Corrected Proof**, doi:DOI: 10.1016/j.carbon.2011.02.068.

162 Gao, F. L., Zhang, L. J. & Huang, S. M. Fabrication Horizontal Aligned Moo2/Single-Walled Carbon Nanotube Nanowires for Electrochemical Supercapacitor. *Materials Letters* **64**, 537-540, doi:10.1016/j.matlet.2009.11.069 (2010).

163 Kim, I.-H., Kim, J.-H., Lee, Y.-H. & Kim, K.-B. Synthesis and Characterization of Electrochemically Prepared Ruthenium Oxide on Carbon Nanotube Film Substrate for Supercapacitor Applications. *Journal of the Electrochemical Society* **152**, A2170-A2178, doi:10.1149/1.2041147 (2005).

164 Kim, I.-H. & Kim, K.-B. Ruthenium Oxide Thin Film Electrodes for Supercapacitors. *Electrochemical and Solid-State Letters* **4**, A62-A64, doi:10.1149/1.1359956 (2001).

165 Conway, B. E. & Pell, W. G. Double-Layer and Pseudocapacitance Types of Electrochemical Capacitors and Their Applications to the Development of Hybrid Devices. *Journal of Solid State Electrochemistry* **7**, 637-644, doi:10.1007/s10008-003-0395-7 (2003).

166 Campagna, S., Serroni, S., Bodige, S. & MacDonnell, F. M. Absorption Spectra, Photophysical Properties, and Redox Behavior of Stereochemically Pure Dendritic Ruthenium(Ii) Tetramers and Related Dinuclear and Mononuclear Complexes. *Inorganic Chemistry* **38**, 692-701 (1999).

167 Chen, J. H. *et al.* Electrochemical Characterization of Carbon Nanotubes as Electrode in Electrochemical Double-Layer Capacitors. *Carbon* **40**, 1193-1197, doi:Doi: 10.1016/s0008-6223(01)00266-4 (2002).

168 Lin, Z. *et al.* Superior Capacitance of Functionalized Graphene. *The Journal of Physical Chemistry C* **115**, 7120-7125, doi:10.1021/jp2007073 (2011).

169 Dresselhaus, M. S., Dresselhaus, G. & Jorio, A. Unusual Properties and Structure of Carbon Nanotubes. *Annual Review of Materials Research* **34**, 247-278, doi:doi:10.1146/annurev.matsci.34.040203.114607 (2004).

170 Arepalli, S., Freiman, S. W., Hooker, S. & Migler, K. Measurement Issues in Single-Wall Carbon Nanotubes. 72 (NIST, March 15, 2008).

APPENDIX A: OXIME CHEMISTRY

The synthesis of an oxime involves a condensation reaction between a carbonyl and hydroxylamine. Oximes, in organic chemistry are compounds containing the functional group pictured in (FIGURE A.1).

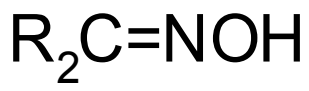

FIGURE A.1. The oxime functional group is a double bonded carbon and nitrogen with a nitrogen bound hydroxyl.

These functional groups are formed from aldehydes and ketones by condensing them with hydroxylamine. The general reaction equation is shown in (FIGURE A.2).

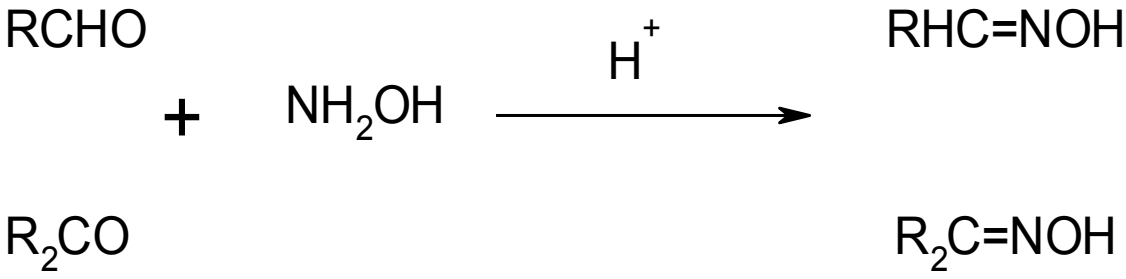

FIGURE A.2. Oxime synthesis from Aldehydes and Ketones.

The reaction begins with nucleophilic addition to the carbonyl group. The lone pair of the amine will attack the carbon of a carbonyl group on the molecule. The addition product is in equillibrium with the original reactants. In the next step, protonation of the anionic oxygen occurs in one part of the molecule while a proton is also lost from amine adduct. The hydroxyl group created in this process is a very

poor leaving group. Further protonation of the hydroxyl group makes it into a very good leaving group. Subsequent loss of the water allows the coordination of the lone pair on the amine to donate to the carbenium left by the dehydration. The result is a positively charged bioxime. Upon abstraction of the remaining hydrogen of the bioxime leaves the target oxime molecule. The detailed reaction mechanism with curly arrows is pictured in (FIGURE A.3), where B is a proton acceptor. Because of the geometry of nitrogen, if the parent is an aldehyde or an asymmetrical ketone, two stereoisomers of oxime are possible shown in (FIGURE A.4).

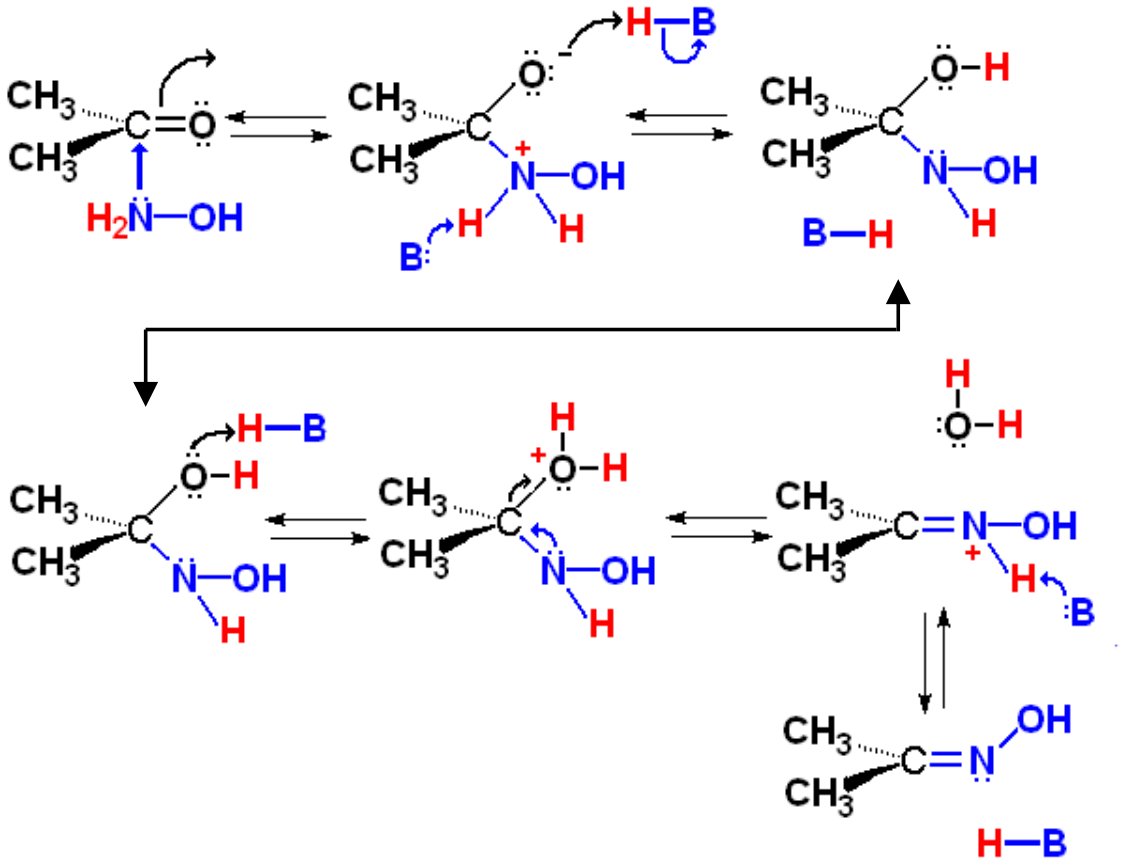

FIGURE A.3. Detailed reaction mechanism of Oxime synthesis with curly arrows, where B in the case of our reaction is $BaCO_3$.

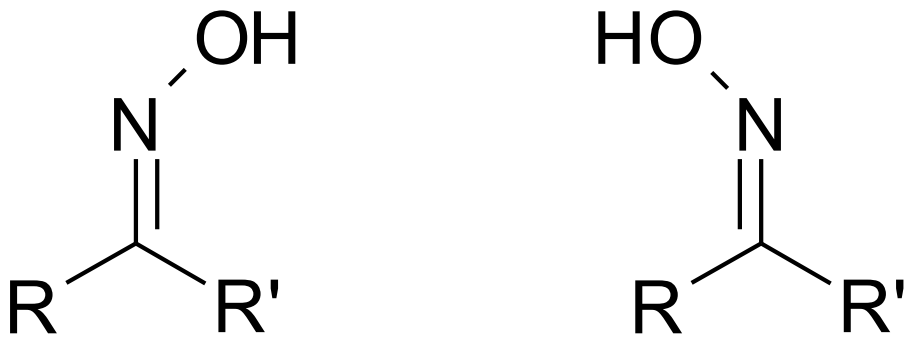

FIGURE A.4. Two oxime stereoisomers from asymmetrical parent carbonyl.

From this reaction two types of oximes can be synthesized; aldoximes, a combination of aldehydes with hydroxylamine and ketoximes, a combination of ketones with hydroxylamine. The product, 5,6-dioxime-1,10-phenanthroline, discussed in section 2 is a cyclic di-ketoxime. Oximes can be either colorless liquids or cystaline solids. They are both basic due to the oxime nitrogen and acidic due to the hydroxyl group. The duel basic and acidic character is what makes the synthesis of 5,6-dioxime-1,10-phenanthroline so sensitive to pH and is why in our reaction we chose to use hydroxylamine hydrochloride to control the free base hydroxylamine. In dilute mineral acids they are hydrolyzed producing reactive species which can recombine into other products, often times reproducing the hydroxylamine and the original aldehyde or ketone. The chemistry which is pertinent to this work is the reduction of the oxime to produce primary amines.

APPENDIX B: SWCNT DIMENSIONS AND DISPERSION CONCENTRATION

B.1 Differences Between HiPco and CoMoCAT SWCNTs.

As produced high-pressure CO conversion (HiPco) synthesis and Co-Mo catalysis (CoMoCAT) synthesis single-walled carbon nanotubes can vary significantly in their chiral distribution. HiPco produced SWCNTs are polydisperse, containing two-thirds semiconducting and one third metallic chiralities, while the CoMoCAT synthesis technique is far more tunable to selectively produce large quantities of single chirality SWCNTs. The SG65 branded SWCNTs (South West Nano Technologies) used in our study contain >90% nanotubes that display semiconducting properties and >50% of those are in the (6,5) chiral configuration. Previous work by our group established characterization protocols in which UV-vis-NIR spectra are calibrated to measure the concentrations of HiPco SWCNT (Carbon Nanotechnologies Inc. Grade P) dispersions.[4,9]

B.2 UV-vis-NIR Spectra and Extinction Coefficients

Differences between the dispersions of HiPco and CoMoCAT are shown by UV-Vis-NIR spectroscopy (FIGURE B.1). FIGURE B.1 is an overlay of the UV-Vis-NIR spectra of the HiPco and SG65 SWCNTs. The van Hove singularities are attributed to the near one-dimensionality of the nanotubes[169] and can be used to highlight the differences in chirality distribution between the two samples. FIGURE B.2 is the density of states (DOS) for both metallic and semiconducting SWCNTs that are the electronic transitions from the valence to conduction bands. The corresponding transitions are labeled on the spectra in FIGURE B.1. With respect to

identical transitions in the HiPco sample, both the first and second semiconducting transitions of the SG65 are blue shifted. The peak near 1000 nm indicates a large percentage of (6,5) semiconducting SWCNTs in the SG65 sample. SWCNT dispersion quality can be evaluated by the ratio of peak heights of the van Hove singularities and the underlying π-plasmon absorption.[2,170] The amplitude of the peak corresponds to the relative amount of a given chirality present in dispersion. From the tight binding approximation,[2] absorption wavelength should vary linearly with the semiconductor tube diameter by the relationship

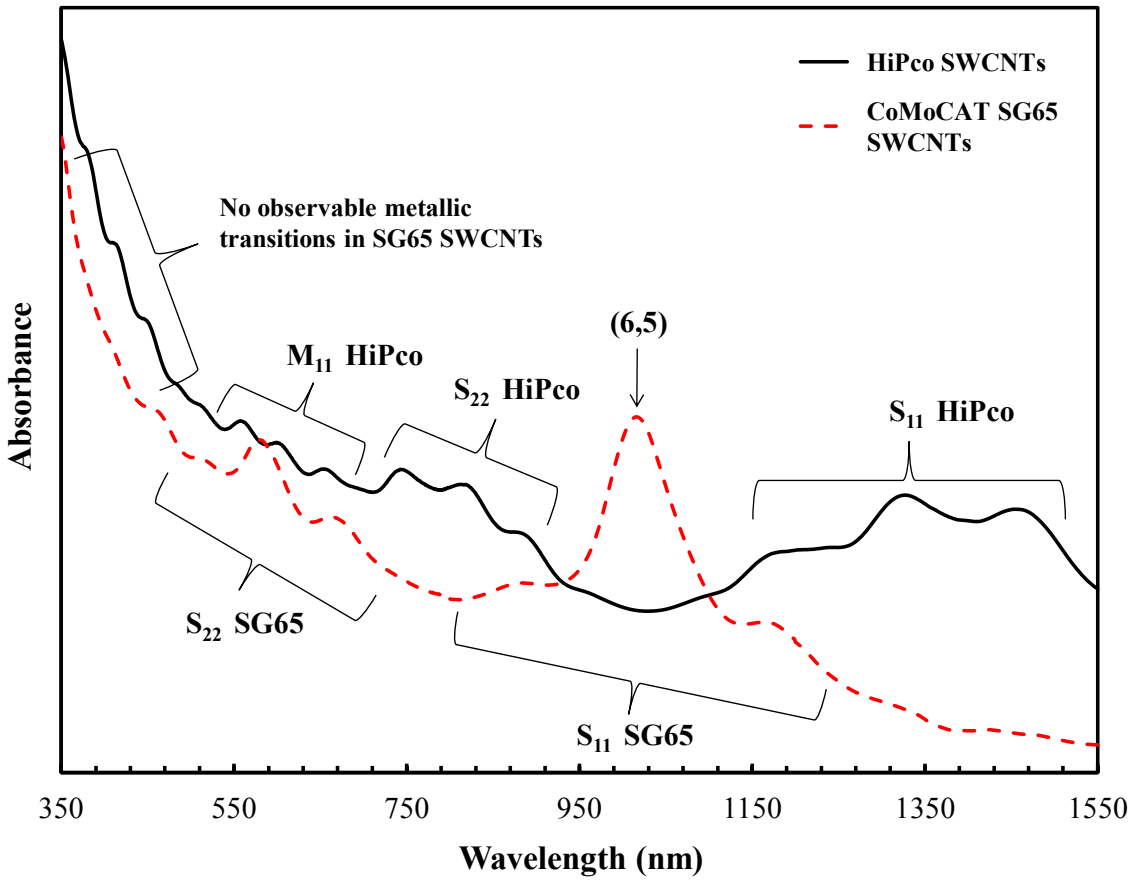

FIGURE B.1. UV-visible-NIR absorbance spectra of a HiPco SWCNT dispersion (black solid line) and a CoMoCAT SG65 dispersion (red dashed line). Both samples are dispersed in dry DMF.

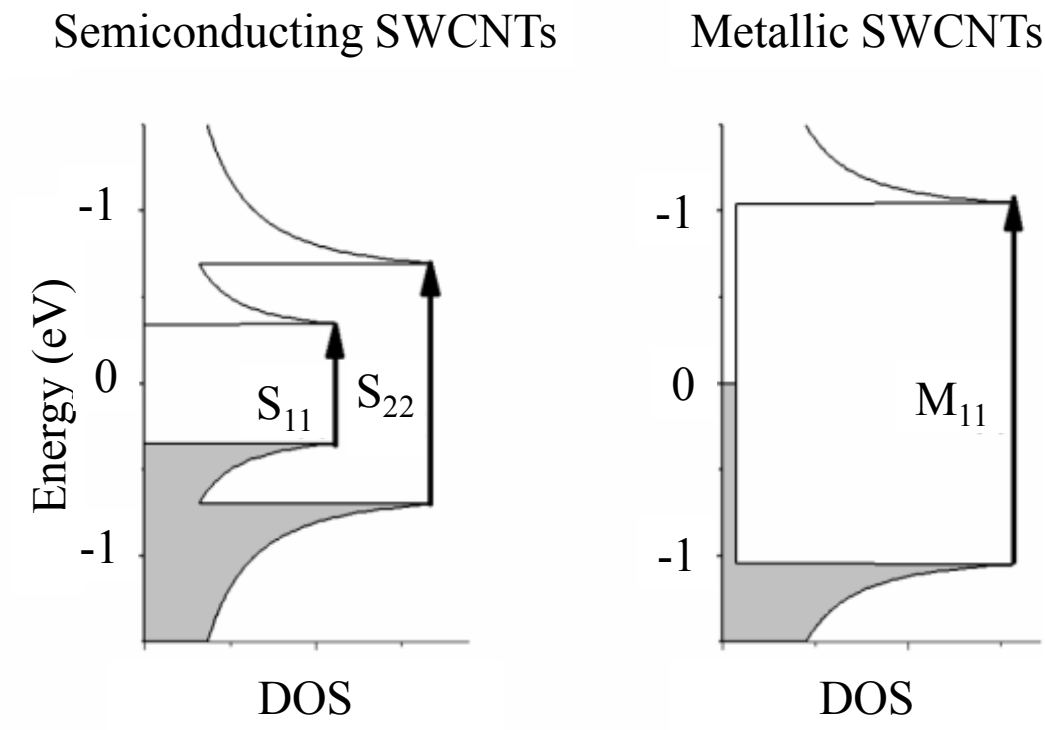

FIGURE B.2. Density of States (DOS) for semiconducting and metallic SWCNTs.

$$\lambda_{11} = \frac{hcd_t}{2a_{c-c}\gamma_0} \quad \text{(B.1)}$$

where a_{c-c} is the C-C bond distance measured to be 0.142 nm, γ_0 is the interaction energy 2.7 eV, and d_t is the tube diameter (nm). By rearranging equation (B.1) the diameter, and subsequently the chirality attributed to an individual peak can be determined by λ_{11}, the absorbance wavelength of the 11 transition;

$$d_t = [(6.184 \times 10^{-4})\lambda_{11}]^{1/1.3} \quad \text{(B.2)}$$

There are both semiconducting and metallic electronic transitions present in the HiPco spectrum, while no obvious metallic transitions (λ < 500 nm) are observed in the SG65 spectrum. This confirms that the SG65 sample has a much higher concentration of semiconducting SWCNTs when compared to the HiPco sample.

Determining the extinction coefficient for the SG65 SWCNTs was carried out in DMF using a UV-visible-NIR spectrometer. Beer's Law directly relates absorbance from a UV-Vis-NIR spectrum to concentration of the sample by equation (B.3).

$$A = \varepsilon bc \quad \text{(B.3)}$$

where A is the measured absorbance, ε is the extinction coefficient and b is the distance (cm) that the beam of light travels through a sample with concentration c. At a constant path length, the extinction coefficient is therefore a measure of how well a solution or dispersion absorbs light at a particular wavelength as a function of concentration. To created a calibration curve a dispersion of SG65 SWCNTs in DMF was prepared by the following procedure.

20 ml of dry DMF (sparged with argon to remove any dissolved air) is added to ~

0.4 mg of nanotube powder. The mixture is ultrasonicated for 30 minutes at 10 W (RMS) (Fisher Model 60 1/8" probe tip). Care must be taken regarding the length of ultrasonication in DMF. Exposing the DMF to excess ultrasonication can breakdown DMF into free radical forms which instigate aggregation of the dispersed SWCNTs.[60] The dispersion is then ultracentrifuged (Beckman Optima XL-100K) at 14500 rpm (~ 20000 g) for 20 min to remove any large aggregates. The supernatant dispersion is then carefully collected and ultrasonicated again for 10 minutes at 10 W (RMS). The final dispersion is used as the stock solution for the subsequent serial dilutions and measurement in the spectrometer. To determine the exact concentration of the stock dispersion, a volume (± 0.1%) was filtered through a 0.2 μm pore size PTFE filter and dried overnight in a vacuum oven. The mass of the filter was subtracted from the measured weight after filtration and drying and from that mass the concentration of SWCNTs (mg) per volume of DMF (L) was determined. FIGURE B.3 shows the extinction coefficients for a SG65 dispersion in DMF plotted as a function of wavelength. The 825 nm extinction coefficient (ε = 0.0200 $A(mg/L)^{-1}(cm)^{-1}$) was determined to be a best fit to a Lorentzian curve and was used in this study, as it better corresponds to the absorbance of the whole sample rather than a single chirality.[170]

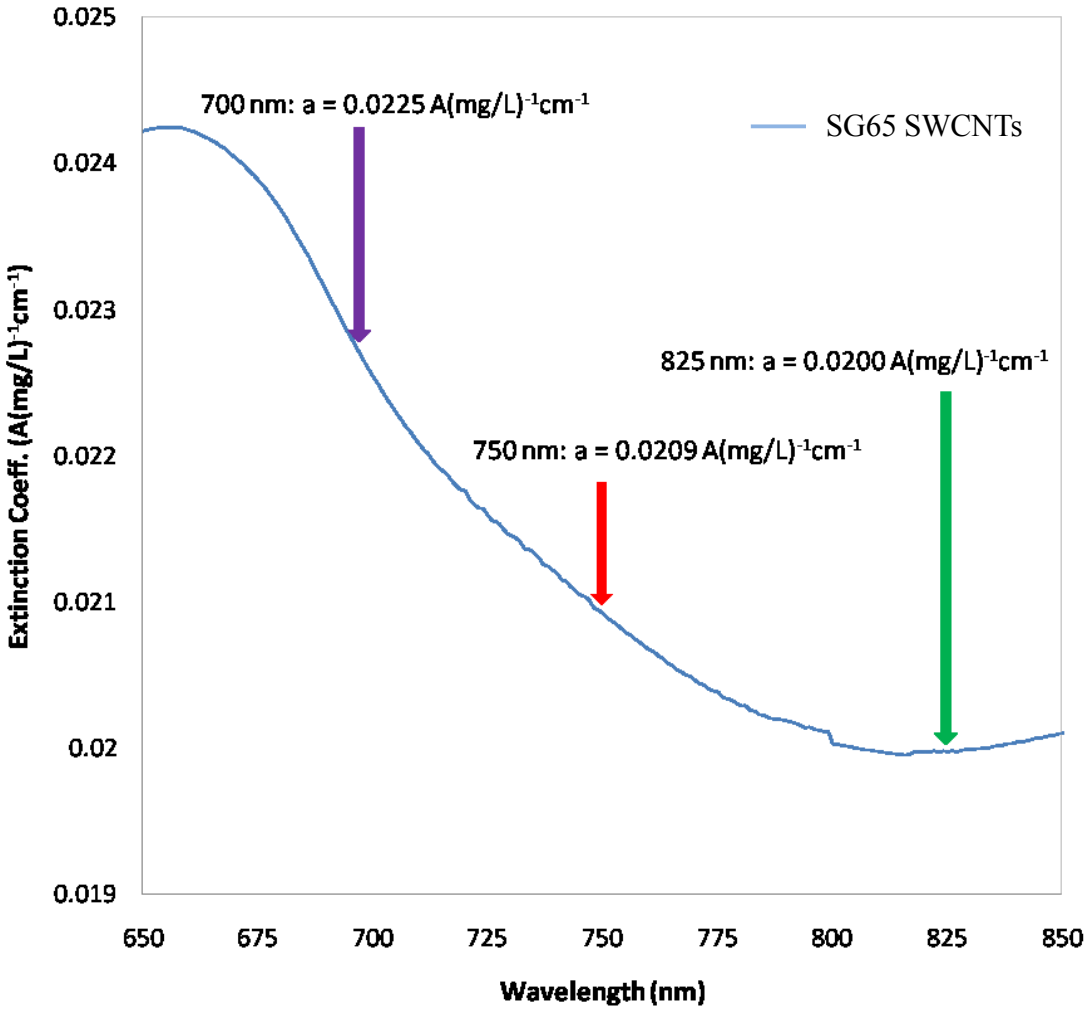

FIGURE B.3. Extinction coefficient as a function of wavelength for the SG65 SWCNTs in DMF.

B.3 Specific Surface Area of CNTs for Stoichiometric Measurements.

The molecular weight of a carbon nanotube is commonly thought of as a difficult value to assign, mostly because of the various lengths, widths and layers of carbon which can make up a carbon nanotube and cause the mass of tube to vary widely. To begin making measurements involving CNTs and to calculate thermodynamic values that are classically determined on a per mole basis, it is helpful to define a molar value that is not dependant on the three variables mentioned above. As with well defined molecules, the molar weight of a nanotube can be directly related to its mass. This can be accomplished by relation to the unit cell and the theoretical maximum specific surface area (SSA) of a single-walled carbon nanotube (SWCNT) as determined by Peigney et al.[57]

The work of Peigney et al. makes theoretical predictions of the external surface area of single- and multi-walled carbon nanotubes.[57] These predictions are in good agreement with microscopic characterization and the specific surface area measurements of carbon nanotubes that were previously made in the literature. By Peigney's relationship, the SSA of a SWCNT is related to the surface area, S_h, and weight, W_h,of a single graphene hexagon. The surface area of a graphene hexagon is given by

$$S_h = 3d_{C-C}^2 \frac{\sqrt{3}}{2} = 5.246 \times 10^{-20}\ m^2 \tag{B.4}$$

where d_{C-C} is the bond length of the carbon atoms that define a graphene hexagon (unit cell),[58] so that the area for each hexagon in a graphene structure has the weight W_h, so that

$$W_h = \left(\frac{2M_C}{N_A}\right) = 3.988 \times 10^{-23}\ g \quad \text{(B.5)}$$

M_C is the atomic weight of carbon and N_A is Avogadro's number. From equation (3.1) a fundamental unit of SWCNT surface area can be defined as

$$SWCNT_{\mathrm{A}} = S_h \times N_A = 31591\, m^2/mol \quad \text{(B.6)}$$

and the mass per mole of any length or diameter SWCNT, M_{SWCNT}, is given by

$$M_{SWCNT} = SWCNT_{\mathrm{A}} \frac{W_h}{S_h} = 24.02\ g/mol \quad \text{(B.7)}$$

From equation (B.7) it is now possible to assign a molar value to dispersions of SWCNTs that are typically measured mass per volume units. Because the theoretical maximum SSA of SWCNTs is directly related to the mass, M_{SWCNT} provides useful information and gives physical meaning to a concentration of SWCNTs. M_{SWCNT} relates measurements to the unit cell of graphene, illustrated in (FIGURE 3.5), which can be used to standardized observations across different experiments with different fullerene analytes. In the context of binding isotherms and titration calorimetry, stoichiometry, n, and binding constants, K, can be related to the available surface area of a dispersion, and allows units to cancel properly within equilibrium equations when SWCNTs are involved.

APPENDIX C: ELECTROCHEMICAL ANALYSIS

C.1 Electroanalytical Conventions

There are two conventions used for the presentation and discussion of data in the electrochemical field, the older polarographic (American or classical) convention and the newer IUPAC (European) convention. In contrast to most fields of study in the scientific community, the IUPAC standard has not been widely adopted for electrochemical analysis in the United States of America. So it is important to understand the differences in the conventions because both are presented regularly. FIGURE C.1 illustrates the differences of the two conventions. While both conventions plot potential on the x-axis, the polarographic convention (left) is plotted on an atypical x-axis with positive potential values on the left while experimental "runs" are typically scanned from positive working electrode potentials to more negative working electrode potentials on the right. The IUPAC convention is opposite the polarographic, with runs scanning from negative potential to positive potential on the right.

A difference in the mathematical sign attributed to current direction is the largest source of confusion when comparing IUPAC and polarographic conventions. It is helpful when digesting the convention differences to first understand that the types of electrochemical reactions and the naming of electrodes at which they occur is consistent. In both cases the terminology for electrochemical processes which occur at the working electrode are referred to as anodic (oxidative) or cathodic (reductive).

The working electrode in a cyclic voltammagram (polarogram) behaves both as a cathode or an anode

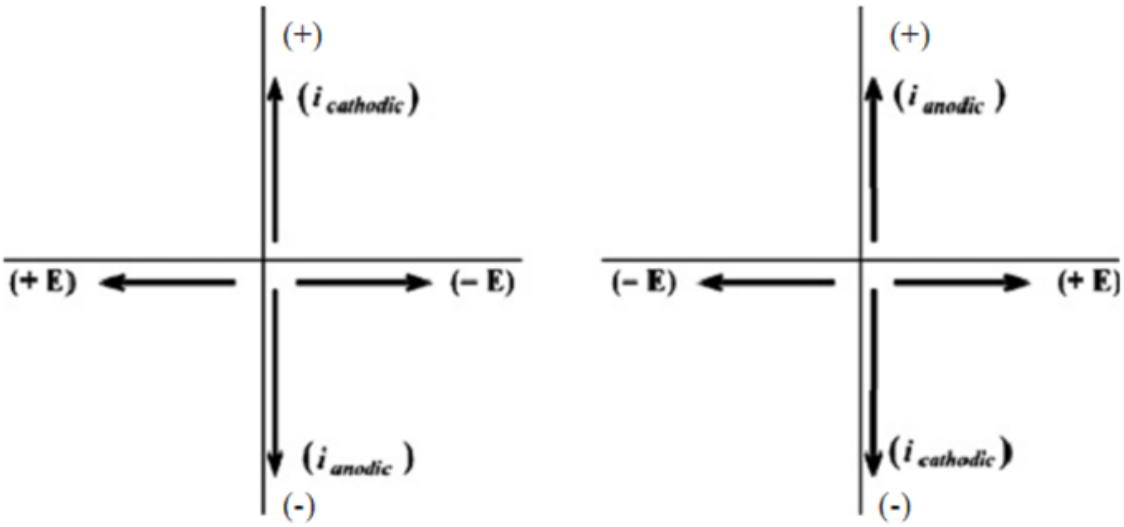

FIGURE C.1. Voltammetry (Polarography) Conventions. Polarographic (American) left. IUPAC (European) right.

depending on the potential at which it is held. Anodes and cathodes are named as such because of the observation that in an electrolyte solution, anions diffuse towards the anode electrode and cations diffuse towards the cathode electrode.

The discrepancy in current value interpretation (positive or negative) is due to the history of our understanding of electricity and charge carriers. The polarographic convention, often called "American", is typically attributed to Benjamin Franklin, a well known American scientist. Mr. Franklin imagined electricity as a fluid. He, like many scientists of his day, pictured an electrode with excess fluid (electricity) and described it as full or positive. Current resulted when excess fluid would flow "downhill" to the less full (negative) electrode. This early definition turned out to be the opposite of what is physically occurring when current flows, however the convention persists even more than 100 years after English physicist and Nobel laureate J.J. Thomson discovered the electron in 1897. FIGURE C.2 is a helpful illustration depicting the polarographic standard, where the pre-electron understanding of current consequently gives positive values to the movement of electrons out of the working electrode (reductive or cathodic) and negative current to the movement of electrons into the working electrode (oxidative or anodic).

Our modern understanding of electricity tells us that the main carrier during charge movement (current) is electrons, and in an electrolytic cell also due to the subsequent movement of ions. IUPAC convention defines current by understanding the direction of electron flow into and out of the working electrode. There-by positive current is attributed to the flow of electrons into the working electrode (anodic current) and the oxidation of reactants at the surface, and negative current as

the flow of electrons out of the working electrode (cathodic current) reducing reactants at the surface.

C.2 Common Misconceptions

An equally important concept to understand is that there is no correlation between positive and negative potentials and oxidations and reductions. Reversible redox couples often have oxidation peak potentials (E_{pa}) and reduction peak potentials (E_{pc}) that occur near the same electrode potential. The formal reduction potential ($E^{o'}$) for a reversible couple is centered between the anodic (E_{pa}) and cathodic (E_{pc}) peak potentials.

$$E^{o'} = (E_{pa} + E_{pc})/2 \qquad \text{C.1}$$

Because potential values are quoted relative to a reference electrode potential, which in turn is relative to an arbitrary zero (standard hydrogen electrode), reductions can occur at positive potentials and oxidations can occur at negative potentials.

It is often erroneously assumed that the cathode and anode always have the mathematical signs positive and negative associated with them. The assignment of mathematical sign actually depends on the type of cell being observed; whether it is a spontaneous, galvanic system such as a battery, or an electrolytic cell with current or potential driving a reaction.

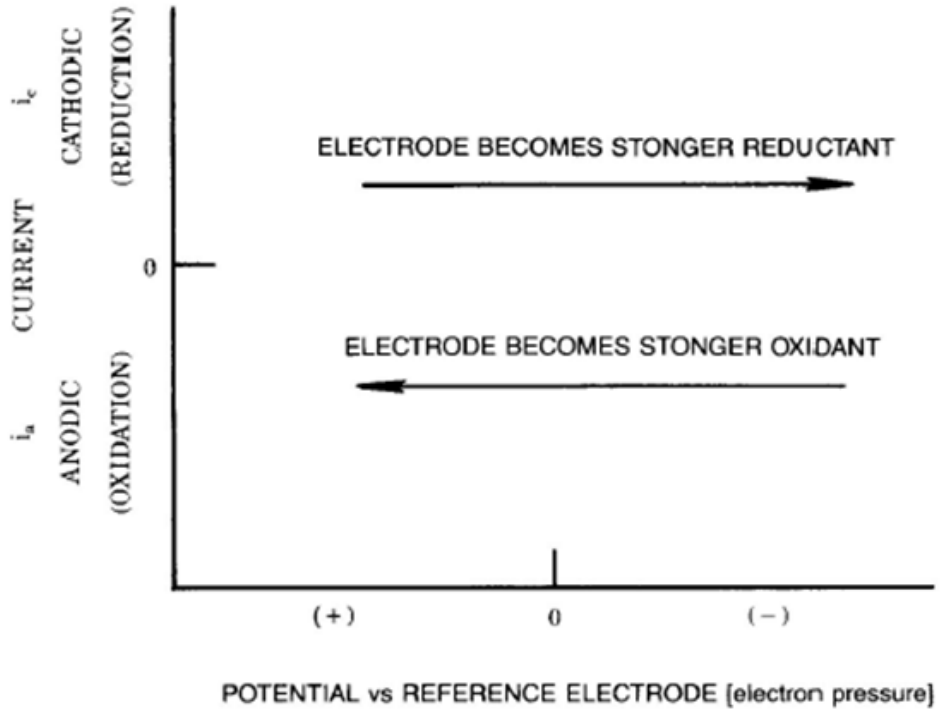

FIGURE C.2. The polarographic (American) convention for plotting voltammetry data.

APPENDIX D: CLEANING PROCEDURES AND PURIFICATION

During this work it quickly became apparent that to have reproducible results and establish reliable techniques everything must be clean. From clean tools to clean glassware to clean substrates, the difference between a bright red ruthenium complex and black/green insoluble goo could simply be a dirty round bottom flask. And the difference between a transparent and attached SWCNT film and a flakey peeling mess could be 10 min of sonication in a clean solvent. Those examples and many others are the fruit of many hours (days) of trial and error. The purpose of this appendix is to pass along the cleaning techniques and procedures which have served this work well. The following section should provide the basic instructions to allow anyone to maintain and clean the various glassware, slides and tools that are used in everyday lab work. However, even with a perfectly clean setup sometimes things just don't work. When this happens, refer back to this section; make sure a set was not missed.

D.1 Procedure for Washing Glassware

First and foremost, rinse out glassware soon after use so the minimal amount of contaminant remains and then place it in the appropriate glassware tray.

D.1.1 General Cleaning Procedure

1) Put away glassware from the rack. If you do not know where something goes, ASK. Do not put glassware just anywhere. The next person that needs it may never find it.

2) Unload the base bath. This involves taking out each piece of glassware and individually rinsing it with tap water, followed by dilute HCl then D.I. water. Hang it on the rack to dry.
3) Unload the acid bath and transfer its contents to the base bath. Each piece of glassware must be rinsed with water and then isopropanol (IPA) before being transferred to the base bath. Frits and pfrom the acid bath are not transferred to the base bath. Simply rinse them with copious DI water and place them on the try to dry. **Glassware must be completely submerged in the baths. Glass floating on the top does not get clean.**
4) Wash "organic" glassware with soap and water, followed by acetone, and a final rinse methanol. If more cleaning is needed. Follow advanced "organic" cleaning methods detailed bellow.
5) Load "inorganic" glass into the acid bath. Each piece must first be cleaned with soap and water and followed by acetone to prevent excessive contamination of the acid bath. Ink must be removed from the glassware before introducing it in the bath. **NO** plastic or rubber items may be placed in the baths.

D.1.2 Specific Glassware Cleaning Procedures

D.1.2.1 Organic Glassware

This is glassware which was used solely for organics. Organic glassware should be attempted to be cleaned with Alconox or Simple Green and warm water followed by rinsing with acetone. If this does not adequately clean the glassware then it

should be cycled through the base bath (about 6-8 hours should be sufficient, but can be left overnight) and if necessary cycled through the acid bath.

Before putting glassware in the base bath one should rinse with IPA, since NO WATER SHOULD BE TRANSFERRED TO THE BASE BATH.

D.1.2.2 Inorganic Glassware (Any metal complex synthesis w/ or wout/ Organics)

Inorganic glassware is any glass which has been treated with metal. The procedure for washing metal-containing glassware is different from organics and should be strictly followed to remove the trace metal from the surface of the glass. **Cyclization through both the acid and base baths is ABSOLUTELY necessary** and should begin with the acid bath followed by the procedure as described in the "organic" washing procedure. It is most important for this glassware to be scrubbed before being placed in the acid bath, to avoid the buildup of metal contaminants in the bath.

D.1.2.3 NMR tubes

Again, prompt rinsing with acetone or alcohol should be done immediately. In many cases this is all that is necessary. If the tube is still dirty, it should be rinsed with dilute HCl, water, and acetone. If this is ineffective, try a pipette or two of the base bath solution, followed immediately by dilute HCl, water, and acetone. If solid still remains, the tube can be scrubbed out with a pipe cleaner.

***Note: NMR tubes should NOT go in the base bath!**

D.1.2.4 Fritted Funnels

DO NOT soak frits in the base bath, as this will corrode the fritted glass material. If you have been using a frit with purely organic compounds or with Celite you

should scrub it and rinse it through with water, alcohol, and acetone immediately after use, and return it to the drawer. Only those frits that cannot be cleaned in this way, particularly those that have insoluble metal contaminants, should be treated in the following manner:

1) Try washing through with dilute HCl.
2) If this fails, try washing through with NoChromix cleaner. (we currently do not have this)
3) If this fails, use the **singlet oxygen procedure** below. (piranha etch)
4) In each case, thorough rinsing with water and alcohol, followed by air-drying, should be performed.

D.1.2.4.1 Singlet oxygen procedure: (DANGER! DO NOT attempt this for first time, without instruction)

1) make sure the frit to be cleaned is dry, and that there are **NO** organic solvents around.
2) add to the frit a little conc. sulfuric acid (1-2 mL)
3) add a little 30% hydrogen peroxide (about 1 mL), and swirl to mix **(generates heat, can spatter)**
4) add a squirt of Clorox (dilute sodium hypochlorite) solution and swirl **(generates a lot of heat!)**
5) pull the mixture through the frit by vacuum. Make sure **ALL GLASSWARE** has no organic material, it can ignite in the strong oxidizing conditions of this procedure.
6) Rinse the frit well with water

D.1.3 Preparation of Acid and Base Baths

D.1.3.1 Preparation of Acid Bath

The acid bath contains 10% aqueous HCl, and should be filled to about half full.

D.1.3.2 Preparation of Base Bath

1) Put on thick black gloves and eye protection!
2) Use the Square Teflon Container
3) Add approximately 200-300g of solid KOH pellets
4) Add 4 L of IPA (get reagent grade from stockroom, don't use HPLC)
5) Carefully add 1L of deionized water
6) Leave the bucket in secondary containment (i.e. sink) until KOH is dissolved and it has cooled back to room temperature before storing

D.1.3.3 Removing Glassware from Baths

1) When removed from the base bath: Glassware should be rinsed with warm tap water, dilute HCl acid, then DI water and hung on the rack to dry.
2) If Removed from Acid Bath: Glassware should be rinsed with warm tap water, and DI water, and hung on the rack to dry.

***Always use eye protection and thick black gloves when manipulating glassware around the basebath! Rinse gloves after use to prevent spreading KOH all over your work area.**

***Note: base bath will destroy glass fritted funnels and NMR tubes. Refer to noted sections for alternative cleaning procedures**

D.1.4 Cuvettes used for Ru Complex Measurements - Cleaning Method

This procedure is best done, both before first use and after the measurement of μM concentrations or higher of Ru Complexes.

1) Rinse with Acetone (x3)
2) *Bath Sonicate with Acetone in Cuvette (10 min)
3) Dry Cuvette with N_2
4) *Bath Sonicate with 10% $HCl_{(aq)}$ (10 min)
5) Rinse Copiously with DI H_2O
6) Rinse with MeOH (x3)
7) Dry Cuvette with N_2

*Bath sonication has proven to be destructive to the joints of some glass and quarts cuvettes. These steps should only be used as a last case scenario, if the cuvette surface is contaminated beyond repair and the cuvette would have to be discarded anyway.

*In place of bath sonication, these steps can be replaced with prolonged soaking (3 – 24 hours).

D.2 Glass Substrate and ITO coated Glass Cleaning Procedure

A large portion of this work with SWCNT films involved transferring and adhesion of the films to glass and ITO coated glass substrates. All surfaces that have not been cleaned by a method as effective as those in this section have a large amount of environmental gunk on their surface. This gunk is mostly organic residue and water, but can also include dust and other inorganic particles. Water will always be on the surface because it is so abundant in normal atmospheric conditions. However, we can remove the other debris that has built up on the surface of a substrate and it is necessary for van der Walls contact and strong adhesion of the SWCNTs to the surface.

D.2.1 Cleaning Glass Substrate (Piranha etch)

1. Mix a solution of piranha etch (3:1 H_2SO_4:H_2O_2)
    a. When preparing the piranha solution, always add the peroxide to the acid. The H2O2 is added immediately before the etching process because it immediately produces an exothermic reaction with gas (pressure) release.

       *Caution!: If the H_2O_2 concentration is at 50% or greater, an explosion could occur.
2. The hot solution will clean organic compounds off substrates, and oxidize/hydroxylate most metal surfaces.
3. Cleaning requires 10 to 40 minutes
4. After cleaning the substrates can be removed from the solution and rinsed until the etchant has been removed

D.2.2 Cleaning ITO coated Glass

1) Label the substrate using a glass scribe.
2) Arrange the ITO glass inside the vial labelled 'For cleaning ITO – acetone'. Alternatively instead of using a vial, place the ITO glass face up inside the beaker.
3) Place the place in the fume hood and pour acetone into the vial to a level above the substrates, so that the substrates are immersed in solvent.
4) Seal the vial with a cap or the beaker with a piece of foil.
5) Place vial in a bath sonicator and sonicate for 10 minutes.
6) After this step, remove a substrate with a clean tweezer and blow-dry the substrate with the compressed nitrogen
7) Repeat step 2, but this time label 'For cleaning ITO – IPA only'.
8) Pour isopropanol into the vial to a level above the substrates.
9) Cover and sonicate for 10 minutes.
10) Remove a substrate with a clean tweezer and blow-dry the substrate with the compressed nitrogen*

*Note: If immediately attaching a nanotube film, rinse the substrate and wet with the appropriate solvent.

D.3 ITC Cleaning Procedures

D.3.1 Simple Cleaning and Checking for "Clean"

1) Using the filling syringe, remove sample cell contents.†
2) Rinse/Flush sample cell with clean solvent that will be used in the following experiment.
3) Repeat flushing process a minimum of 10 times (20 recommended).
4) Flush sample cell 2 more times with clean, degassed solvent
5) Load sample cell with 300 µL clean, degassed solvent
6) Rinse/Flush burette syringe with clean solvent that will be used in following experiment.
7) Repeat flushing process a minimum of 10 times (20 recommended).
8) Flush burette syringe 2 more times with clean, degassed solvent
9) Fill burette syringe to capacity (>50 µL), then remove and replace the plunger to introduce a 2-3 µL cushioning bubble.
10) Load burette syringe into burette handle
11) Insert burette syringe-burette handle into the ITC
12) Monitor signal in the signal window. When the signal in returning to baseline, close the ITCrun software for 30 seconds. (As of writing this dissertation this is the only way to reset data collect for the baseline. Hopefully in the future this will be a software feature.)
13) Reopen ITCrun. Load solvent-solvent titration experiment. Run solvent-solvent titration.*

D.3.1.1 Typical Solvent-Solvent Titration Parameters

- 10 – 2 μL injections (1st injection 1 μL)
- 200 second injection intervals
- 350 RPM stirring speed
- 25 °C
- "small" heat expectation auto equilibrate
- Initial baseline 200 seconds
- Final baseline 100 seconds

D.3.1.2 Expected Results

Solvent-solvent titrations should result in small exothermic peaks, with no endothermic processes. The only evolution of heat will be due to the small frictional heat generated during injection. (FIGURE D.1) is an example of a clean solvent-solvent titration using N-methyl pyroladone (NMP) as the solvent. If endothermic processes are present in the raw signal or excessive exothermic heat is present compared to **(**FIGURE D.1**)**, repeat the rinsing process described above and repeat the solvent-solvent titration until it looks similar to (FIGURE D.1). Different solvents will have slightly different frictional heats during injection, but all solvent-solvent titrations should be only exothermic and look very similar to (FIGURE D.1).

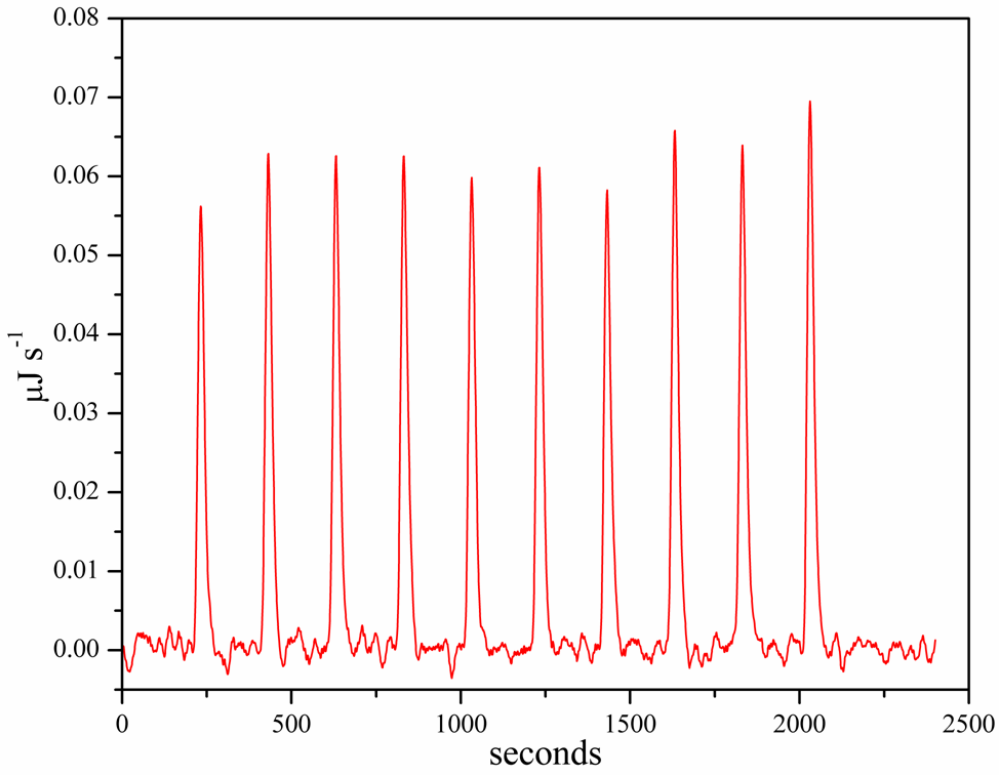

FIGURE D.1. Titration of Clean NMP into Clean NMP.

†: If the solvent is being changed between experiments, refer to section D.3.2 Rigorous Cleaning and Switching between Solvents

D.3.2 Rigorous Cleaning and Switching between Solvents

When working with sticky ruthenium complexes or other analytes that may be left behind in the ITC sample cell, ie., proteins, polymers, and maybe carbon nanotubes, it will be necessary to clean the system more rigorously than simple solvent rinsing once in a while. This process involves the use of aqueous acid and base solutions, so in this section the techniques I used to switch between organic and aqueous solvent is presented.

D.3.2.1 Switching from Organic to Aqueous Solvent

1) Using the filling syringe remove the organic solvent from both the sample and reference cells
2) With a low residue, low boiling point solvent, miscible with the organic solvent being removed (methanol works well for DMF and NMP), and the filling syringe rinse the reference cell a minimum of 10 times (20 recommended).
3) With same low res., low BP. solvent use the cleaning apparatus to flush the sample cell with 1 liter of solvent. (for instruction and proper use of the cleaning apparatus refer to the manual for the TA Instruments NanoITC or the TA website)
4) After flushing the sample cell, remove any excess solvent from the cells by increasing the cell temperature to 70 °C for 1 hour.
5) Reduce temperature back to 25 °C.
6) With the filling syringe rinse both cells with 18 MΩ water a minimum of 10 times.*

   *Note: To switch the system from aqueous to organic solvent reverse the above procedure. If the final intention is to switch the system between solvents, stop here and refer to section D.3.1 Simple Cleaning and Checking for "Clean" to check the system for cleanliness.

D.3.2.2 Rigorous Cleaning

1) After switching the system to an aqueous environment, use the filling syringe to remove the water from the sample cell.
2) Fill the sample cell with 4 M $NaOH_{(aq)}$ (500 µL) and set the cell temperature to 60 °C.
3) Let the cell soak at 60 °C for 3+ hours
4) After soaking, remove the NaOH and use the filling syringe to rinse the sample cell with DI water a minimum of 10 times.
5) Then use a 50% formic acid solution to rinse the sample another 10 times (minimum)
6) Use the cleaning apparatus to run 1-2 liters of DI water through the sample cell
7) Check the system to see if it is clean (refer to section D.3.1 Simple Cleaning and Checking for "Clean")

D.4 Basic Recrystallization Procedure

Recrystallization is a laboratory technique used to purify solids based on their different solubility. To perform a recrystallization a small amount of solvent is added to a flask containing an impure solid. The contents of the flask are then heated until the solid dissolves. Once the solid is completely dissolved the solution is cooled. As a result a more pure solid precipitates, hopefully leaving impurities dissolved in the solvent. Vacuum filtration is then used to isolate the crystals, and the waste solution is discarded.

D.4.1 Summary of Recrystallization Steps

1) Add a small quantity of appropriate solvent to an impure solid.
2) Apply heat to dissolve the solid.
3) Cool the solution to recrystallize the product.
4) Use vacuum filtration to isolate and dry the purified solid.

D.4.2 Add the Solvent

Choose a solvent such that the impure compound has poor solubility at low temperatures, yet is completely soluble at higher temperatures. The point is to fully dissolve the impure substance when it is heated, yet have it crash out of solution upon cooling. Add as small a quantity as possible to fully dissolve the sample. It's better to add too little solvent than too much. More solvent can be added during the heating process, if necessary.

D.4.3 Heat the Suspension

After the solvent has been added to the impure solid, heat the suspension to fully dissolve the sample. A hot water bath or steam bath is typically used because they are gentle, controlled heat sources. A hot plate or gas burner can be used in some situations.

D.4.4 Cool the Solution

Once the sample is dissolved, cool the solution to force recrystallization. Slower cooling may potentially lead to a higher purity product, so it is generally a good idea to allow the solution to cool to room temperature before cooling the flask further in an ice bath or refrigerator.

Crystals should begin forming on the bottom of the flask. However, it is possible to initiate crystallization by scratching the flask with a glass rod at the air-solvent junction, or 'seed' the solution by adding a small crystal of the desired pure solid to the cooled solution. Be sure the solution is cool, or else the crystal could dissolve. If no crystals fall out of solution, it's possible too much solvent was used. Allow some of the solvent to evaporate. If crystals do not spontaneously form, reheat/cool the solution.

D.4.5 Separation / Filtration

Once crystals have formed purified solid is isolated by filtration. This is usually done with vacuum filtration, sometimes washing the purified solid with chilled solvent. If the product must be washed, be sure the solvent is cold, or else there is a risk of dissolving the sample. A final rinse with diethyl ether is helpful for drying the crystals.

The product is now dried. Aspirating the product via vacuum filtration should remove much of the solvent. Open-air or vacuum oven drying may be used as well. If needed the recrystallization may be repeated to further purify the sample

APPENDIX E: POSSIBLE SYNTHESIS ROUTES

(FIGURE E.1)

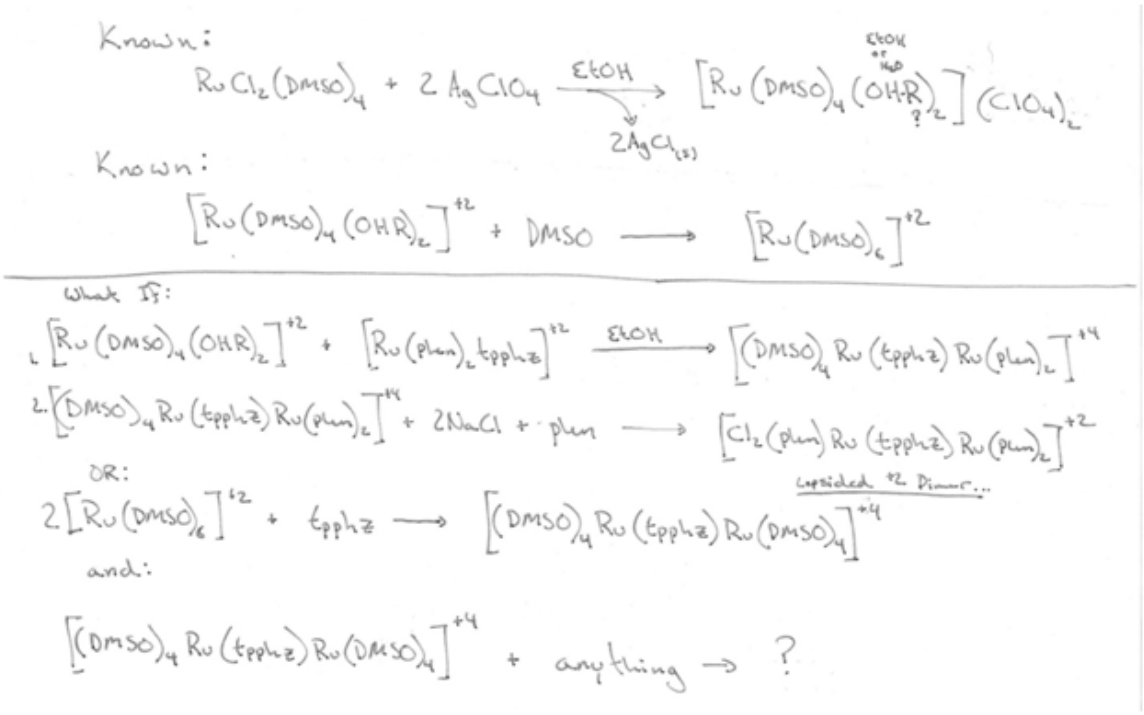

FIGURE E.1. Reaction Scheme for octokis DMSO cooridinated dinuclear Ru complex. Based on known reactions reported in, I. P. Evans, A. Spencer and Wilkinso.G, Journal of the Chemical Society-Dalton Transactions (2), 204-209 (1973).

(FIGURE E.2)

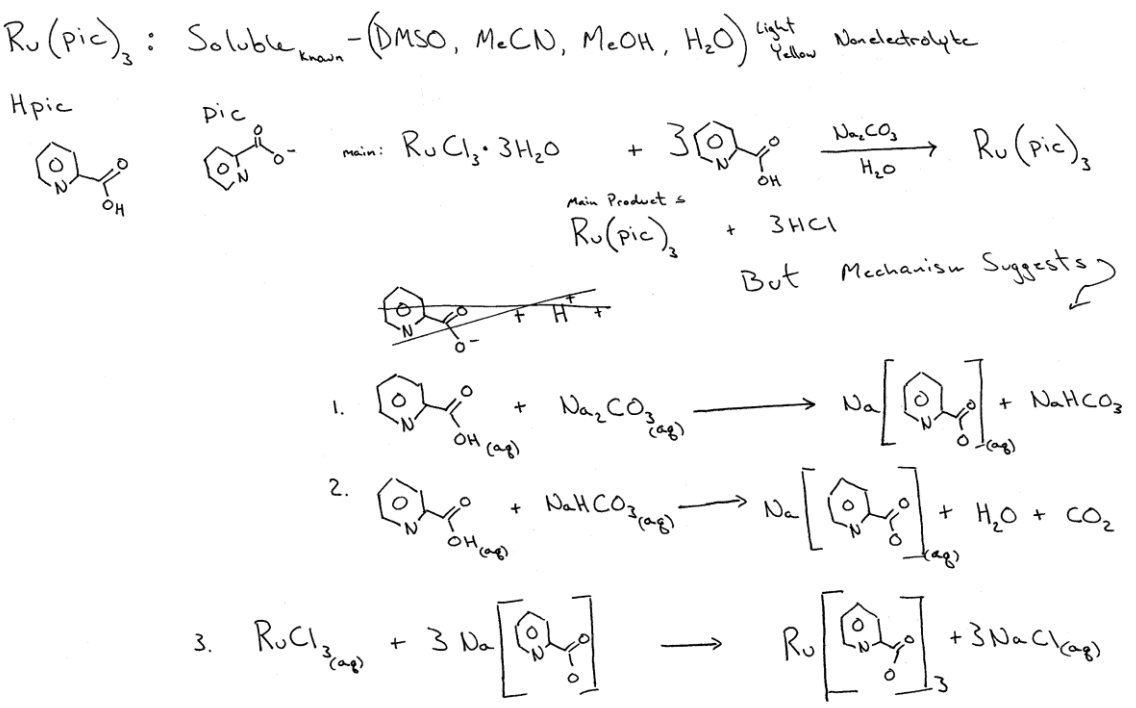

FIGURE E.2. Theoretical reaction scheme for tris-picalinato ruthenium, based on chemistry reported in Ghatak, N., Chakravarty, J. & Bhattacharya, S. Synthesis, Characterization and Electron-Transfer Properties of Some Picolinate Complexes of Ruthenium. Polyhedron 14, 3591-3597 (1995).